New Statistical Methods in Gravity and Magnetics

Von der Gemeinsamen Naturwissenschaftlichen Fakultät der
Technischen Universität Carolo-Wilhelmina zu Braunschweig

von Stefan Maus
aus Hamburg

angenommene Habilitationsschrift
zur Erlangung der Venia legendi für das Lehrgebiet Geophysik

Braunschweig
2001

Contents

Summary

Mapping the gravity and the magnetic field at the Earth's surface continues to be one of the most efficient ways to unravel subsurface structure and lithology. However, the interpretation of potential field data is complicated by the inherent non-uniqueness of the corresponding inverse problem, in the sense that completely different subsurface source distributions may give rise to the same field at the Earth's surface. In this situation a statistical approach can be helpful. Central to the statistical methods is a characterization of spatial variability of the fields and their sources by a spatial power spectrum. This power spectrum is useful in two ways, either as an estimated output, or as an *a priori* input. In the first sense, the power spectrum estimated from gravity and magnetic data can be used to identify different types of sources (Chapter 2), estimate maximum (Chapter 3) and minimum (Chapters 4-6) source depth, and identify data noise levels (Chapter 7). In the reverse sense, the presumed true power spectrum of the field or its sources may serve as an additional input in an inversion (Chapter 7) and can act as a guide to an efficient parametrization of a model space (Chapter 8).

Before discussing these methods and their applications, I define a 2D spatial power spectrum and derive its respective estimators in plane and spherical coordinates (Chapter 1). A conveniently defined spatial power spectrum is independent of the coordinate system and, to avoid mis-interpretation, has a flat spectrum for spatially uncorrelated white noise. In contrast, the spherical harmonic coefficient spectrum used in geomagnetism is incompatible between spheres of different radii and has an upward sloping white spectrum. To become independent of the spherical radius, the spherical spectrum is sometimes divided by the wavenumber in geodetic studies. Here, I propose a spherical spectrum which has a flat white spectrum and is compatible with the azimuthally averaged spectrum commonly used in plane coordinates. An interesting aside is that the new magnetic vector spectrum no longer creates the incorrect impression of a white noise field at the core-mantle boundary. I also derive a relationship for the estimation of the magnetic vector spectrum from total intensity data. Tests on synthetic and real data confirm the compatibility and demonstrate the utility of the various estimators. Using these estimators, power spectra can be compared not only in shape, but also in absolute terms, regardless of spherical radii, grid sizes and sampling intervals.

With the above definitions, the spatial power spectrum can be estimated globally from spherical harmonic coefficients, as well as locally from regional grids. In a study undertaken with Chris Tarlowski of the Australian Geological Survey Organisation (AGSO), we compare global spherical harmonic gravity and magnetic power spectra with their regional counterparts in Chapter 2. The global gravity spectrum has a bend at wavelengths of 1000 - 2000 km. Local high resolution free air gravity grids provide independent evidence for this bend. Most likely, it separates static from dynamically supported gravity anomalies. Turning to the magnetic field, we compare the global spherical harmonic magnetic power spectrum with local spectra estimated from continental aeromagnetic compilations, finding that the continental crustal magnetic field is significantly stronger than the global average. This could be due to the different thickness of the magnetized layer. Indeed, a depth extent of 30 km for continental magnetization versus 10 km for the global average would explain the discrepancy.

The effect of the limited depth extent of the crustal magnetization on the magnetic field is further analyzed in Chapter 3. The Earth's crust is magnetized down to the Curie temperature depth at about 10 km to 50 km. This limited depth extent of the crustal magnetization is discernible in the power spectra of magnetic maps of South Africa and Central Asia. At short wavelengths the power increases as rapidly towards longer wavelengths as expected for a self-similar magnetized crust with unlimited depth extent. Above wavelengths of around 100 km the power starts increasing less rapidly, indicating the absence of deep seated sources. To quantify this effect the theoretical power spectrum due to a slab carved out of a self-similar magnetization distribution is derived. This model power spectrum matches the power spectra of South Africa and Central Asia for a self-similarity parameter of $3.5 \leq \beta \leq 4$ and Curie temperature depths of 15 to 40 km.

Chapter 4 provides the theory for the high resolution mapping of source parameters using a spectral model which has been shifted to the space domain for improved performance. Model variograms describe the spatial variability of magnetic and gravity data in the sapce domain. Variogram analysis can be utilized to map intensity, depth and scaling exponent (self-correlation) of the source. In previous statistical methods the measured data were gridded, transformed to the wavenumber domain, and their power spectrum was analyzed using a spectral model. To avoid the loss and distortion of information during gridding and wavenumber domain transform, I transform the spectral model to the space domain, instead. Variograms are the appropriate space domain counterparts of magnetic and gravity power spectra. The variogram of the field above a self-similar half-space model is governed by three parameters: intensity, depth and scaling exponent. These source parameters can be mapped with high resolution and accuracy by fitting model variograms directly to magnetic and gravity line data variograms.

In collaboration with the helicopter group of BGR Hannover, this new variogram

analysis method has been applied to a number of synthetic and real magnetic data sets (Chapters 5 and 6). The geomagnetic field over sedimentary basins is very sensitive to variations in basement depth. Therefore, magnetic surveys are widely used to map basement topography in petroleum and groundwater exploration. We use variogram analysis as a more accurate alternative to the conventional power spectral methods. Data variograms are computed directly from the aeromagnetic flight line data. To estimate depth, the data variograms are compared with the model variograms derived in Chapter 4 for a range of source depths. Variogram analysis makes maximum use of the short wavelength magnetic signal, which is the key to the resolution of shallow basement topography. In Chapter 5 we map the basement topography of the Omaruru Alluvial Plains in Namibia. A comparison with EM resistivities and drilling information confirms the accuracy, but also shows the limitations of variogram analysis depth estimation. In a second study (Chapter 6), we further test the accuracy and resolution of the variogram analysis method on synthetic and real data. Synthetic magnetic flight line data are generated for basement models of idealized geological setups. Comparing variogram depths of the data with true model depths shows that variogram depths are accurate and unbiased as long as the data analysis window is larger than 10 times the depth to be estimated. However, basement features smaller than this window size are not resolved. We investigate the trade-off between window size and lateral resolution by comparing variogram depth with drilled basement depth in the Kuiseb Dune Area, Namibia. For this difficult data set the optimum window size is more than 20 times the depth to be resolved. Arguably, accuracy and lateral resolution of depth would have been better if the main survey lines had followed the dune valleys and more tie lines had been flown. A provocative conclusion from our study is that one should consider arranging survey lines in a regular mesh, instead of the current practice of flying a dense set of parallel main lines and only a few perpendicular tie lines. Flying a regular mesh would optimize the retrieval of depth information per line-km surveyed.

Turning to the second sense in which a power spectrum may be used, the presumed power spectrum of the gravity field is utilized to constrain the smoothness of geoid solutions from satellite altimeter data (Chapter 7). The ocean geoid can be inferred from the topography of the mean sea surface. Satellite altimeters transmit radar pulses and determine the return travel time to measure sea surface height. The ERS-1 altimeter stacks 51 consecutive radar reflections on-board the satellite to a single waveform. Tracking the time shift of the waveform gives an estimate of the distance to sea surface. In a study together with Derek Fairhead and Chris Green of GETECH (University of Leeds), we retrack the ERS-1 radar travel times using a model which is focused on the leading edge of the waveforms. While earlier methods regarded adjacent waveforms as independent statistical events, we invert a whole sequence of waveforms simultaneously for a spline geoid solution. Smoothness is controlled by spectral constraints on the spline coefficients. Our geoid solutions have average power spectra equal

to the expected power spectrum of the true geoid. The coherence of repeat track solutions indicates a spatial resolution of 31 km, as compared to 41 km resolution for the European Space Agency's *ERS-1 Ocean Product*. While the resolution of the latter deteriorates to 47 km for wave heights above 2 m, our geoid solution maintains its resolution of 31 km for rough sea. Retracking altimeter waveform data and constraining the solution by a spectral model leads to a realistic geoid solution with significantly improved along-track resolution.

In view of the new Ørsted and upcoming Champ satellite missions, discussions with Nils Olsen and Peter Weidelt on the presumed spatial distribution and radial decay of field-aligned electric currents have motivated an investigation on the efficient parametrization of the magnetic field at satellite altitude (Chapter 8). An efficient parametrization of the magnetic field is essential for the processing and analysis of satellite magnetic data. We use two poloidal scalars for the internal and external magnetic fields and one toroidal scalar for the magnetic field due to field-aligned electric currents. While the radial behavior of the poloidal scalars is well known, we derive a radial expansion for the toroidal scalar, based on statistical features of a dipolar system of field-aligned currents. The upcoming situation with multiple magnetic field measuring satellites in orbit may permit the resolution of further field parameters. For this purpose, we propose an additional poloidal field scalar for toroidal currents within the shell of measurements, and further higher order toroidal magnetic field scalars for the poloidal currents. This optimum choice of parameters should provide the key for improved internal and external magnetic field models.

In summary, statistical methods are important tools for the processing and interpretation of gravity and magnetic data. The straight-forward analysis of spatial power spectra and their variogram counterparts provides information on source parameters and noise levels. In the inversion of measured data, the inclusion of power spectra and variograms as statistical constraints on the model parameters leads to physically meaningful solutions. While statistical techniques are sometimes regarded as inaccurate and unreliable, I show here that they complement other techniques in gravity and magnetic mapping, leading to significant gains in resolution and accuracy.

Chapter 1

Compatible spherical harmonic and plane power spectra

There is an increasing interest in spherical harmonic whole Earth models of various geophysical parameters. An interesting characteristic of these models is their spatial power spectrum (Kaula, 1967) which may reveal important properties of the underlying geophysical processes. For example, the Mauersberger/Lowes geomagnetic spectrum (Lowes, 1974; Langel and Estes, 1982) clearly indicates the dominance of the magnetic core field at long wavelengths and the crustal magnetic field at short wavelengths. Attempts have been made to infer the spectrum of the crustal magnetic field from statistical models of the crustal magnetization (Jackson, 1996; McLeod, 1996; Maus et al., 1997). McLeod and Coleman (1980) derived the power spectra of magnetic field vector components on average great circles (circles with the same diameter as the sphere) from the spherical harmonic coefficients of the magnetic potential. O'Brian et al. (1999) invert these relations to estimate the Mauersberger/Lowes spectrum from vector component aeromagnetic survey lines over the oceans. Spherical harmonic gravity potential spectra have been estimated from gravity anomalies on land (Forsberg, 1984), and from satellite altimetry data of the ocean geoid (Rapp, 1986). In a study on the decay of topography and geoid spectra of the Earth, Rapp (1989) uses a spectral density obtained from dividing the usual spherical harmonic coefficient spectrum by the wavenumber k. This quantity is independent of the spherical radius and was originally defined by Turcotte (1987) to compare topography and geoid spectra of the Earth, Moon, Venus and Mars. Corresponding azimuthally summed cross-spectral densities for spherical and plane coordinates were defined by McKenzie (1994) to study the admittance between topography and gravity on Earth and Venus. The admittance $Z(\mathbf{k})$ is defined as the transfer function in $\tilde{g}(\mathbf{k}) = Z(\mathbf{k})\tilde{h}(\mathbf{k})$, where $\tilde{g}$ and $\tilde{h}$ are the Fourier transforms of gravity and topography, respectively, and $\mathbf{k}$ is the wavevector.

The spherical harmonic power spectrum can be seen as the global average of a local spatial power spectrum. This local power spectrum is a continuous quantity which is defined *a priori*, hence, it exists independently of any measurements that may have been made and

independently of the chosen coordinate system. It is not expected to be stationary over the sphere, as the intermediate to short wavelength variability of a geophysical parameter usually changes with location, e.g., between oceans and continents. In this sense, the global spherical harmonic spectrum may serve as an estimate of the local spatial spectrum and can be compared with spectrum estimates from local grids to study regional variability in a global context (Chapter 2). For this purpose, I define spherical harmonic and plane spectrum estimators which are compatible, regardless of coordinate system orientation, spherical radius, grid size, and sampling interval. While the plane spectrum estimator resembles the commonly utilized plane azimuthally averaged "radial" spectrum (Spector and Grant, 1970), the new spherical spectrum estimator differs from the usual spherical harmonic coefficient spectrum of degree ℓ by a factor $\pi^{-1}\,(2\ell+1)^{-1}\,r^2$. I also define a magnetic field vector spectrum which can be estimated from total intensity data under the assumption of a poloidal and primarily dipolar field. The validity and accuracy of the theory is demonstrated in tests, where spherical harmonic spectra are compared with plane spectra of one and the same function.

1.1 Spatial power spectrum

Let ψ be the scalar geophysical parameter we are interested in. For example, this could be the topographic altitude, gravity acceleration, or the total intensity of the magnetic field. We would like to quantify the spatial variability of ψ on some arbitrarily curved, but reasonably smooth surface. From a statistical point of view, $\psi(x_1, x_2)$ is a scalar random field (Yaglom, 1986). Then, $\psi(x_1, x_2)$ has an expected value $E\{\psi(x_1, x_2)\}$, and a variance

$$E\{[\psi(x_1, x_2) - E\{\psi(x_1, x_2)\}]^2\} = E\{\psi(x_1, x_2)^2\} - E\{\psi(x_1, x_2)\}^2. \tag{1.1}$$

The quantity $E\{\psi(x_1, x_2)^2\}$ shall be referred to as the expected power. This expected power can be written as an integral of the 2D power spectral density $P(k_1, k_2)$ over the 2D wavenumber domain (k_1, k_2). Using established terms of the applied literature, I shall refer to the power spectral density $P(k_1, k_2)$ as a power spectrum or just spectrum. Then the expected power is related to the spectrum as

$$E\{\psi(x_1, x_2)^2\} = \int_{-\infty}^{\infty}\int_{-\infty}^{\infty} P(k_1, k_2)\, dk_1\, dk_2 \tag{1.2}$$

$$= \int_0^{\infty}\int_0^{2\pi} P(k\cos\alpha, k\sin\alpha)\, d\alpha\, k\, dk, \tag{1.3}$$

where $k = \sqrt{k_1^2 + k_2^2}$ is the wavenumber measured in radians per km, and α is the azimuth. In contrast to the wavenumber, the azimuth depends on the orientation of the local coordinate system. There are three possibilities to define a reduced power spectrum $P(k)$ which is only a function of the wavenumber and independent of the azimuth. They are listed in Table 1.1. The azimuthally integrated spectrum

TABLE 1.1: Three coordinate independent spatial spectra are defined in the first column and their relation to the expected power is given in the second column. The first spectrum slopes upward for white noise, while the third is impractical. Remains the second which is advocated here.

	definition of $P_i(k)$ relative to $P(k_1, k_2)$	$E\{\psi(x_1, x_2)^2\}$	type
$P_1(k)$	$k \int_0^{2\pi} P(k\cos\alpha, k\sin\alpha)\, d\alpha$	$\int_0^{\infty} P_1(k)\, dk$	az. integr.
$P_2(k)$	$\frac{1}{2\pi} \int_0^{2\pi} P(k\cos\alpha, k\sin\alpha)\, d\alpha$	$\int_0^{\infty} P_2(k)\, 2\pi k\, dk$	az. av. 2D
$P_3(k)$	$\frac{1}{2\pi} \int_0^{2\pi} \int_{-\infty}^{\infty} P(k\cos\alpha - k_2'\sin\alpha, k\sin\alpha + k_2'\cos\alpha)\, dk_2'\, d\alpha$	$2 \int_0^{\infty} P_3(k)\, dk$	az. av. 1D

$$P_1(k) = k \int_0^{2\pi} P(k\cos\alpha, k\sin\alpha)\, d\alpha \tag{1.4}$$

is popular in whole Earth studies. Its major shortcoming is that its white noise spectrum slopes upward. A better option, therefore, is to average over the azimuth as in

$$P_2(k) = \frac{1}{2\pi} \int_0^{2\pi} P(k\cos\alpha, k\sin\alpha)\, d\alpha. \tag{1.5}$$

This azimuthally averaged 2D spectrum is popular in local studies. As a third possibility, one could use the expected 1D spectrum for an arbitrarily oriented profile. Introducing a coordinate system (x_1', x_2'), rotated counter-clockwise by the angle α as

$$(x_1, x_2) = (x_1'\cos\alpha - x_2'\sin\alpha, x_1'\sin\alpha + x_2'\cos\alpha), \tag{1.6}$$

the slice theorem (Parker and O'Brien, 1997, eq. 12) gives the spectrum $P_{1D}^{\alpha}(k_1')$ for a profile oriented in the x_1'-direction as

$$P_{1D}^{\alpha}(k_1') = \int_{-\infty}^{\infty} P_{2D}^{\alpha}(k_1', k_2')\, dk_2' \tag{1.7}$$

$$= \int_{-\infty}^{\infty} P(k_1'\cos\alpha - k_2'\sin\alpha, k_1'\sin\alpha + k_2'\cos\alpha)\, dk_2'. \tag{1.8}$$

Averaging over all of the possible profile directions α gives

$$P_3(k) = \frac{1}{2\pi} \int_0^{2\pi} \int_{-\infty}^{\infty} P(k\cos\alpha - k_2'\sin\alpha, k\sin\alpha + k_2'\cos\alpha)\, dk_2'\, d\alpha. \tag{1.9}$$

However, this azimuthally averaged 1D spectrum is impractical to estimate. Thus, definition (1.5) turns out to be the best option for a coordinate independent spectrum.

For magnetic power spectra it has advantages to use the geometric mean, instead of the arithmetic mean, in the azimuthal average of eq. (1.5) (see Chapter 3, p. 42). However, this complicates the normalization of the spectra according to eq. (1.3). Therefore, this possibility shall not be pursued further here.

With definition (1.5) the expected power can be written as

$$E\{\psi(x_1, x_2)^2\} = \int_0^\infty P_2(k)\, 2\pi k\, dk. \tag{1.10}$$

Values of $P_2(k)$ carry the units $[\psi]^2\,\mathrm{km}^2$, which are the units of a 2D power spectral density (PSD). The azimuthally averaged power spectrum $P_2(k)$ can be estimated from data given in any coordinate system and thus provides a universally comparable measure for the spatial variability of ψ. From one location to another, this spatial spectrum can vary gradually, in the sense that the wavelength of variations in $P_2(k)$ must be long compared with $2\pi/k$. A full formal definition of non-stationary spectra can be found in Priestley's book (1981). It is important to be aware of the difference between the local spatial power spectrum and the estimators thereof. Using an estimator, we can compute an estimate of the spatial power spectrum, for example from plane Fourier or spherical harmonic coefficients. The estimates would be identical to the true spatial spectrum only if the expansion coefficients were known accurately and the spectrum were stationary over the entire area, which should rarely be the case. For example, the global spherical harmonic spectrum of Earth topography overestimates the true spatial power spectrum of topography in the Netherlands and underestimates it in the Himalayas.

To avoid mis-interpretation, power spectrum estimators should be independent of grid size, sampling interval and spherical radius, which is fulfilled if they are normalized according to (1.10). Furthermore, spatially uncorrelated white noise should have a flat spectrum. as is the case for the 2D azimuthally averaged spectrum advocated here, but not for an azimuthally integrated spectrum. This can be seen by azimuthally integrating the spectrum $P(k_1, k_2)$ obtained from applying Khinchin's formula (Yaglom, 1986, eq. 4.56)

$$P(k_1, k_2) = \frac{1}{(2\pi)^2} \int_{-\infty}^{\infty} \int_{-\infty}^{\infty} e^{-i(\tau_1 k_1 + \tau_2 k_2)}\; ACF(\tau_1, \tau_2)\, d\tau_1\, d\tau_2 \tag{1.11}$$

to a 2D white noise auto-correlation function (ACF) (Yaglom, 1986, eq. 4.62)

$$ACF(\tau_1, \tau_2) = \delta(\tau_1)\; \delta(\tau_2), \tag{1.12}$$

where δ is Dirac's delta function.

The azimuthally averaged "radial" power spectra commonly used in applied gravity and magnetics have a flat white noise spectrum, but may have to be multiplied by a constant grid dependent factor in order to fulfill (1.10). In contrast, the spherical harmonic coefficient spectrum used in whole Earth studies (Kaula, 1967; Lowes, 1974) slopes upward for a white noise and can only be utilized to compare variability among equally sized spheres, because the spacing of the degrees ℓ in the wavenumber domain changes with the spherical radius. Both shortcomings can be avoided by using spherical harmonic spectrum estimators which comply with definition (1.5) and normalization (1.10).

1.1.1 Spherical harmonic power spectrum estimator

In geocentric spherical polar coordinates with radius r, colatitude θ and longitude ϕ we can write a scalar function ψ defined on the surface of a sphere of radius r as a sum of spherical harmonic contributions ψ_ℓ^m of degree ℓ and azimuthal order m as

$$\psi(\theta,\phi) = \sum_{\ell=0}^{\infty} \sum_{m=-\ell}^{\ell} \psi_\ell^m(\theta,\phi), \tag{1.13}$$

where increasing values of ℓ correspond to decreasing wavelengths $\lambda = 2\pi r/(\ell+1/2)$. The contributions are orthogonal in the sense that

$$\langle \psi_\ell^m(\theta,\phi)\psi_{\ell'}^{m'}(\theta,\phi)\rangle = 0 \quad \text{for } \ell \neq \ell' \text{ or } m \neq m', \tag{1.14}$$

where $\langle\cdot\rangle$ denotes averaging over the surface of the sphere. Using the global mean power as an estimator $\widehat{E}\{\cdot\}$ for the locally expected power as

$$\widehat{E}\{\psi(\theta,\phi)^2\} = \langle\psi(\theta,\phi)^2\rangle = \sum_{\ell=0}^{\infty} \sum_{m=-\ell}^{\ell} \langle\psi_\ell^m(\theta,\phi)^2\rangle \tag{1.15}$$

defines a discrete representation of the estimated local power in terms of contributions of degree ℓ and azimuthal order m. Let us choose a set of spherical harmonic basis functions $\beta_\ell^m(\theta,\phi)$ (Backus et al., 1996, p. 141-142) with

$$\beta_\ell^m = \sqrt{(2\ell+1)N_\ell}\,\cos m\phi\;\breve{P}_\ell^m(\cos\theta), \quad 0 \le m \le \ell \tag{1.16}$$

$$\beta_\ell^{-m} = \sqrt{(2\ell+1)N_\ell}\,\sin m\phi\;\breve{P}_\ell^m(\cos\theta), \quad 1 \le m \le \ell, \tag{1.17}$$

where $N_\ell = 1$ for a fully normalized basis, and $N_\ell = 1/(2\ell+1)$ for the Schmidt normalized basis commonly used in magnetics. Here, the functions $\breve{P}_\ell^m(\mu)$ are defined as

$$\breve{P}_\ell^m(\mu) = \begin{cases} \sqrt{2\frac{(\ell-m)!}{(\ell+m)!}}P_\ell^m(\mu) & \text{if } 1 \le m \le \ell \\ P_\ell(\mu) & \text{if } \quad m = 0, \end{cases} \tag{1.18}$$

where $P_\ell^m(\mu)$ are the associated Legendre functions (Backus et al., 1996, eq. 3.7.2). With respect to this basis, define spherical harmonic coefficients c_ℓ^m as

$$\psi_\ell^m(\theta,\phi) = c_\ell^m\,\beta_\ell^m(\theta,\phi) \tag{1.19}$$

and the discrete representation of the estimated local power (1.15) becomes

$$\begin{aligned} \widehat{E}\{\psi(\theta,\phi)^2\} &= \sum_{\ell=0}^{\infty} \sum_{m=-\ell}^{\ell} (c_\ell^m)^2 \langle\beta_\ell^m(\theta,\phi)^2\rangle \\ &= \sum_{\ell=0}^{\infty} \sum_{m=-\ell}^{\ell} (c_\ell^m)^2 N_\ell. \end{aligned} \tag{1.20}$$

In (1.20) we have a sum over the azimuthal index m, followed by a sum over the harmonic degree ℓ. In contrast to ℓ, the azimuthal index m depends on the orientation of the coordinate system. As in definition (1.5), we become independent of the coordinate system by averaging over the azimuthal index m. Performing the inner azimuthal sum in (1.20) then gives

$$\widehat{E}\{\psi(\theta,\phi)^2\} \;=\; \sum_{\ell=0}^{\infty} N_\ell (2\ell+1)\overline{c_\ell^2} \tag{1.21}$$

where the azimuthal average $\overline{c_\ell^2}$ is defined as

$$\overline{c_\ell^2} = \frac{1}{2\ell+1} \sum_{m=-\ell}^{\ell} (c_\ell^m)^2. \tag{1.22}$$

Now, let us proceed from a discrete to a continuous representation of the estimated power. Extending the discrete functions N_ℓ and $\overline{c_\ell^2}$ into continuous functions $N(\ell)$ and $\overline{c^2}(\ell)$, e.g. as step functions, we can write eq. (1.21) as

$$\widehat{E}\{\psi(\theta,\phi)^2\} \;=\; \int_{-1/2}^{\infty} N(\ell)(2\ell+1)\;\overline{c^2}(\ell)\;d\ell. \tag{1.23}$$

Next, let us transform the integrand to a function of the wavenumber k. The wavenumber of a spherical harmonic of degree ℓ is (Backus et al., 1996, p. 103)

$$k = \frac{\sqrt{\ell(\ell+1)}}{r} \approx \frac{\ell+1/2}{r}. \tag{1.24}$$

We can substitute $d\ell = r\;dk$, giving

$$\begin{aligned}
\widehat{E}\{\psi(\theta,\phi)^2\} &= \int_0^{\infty} N(\ell)\;(2\ell+1)\;\overline{c^2}(\ell)\;r\;dk \\
&= \int_0^{\infty} N(rk-1/2)\;r^2\;\overline{c^2}(rk-1/2)^2\;2k\;dk \\
&= \int_0^{\infty} \underbrace{\frac{4\pi r^2\;N(rk-1/2)\;\overline{c^2}(rk-1/2)^2}{(2\pi)^2}}_{\widehat{P}_\ominus(k)} 2\pi k\;dk
\end{aligned} \tag{1.25}$$

Hence, the estimated power $\widehat{E}\{\psi(\theta,\phi)^2\}$ can be written as an integral over the azimuthally averaged power spectrum estimator $\widehat{P}_\ominus(k)$, as prescribed in the normalization condition (1.10). The spherical harmonic coefficients c_ℓ^m provide the estimator $\widehat{P}_\ominus(k)$ at wavenumbers $k_\ell = (\ell+1/2)/r$ with

$$\widehat{P}_\ominus(k_\ell) = \frac{4\pi r^2\;N(\ell)\;\overline{c^2}(\ell)^2}{(2\pi)^2} = \frac{4\pi r^2\;N(\ell)}{(2\pi)^2\;(2\ell+1)} \sum_{m=-\ell}^{\ell} (c_\ell^m)^2 \tag{1.26}$$

This estimator $\widehat{P}_\ominus(k_\ell)$ is related by a factor $4\pi r^2(2\pi)^{-2}(2\ell+1)^{-1}$ to Kaula's spherical harmonic power spectrum (Kaula, 1967). Multiplication by the surface area of the sphere $4\pi r^2$

makes the new estimator independent of the spherical radius. Thus, using (1.26), we can directly compare power spectra of the Earth with other celestial bodies, regardless of their size. Division by $(2\pi)^2$ is required in order to fulfill (1.10). Finally, we switch from an azimuthally summed to an azimuthally averaged spectrum in dividing by $(2\ell+1)$, arriving at a definition in which white noise really has a white spectrum.

1.1.2 Potential field power spectra

In many cases, the parameter $\psi(r,\theta,\phi)$ satisfies Laplace's equation. Then, for internal sources, the spherical harmonic expansion can be extended radially by

$$\psi(r,\theta,\phi) = a\sum_{\ell=0}^{\infty}\left(\frac{a}{r}\right)^{\ell+1}\sum_{m=-\ell}^{\ell} c_\ell^m \beta_\ell^m(\theta,\phi). \tag{1.27}$$

Spectrum of the potential

Sometimes, ψ itself is the parameter under consideration. In geodesy, for example, it is common practice to consider the spectrum of the gravity potential. Then the estimator $\widehat{P}_\ominus(k)$ for the azimuthally averaged power spectrum in the location (r,θ,ϕ) is

$$\widehat{P}_\ominus(r,k_\ell) \;=\; a^2\left(\frac{a}{r}\right)^{2\ell+2}\frac{4\pi r^2\ N_\ell}{(2\pi)^2\ (2\ell+1)}\sum_{m=-\ell}^{\ell}(c_\ell^m)^2. \tag{1.28}$$

Spectrum of the radial derivative

In gravity and magnetics we often have the spherical harmonic coefficients of the potential, while we are actually interested in the radial derivative thereof. The estimator for the spectrum of the radial derivative of ψ is given by

$$\widehat{P}^r_\ominus(r,k_\ell) \;=\; \left(\frac{a}{r}\right)^{2\ell+4}\frac{4\pi r^2\ (\ell+1)^2\ N_\ell}{(2\pi)^2\ (2\ell+1)}\sum_{m=-\ell}^{\ell}(c_\ell^m)^2. \tag{1.29}$$

Spectrum of the field vector

Note the difference between the field vector spectrum describing $|\mathbf{B}_k|^2$ and the total intensity spectrum describing $|\mathbf{B}|^2_k$. The Mauersberger/Lowes vector spectrum of the magnetic field (Mauersberger, 1956; Lowes, 1966; Langel and Estes, 1982) is

$$\langle|\nabla\psi_\ell|^2\rangle = \left(\frac{a}{r}\right)^{2\ell+4}(\ell+1)(2\ell+1)N_\ell\sum_{m=-\ell}^{\ell}(c_\ell^m)^2, \tag{1.30}$$

while an estimator for the azimuthally averaged spatial vector spectrum is given by

$$\widehat{P}^{\mathbf{B}}_\ominus(r,k_\ell) = \left(\frac{a}{r}\right)^{2\ell+4}\frac{4\pi r^2\ (\ell+1)}{(2\pi)^2}N_\ell\sum_{m=-\ell}^{\ell}(c_\ell^m)^2. \tag{1.31}$$

1.1.3 Total intensity spectrum

Aeromagnetic surveys usually record only the total intensity of the field. To compare such data with global field models, one can estimate the total intensity spectrum from the aeromagnetic data and compare it with the global total intensity spectrum. Another possibility, discussed later, is to estimate a vector spectrum from the local total intensity data and compare it with the global magnetic vector spectrum.

There are two ways of obtaining a globally averaged total intensity spectrum from the spherical harmonic coefficients of the magnetic potential. The exact approach is to compute a longitude/latitude grid of the magnetic field $\mathbf{B}$ from the coefficients c_ℓ^m by a reverse spherical harmonic transform. Then compute $|\mathbf{B}|$ and obtain the spherical harmonic coefficients of $|\mathbf{B}|$ by a forward transform. These coefficients can then be used to compute the exact globally averaged total intensity spectrum by eq. (1.26). The blue spectra in Fig. 1.1 were computed in this way.

Alternatively, the total intensity spectrum can be estimated directly from the spherical harmonic coefficients of the magnetic potential. Given the dominance of the main magnetic field, a high order magnetic field harmonic $\mathbf{B}_\ell^m$ contributes to the total intensity only with its component $\mathbf{B}_{\ell,m}^{||}$ parallel to the main field. Hence, what we need to do is derive an estimate of the expected power $E\{|\mathbf{B}_\ell^{||}|^2\}$. If all power of the magnetic field vector were distributed equally in the radial and two tangential directions, $E\{|\mathbf{B}_\ell^{||}|^2\}$ would simply be one third of $E\{|\mathbf{B}_\ell^m|^2\}$ (Lowes, 1974). However, this relation is only approximately valid for the Earth's magnetic field, which is more radial than tangential at the Earth's surface. Indeed, a more precise relation can be derived as follows:

Let us assume that the crustal magnetic field has stationary and isotropic statistical properties over the Earth's surface. Then the contribution of $\mathbf{B}_\ell^m$ to the power of the total intensity is

$$E\{|\mathbf{B}_\ell^{||}|^2\} = E\{(\mathbf{b}\cdot\mathbf{B}_\ell^m)^2\} = E\{(b_r B_{\ell,m}^r + \mathbf{b}_t\cdot\mathbf{B}_{\ell,m}^t)^2\} \tag{1.32}$$

where $\mathbf{b}$ is a unit vector in the direction of the main field and the indices r and t denote the radial ($\parallel \mathbf{r}$) and tangential ($\perp \mathbf{r}$) parts of the vectors at the location $\mathbf{r}$. We want to derive a relation which depends only on the local inclination I of the main field. The inclination is the angle of the field against the local horizontal plane. In this case, statistical expectation means that we have to average not only over all locations on the sphere, but also over all the possible azimuths α of the main field declination (its angle against local North), as

$$\begin{aligned} E\{(\mathbf{B}_{\ell,m}^{||})^2\} &= \langle \frac{1}{2\pi}\int_0^{2\pi} (b_r B_{\ell,m}^r + \mathbf{b}_t\cdot\mathbf{B}_{\ell,m}^t)^2\, d\alpha\rangle & (1.33)\\ &= \langle (b_r B_{\ell,m}^r)^2 + \underbrace{\frac{1}{\pi}\int_0^{2\pi} b_r B_{\ell,m}^r \mathbf{b}_t\cdot\mathbf{B}_{\ell,m}^t d\alpha}_{=0} + \frac{1}{2\pi}\int_0^{2\pi} (\sin^2\alpha\, |\mathbf{b}_t|^2 |\mathbf{B}_{\ell,m}^t|^2\, d\alpha\rangle \\ &= b_r^2\langle (B_{\ell,m}^r)^2\rangle + \frac{1}{2}|\mathbf{b}_t|^2\langle |\mathbf{B}_{\ell,m}^t|^2\rangle & (1.34) \end{aligned}$$

$$= \sin^2 I \, \langle (B^r_{\ell,m})^2 \rangle + \frac{1}{2} \cos^2 I \, \langle |\mathbf{B}^t_{\ell,m}|^2 \rangle. \tag{1.35}$$

Here, the radial part $B^r_{\ell,m}$ and tangential part $\mathbf{B}^t_{\ell,m}$ of $\mathbf{B}^m_\ell$ are

$$B^r_{\ell,m}(r,\theta,\phi) = (\ell+1) \left(\frac{a}{r}\right)^{\ell+2} c^m_\ell \beta^m_\ell(\theta,\phi) \tag{1.36}$$

$$\mathbf{B}^t_{\ell,m}(r,\theta,\phi) = -\left(\frac{a}{r}\right)^{\ell+2} c^m_\ell \boldsymbol{\nabla}_1 \beta^m_\ell(\theta,\phi), \tag{1.37}$$

where $\boldsymbol{\nabla}_1 = r\boldsymbol{\nabla} - \mathbf{r}\partial_r$ is the surface gradient and c^m_ℓ are the Gauss coefficients of the internal field. On average, the strengths of the radial and tangential parts are

$$\langle (B^r_{\ell,m})^2 \rangle = (\ell+1)^2 \left(\frac{a}{r}\right)^{2\ell+4} (c^m_\ell)^2 \langle (\beta^m_\ell)^2 \rangle \tag{1.38}$$

$$\begin{aligned} \langle |\mathbf{B}^t_{\ell,m}|^2 \rangle &= \left(\frac{a}{r}\right)^{2\ell+4} (c^m_\ell)^2 \langle \boldsymbol{\nabla}_1 \beta^m_\ell \cdot \boldsymbol{\nabla}_1 \beta^m_\ell \rangle \\ &= \left(\frac{a}{r}\right)^{2\ell+4} (c^m_\ell)^2 \langle -\beta^m_\ell \nabla^2_1 \beta^m_\ell \rangle \\ &= \ell(\ell+1) \left(\frac{a}{r}\right)^{2\ell+4} (c^m_\ell)^2 \langle (\beta^m_\ell)^2 \rangle. \end{aligned} \tag{1.39}$$

For the high degree parts of the magnetic field $\langle B_r^2 \rangle / \langle |\mathbf{B}_t|^2 \rangle = (\ell+1)/\ell \approx 1$, so their strength is half radial and half tangential (Holme and Jackson, 1997). Thus, eq. (1.35) becomes

$$\begin{aligned} E\{(\mathbf{B}^{||}_{\ell,m})^2\} &\approx (\frac{1}{2}\sin^2 I \, + \frac{1}{4}\cos^2 I \,) \langle |\mathbf{B}^m_\ell|^2 \rangle \\ &= \frac{1+\sin^2 I}{4} \, \langle |\mathbf{B}^m_\ell|^2 \rangle. \end{aligned} \tag{1.40}$$

In particular, the ratio is 1/4 for equatorial and 1/2 for polar locations on the globe and its spherical average for a dipolar main field is 5/12. Superimposing a harmonic of degree ℓ onto a harmonic of degree 1 gives harmonics of degree $(\ell-1)$ and $(\ell+1)$. The precise relation (1.60), derived in the Appendix to this chapter (Section 1.5), shows that the term of degree $(\ell-1)$ dominates on average. Hence, $\mathbf{B}^{||}_\ell$ contributes its power mainly to $|\mathbf{B}|_{\ell-1}$, rather than to $|\mathbf{B}|_\ell$. This is also mentioned without derivation by Arkani-Hamed *et al.* (1994). In summary, we obtain the relation

$$E\{|\mathbf{B}|^2_{\ell-1}\} \approx \frac{1+\sin^2 I}{4} \, \langle |\mathbf{B}^m_\ell|^2 \rangle, \tag{1.41}$$

which can be used to relate the local spectrum of the total intensity $P_{|\mathbf{B}|}(r,\theta,\phi)$ to the local spectrum of the field vector $P_{\mathbf{B}}(r,\theta,\phi)$ as

$$P_{|\mathbf{B}|}(r,\theta,\phi,k_{\ell-1}) \approx \frac{1+\sin^2 I(r,\theta,\phi)}{4} \, P_{\mathbf{B}}(r,\theta,\phi,k_\ell), \tag{1.42}$$

where $k_\ell = (\ell+1/2)/r$. For the mean total intensity spectrum of a predominantly dipolar field, the ratio can be replaced by its spherical average as

$$\langle P_{|\mathbf{B}|}(r,\theta,\phi,k_{\ell-1}) \rangle \approx \frac{5}{12} \, \langle P_{\mathbf{B}}(r,\theta,\phi,k_\ell) \rangle. \tag{1.43}$$

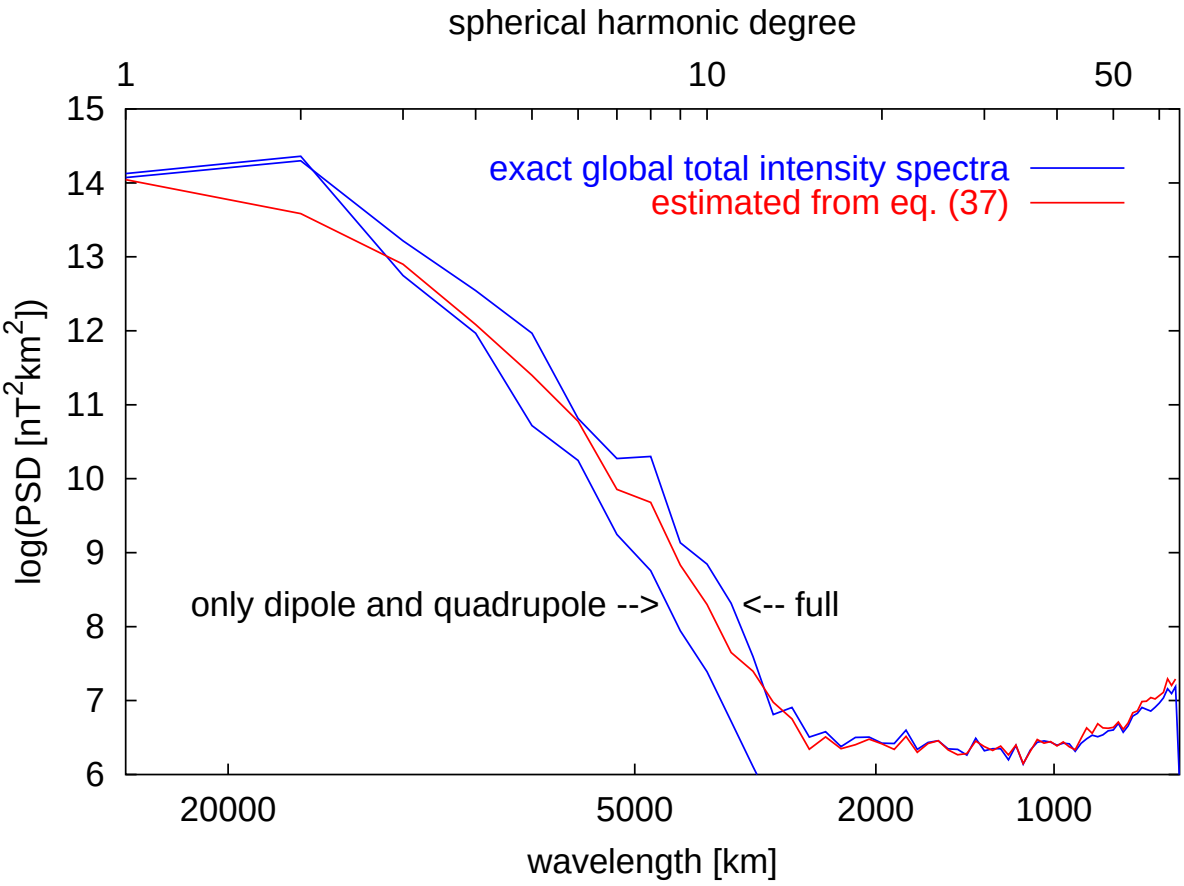

FIG. 1.1: For the exact globally averaged total intensity spectra (blue), the total intensity on a longitude/latitude grid is computed from the spherical harmonic coefficients of the C89 global magnetic field model. A forward spherical harmonic transform gives the coefficients of the total intensity from which the total intensity spectrum is calculated using eq. (1.26). The red line indicates the spectrum estimated from eq. (1.43). The approximation to the crustal field total intensity spectrum is good.

However, relations (1.42) and (1.43) only hold if the decay of the true total intensity spectrum is less steep than the decay of the total intensity spectrum of the lower harmonics of the field. Otherwise, these lower harmonics dominate and (1.42) and (1.43) underestimate the true total intensity spectrum. This happens with the Earth's main field, as is illustrated in Figure 1.1. In contrast, the relation is very accurate for the crustal magnetic field. Finally, note that relations (1.42) and (1.43) can be reversed. While the crustal magnetic vector field cannot be inferred uniquely from total intensity data, we can get a reliable estimate of its vector spectrum.

1.1.4 Plane power spectrum estimator

As in spherical coordinates, we shall write ψ as a sum of orthogonal contributions from decreasing wavelengths. For practical purposes, let an equidistant grid $\psi[x(i_1), y(i_2)]$ with side length D be given by the square Matrix $G(i_1, i_2)$, $i_1, i_2 = 0, .., n-1$. The matrix can

be written as a discrete Fourier sum

$$G(i_1, i_2) = \frac{1}{n} \sum_{j_1=0}^{n-1} \sum_{j_2=0}^{n-1} \exp \frac{2\pi i(i_1 j_1 + i_2 j_2)}{n} \widetilde{G}(j_1, j_2), \tag{1.44}$$

where $\widetilde{G}(j_1, j_2)$ is the discrete complex Fourier transform of $G(i_1, i_2)$ and j_1 and j_2 are integer indices. With definition (1.44) the Fourier transformed matrix fulfills

$$\sum_{i_1=0}^{n-1} \sum_{i_2=0}^{n-1} G(i_1, i_2)^2 = \sum_{j_1=0}^{n-1} \sum_{j_2=0}^{n-1} |\widetilde{G}(j_1, j_2)|^2, \tag{1.45}$$

where $|\widetilde{G}(j_1, j_2)|$ can be referred to as a discrete Fourier amplitude. Indeed, it is recommended in the practical application of the following to check for property (1.45), since fast Fourier transform (FFT) computer programs tend to add factors of n and n^2 to either side of this equation. Since $G(i_1, i_2)$ is real valued, its complex Fourier transform $\widetilde{G}(j_1, j_2)$ has the property $\widetilde{G}(j_1, j_2) = \overline{\widetilde{G}(n - j_1, n - j_2)}$, $j_1, j_2 = 1, .., n-1$, where the bar denotes complex conjugation. Thus, we can introduce a re-arranged Fourier grid $\widetilde{G}'(j_1, j_2)$, where $j_1, j_2 = -n/2 + 1, .., n/2$ are the harmonics of the grid:

$$\begin{aligned} \widetilde{G}'(j_1, j_2) &= \widetilde{G}(j_1, j_2) \\ \widetilde{G}'(-j_1, j_2) &= \widetilde{G}(j_1, n - j_2) \\ \widetilde{G}'(j_1, -j_2) &= \widetilde{G}(n - j_1, j_2) \\ \widetilde{G}'(-j_1, -j_2) &= \widetilde{G}(n - j_1, n - j_2) \end{aligned} \tag{1.46}$$

With this re-arranged grid, and using the estimate

$$\widehat{E}\{\psi[x(i_1), y(i_2)]^2\} = \frac{1}{n^2} \sum_{i_1=0}^{n-1} \sum_{i_2=0}^{n-1} G(i_1, i_2)^2, \tag{1.47}$$

we can write eq. (1.45) as

$$\widehat{E}\{\psi[x(i_1), y(i_2)]^2\} = \frac{1}{n^2} \sum_{j_1, j_2=-n/2+1}^{n/2} \sum |\widetilde{G}'(j_1, j_2)|^2. \tag{1.48}$$

This is the plane counterpart to the discrete spherical harmonic representation of the estimated power in eq. (1.20). Similar to McKenzie's definition of an azimuthally summed plane spectrum (McKenzie, 1994), we can define an azimuthal average $\overline{\widetilde{G}^2}(s)$ as a function of the harmonic $s = \sqrt{j_1^2 + j_2^2}$ as

$$\overline{\widetilde{G}^2}(s) = \frac{1}{n_s} \sum_{n_s} |\widetilde{G}'(j_1, j_2)|^2, \tag{1.49}$$

where the sum extends over all index pairs (j_1, j_2) with $s - 0.5 \leq \sqrt{j_1^2 + j_2^2} < s + 0.5$. The number of such index pairs is denoted by n_s. With definition (1.49) as an azimuthal average, which is continuous in s, we can rewrite eq. (1.48) as

$$\widehat{E}\{\psi[x(i_1), y(i_2)]^2\} = \frac{1}{n^2} \int_0^\infty \overline{\widetilde{G}^2}(s)\, 2\pi s\, ds. \tag{1.50}$$

Finally, expressing the integrand in terms of the wavenumber $k = 2\pi s/D$ and substituting $ds = D/2\pi\ dk$ gives

$$\widehat{E}\{\psi[x(i_1), y(i_2)]^2\} = \int_0^\infty \underbrace{\frac{D^2}{(2\pi)^2\ n^2}\ \overline{\widetilde{G}^2}(\frac{Dk}{2\pi})}_{\widehat{P}_\square(k)}\ 2\pi k\ dk \tag{1.51}$$

as the plane counterpart to eq. (1.25). With definition (1.49), the power spectrum estimator

$$\widehat{P}_\square(k) = \frac{D^2}{(2\pi)^2\ n^2}\ \overline{\widetilde{G}^2}(\frac{Dk}{2\pi}) \tag{1.52}$$

is usually evaluated only for wavenumbers k corresponding to integer harmonics s of the grid. However, the first test in the following section shows that non-integer values of s are also admissible. Definition (1.52) is consistent with the azimuthally averaged power spectrum ("radial power spectrum") commonly used in applied gravity and magnetics, e.g. Spector and Grant (1970) or Blakely (1995). Multiplication by $(D/n)^2$ conveniently makes this estimator independent of the grid size and sampling interval. The division by $(2\pi)^2$ is necessary in order to fulfill condition (1.10), requesting that the integrated power spectral density be equal to the expected power.

Vector power spectrum estimated from plane total intensity data

Equations (1.42) and (1.43) provide an estimate of the total intensity spectrum from the vector spectrum for a location on, or above, the Earth's surface. We can now revert this relation and obtain a vector spectrum estimator $\widehat{P}_\square^{\mathbf{B}}(k)$ from a plane total intensity spectrum estimator $\widehat{P}_\square^{|\mathbf{B}|}(k)$. Using $k_{\ell+1} = k_\ell + 1/r$ we have

$$\begin{aligned} \widehat{P}_\square^{\mathbf{B}}(k + \frac{1}{r}) &\approx \frac{4}{1+\sin^2 I}\ \widehat{P}_\square^{|\mathbf{B}|}(k) \\ &= \frac{4}{1+\sin^2 I}\ \frac{D^2}{(2\pi)^2\ n^2}\ \overline{\widetilde{G}^2_{|\mathbf{B}|}}(\frac{Dk}{2\pi}), \end{aligned} \tag{1.53}$$

where I is the local inclination of the main magnetic field. From this follows an estimator for the Mauersberger/Lowes spectrum by multiplying with $\pi(2\ell+1)/r^2$.

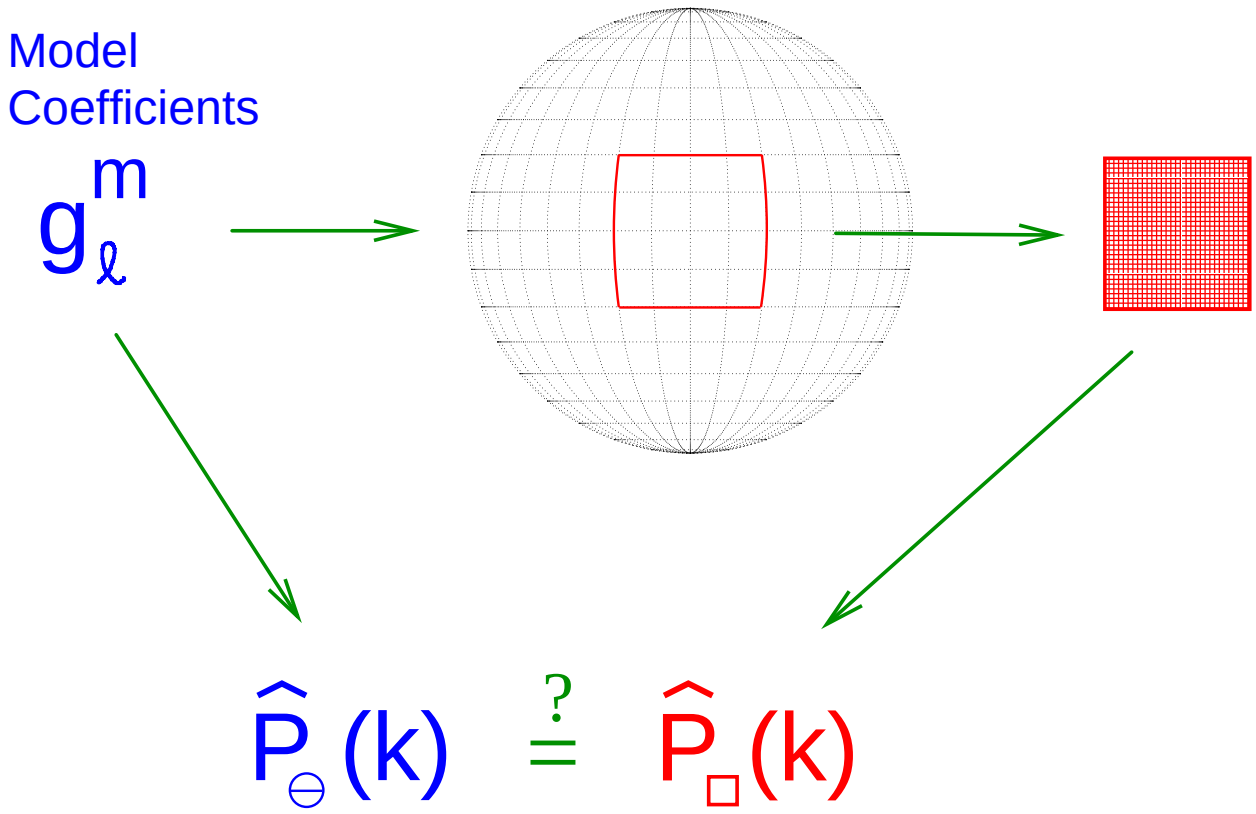

FIG. 1.2: Tests: 40° x 40° windows along the equator are used as sample grids in (nearly) Cartesian coordinates. Figures 1.3 to 1.8 display the average spectrum estimates $\hat{P}_\square$ of 9 adjacent windows versus the exact globally averaged spectrum, given by the estimator $\hat{P}_\ominus$.

1.2 Tests of the compatibility of the estimators

To test the accuracy and demonstrate the usefulness of the above theory, I transform fields given in spherical harmonic coefficients to a 360° x 180° longitude/latitude grid. Then, 9 windows of 40° x 40° are cut out along the equator, where the angular coordinates (θ, ϕ) are approximately Cartesian (Fig. 1.2). The plane power spectra are estimated using eq. (1.52), after applying a taper $T(i_1, i_2)$ with

$$T(i_1, i_2) = \frac{2n}{n+1} \sin(\pi \frac{i_1+1}{n+1}) \sin(\pi \frac{i_2+1}{n+1}), \quad i_1, i_2 = 0, .., n-1, \tag{1.54}$$

which is the first order term of a sinusoidal multitaper series (Riedel and Sidorenko, 1995), extended to a multi-dimensional taper as proposed by Hanssen (1997). The factor $2n/n+1$ compensates for the loss of power in multiplying the grid with the taper. The spectra of the 9 adjacent windows are averaged to the plane power spectrum estimate, which is then compared with the power spectrum of the spherical harmonic coefficients. This procedure is illustrated in Fig. 1.2.

First, the response to a rectangular band limited spectrum on a unit sphere is studied. Then I compare the spherical harmonic power spectrum with grid sample spectrum estimates

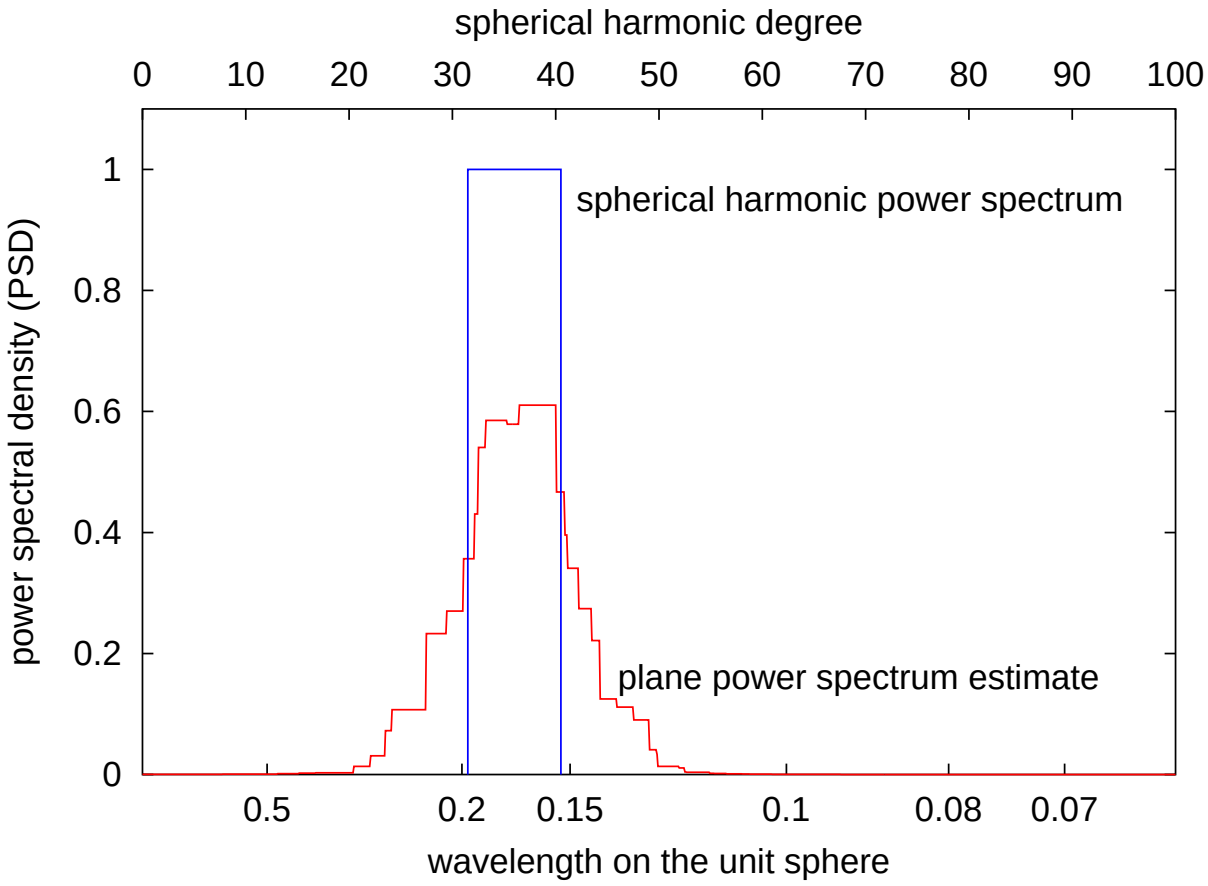

FIG. 1.3: Spherical and plane power spectrum estimators for a function with a band-limited white spectrum on a unit sphere.

for a global gravity and a global magnetic field model. In all plots, the lower abscissa is labeled with the wavelength $2\pi/k$, instead of the wavenumber k itself, and the upper abscissa gives the corresponding spherical harmonic degree ℓ.

Spherical harmonic waveband

A spherical function with band limited white spectrum from degrees 32 to 40 is synthesized by distributing the prescribed constant PSD for each degree randomly into the coefficients of all orders. After transforming to a longitude/latitude grid on a unit sphere, continuous plane power spectra are estimated with (1.52) from 9 sample grids of 40° x 40° along the equator. The 9 power spectra are then averaged and displayed against the true power spectrum in Figure 1.3. The plane spectrum estimate agrees well with the true spherical harmonic spectrum and there is only a limited leakage of power to neighboring harmonics. Furthermore, the integrated power of the plane and spherical spectrum estimators is nearly identical, as demanded by condition (1.10) for the spatial power spectrum and the corresponding normalization of its estimators in (1.25) and (1.51).

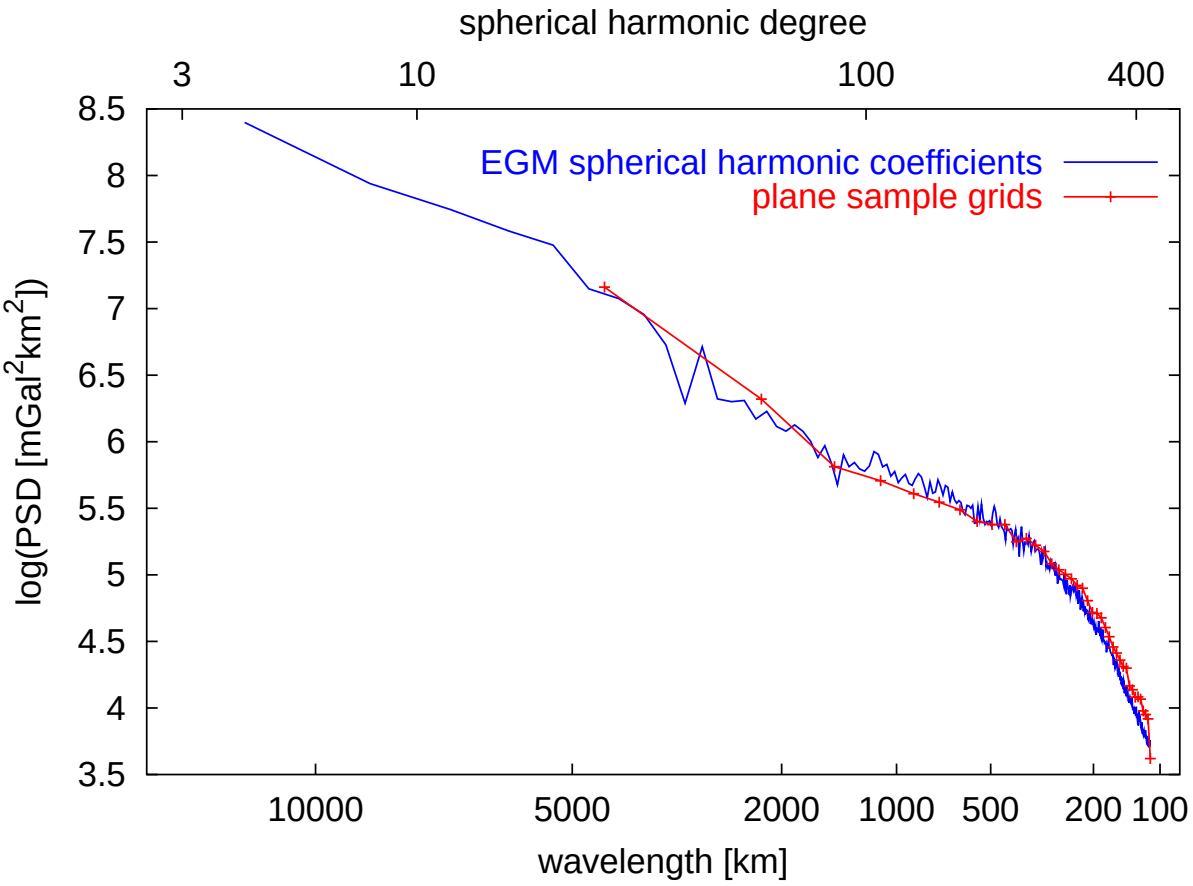

FIG. 1.4: Vertical component gravity power spectrum of eq. (1.29) together with the average local power spectrum estimated from the sample grids using eq. (1.52)

Global gravity field

The EGM96 geopotential model (Lemoine et al., 1998) is transformed to a longitude/latitude grid of vertical component gravity and the average local sample spectrum estimates are compared with the EGM96 spherical harmonic spectrum, displayed in Fig. 1.4. The agreement is good.

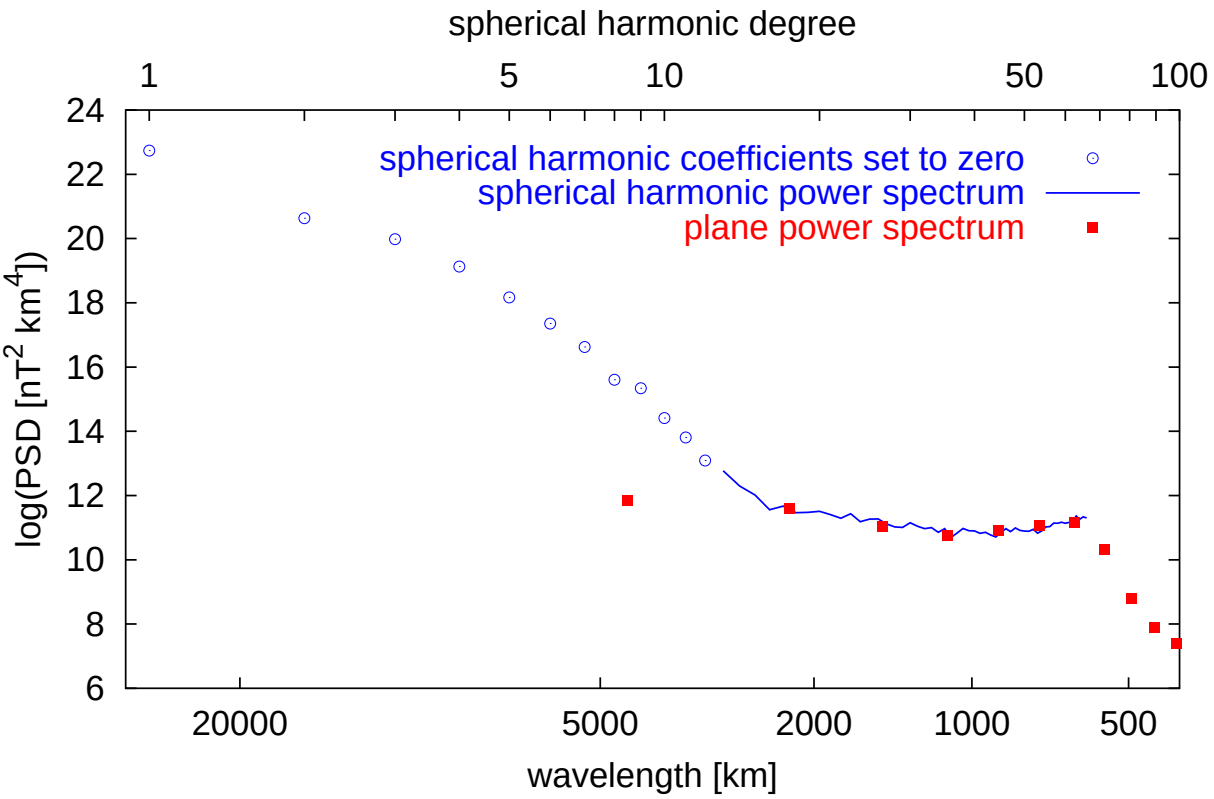

FIG. 1.5: Magnetic potential power spectrum of eq. (1.28) of model C89 with the coefficients of degrees 1-12 set to zero, together with the average local power spectrum, estimated from the sample grids using eq. (1.52)

Global magnetic field

First, the theory is applied to the magnetic potential. I transform the magnetic model C89 (Cain et al., 1989) to a longitude/latitude grid of the magnetic potential, estimate the average spectrum of the equatorial sample grids using eq. (1.52) and compare it with the spherical coefficient power spectrum of eq. (1.28). For Figure 1.5, the coefficients of degrees 1-12 were set to zero. Then the average plane spectrum estimate is in agreement with the spherical harmonic spectrum. However, if the low harmonic degree coefficients are not set to zero, there is a severe power leakage from low spherical harmonic degrees to high wavenumbers (Figure 1.6). This leakage occurs in the estimation of the plane power spectra. Hence, it is not a problem of the spectrum estimator definitions. As illustrated, the usual procedures of detrending, subtracting a second order polynomial or 2D-multi-tapering (Hanssen, 1997) fail to prevent the leakage.

The leakage problem is solved by subtracting, separately from each sample grid G_{ij}, the combination $c^{\ell m}$ of spherical harmonics $\beta_{ij}^{\ell m}$ which minimizes the residual

$$R_n = \sum_{\ell=0}^{n} \sum_{m=-\ell}^{\ell} \left(\sum_{i,j} (G_{ij} - c^{\ell m} \beta_{ij}^{\ell m})^2 + D(c^{\ell m})^2 \right), \tag{1.55}$$

where the damping term with $D \approx 0.001$ is required since the spherical harmonics are not

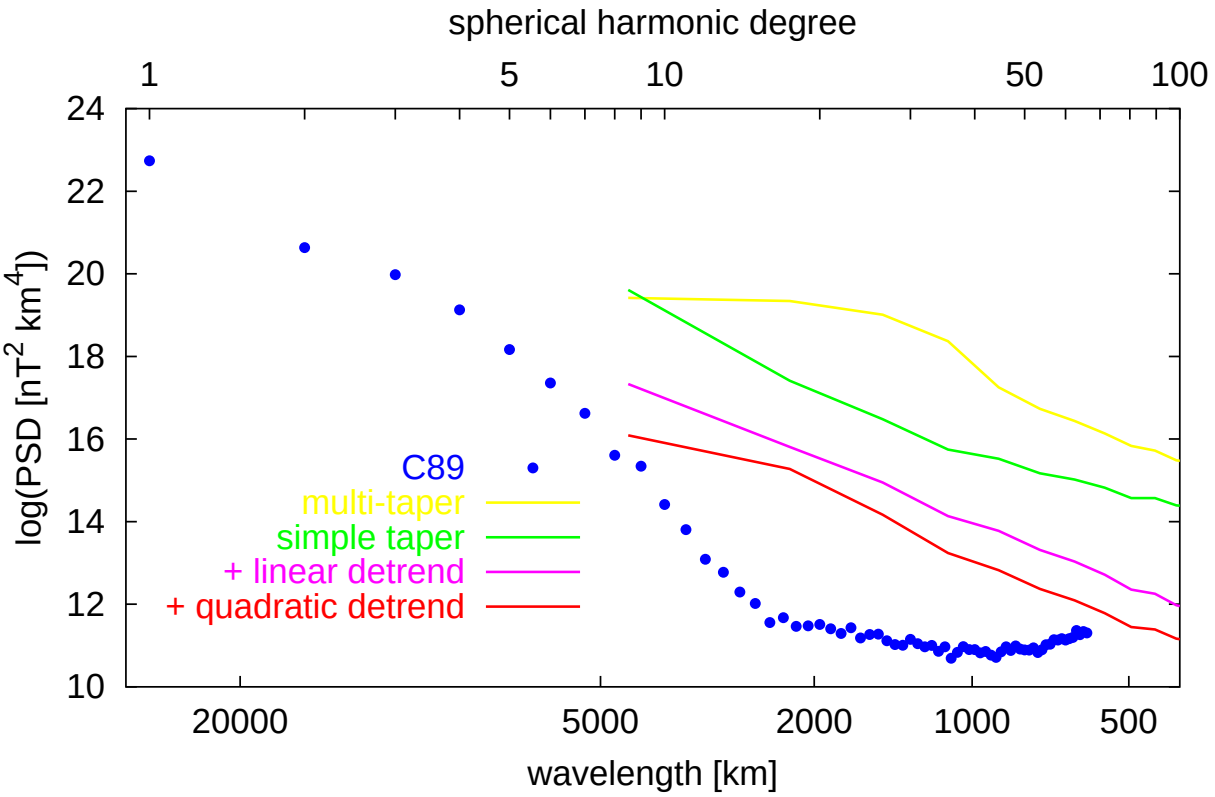

FIG. 1.6: Magnetic potential power spectrum as in Fig. 1.5 but including degrees 1-12. The usual algorithms do not prevent leakage of long wavelength power to high wavenumbers.

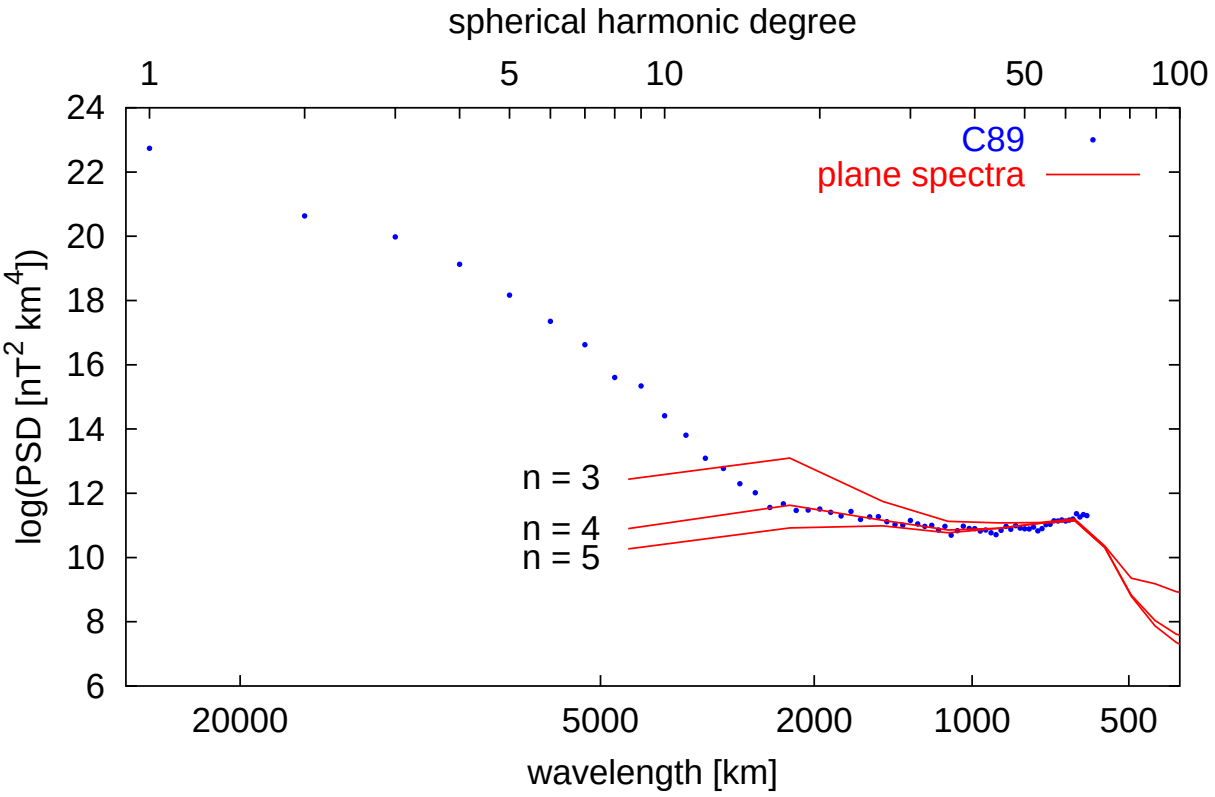

FIG. 1.7: Magnetic potential power spectrum as in Fig. 1.6. Before estimating the plane spectra, the sample grids were cleaned using eq. (1.55) with values of 3 - 5 for n.

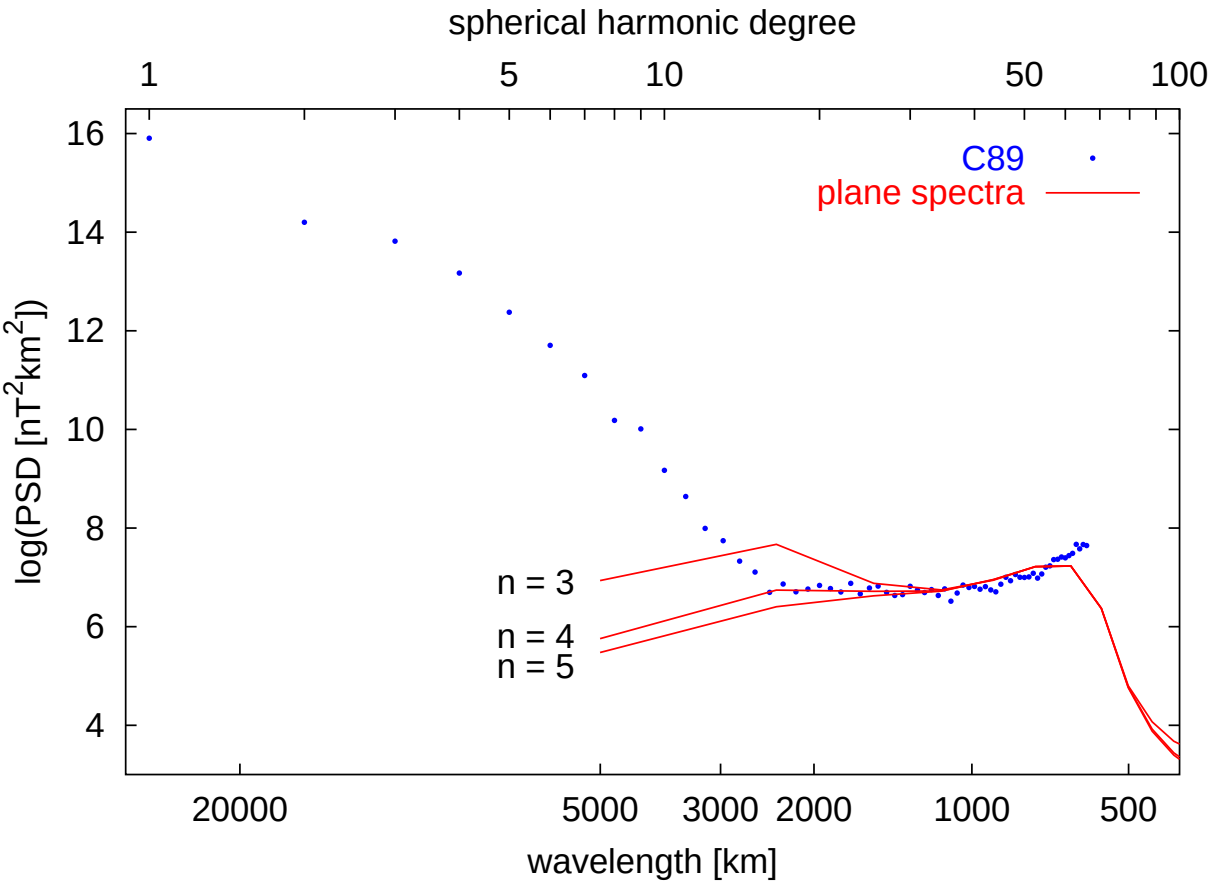

FIG. 1.8: Vector power spectrum of eq. (1.31) together with the average local power spectrum, estimated from the cleaned sample grids using eq. (1.53). Again, cleaning using eq. (1.55) with n = 4 leads to a good agreement of the plane and spherical harmonic power spectrum estimators.

orthogonal on a sub-area of the sphere. This procedure is very efficient and $n = 4$ already removes the entire main field from a grid (see Fig. 1.7). With higher n we start to remove the crustal field as well, which is not intended here.

Finally, let us try to estimate the vector spectrum from total intensity data, using eq. (1.53). For model C89, I compute the longitude/latitude grid of total intensities, clean the 40° x 40° sample grids using eq. (1.55) with n = 4, estimate the average spectrum using eq. (1.53) with $I = 0°$, and demonstrate the consistency with the vector spectrum of eq. (1.31) in Figure 1.8. Obviously, the cleaning procedure of eq. (1.55) works also with total intensity data and it is indeed possible to estimate a vector spectrum from local total intensity data.

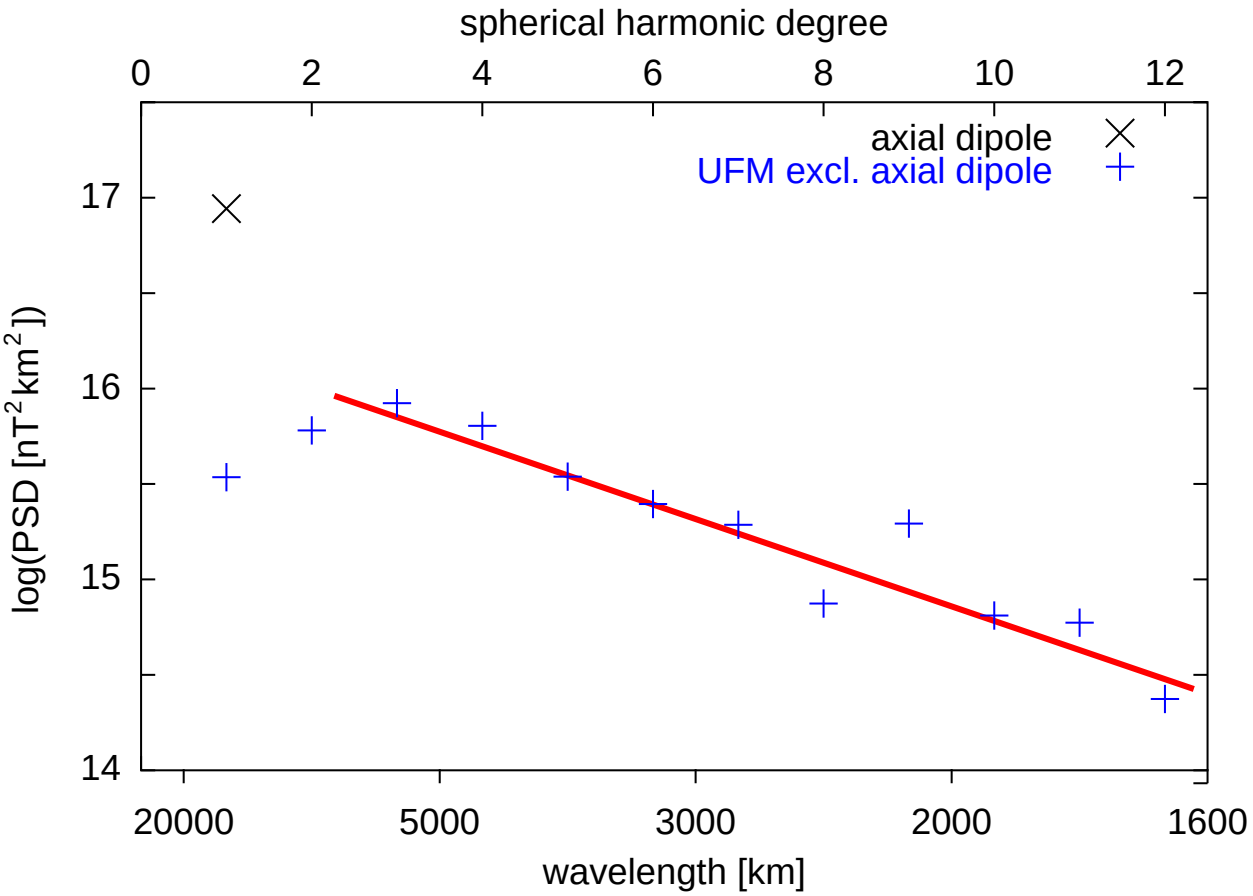

FIG. 1.9: Vector power spectrum (1.31) of the magnetic field at the core-mantle boundary, estimated from the spherical coefficients of the core field model UFM (Bloxham and Jackson, 1992)

1.3 Magnetic field at the core-mantle boundary

Finally, let us look at the new vector spectrum of the magnetic field at the core-mantle boundary. The main magnetic field is often said to be "white" at the core-mantle boundary because its Mauersberger/Lowes spectrum is nearly flat there (Langel and Estes, 1982). However, "whiteness" generally means that all available modes in the wavenumber domain are uncorrelated and have equal mean energy. On a sphere, the available modes are indexed by ℓ and m. Since energy is summed rather than averaged over m, a white noise Mauersberger/Lowes spectrum is not flat but increases by a factor $2\ell + 1$. In contrast, the azimuthally averaged vector spectrum advocated here, which can be estimated using eq. (1.31), is flat for a white noise field. Figure 1.9 shows that for the Earth's magnetic field this spectrum decreases by 2 orders of magnitude from degrees 2 to 12. Hence, even the non-dipole magnetic field is not white but correlated over large distances at the core-mantle boundary.

1.4 Discussion and conclusions

A spatial power spectrum characterizes spatial variance as a function of the wavenumber. It is a continuous quantity, which is defined *a priori*, hence, it exists independently of any measurements that may have been made and independently of the chosen coordinate system. This spatial power spectrum can be estimated, not computed, from measured data. Here, I have treated the 2D case, where measurements are located on a curved, but reasonably smooth surface. We have some freedom in the exact definition and normalization of the spatial power spectrum. To be independent of the coordinate system, one can integrate or average over the azimuth. In whole Earth studies it is common practice to use an azimuthally summed spectrum. This is a peculiar quantity, which carries the units of a 1D spectrum, but does not describe spatial variability on a 1D profile. Contrary to established conventions its white noise spectrum slopes upward. In contrast, the azimuthally averaged spectrum commonly used in local studies is a 2D spectrum which is compatible with the non-averaged 2D spectrum, and its white noise spectrum is flat. After opting for an azimuthally averaged spectrum, we still have the freedom of normalization. It makes intuitive sense to demand that the integral of the power spectral density over the 2D wavenumber domain be equal to the expected local power. This leads to a division by $(2\pi)^2$ in the definitions of the spectrum estimators. Alternatively, one could define the spatial power spectrum as the variability in terms of the spatial frequency in cycles per km. Then the factor $(2\pi)^{-2}$ in the spectrum estimators would disappear. However, in accordance with established conventions and compatibility with the mathematical literature, it is preferable to use wavenumbers instead of spatial frequencies and retain the factor $(2\pi)^{-2}$ in the estimator definitions.

Currently, spatial power spectra are estimated with the primary objective of analyzing their shape in terms of peaks and slopes. However, if one could agree on a common definition and normalization, even the absolute amplitudes of spatial power spectra from different studies could be compared directly, without having to worry about spherical radii, grid sizes and sampling intervals. For example, comparing Figures 1.9 and 1.8 we can say that the power density of the magnetic field at 3000 km wavelength is 10^8 times stronger at the core-mantle boundary than at the Earth's surface. The redefined power spectrum also shows that, contrary to earlier assessments, the magnetic field at the core-mantle boundary is not white.

1.5 Appendix to Chapter 1

In general, superimposing a harmonic of wavenumber ω_1 onto a harmonic of wavenumber ω_2 leads to a sum of harmonics with wavenumbers $(\omega_1 - \omega_2)$ and $(\omega_1 + \omega_2)$. Applied to the situation of an Earth with a dipolar main magnetic field of harmonic degree 1, a high degree harmonic $\mathbf{B}_\ell^m$ makes contributions of degrees $(\ell - 1)$ and $(\ell + 1)$ to the total intensity of the field. As shall be shown in the following, the contribution in terms of power to degree $(\ell - 1)$ is approximately one order of magnitude stronger than to degree $(\ell + 1)$, so the latter should be negligible in most cases.

Let us assume that the coordinate axis is aligned with the dipole axis. Then

$$|\mathbf{B}^{||}_{\ell,m}| = \frac{\mathbf{B}_1^0 \cdot \mathbf{B}_\ell^m}{|\mathbf{B}_1^0|} = \frac{B^r_{1,0} B^r_{\ell,m} + \mathbf{B}^t_{1,0} \cdot \mathbf{B}^t_{\ell,m}}{|\mathbf{B}_1^0|}, \tag{1.56}$$

where $\mathbf{B}^{||}_{\ell,m}$ is the projection of $\mathbf{B}_\ell^m$ onto the direction of the main field. From eqs. (1.36) and (1.37), with $\mathbf{B}_1^0 \propto \cos\theta$ follows

$$\underbrace{\left[c_\ell^m \left(\frac{a}{r}\right)^{\ell+2}\right]^{-1} \sqrt{1 + 3\cos^2\theta}\, |\mathbf{B}^{||}_{\ell,m}|}_{A_\ell^m} = 2(\ell+1)\cos\theta\, \beta_\ell^m - \sin\theta\, \partial_\theta \beta_\ell^m. \tag{1.57}$$

To eliminate all occurrences of θ and ∂_θ, we require the following relations for fully normalized spherical harmonics

$$s^2 \partial_\mu \beta_\ell^m = (\ell+1)\mu\beta_\ell^m - \sqrt{\frac{(2\ell+1)(\ell-m+1)(\ell+m+1)}{2\ell+3}}\beta^m_{\ell+1} \tag{1.58}$$

$$\mu\beta_\ell^m = \sqrt{\frac{(\ell-m)(\ell+m)}{(2\ell-1)(2\ell+1)}}\beta^m_{\ell-1} + \sqrt{\frac{(\ell-m+1)(\ell+m+1)}{(2\ell+1)(2\ell+3)}}\beta^m_{\ell+1}, \tag{1.59}$$

where $s = \sin\theta$ and $\mu = \cos\theta$. Relations (1.58) and (1.59) are valid for all m and can be deduced from properties of the associated Legendre functions (Backus et al., 1996, eqs. 3.7.38 and 3.7.14) with definitions (1.16)-(1.18) and $N_\ell = 1$. Using first (1.58) and then (1.59) in eq. (1.57) gives

$$A_\ell^m = 3(\ell+1)\sqrt{\frac{(\ell-m)(\ell+m)}{(2\ell-1)(2\ell+1)}}\beta^m_{\ell-1} + (\ell+2)\sqrt{\frac{(\ell-m+1)(\ell+m+1)}{(2\ell+1)(2\ell+3)}}\beta^m_{\ell+1}. \tag{1.60}$$

Having used fully normalized spherical harmonics, we can argue that the first term on the right is 3 times stronger in amplitude, hence, roughly one order of magnitude stronger in power than the second term. However, this conclusion is valid only if the expectation for $(\mathbf{B}_\ell^\ell)^2$ and $(\mathbf{B}_\ell^{-\ell})^2$ is not higher than for the lower orders $|m| < \ell$.

Chapter 2

Comparison of global and regional power spectra in gravity and magnetics

Spatial variability of a geophysical parameter ψ is conveniently described by its spatial power spectrum. The spatial spectrum usually changes with location; it is not stationary. Its global mean can be inferred from the coefficients of a spherical harmonic expansion. Locally, it can be estimated from Fourier coefficients in a plane coordinate system. The respective estimators can be made compatible by demanding that their integral over the wavenumber domain should give the expected local power $\{\psi^2\}$. In this sense, the usual spherical harmonic coefficient spectrum (Kaula, 1967; Lowes, 1974) for degree ℓ must be multiplied by $\pi^{-1}\,(2\ell+1)^{-1}\,r^2$ to become compatible with the azimuthally averaged "radial" spectrum commonly used in plane coordinates (see Chapter 2).

For the gravity field, we compare the global spectrum of model EGM96 (Lemoine et al., 1998) with local spectra estimated from regional satellite altimetry and ground gravity grids. The locations of the grids are chosen in such a way as to reflect the natural spread from low to high gravity signal. Particularly interesting is the bend in the global gravity spectrum at wavelengths of 1000 - 2000 km. It is clearly visible in the regional spectra as well, establishing it as a genuine characteristic of the gravity field. The bend probably separates two distinct sources of the field, possibly of static and of dynamic origin.

For the geomagnetic field, McLeod and Coleman (1980) derived formulas relating the power of vector components on great circles to the spherical harmonic coefficients of the potential. O'Brian *et al.* (1999) use these formulas to invert for the global spectrum using vector component aeromagnetic survey lines over the oceans. Their result is in good agreement with the spectra of global field models. Here, we compare the spectra of global field models C89 (Cain et al., 1989) and ALP94 (Arkani-Hamed et al., 1994) with local spectra estimated from continental aeromagnetic compilations. The continental spectra are around one order of magnitude stronger than the global average. This behavior is reflected in equa-

torial sample grids taken from the global field models themselves. The mean of the sample spectra is equivalent to the global average, while the oceanic spectra are weaker and the continental spectra are stronger. We attribute the difference to a varying depth extent of the magnetized layer. Model spectra of slabs with varying thickness support this interpretation.

2.1 Spatial power spectrum estimators

We list the spectrum estimators used in the following applications. Derivations and further details are given in Chapter 1. Compatibility of the global spherical and local plane estimators has been tested there. The estimators for the global spectrum of the potential, its radial derivative, and its gradient are

$$\widehat{P}(r, k_\ell) = a^2 \left(\frac{a}{r}\right)^{2\ell+2} \frac{r^2\, N_\ell}{\pi(2\ell+1)} \sum_{m=-\ell}^{\ell} (c_\ell^m)^2 \tag{2.1}$$

$$\widehat{P}_r(r, k_\ell) = \left(\frac{a}{r}\right)^{2\ell+4} \frac{r^2\, (\ell+1)^2\, N_\ell}{\pi(2\ell+1)} \sum_{m=-\ell}^{\ell} (c_\ell^m)^2 \tag{2.2}$$

$$\widehat{P}_{\mathbf{B}}(r, k_\ell) = \left(\frac{a}{r}\right)^{2\ell+4} \frac{r^2\, (\ell+1)}{\pi N_\ell} \sum_{m=-\ell}^{\ell} (c_\ell^m)^2, \tag{2.3}$$

where $k_\ell = (\ell + 1/2)/r$ is the wavenumber, a is the reference radius, $N_\ell = 1$ for a fully normalized and $N_\ell = 1/(2\ell+1)$ for a Schmidt normalized basis, and c_ℓ^m are the spherical harmonic coefficients of degree ℓ and order m. From the local grids we estimate the spatial spectrum using

$$\widehat{P}(k) = \frac{D^2}{(2\pi)^2\, n^2}\, \overline{\widetilde{G}^2}(\frac{Dk}{2\pi}), \tag{2.4}$$

where D/n is the sampling interval of the grid, and $\overline{\widetilde{G}^2}(\frac{Dk}{2\pi})$ is the azimuthal average of the squared discrete Fourier amplitudes (see definition in eq. 1.49). Finally, due to the poloidal and primarily dipolar nature of the magnetic field at the Earth's surface, the total intensity spectrum $P_{|\mathbf{B}|}$ is related to the vector spectrum $P_{\mathbf{B}}$ by

$$P_{|\mathbf{B}|}(k_\ell) \approx \frac{1}{4}(1 + \sin^2 I)\; P_{\mathbf{B}}(k_{\ell+1}), \tag{2.5}$$

where I is the local inclination of the geomagnetic field. The global average of the factor $(1 + \sin^2 I)/4$ for a dipolar main field is $5/12$.

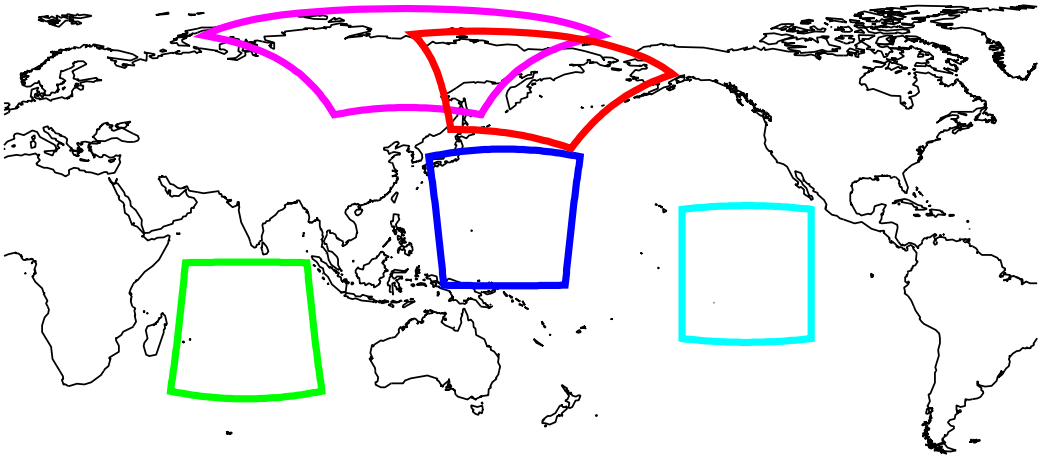

FIG. 2.1: Gravity grids used for Figs. 2.2 and 2.3

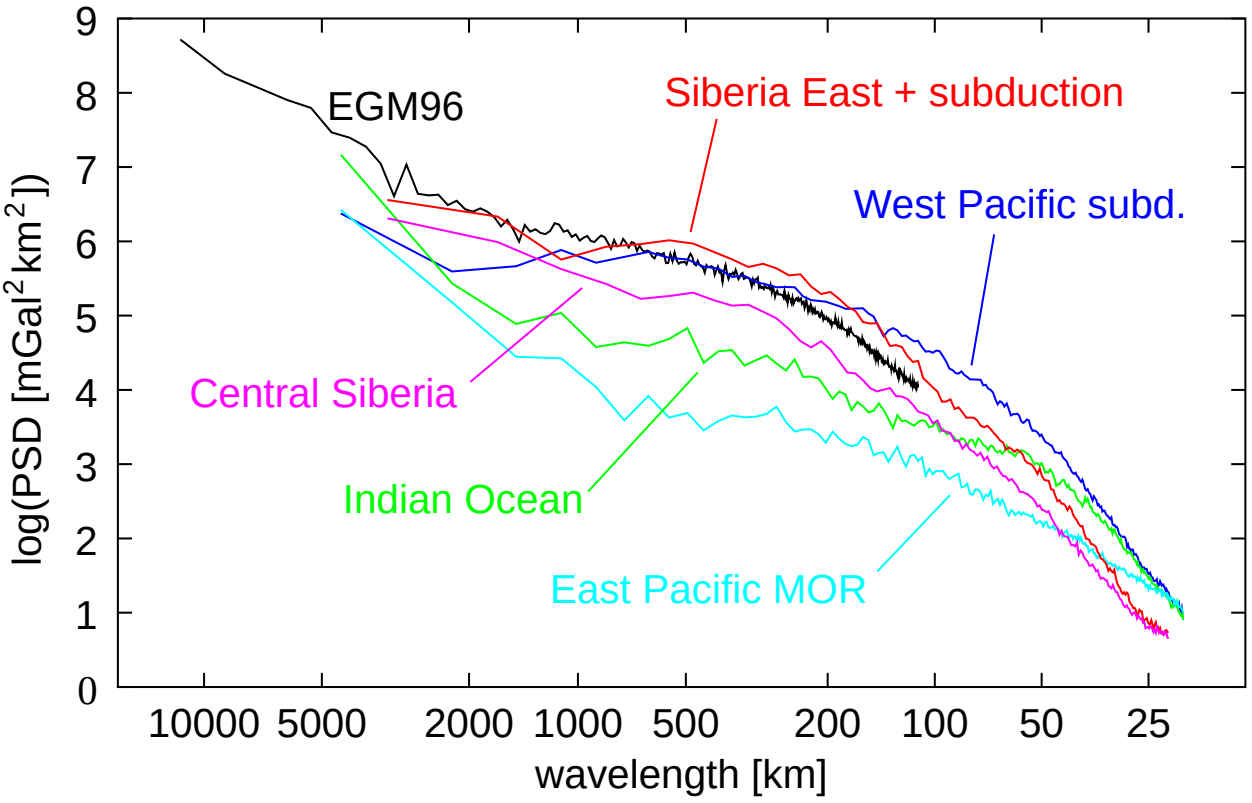

FIG. 2.2: Combined gravity power spectra, estimated using eqs. (2.2) and (2.4)

2.2 Gravity field

The EGM96 spherical harmonic gravity model was compiled from satellite tracking, satellite altimetry and land gravity. Its spectrum has a bend at wavelengths of 1000 - 2000 km, similar to the 'knee' in the geomagnetic spectrum, but less pronounced. To investigate the significance of this bend, we compare the EGM96 spectrum with local spectra estimated from high resolution gravity grids of selected areas, projected onto Cartesian coordinates. From

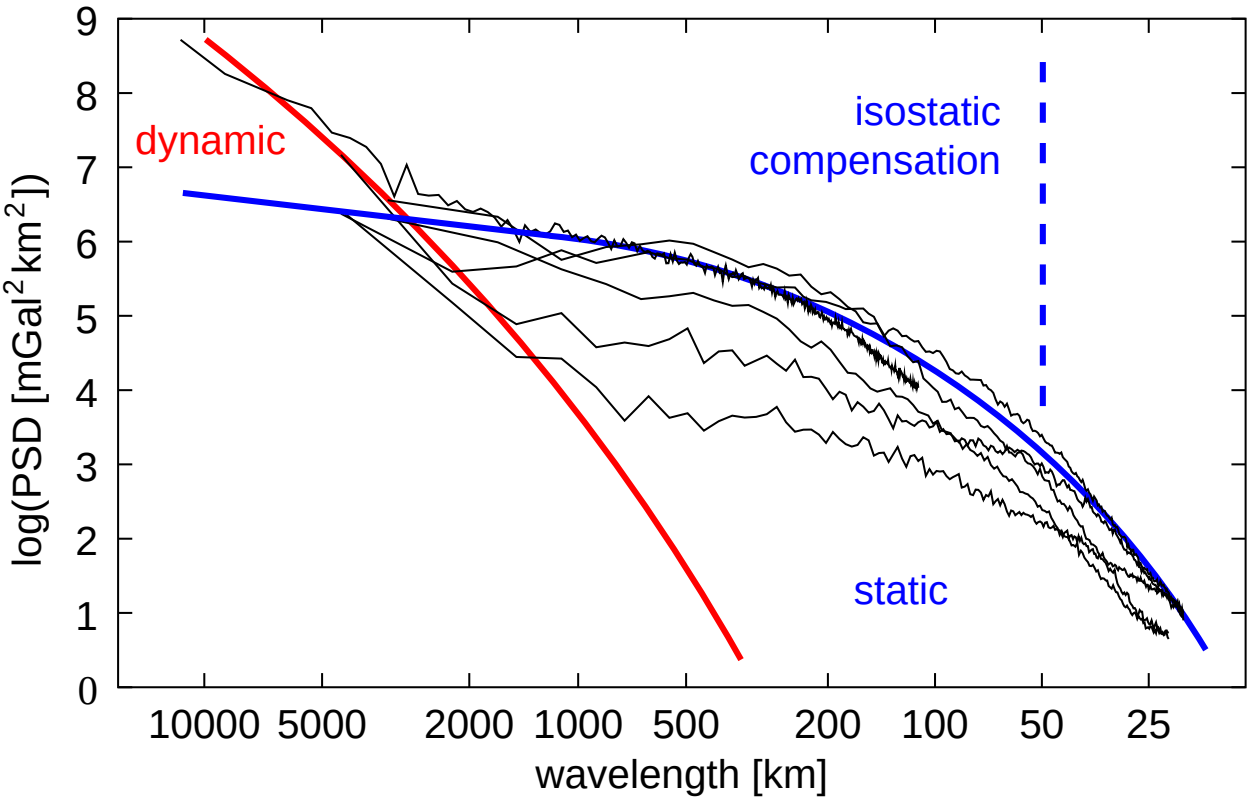

FIG. 2.3: Our interpretation of Fig. 2.2. Isostatic compensation sets in above 50 km wavelength, allowing dynamically supported anomalies to dominate the gravity field at long wavelengths

Sandwell's global ocean gravity grid (Sandwell and Smith, 1997) areas of low gravity signal from the eastern Pacific, medium signal from the Indian Ocean, and strong signal from the western Pacific are selected. Furthermore, we include areas from central and eastern Siberia, covered by the University of Leeds free air gravity compilation. The locations of the grids are indicated in Figure 2.1. We plot the power spectral density (PSD) in logarithmic scale (Fig. 2.2). Considering that the arithmetic average of the spectra is closer to the maximum than to the minimum in logarithmic scale, the EGM96 global spectrum is a realistic average of the local spectra. The bend is present in each, establishing it as a genuine characteristic of the global gravity field. As in the case of the geomagnetic field, the bend is likely to separate two different kinds of source, probably of static and dynamic origin (Fig. 2.3). The static field slopes steeply at short wavelengths and levels off towards long wavelengths due to isostatic compensation. Dynamically supported density anomalies then dominate the global gravity field at wavelengths of more than 1000 km. Finally, it is interesting to see that the satellite altimetry grids in Figure 2.2 have higher power than the Siberian ground data at wavelengths smaller than 30 km. Either topography is more rugged in the oceans than on land, or the altimetry data have higher noise levels.

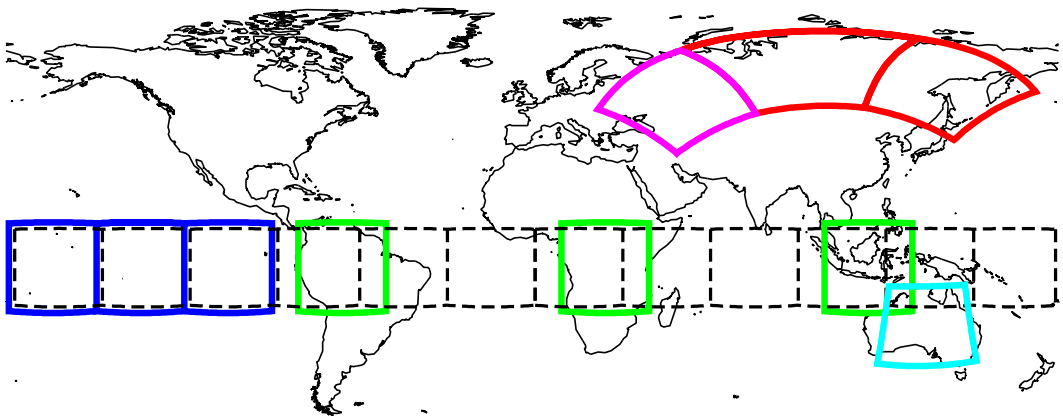

FIG. 2.4: Magnetic grids used for Figs. 2.5 and 2.6

2.3 Magnetic field

We compare the global spectra of models C89 and ALP94, estimated using eq. (2.3), with local magnetic grids chosen from continental scale compilations of aeromagnetic surveys, from which the appropriate Geomagnetic Reference Field had previously been subtracted. 3 areas are chosen from the Soviet Ministry of Geology aeromagnetic compilation of the former Soviet Union (FSU), digitized by the National Geophysical Data Center (NGDC). Furthermore, we use the Australian Geological Survey Organisation (AGSO) aeromagnetic compilation of Australia. Data were projected onto Cartesian coordinates before extracting square grids (Fig. 2.4). After estimating their total intensity spectra from eq. (2.4), these are converted into vector spectra using eq. (2.5). The continental grids have significantly higher power than the global models in the overlapping waveband (Fig. 2.5). We can rule out an inconsistency in the spectrum estimators, data errors, and power leakage from the main field as sources of the discrepancy. The crustal magnetic field at the locations of our sample grids must indeed be stronger than the globally averaged crustal field. This could either be due to the difference in continental/oceanic magnetization, or due to an increase of crustal magnetization with latitude. All grids in Fig. 2.5 are from higher latitudes. For equal lithology, the power of induced magnetic field anomalies increases by a factor 4 from the equator to the poles. Locally acquired and viscous remanent magnetizations could behave in a similar way (Arkani-Hamed and Dyment, 1996).

To investigate the relative importance of geomagnetic latitude versus continent/ocean differences, we use a spherical harmonic expansion of the ALP94 total intensity at 400 km altitude. The global total intensity spectrum is estimated from the expansion coefficients

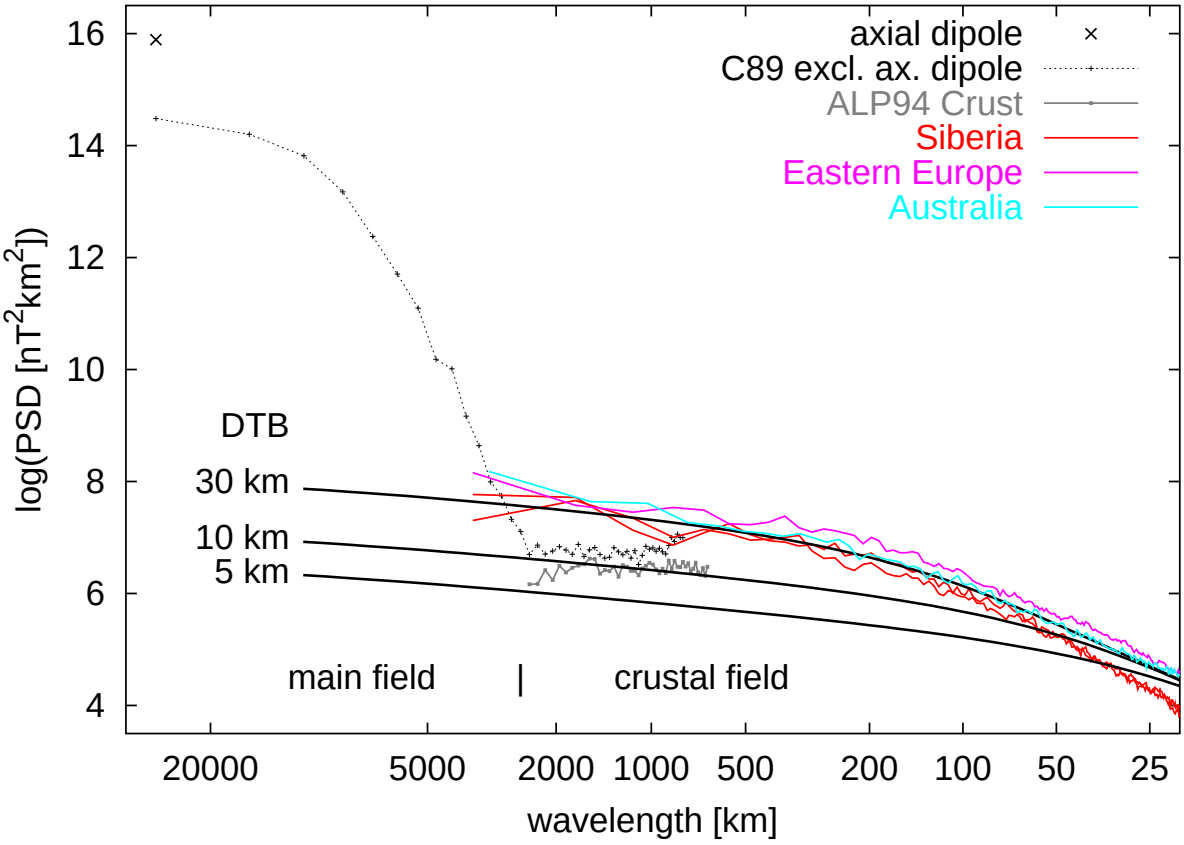

FIG. 2.5: Magnetic vector power spectra estimated using (2.3) and eqs. (2.4) combined with (2.5). Models of eq. (2.6) for $\beta = 3.5$ and depth to bottom (DTB) of 5 km, 10 km, and 30 km are superimposed

using eq. (2.1) and then converted into a vector spectrum with the global mean factor of 5/12 in eq. (2.5). For the local grids, we extract a line of $30° \times 30°$ samples along the equator, as indicated in Fig. 2.4. Their vector spectra are estimated using eqs. (2.4) and (2.5). The equatorial average spectrum agrees well with the global mean spectrum (Fig. 2.6). A possible effect of geomagnetic latitude must therefore be of secondary importance. In contrast, the power of the grids with continental crust is more than one order of magnitude stronger than of those with oceanic crust.

Thickness of magnetized crust

A primary factor in the continent/ocean difference may be the thickness of the magnetized layer. The greater the magnetic depth to bottom (DTB), the stronger the power in long wavelengths. This effect can be quantified by a simple model. It is known that the crustal distribution of apparent susceptibility (including remanent magnetization parallel and anti-parallel to the main field) is approximately self-similar (Pilkington and Todoeschuck, 1993). Hence, let us consider the magnetic field induced by a constant main field $\mathbf{B}$ in a slab of

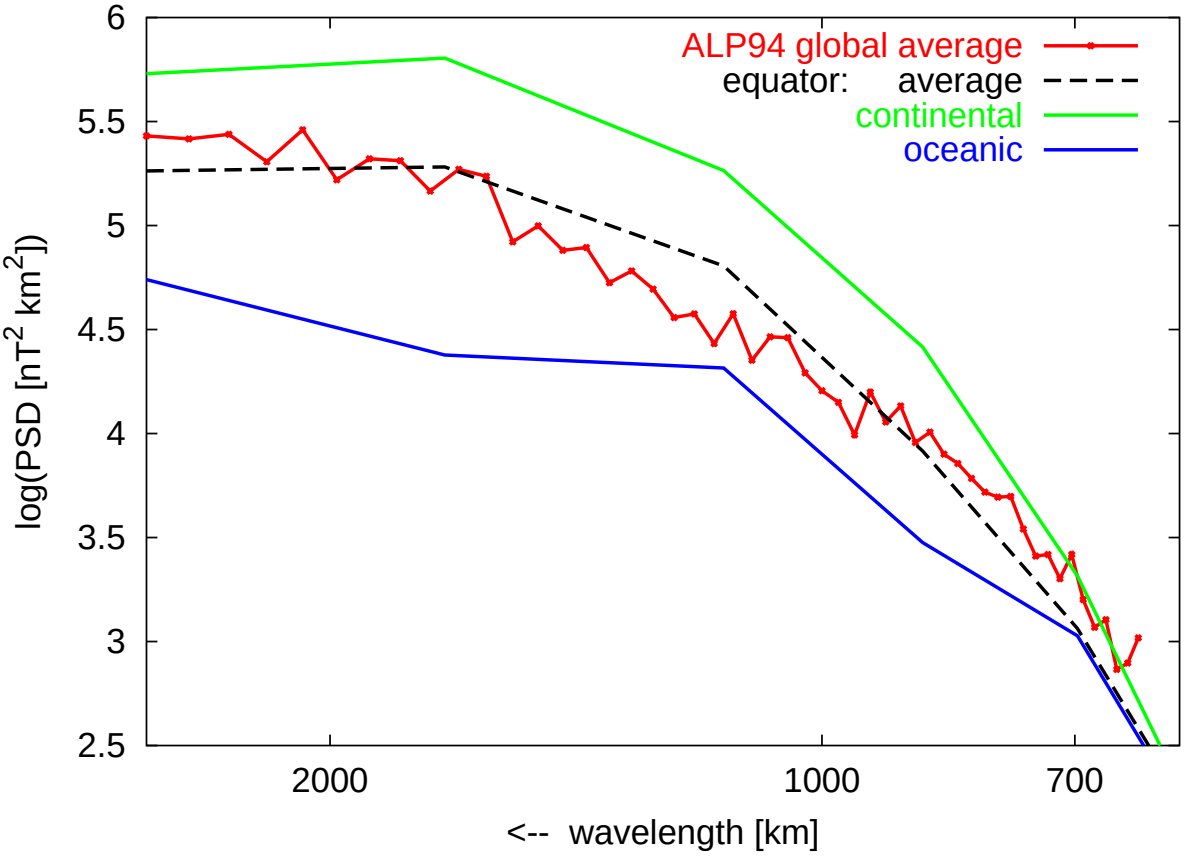

FIG. 2.6: Magnetic vector power spectra of ALP94 at 400 km altitude

uniform thickness t carved out of a self-similar 3D susceptibility distribution with power spectrum $\propto |\mathbf{k}|^{-\beta}$, where $\mathbf{k}$ is the 3D wavevector and β is a scaling exponent. Realistic values for β are in the range of about 3-4, and in the following a value of $\beta = 3.5$ shall be assumed. The total intensity spectrum of the magnetic field over the surface of the slab is given in eq. (3.21), derived in Chapter 3. Taking its azimuthal average leads to

$$P(s,t) \;=\; C\exp(-ts)\; s^{-\beta} \int_0^\infty [\cosh(ts) - \cos(tk_z)](1 + \frac{k_z^2}{s^2})^{-1-\beta/2}\; dk_z, \qquad (2.6)$$

which provides a model accounting for the depth to bottom t. In logarithmic scale, the constant C acts as a vertical offset. We determine C by the best visual fit with the Australian spectrum at high wavenumbers. The model curves for 5, 10, and 30 km DTB (Fig. 2.5) demonstrate that the increased power in the continental grids is indeed explained by a 30 km depth extent of the continental magnetization versus 10 km depth for the global average.

2.4 Discussion and conclusions

A spatial power spectrum can be estimated from spherical harmonic coefficients as well as from plane Fourier coefficients. While the latter gives local estimates, the former provides a global average. A combination of both was used here to study regional variability in a global context. Our comparison of model EGM96 with local high resolution free air gravity grids shows that a bend in the global gravity spectrum is also present in all of the local spectra. Most likely, it separates short wavelength static sources from long wavelength dynamically supported sources of the anomalous gravity field. A similar comparison of global and local magnetic spectra reveals that the continental crustal field is significantly stronger than the oceanic crustal field. A primary cause may be the depth extent of the magnetized layer. Indeed, a 3D self-similar magnetized slab model with 30 km thickness for continental crust versus 10 km on a global average explains the difference. We did not find an indication for the presumed increase of crustal magnetic field power with latitude.

Chapter 3

Curie temperature depth estimation using a self-similar magnetization model*

Ferrimagnetic minerals become paramagnetic (i.e. essentially non-magnetic) at temperatures above their individual Curie temperature. A paramagnetic mineral responds to an external magnetic field by aligning its uncoupled spins, generating a weak secondary magnetic field which is aligned with the inducing field. In ferromagnetic minerals, the uncoupled spins are aligned by an additional quantum-mechanical effect, leading to very strong induced and remanent (stable) magnetizations. In the presence of two ferromagnetic sub-lattices, the mineral is called anti-ferromagnetic when the magnetizations of the two sub-lattices cancel (e.g. in Hematite), and ferrimagnetic if the cancellation is only partial (e.g. in Magnetite). Low titanium titano-magnetite is likely to be the dominant source of the magnetic field in the lower continental crust (Schlinger, 1985; Frost and Shive, 1986). This mineral has Curie temperatures of 575^o - 600^o C (Schlinger, 1985; Frost and Shive, 1986; Wasilewski and Mayhew, 1992), which corresponds to depths in the range of 10 - 50 km. Beneath this Curie temperature depth the lithosphere is virtually nonmagnetic. Furthermore, there is considerable petrological evidence from xenoliths that the Moho is also a magnetic boundary (Wasilewski et al., 1979; Mayhew et al., 1985). While total magnetization levels can reach up to 100 Am^{-1} in mafic lower crustal xenoliths, unaltered upper mantle ultramafics have low magnetizations (Wasilewski and Mayhew, 1992). In the following we will therefore use the more general term depth to bottom (DTB), leaving open whether the bottom is in fact a petrological or a temperature boundary.

Due to the limited depth extent of the crustal magnetization, magnetic anomalies at the Earth's surface are damped at long wavelengths. The lack of long wavelength power has been quantified in numerous studies to derive the DTB from magnetic surveys (Vacquier and Affleck, 1941; Bhattacharyya and Leu, 1975; Shuey et al., 1977; Connard et al., 1983;

*Published in *Geophysical Journal International* (Maus, Gordon and Fairhead, 1997)

Negi et al., 1983; Blakely, 1988; Herzfeld and Brodscholl, 1994; Okubo et al., 1985; Okubo and Matsunaga, 1994). Most of these investigations have been based on the explicit or implicit assumption that long wavelength anomalies necessarily originate only from deep seated sources. If this were really the case, the limited depth extent of the crustal magnetization would already be visible in magnetic maps covering less than 100 km x 100 km. Indeed, Okubo (1985) has derived a detailed Curie isotherm map of the Island of Kyushu using 60 km x 90 km windows. Blakely (1995) recommends a minimum survey dimension of 50 km and 160 km for DTB of up to 10 km and up to 50 km, respectively. On the other hand, Serson (1957) analyzed aeromagnetic profiles extending over several thousand kilometers and failed to see the DTB because the autocorrelation did not taper off to zero, even for lags of several hundred kilometers.

Any method of DTB estimation requires a model for the magnetization distribution in the crust. Earlier models often failed to account for shallow long wavelength variations in the magnetization. These variations are caused by regional geological features, such as extensive sedimentary basins, or contrasts between continental and oceanic lithosphere. One can argue that on average, magnetization contrasts at long scales are similar to the the ones observed at small scales. This idea leads to the powerful concept of self-similarity (Kolmogorov, 1941; Mandelbrot, 1983), which is consistent with susceptibility logs (Pilkington and Todoeschuck, 1993; Maus and Dimri, 1995b), susceptibility surveys (Pilkington and Todoeschuck, 1995) and magnetic maps (Gregotski et al., 1991; Pilkington and Todoeschuck, 1993; Maus and Dimri, 1995b; Maus and Dimri, 1996).

Here we derive a spectral density model for the anomaly of the total intensity of the magnetic field. The model accounts for the self-similarity as well as the limited depth extent of the crustal magnetization. We apply this model to investigate the expected difference in the spectral density of magnetic maps for different DTB.

3.1 Theory

The potential of the magnetic field in a horizontal observation plane at a height z above a slab with thickness t of magnetic sources has been given by Naidu (1968, eq. 43, with $\mathrm{d}_1 = \mathrm{z}$ and $\mathrm{d}_2 = \mathrm{z} + \mathrm{t}$)

$$\begin{aligned} \psi(x,y,z) &= \frac{\mu_0}{2} \int_{-\infty}^{\infty}\int_{-\infty}^{\infty}\int_{-\infty}^{\infty} \widetilde{\mathbf{M}}(u,v,w)\cdot(u\mathbf{e_x}+v\mathbf{e_y}+is\mathbf{e_z}) \\ &\quad \frac{\exp(-sz)[\exp(-st-iwt)-1]}{is\,(s+iw)} \exp(iux+ivy)\,dudvdw, \end{aligned} \tag{3.1}$$

where $\widetilde{\mathbf{M}}(u,v,w)$ is a spectral representation (e.g. Fourier transform) of the vector magnetization; $\mathbf{e_x}$, $\mathbf{e_y}$ and $\mathbf{e_z}$ are the unit vectors of the coordinate system, $\mathbf{s} = (u,v)^T$ is the horizontal wavevector and $s = |\mathbf{s}|$.

Assuming that any remanent magnetization is either parallel or antiparallel to the geomagnetic field $\mathbf{N} = (n_x, n_y, n_z)^T$, we can describe the magnetization by an apparent scalar susceptibility function $\chi(x, y, z)$ as $\mathbf{M}(x, y, z) = \chi(x, y, z)\ \mathbf{N}$. From the linearity of the spectral representation follows that $\widetilde{\mathbf{M}}(u, v, w) = \widetilde{\chi}(u, v, w)\ \mathbf{N}$, and eq. (3.1) can be simplified to

$$\begin{aligned}\psi(x,y,z) &= \frac{\mu_0}{2}\int_{-\infty}^{\infty}\int_{-\infty}^{\infty}\int_{-\infty}^{\infty}(un_x + vn_y + isn_z)\widetilde{\chi}(u,v,w) \\ &\quad \frac{\exp(-sz)[\exp(-st-iwt)-1]}{is\ (s+iw)}\exp(iux+ivy)\ dudvdw. \end{aligned} \tag{3.2}$$

3.1.1 Power spectrum of the magnetic field

The anomaly of the total intensity of the magnetic field $T_\Delta(x, y, z)$, referred to in later chapters by the established term ΔT, is related to the potential by $T_\Delta = \frac{\mathbf{N}}{|N|} \cdot \nabla\psi$. Hence,

$$\begin{aligned}T_\Delta(x,y,z) &= \frac{\mu_0}{2|N|}\int_{-\infty}^{\infty}\int_{-\infty}^{\infty}\int_{-\infty}^{\infty} i(un_x + vn_y + isn_z)^2\widetilde{\chi}(u,v,w) \\ &\quad \frac{\exp(-sz)[\exp(-st-iwt)-1]}{is\ (s+iw)}\exp(iux+ivy)\ dudvdw. \end{aligned} \tag{3.3}$$

Then a 2D spectral representation of the magnetic field is given by

$$\widetilde{T}_\Delta(u,v,z) = \frac{\mu_0}{2|N|} i(un_x + vn_y + isn_z)^2\exp(-sz)\int_{-\infty}^{\infty}\widetilde{\chi}(u,v,w)\frac{[\exp(-st-iwt)-1]}{is\ (s+iw)}dw. \tag{3.4}$$

Let us denote the horizontal component of the geomagnetic field by H and the angle between the horizontal projection $\mathbf{H}$ of the field and the horizontal wavevector $\mathbf{s}$ by θ. Then

$$\widetilde{T}_\Delta(u,v,z) = \frac{\mu_0}{2|N|}(n_z + iH\cos\theta)^2 s\exp(-sz)\int_{-\infty}^{\infty}\widetilde{\chi}(u,v,w)\frac{[1-\exp(-st-iwt)]}{(s+iw)}dw. \tag{3.5}$$

The spectral representation $\widetilde{T}_\Delta(u, v, z)$ of the magnetic field can be regarded as a convolution of the spectral representation $\widetilde{\chi}(u, v, w)$ of the susceptibility distribution with a function $\varphi(w)$

$$\widetilde{T}_\Delta(u,v,z) = \int_{-\infty}^{\infty}\ \varphi(w)\ \widetilde{\chi}(u,v,w)dw \tag{3.6}$$

where

$$\varphi(w) = \frac{\mu_0}{2|N|}(n_z + iH\cos\theta)^2 s\exp(-sz)\ \frac{[1-\exp(-st-iwt)]}{(s+iw)} \tag{3.7}$$

Up to here one could think of the spectral representations as Fourier transforms on the basis of the usual Riemann integral. Taking this view, $\widetilde{T}_\Delta(u, v, z)$ and $\widetilde{\chi}(u, v, w)$ are deterministic functions, obtained by an integral transform from the space domain magnetic field $T_\Delta(x, y, z)$ and the space domain susceptibility distribution $\chi(x, y, z)$. In the following we shall take a stochastic point of view. Then $T_\Delta(x, y, z)$ and $\chi(x, y, z)$ are regarded as the

outcome of some kind of random experiment. Their spectral representations are given by Fourier-Stieltjes integrals (Yaglom, 1986) in the following sense:

$$R(x) = \int_{-\infty}^{\infty} \exp(iux) Z(du), \tag{3.8}$$

where R(x) is the random function in the space domain and $Z(du)$ is a complex random measure determined for any interval du and having the properties

1. $\langle Z(du) \rangle = 0$ for all intervals du;

2. $\langle Z(du)\overline{Z(du')} \rangle = 0$ for nonintersecting intervals du and du'

3. $Z(du \cup du') = Z(du) + Z(du')$ for nonintersecting intervals du and du'

The spectral density (power spectrum) $P(u)$, if it exists, is related to $Z(du)$ by

$$\langle Z(du)\overline{Z(du)} \rangle = P(u)du \tag{3.9}$$

Finally

$$\langle Z(du)\overline{Z(du')} \rangle = \delta(u - u')\, P(u)\, dudu'. \tag{3.10}$$

Here, $\langle \cdot \rangle$ stands for the expected value and $\delta(u)$ is the Dirac δ-function.

In this notation equation (3.6) becomes

$$\widetilde{T}_{\Delta}(du, dv, z) = \int_{-\infty}^{\infty} \varphi(w)\ \widetilde{\chi}(du, dv, dw), \tag{3.11}$$

where $\widetilde{T}_{\Delta}(du, dv, z)$ and $\widetilde{\chi}(du, dv, dw)$ are two random measures, corresponding to $Z(du)$ in equation (3.8). An application of the Fourier-Stieltjes Integral to a related problem can be found in Maus and Dimri (1996). To derive an expression for the spectral density of the magnetic field, we multiply both sides of (3.11) with their complex conjugates

$$\widetilde{T}_{\Delta}(du, dv, z)\overline{\widetilde{T}_{\Delta}(du, dv, z)} \;=\; \int_{-\infty}^{\infty}\int_{-\infty}^{\infty} \varphi(w)\widetilde{\chi}(du, dv, dw)\overline{\varphi(w')\widetilde{\chi}(du, dv, dw')} \tag{3.12}$$

and make use of relation (3.9) for u and v, and of relation (3.10) for w and w', giving

$$P_T(u, v, z)dudv \;=\; \int_{-\infty}^{\infty}\int_{-\infty}^{\infty} \varphi(w)\overline{\varphi(w')}\ \delta(w - w')P_{\chi}(u, v, w)dudvdwdw' \tag{3.13}$$

$$P_T(u, v, z) \;=\; \int_{-\infty}^{\infty} \varphi(w)\overline{\varphi(w)}P_{\chi}(u, v, w)\ dw, \tag{3.14}$$

where $P_T(u, v, z)$ is the spectral density of the total intensity of the magnetic field and $P_{\chi}(u, v, w)$ is the spectral density of the susceptibility distribution within the slab. Recalling

the definition of $\varphi(w)$ from equation (3.7)

$$\begin{aligned}
\varphi(w)\overline{\varphi(w)} &= \frac{\mu_0^2}{4N^2}(n_z + iH\cos\theta)^2\overline{(n_z + iH\cos\theta)^2}s^2\exp(-2sz) \\
&\quad \frac{1-\exp(-st-iwt)}{s+iw}\overline{\left(\frac{1-\exp(-st-iw't)}{s+iw'}\right)} \qquad (3.15)\\
&= \frac{\mu_0^2}{4N^2}(n_z^2 + H^2\cos^2\theta)^2 s^2\exp(-2sz) \\
&\quad [1-\exp(-ts-itw)-\exp(-ts+itw)+\exp(-2ts)](s^2+w^2)^{-1} \qquad (3.16)\\
&= \frac{\mu_0^2}{4N^2}(n_z^2 + H^2\cos^2\theta)^2 s^2\exp(-2sz) \\
&\quad 2\exp(-ts)[\cosh(ts)-\cos(tw)](s^2+w^2)^{-1}. \qquad (3.17)
\end{aligned}$$

Combining equations (3.14) and (3.17) leads to a relationship between the spectral density of the magnetic field and the spectral density of the susceptibility distribution within the slab as

$$\begin{aligned}
P_T(u,v,z) &= \frac{\mu_0^2}{2N^2}(n_z^2 + H^2\cos^2\theta)^2\exp(-2sz-ts) \\
&\quad \int_{-\infty}^{\infty}[\cosh(ts)-\cos(tw)](1+\frac{w^2}{s^2})^{-1} \\
&\quad P_\chi(u,v,w)\ dw. \qquad (3.18)
\end{aligned}$$

3.1.2 Self-similar magnetized slab model

Assuming self-similarity of $\chi(x,y,z)$ is expressed by

$$\begin{aligned}
P_\chi(u,v,w) &= c_s(u^2+v^2+w^2)^{-\beta/2} \qquad (3.19)\\
&= c_s s^{-\beta}\ (1+\frac{w^2}{s^2})^{-\beta/2}, \qquad (3.20)
\end{aligned}$$

where c_s and β are constants, β being called the 3D scaling exponent of the susceptibility distribution. Substituting equation (3.20) into equation (3.18) gives the 2D spectral density (power spectrum) of the magnetic field due to a slab of self-similar sources

$$\begin{aligned}
P_T(u,v,z) &= c_s\frac{\mu_0^2}{N^2}(n_z^2 + H^2\cos^2\theta)^2\exp(-2sz-ts)s^{-\beta} \\
&\quad \int_0^{\infty}[\cosh(ts)-\cos(tw)](1+\frac{w^2}{s^2})^{-1-\beta/2}\ dw. \qquad (3.21)
\end{aligned}$$

It is common practice to regard the logarithm of the azimuthally averaged "radial" power spectrum (Spector and Grant, 1970). However, instead of the logarithm of the azimuthal average power, it is advisable to take the azimuthal average of the logarithm of the power (Maus and Dimri, 1995b). This is equivalent to using the geometric mean instead of the

arithmetic mean in the azimuthal averaging. Then eq. (3.21) becomes

$$\frac{1}{2\pi}\int_0^{2\pi}\ln(P_T)d\theta = \underbrace{\frac{1}{2\pi}\int_0^{2\pi}\ln[c_s\frac{\mu_0^2}{N^2}(n_z^2+H^2\cos^2\theta)^2]d\theta}_{C} - 2sz - ts - \beta\ln(s) + \ln\left[\int_0^{\infty}[\cosh(ts)-\cos(tw)](1+\frac{w^2}{s^2})^{-1-\beta/2}\,dw\right]. \quad (3.22)$$

The anisotropy of the field is then reflected only in a term C which is independent of the wavenumber s. Consequently, it is not necessary to reduce the spectrum to the pole. In a reduction to the pole the spectrum is divided by $(n_z^2+H^2\cos^2\theta)^2$. This is dangerous at low magnetic latitudes, because $n_z^2+H^2\cos^2\theta$ vanishes at $\theta = 90^o$.

3.1.3 Limitations of the theory

Equation (3.1) is based on the implicit assumption that the magnetic field as well as its source distribution can be written as a Fourier integral. This contradicts the self-similarity assumption in equation (3.20). A self-similar random function cannot be represented as a sum of harmonic waves. The same objection applies to *white noise*, which is often used as a model for source distributions. In this case the problem of a diverging Fourier integral is commonly avoided by assuming *band limited white noise*. In the same way one can assume that the self-similarity of a stochastic process is restricted to a limited band of wavenumbers (Goff and Jordan, 1988; Maus and Dimri, 1996). Nevertheless, equations (3.21) and (3.22) have to be regarded as approximations rather than exact relations. The quality of the approximation is likely to vary with the value of β.

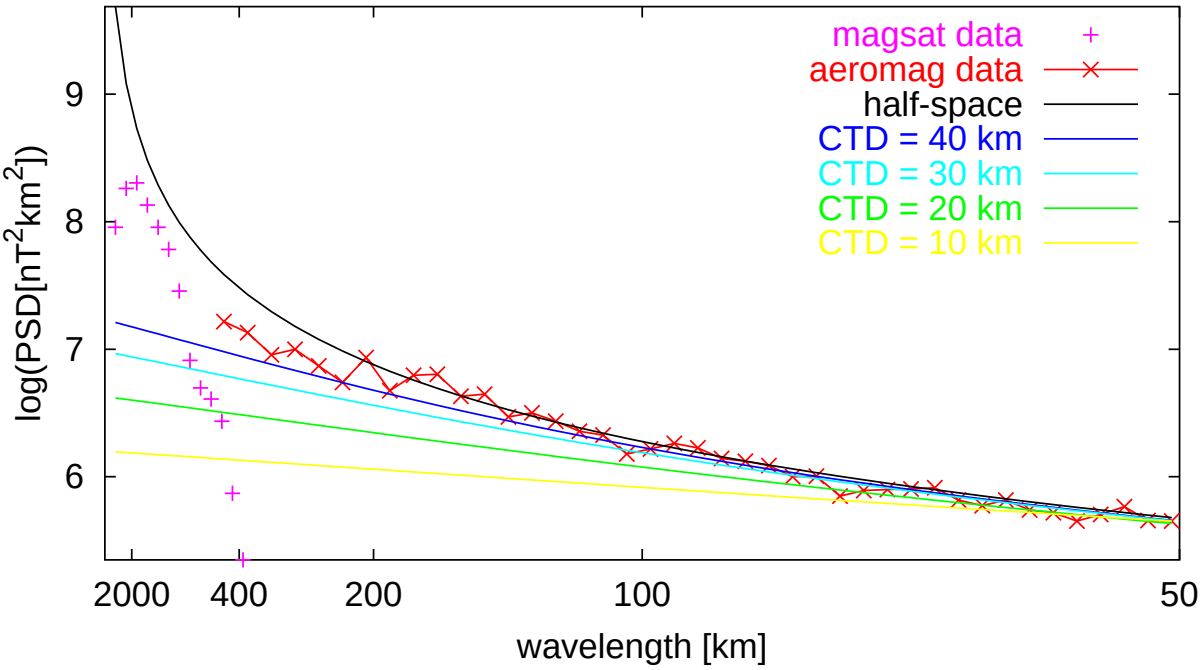

FIG. 3.1: Power spectra of aeromagnetic and Magsat grids over S. Africa (after Whaler, 1994, Fig. 10), together with the model power spectra of equation (3.22) for $\beta = 3$, $z = 0$ and various DTB. The half-space model corresponds to an infinite DTB.

3.2 Applications

Using equation (3.22), we investigate the possibilities and limitations of DTB estimation from the power spectrum of total field magnetic anomaly maps. The model power spectra are obtained by numerical evaluation of (3.22) for a particular set of model parameters. These model power spectra are then plotted against power spectra of different survey areas. The constant C in equation (3.22) is chosen in such a way that the model power spectrum fits the power spectrum of the magnetic map at high wavenumbers.

3.2.1 Survey areas

Our first sample power spectrum is taken from the literature. It was estimated in the usual way by Whaler (1994) from aeromagnetic and Magsat data of South Africa downward continued to surface level. This power spectrum is displayed together with the model power spectra of equation (3.22) for $z = 0$ and varying scaling exponents and slab thicknesses in Figures 3.1-3.3.

Since equation (3.22) is actually a model for the azimuthal average of the log power and not for the log of the azimuthally averaged power, we have estimated our own power spectra from two large magnetic grids of the former Soviet Union (FSU), available from National Geophysical Data Center (NGDC), Boulder, Colorado. The grids were compiled

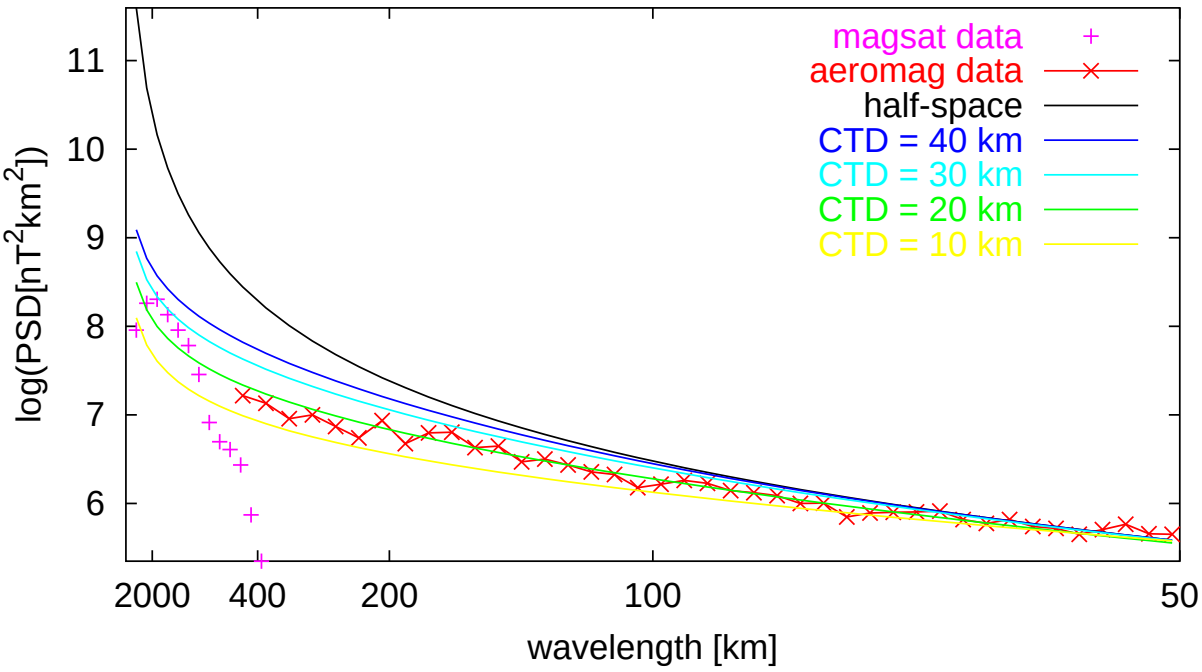

FIG. 3.2: Data of Figure 3.1 together with the model power spectra for $\beta = 4$.

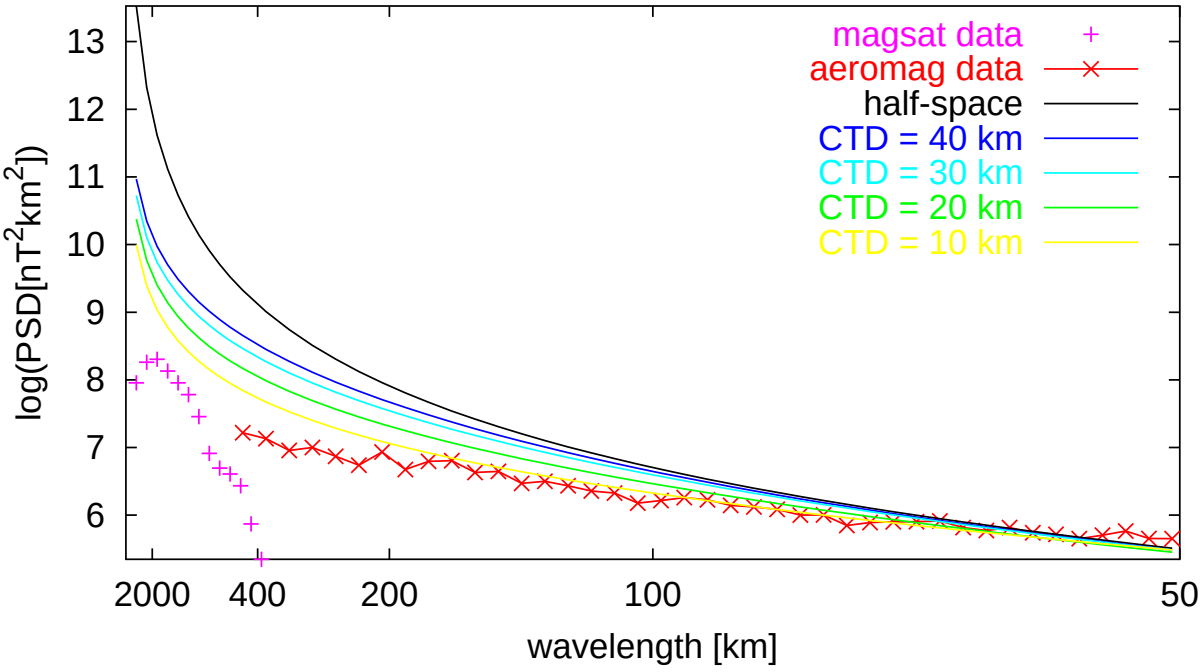

FIG. 3.3: Data of Figure 3.1 together with the model power spectra for $\beta = 5$.

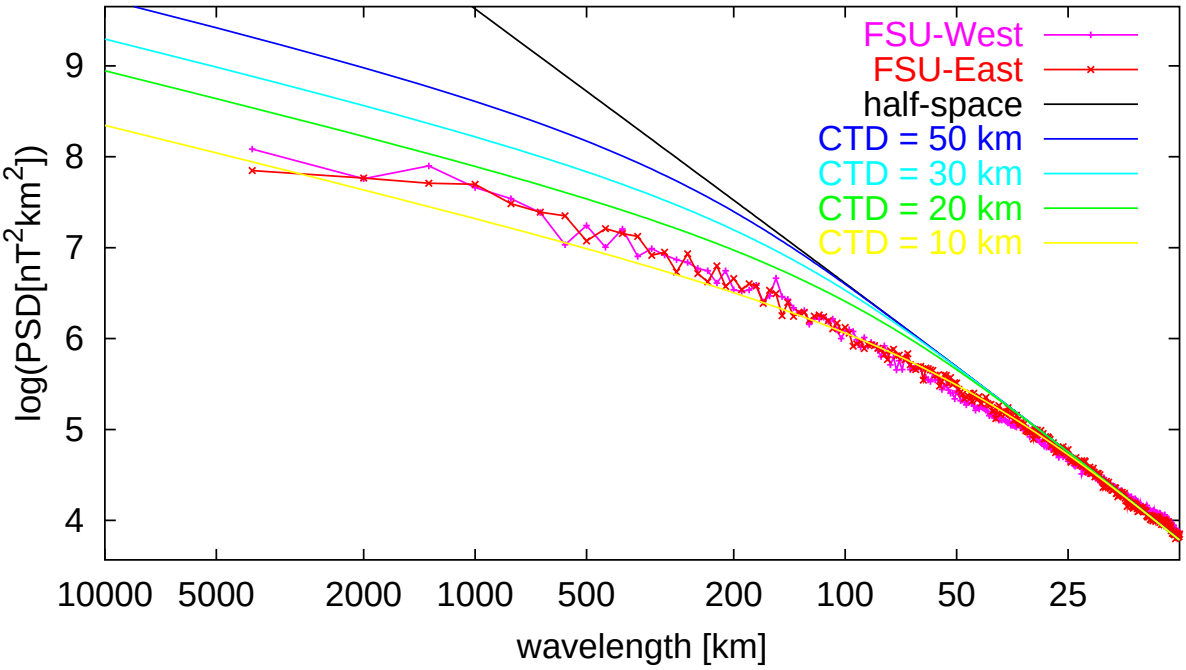

FIG. 3.4: Power spectra of the former Soviet Union together with the model power spectra for $\beta = 4$ and $z = 300$ m in log-log scale. At high wavenumbers the magnetic field is self-similar and its log-log power spectrum is a straight line. At wavelengths above 50 km (corresponding to wavenumbers below 0.02 cycles/km) the power is decreased due to the limited depth extent of the crustal magnetization. The model indicates a DTB of around 15 km under the assumption of $\beta = 4$.

from surveys flown at 200 m to 500 m topographic altitude. The grid FSU-West extends from 35^o to 78^o latitude and 61^o to 104^o in longitude, while the grid FSU-East has the same latitude but extends from 104^o to 147^o in longitude. The international geomagnetic reference field (IGRF) of 1965 and a first order trend were removed from the data. Their power spectra are shown in Figures 3.4 to 3.6. The graphs in Figures 3.4 and 3.5 are plotted in log-log scale to demonstrate the self-similarity of the magnetic field at high wavenumbers and the departure from self-similarity at low wavenumbers.

3.2.2 Resolution of the depth to bottom (DTB)

It is not our intention to derive precise DTB estimates of the survey areas, but to investigate the possibilities and limitations of DTB estimation in general. From the plots in Figures 3.1-3.5 we draw the following conclusions:

1. A noticeable difference between the model power spectra for different DTB occurs only at wavelengths above 100 km (see in particular Figure 3.5).

2. We find a trade-off between increasing susceptibility scaling exponents β and a decreasing DTB. A scaling exponent of $\beta = 4$ gives a realistic DTB of around 20 km for South

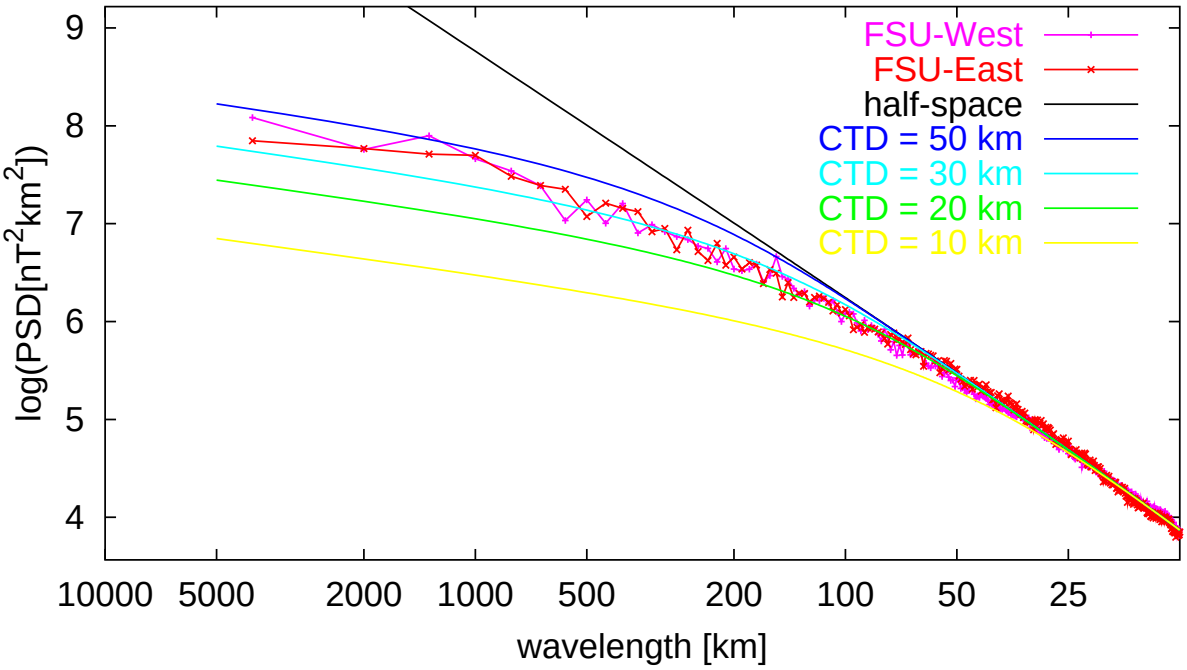

FIG. 3.5: Power spectra of the FSU in log-log scale as in Figure 3.4 but with the model power spectra for $\beta = 3.5$. The lower the assumed scaling exponent of the crustal susceptibility distribution, the greater the resulting estimate for the DTB.

Africa (Figure 3.2). For Central Asia a scaling exponent of $\beta = 4$ leads to a DTB of 15 ± 5 km (Figure 3.4). This may be too shallow. Choosing a lower scaling exponent of $\beta = 3.5$ leads to a DTB estimate around 40 km (Figure 3.5). Hence, the fact that the exact value of the scaling exponent β of the crustal susceptibility distribution is unknown leads to large uncertainties in absolute DTB estimates.

3. To resolve the power at long wavelengths with sufficient precision, large survey areas are required. It is unlikely that a reliable estimate of the DTB can be obtained from an area smaller than 1000 km x 1000 km. Consequently, it should be difficult to estimate the DTB from individual aeromagnetic surveys, typically having dimensions of not more than a few hundred kilometers. The situation may, however, be more favorable for young oceanic crust with shallower DTB.

4. A consequence of the large survey areas required is that realistic maps of the DTB would have a very low lateral resolution. It is unlikely that it will be possible to resolve lateral DTB variations for distances of less than several 100 km from magnetic data by spectral methods. Such DTB maps would not shed much light on geological features with strong lateral temperature variations, such as subduction zones.

One also has to take into consideration that long-wavelength anomalies in continental scale magnetic compilations can be severely compromised by survey stitching procedures, non-

uniform data acquisition parameters (especially, the elevation) and by the choice of geomagnetic reference field.

3.2.3 Long range correlation

We infer from Figures 3.1-3.5 that a susceptibility scaling exponent of $3.5 \leq \beta \leq 4$ is consistent with the magnetic maps of S. Africa and Central Asia. This is an important result, because it implies that the same scaling law observed by Pilkington and Todoeschuck (1993; 1994) for susceptibility logs and surveys on a local scale can be valid at regional scales of up to thousands of kilometers, as well. In particular, the crustal magnetization can be correlated over considerable distances. This contradicts earlier assumptions of correlation lengths only up to several tens of kilometers (Jackson, 1990; Jackson, 1994).

3.2.4 White depth models

To compare our results with those of earlier studies, let us attempt to interpret the FSU spectra in the conventional way (Spector and Grant, 1970; Connard et al., 1983). Then the slope of the power spectrum indicates the depth to the top of some kind of statistical ensemble of prisms. The limited depth extent of these prisms leads to a maximum in the power spectrum (Spector and Grant, 1970). The wavenumber of this maximum is directly related to the DTB (Blakely, 1995). This interpretation is based on the implicit assumption of a white power spectrum of the magnetic field at source level. Hence, it corresponds to $\beta = 1$ in terms of our model. Figure 3.6 shows the corresponding power spectra. The obvious disagreement with the observed power spectra, in particular the missing maximum, is a further indication against using white depth models to estimate the depth to the bottom of a magnetic layer.

3.3 Discussion and conclusions

We have derived a spectral model for magnetic maps at a regional scale. Long range correlation is accounted for by the scaling exponent of an apparent susceptibility distribution. The higher the values of β, the stronger the long range correlation.

For $\beta = 1$ our model describes the field due to a weakly correlated crustal magnetization as assumed by the popular *white noise* field models (Hahn et al., 1976). Many earlier DTB estimates are based on such models. Figure 3.1 shows, however, that realistic values of β are certainly above $\beta = 3$. Consequently, the DTB is manifested much less prominently in magnetic maps than assumed in earlier studies.

Nevertheless, it seems possible to compute maps of the DTB. Main obstacles are the low resolution and the trade-off between higher scaling exponents β and shallower DTB.

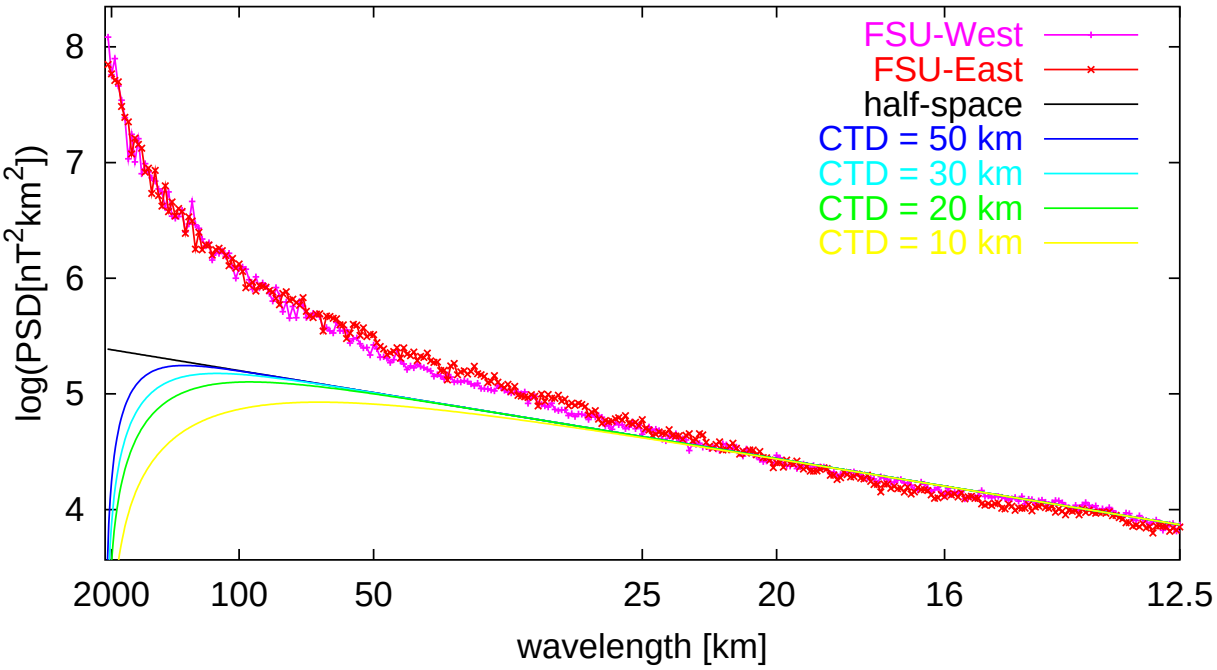

FIG. 3.6: Power spectra of the FSU with the model power spectra for $\beta = 1$ and $z = 3.5$ km. This corresponds to an interpretation using the white depth models which were utilized in earlier studies to derive DTB from the location of a maximum in the power spectrum. There is no maximum in the FSU power spectra. Maxima are only found in power spectra which are inaccurately derived from small survey areas.

Resolution of the DTB requires an assumption on β. Values of β could be larger in the lower crust, indicating a smoother distribution of magnetization. However, assuming a constant value of $\beta = 4$ and moving a window over a very large area would probably lead to a smooth DTB relief, with a certain degree of uncertainty in the absolute depth.

Perhaps our most interesting finding is that the self-similarity of the crustal magnetization extends with a high scaling exponent of β_{3D} close to 4 up to regional wavelengths. The 3D scaling exponent β_{3D} of the susceptibility distribution is related to the scaling exponents of lower-dimensional cross-sections of the same distribution by $\beta_{3D} = \beta_{2D} + 1 = \beta_{1D} + 2$ (Maus and Dimri, 1994). A β_{3D} close to 4 therefore fits well to the results of earlier studies which suggest that the susceptibility distribution in the crust has scaling exponents of $\beta_{1D} \approx 2$ (Pilkington and Todoeschuck, 1993) and $\beta_{2D} \approx 3$ (Pilkington and Todoeschuck, 1995). Furthermore, the corresponding magnetic field at surface level should have a 2D scaling exponent of $\gamma_{2D} = \beta_{3D} - 1$. Indeed, Gregotski, Jensen and Arkani-Hamed (1991) found scaling exponents of $\gamma_{2D} \approx 3$ for local magnetic anomalies in North America. However, significantly lower scaling exponents of $\beta_{1D} = 0.4$ and $\gamma_{2D} \approx 2$ were found for the susceptibility distribution and the magnetic field in the area of the German Continental Deep Drilling Project (KTB) (Maus and Dimri, 1995b).

Chapter 4

Variogram analysis theory*

Density and susceptibility distributions in the Earth's continental crust are self-similar (scaling, fractal), with a power spectrum $P(\mathbf{k})$ proportional to $|\mathbf{k}|^{-\beta}$, where $\mathbf{k}$ is the wavevector and β is called the scaling exponent (Pilkington and Todoeschuck, 1990; Pilkington and Todoeschuck, 1993; Pilkington and Todoeschuck, 1995). Self-similar random functions were first proposed by Kolmogorov (1941; 1961) to model velocity fluctuations in a 3D turbulent medium. Their importance for the Earth sciences was discovered by Mandelbrot (1983).

The spectra of gravity and magnetic fields can be related to the spectra of their respective source distributions (Naidu, 1968). Self-similar source models lead to realistic spectral models for gravity and magnetic data (Gregotski et al., 1991; Pilkington and Todoeschuck, 1993; Pilkington et al., 1994; Maus and Dimri, 1995b; Maus and Dimri, 1996). Such models can play an important role in the processing and interpretation of potential field data (Maus, 1996), for example in gridding (Pilkington et al., 1994), susceptibility mapping (Gregotski et al., 1991), depth estimation (Pilkington et al., 1994; Maus and Dimri, 1995a) and the computation of isostatic gravity residuals (Chapin, 1996).

In depth estimation by spectral analysis, magnetic data are interpolated to a regular grid, transformed by FFT to wavenumber domain and their azimuthally averaged power spectrum is analyzed (Spector and Grant, 1970). However, even if the former spectral slope models are substituted by the more realistic self-similar models, depth from magnetic power spectra remains inaccurate (Maus and Dimri, 1996). This is due to the distorting effects of gridding, preparation for FFT, and azimuthal averaging on the data power spectra.

Here, I transform a self-similar spectral model analytically to the space domain in order to avoid the distorting effects of transforming measured data to the wavenumber domain. I argue that variograms are the appropriate space domain statistical models for analyzing magnetic and possibly gravity data. After describing my spectral model for the magnetic field, I derive the corresponding variogram model for the complex case of aeromagnetic profiles in a non-vertical inducing field. The variogram model for gravity data is subsequently

*Published in *Geophysics* (Maus, 1999)

derived as a special case. Graphs of the model variograms illustrate the influence of profile orientation, depth, source intensity and scaling exponent. Finally, a section on practical aspects proposes solutions to key difficulties in implementing a variogram analysis algorithm. Case studies, including further explanations, a comparison with Spector and Grant's method, and tests on synthetic data are given in Chapters 5 and 6.

4.1 Spectral models

4.1.1 Magnetic field power spectrum

Let us assume that magnetization as a function of the location $\mathbf{r}$ can be expressed as the product of a scalar susceptibility $\chi(\mathbf{r})$ and a constant geomagnetic field $\mathbf{N}$. This implies, in particular, that no significant component of remanent magnetization exists in any direction other than $\mathbf{N}$. Then the power spectrum $P_{\Delta T}(\mathbf{k})$ of the total intensity anomaly ΔT in a horizontal observation plane due to a slab of scaling sources is given by substituting eqs. 3.16 and 3.20 into eq. 3.14 as

$$\begin{aligned} P_{\Delta T}(\mathbf{s}) \;=\; & \frac{\mu_0^2}{4N^2}(n_z^2 + H^2\cos^2\theta)^2 s^2 \exp(-2sz) \\ & \int_{-\infty}^{\infty} [1 - \exp(-ts - itw) - \exp(-ts + itw) + \exp(-2ts)] \\ & (s^2 + w^2)^{-1}\; c_s(s^2 + w^2)^{-\beta/2}\; dw \end{aligned} \tag{4.1}$$

where $\mathbf{s} = (u, v)$ is the horizontal wavevector, $s = |\mathbf{s}|$, w is the vertical component of the wavevector, z is the distance between the observation plane and the top of the slab, t is the thickness of the slab, $\mathbf{N} = (n_x, n_y, n_z)$ is the geomagnetic field, $N = |\mathbf{N}|$ its intensity, $H = |(n_x, n_y)|$ its horizontal intensity, θ is the angle between $\mathbf{s}$ and $\mathbf{H}$, and μ_0 is the magnetic permeability of free space. The parameters c_s and β refer to the susceptibility distribution $\chi(\mathbf{r})$ on a full-space with power spectrum

$$P_\chi(u, v, w) = c_s(u^2 + v^2 + w^2)^{-\beta/2}, \tag{4.2}$$

of which the slab is a spatial subset. Hence, the slab is thought to be carved out of an imagined self-similar 3D susceptibility distribution. Note that the slab in an otherwise empty space is neither self-similar nor does it have a power spectrum as in equation (4.2).

The limited depth extent of crustal magnetization has no noticeable effect on the power spectrum of the magnetic field up to wavelengths of about three times the depth to bottom (see Figures 3.4 and 3.5). For most practical cases in basement depth estimation, where the size of the data analysis window is much smaller, we can simplify equation 4.1 by utilizing

a half-space model, corresponding to t=∞. Then

$$
\begin{aligned}
P_{\Delta T}(\mathbf{s}) &= c_s \frac{\mu_0^2}{4N^2}(n_z^2 + H^2\cos^2\theta)^2 s^2 \exp(-2sz) \\
&\quad \int_{-\infty}^{\infty} (s^2 + w^2)^{-\beta/2-1}\, dw \qquad (4.3) \\
&= c_s \frac{\mu_0^2}{4N^2}(n_z^2 + H^2\cos^2\theta)^2 s^{-\beta} \exp(-2sz) \\
&\quad \int_{-\infty}^{\infty} [1 + (w/s)^2]^{-\beta/2-1}\, dw \qquad (4.4) \\
&= c_s \frac{\mu_0^2}{2N^2}(n_z^2 + H^2\cos^2\theta)^2 s^{-\beta+1} \exp(-2sz) \\
&\quad \int_{0}^{\infty} [1 + a^2]^{-\beta/2-1}\, da, \qquad (4.5)
\end{aligned}
$$

with $a = w/s$. Solving the integral using Gradshteyn (1994, eq. 3.251.2) gives

$$
P_{\Delta T}(\mathbf{s}) = c_s (\frac{\mu_0}{2N})^2 B[1/2, (\beta+1)/2] \underbrace{(n_z^2 + H^2\cos^2\theta)^2}_{Dir(\theta)} \underbrace{s^{-\beta+1}\exp(-2sz)}_{Q(s)}, \qquad (4.6)
$$

where B is the beta function $B(x, y) = \Gamma(x)\Gamma(y)/\Gamma(x+y)$.

4.1.2 Gravity field power spectrum

The spectrum P_g of the vertical derivative of the anomalous gravity potential due to a self-similar density distribution within a half-space can be written (Naidu, 1968; Maus and Dimri, 1995b) as

$$
\begin{aligned}
P_g(\mathbf{s}) &= c_s \frac{4\sigma^2}{\pi^2} \exp(-2sz) \int_{-\infty}^{\infty} (s^2 + w^2)^{-\beta/2-1}\, dw \qquad (4.7) \\
&= c_s \frac{4\sigma^2}{\pi^2} B[1/2, (\beta+1)/2] s^{-\beta-1} \exp(-2sz), \qquad (4.8)
\end{aligned}
$$

where σ is the universal gravity constant and c_s and β are parameters describing the anomalous density distribution of a half-space model as in (4.2).

Comparing equations (4.6) and (4.8) shows that the gravity model is very similar to the ΔT model for the special case of a vertical inducing field $\mathbf{N} = (0, 0, N)$.

4.1.3 Scaling exponents

The 3D scaling exponents of crustal susceptibility and density can be inferred from 1D and 2D cross-sections, such as bore wells and surveys at the surface. Furthermore, they can be derived from the respective magnetic and gravity fields. Relationships between the scaling exponents of a field and its sources in different dimensions have been derived by Maus and Dimri (1994).

Marine gravity off Norway and south of Japan, as well as free air and Bouguer gravity of the Former Soviet Union have a consistent $\beta = 3.5$ (Chapter 7.5). Pilkington and Todoeschuck (1990) derived scaling exponents of around 1, corresponding to $\beta \approx 3$ from density logs.

Gregotski et al. (1991) estimated scaling exponents from 8 aeromagnetic data sets finding values in the range of 2.8 to 3.4, corresponding to $3.8 < \beta < 4.4$. An average scaling exponent of $\beta = 4$ was further confirmed by Pilkington *et al.* (1993; 1994; 1995) from susceptibility logs, aeromagnetic data and susceptibility surveys. In contrast, Maus and Dimri (1995b) derived scaling exponents of $\beta < 3$ from helicopter magnetic data and a 4 km vertical rock susceptibility profile at the German Continental Deep Drilling site.

In general, density logs are smoother than susceptibility logs. The scaling exponent of density should therefore be higher than that of susceptibility, at least on a local scale.

4.2 Space domain counterparts

4.2.1 ACF versus variogram

The most obvious space domain counterpart of a power spectrum is the auto-correlation function (ACF)

$$ACF(\boldsymbol{\tau}) \;=\; \langle X(\mathbf{r}+\boldsymbol{\tau})X(\mathbf{r})\rangle, \tag{4.9}$$

which is related to the power spectrum by a Fourier transform

$$ACF(\boldsymbol{\tau}) = \int_{-\infty}^{\infty}\int_{-\infty}^{\infty} \exp(i\boldsymbol{\tau}\cdot\mathbf{s})\; P(\mathbf{s})\, du\, dv. \tag{4.10}$$

However, if we use (4.10) to derive the ACF counterpart of the spectral model defined by (4.6), we face the problem that the integrals do not converge for $\beta > 3$. This reflects the fact that for $\beta > 3$ equation (4.6) describes an inhomogeneous random function (equivalent to a nonstationary process in 1D) with infinite variance and a variable mean value. This is not just a mathematical problem. Anyone having attempted to estimate an ACF from magnetic data must have faced the difficulty of estimating the baseline, i.e. estimating ACF(0). Thus, the ACF is an inappropriate device for the statistical characterization of ΔT magnetic data.

For $3 < \beta < 5$, equation (4.6) describes a random function which belongs to the class of locally homogeneous random functions (corresponding to processes with stationary increments in 1D). For these, the difference between two values, measured at a constant vector separation, is stationary. A locally homogeneous random function is characterized by its variogram (Cressie, 1993, pp. 58)

$$V(\boldsymbol{\tau}) \;=\; \langle [X(\mathbf{r}) - X(\mathbf{r}+\boldsymbol{\tau})]^2\rangle. \tag{4.11}$$

This variogram has a spectral representation (Yaglom, 1986, p. 435)

$$V(\boldsymbol{\tau}) = \int_{-\infty}^{\infty}\int_{-\infty}^{\infty} [1 - \cos(\boldsymbol{\tau}\cdot\mathbf{s})]\; P(\mathbf{s})\, du\, dv. \tag{4.12}$$

For the magnetic model (4.6) the integrals in equation (4.12) converge for $\beta < 5$ (see discussion below). Thus, the variogram is applicable to a wider and more realistic range of scaling exponents than the ACF.

Whether it is better to utilize the ACF or the variogram to characterize the statistics of measured data is an important question. To further illustrate the problem, let us consider the ΔT measurements along an aeromagnetic profile as a 1D random process. One can estimate the variogram of this process using equation (4.11). The ACF can then be derived from the variogram using the relationship (Yaglom, 1986, eq. 4.233)

$$ACF(\tau) \;=\; 1/2[V(\infty) - V(\tau)]. \tag{4.13}$$

However, to be able to use this relationship, the variogram has to level off to a constant value for a lag τ smaller than the window size. Otherwise, $V(\infty)$ remains unknown. This is exactly where the problem lies. Variograms of ΔT data tend to keep increasing, even for large lags.

Generally speaking, the use of variograms instead of ACFs in the interpretation of ΔT magnetic data - and probably of gravity data as well - makes sense both from a theoretical and a practical point of view.

4.2.2 Magnetic variogram

Let us introduce horizontal polar coordinates (s, ϕ) in the 2D wavenumber domain of the observation plane, where s is the wavenumber and ϕ is the azimuth. We are interested in changes of lag $\boldsymbol{\tau}$ along profiles with a constant direction. Let us choose the coordinate system in such a way that $\phi = 0$ for this direction. Then the scalar product $\boldsymbol{\tau} \cdot \mathbf{k}$ in (4.10) and (4.12) reduces to $\tau s \cos\phi$ and we can write (4.12) as

$$V(\tau) \;=\; \int_0^\infty \int_0^{2\pi} [1 - \cos(\tau s \cos\phi)] P_{\Delta T}(s, \phi) d\phi \; s ds, \tag{4.14}$$

where $P_{\Delta T}(s, \phi)$ is the power spectrum defined by equation (4.6) in horizontal polar coordinates. If the integrals converge, the right hand side of equation (4.14) is well defined, and we obtain a space domain model for the variogram of measured profiles with a constant direction.

Denoting the declination of the normal field $\mathbf{N}$ in terms of our new coordinate system (x-axis parallel to the profiles) by α, we obtain $\theta = \phi - \alpha$. Here, ϕ is the angle between the wavevector and the profiles and θ is the angle between the wavevector and the horizontal component of $\mathbf{N}$ (see also the text following equation (4.1)). Then equation (4.14) can be written as

$$V(\tau) = c_s (\frac{\mu_0}{2N})^2 B[1/2, (\beta+1)/2] \int_0^\infty \int_0^{2\pi} [1 - \cos(\tau s \cos\phi)] \; Dir(\phi - \alpha) d\phi \; Q(s) s ds. \tag{4.15}$$

To solve the inner, angular integral in equation (4.15)

$$I_{angular}(\tau s) = \int_0^{2\pi} [1 - \cos(\tau s \cos\phi)]\ Dir(\phi - \alpha) d\phi, \tag{4.16}$$

the term $Dir(\phi - \alpha)$ defined in equation (4.6) can be expressed in terms of powers of $\sin\phi$

$$\begin{aligned}
Dir(\phi - \alpha) &= \{n_z^2 + H^2[\cos(\phi - \alpha)]^2\}^2 && (4.17)\\
&= \{n_z^2 + H^2[\cos\phi\cos\alpha + \sin\phi\sin\alpha]^2\}^2 && (4.18)\\
&= [n_z^2 + (n_x\cos\phi + n_y\sin\phi)^2]^2 && (4.19)\\
&= (n_y^4 - 6n_y^2n_x^2 + n_x^4)\ \sin^4\phi + (4n_xn_y^3 - 4n_yn_x^3)\ \cos\phi\sin^3\phi \\
&\quad +(6n_y^2n_x^2 + 2n_y^2n_z^2 - 2n_x^4 - 2n_x^2n_z^2)\ \sin^2\phi \\
&\quad +(4n_yn_xn_z^2 + 4n_yn_x^3)\ \cos\phi\sin\phi + n_z^4 + n_x^4 + 2n_z^2n_x^2 && (4.20)\\
&=: T_4\sin^4\phi + T_3\cos\phi\sin^3\phi + T_2\sin^2\phi + T_1\cos\phi\sin\phi + T_0, && (4.21)
\end{aligned}$$

where =: denotes the definition of $T_0, ..., T_4$. The inner integral $I_{angular}(\tau s)$ of equation (4.16) can then be written as

$$\begin{aligned}
I_{angular}(\tau s) &= \int_0^{2\pi} [1 - \cos(\tau s\cos\phi)](T_4\sin^4\phi + T_3\cos\phi\sin^3\phi + T_2\sin^2\phi \\
&\qquad +T_1\cos\phi\sin\phi + T_0)\ d\phi && (4.22)\\
&= 4\int_0^{\pi/2} [1 - \cos(\tau s\cos\phi)](T_4\sin^4\phi + T_2\sin^2\phi + T_0)\ d\phi. && (4.23)
\end{aligned}$$

This integral can be solved using Bessel functions J_n of integer order n (Gradsteyn and Ryzhik, 1994, eq. 4.411.4)

$$J_n(x) = \frac{2(x/2)^n}{\sqrt{\pi}\Gamma(n + 1/2)} \int_0^{\pi/2} \cos(x\cos\phi)\sin^{2n}\phi\ d\phi, \tag{4.24}$$

where Γ is the gamma function, and the formulae

$$\begin{aligned}
\int_0^{\pi/2} \sin^m\phi\ d\phi &= \frac{\Gamma[(m+1)/2]\sqrt{\pi}}{2\Gamma[(m+2)/2]}, && (4.25)\\
\Gamma(1/2) &= \sqrt{\pi}, && (4.26)\\
\text{and } \Gamma(x+1) &= x\Gamma(x). && (4.27)
\end{aligned}$$

Equation (4.23) then becomes

$$I_{angular}(\tau s)/\pi = 2T_0 - 2T_0J_0(\tau s) + T_2 - \frac{2T_2}{\tau s}J_1(\tau s) + \frac{3}{4}T_4 - \frac{6T_4}{\tau^2 s^2}J_2(\tau s), \tag{4.28}$$

and with (4.15) we obtain the final equation

$$\begin{aligned}
V(\tau) &= \pi c_s(\frac{\mu_0}{2N})^2 B[1/2, (\beta+1)/2] \int_0^\infty [T - 2T_0J_0(\tau s) - \frac{2T_2}{\tau s}J_1(\tau s) \\
&\qquad -\frac{6T_4}{\tau^2 s^2}J_2(\tau s)]e^{-2zs}\ s^{2-\beta}\ ds && (4.29)
\end{aligned}$$

$$T = \frac{3}{4}(n_y^2 + n_x^2)^2 + 2n_z^2(n_y^2 + n_x^2 + n_z^2) \quad (4.30)$$

$$= \frac{3}{4}H^4 + 2n_z^2N^2 \quad (4.31)$$

$$T_0 = n_z^4 + n_x^4 + 2n_z^2n_x^2 \quad (4.32)$$

$$T_2 = 6n_y^2n_x^2 + 2n_y^2n_z^2 - 2n_x^4 - 2n_x^2n_z^2 \quad (4.33)$$

$$T_4 = n_y^4 - 6n_y^2n_x^2 + n_x^4 \quad (4.34)$$

Here, $\mathbf{N} = (n_x, n_y, n_z)$ is expressed in coordinates relative to the flight lines. Since only even powers of n_x, n_y, and n_z appear, we need not take care of the orientation of the coordinate system, as long as $n_y = 0$ for $\mathbf{H}$ parallel to the profiles and $n_x = 0$ for $\mathbf{H}$ perpendicular to the direction of the profiles.

4.2.3 Gravity variogram

The gravity spectrum of (4.8) is very similar to, and somewhat simpler than the magnetic spectrum of (4.6). The corresponding variogram model for g_z gravity data can be obtained from equation (4.29) as the special case of $n_x = n_y = 0$ and $n_z = 1$. Further substituting $-\beta$ for $2 - \beta$ and adjusting the constants provides

$$V(\tau) = \frac{8\sigma^2 c_s}{\pi} B[1/2, (\beta+1)/2] \int_0^\infty [1 - J_0(\tau s)] e^{-2zs}\ s^{-\beta}\ ds. \quad (4.35)$$

In this case, the variogram is horizontally isotropic. Consequently, the model is applicable to any set of gravity measurements located in a horizontal observation plane, whereas equation (4.29) requires the magnetic measurements to be located on a profile with constant direction.

4.2.4 Convergence of the integrals in 4.2.2 and 4.2.3

The variogram models of equations (4.29) and (4.35) are defined only for a limited range of scaling exponents. Using the relationship (Yaglom, 1986, p. 355)

$$\frac{J_{(n-2)/2}(x)}{x^{(n-2)/2}} = \frac{2^{(2-n)/2}}{\Gamma(n/2)} \left[1 - \frac{x^2}{2n} + \frac{x^4}{2 \cdot 4n(n+2)} - ...\right] \text{ for } n = 2, 3, ... \quad (4.36)$$

it can be shown that the integral in equation (4.29) converges in the interval $s \in (0, 1]$ for $\beta < 5$ and any z. In the remaining interval $s \in (1, \infty)$ the integral converges always if $z > 0$. In case $z = 0$, however, the integral converges only for $\beta > 3$. This latter restriction is probably of little practical consequence, since a small distance between the sources and the observation plane can always be assumed. The restrictions for the gravity variogram can be found by a similar line of reasoning.

In summary, the magnetic variogram (4.29) exists for $\beta < 5$ while the gravity variogram (4.35) exists for $\beta < 3$.

4.2.5 Limitations

The statistical model developed here has the following known limitations:

1. It does not account for components of remanent magnetization perpendicular to the normal magnetic field.

2. It does not account for anomalies caused by topography. In particular, topographic gravity anomalies are often stronger than gravity anomalies caused by subsurface density variations.

3. It is based on the simplifying assumption that measurements are located in a horizontal plane, whereas ground and even airborne surveys usually follow surface topography.

4. Within a particular data analysis window, the source parameters z, β and c_s are assumed to be constant. Hence, variations in z, β and c_s can only be detected if their wavelength is larger than the size of the analysis window.

5. The case of multiple source layers is not considered.

6. For a susceptibility distribution with $\beta < 3$, the model does not provide for the variogram of the magnetic field at ground level, due to a diverging integral in equation (4.29).

7. A density distribution with $\beta \geq 3$ leads to a diverging integral in equation (4.35).

8. The integral in equation (4.29) has to be evaluated numerically. Equation (4.35) has an analytical solution (personal communication by Peter Weidelt).

4.3 Graphs of the variogram

Some special cases of the variograms V defined by equation (4.29) and of V_y defined later in equation (4.49) shall now be illustrated. In particular, the effect of the model parameters $\mathbf{N}$, c_s, z, and γ on the graphs of the variograms are demonstrated. For compatibility between the ΔT and g_z spectral models, given by equations (4.29) and (4.35), let us introduce γ as the 2D scaling exponents of the fields in the horizontal observation plane, related to the scaling exponents of their 3D source distributions by $\gamma_{\Delta T} = \beta_{susc} - 1$ and $\gamma_g = \beta_{dens} + 1$, respectively (see also Maus and Dimri, 1994).

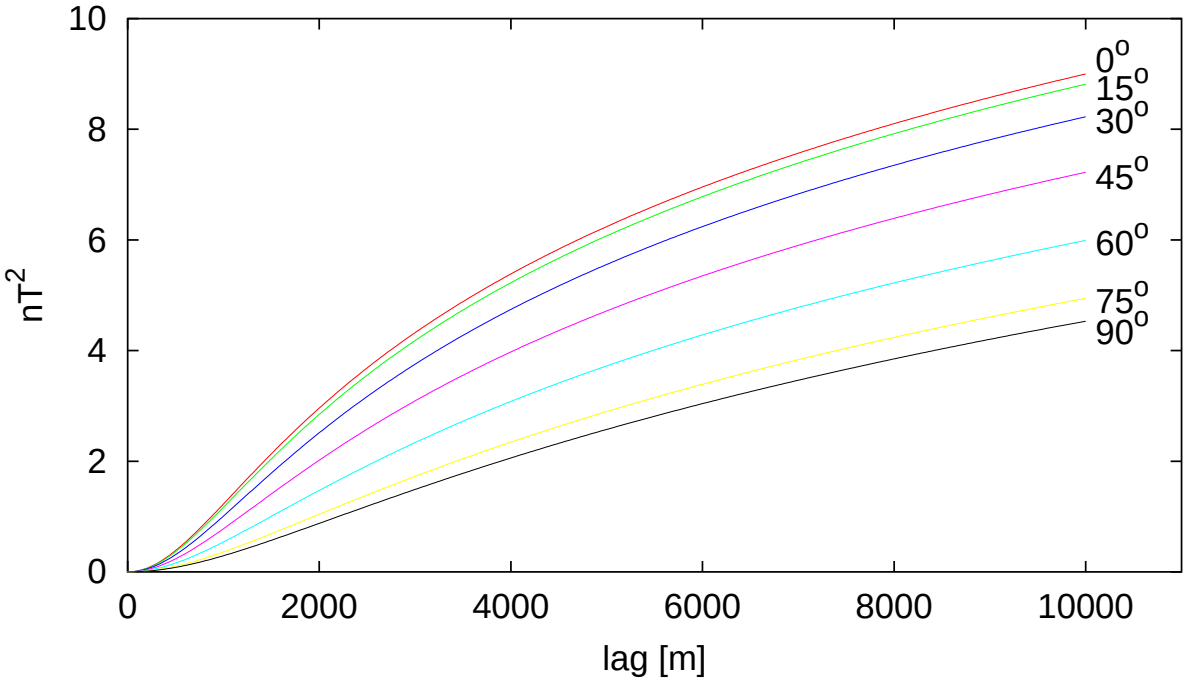

FIG. 4.1: Effect of the profile orientation relative to the horizontal component of the magnetic field **H**. Displayed are the model variograms V of eq. (4.29) for different profile azimuth angles with $z = 500$ m, $\gamma = 2$ and $n_z = 0$, hence at the magnetic equator where the effect of profile orientation is strongest.

4.3.1 Orientation of the profiles relative to the normal field

The parameter **N** is determined by the orientation of the measured profiles with regard to the direction and intensity of the Earth's normal magnetic field. It is not a variable model parameter. Figures 4.1 and 4.2 show the model variograms V and V_y for different orientations of the profiles near the magnetic equator ($n_z = 0$), where the effect of profile orientation is greatest. The variations are least for profiles perpendicular to the geomagnetic field and strongest for profiles parallel to the field. At higher geographic latitudes the anisotropy of the variations of the magnetic field is less pronounced. Figure 4.3 demonstrates that the variograms differ not only in amplitude, but also in shape.

4.3.2 Intensity of susceptibility variations

The parameter c_s may be of considerable practical interest, since it reflects the intensity of source variations. For magnetic data, the square root of c_s is possibly related to the magnetization of the source rocks. On the graph of the variogram, however, the parameter c_s acts only as a constant factor.

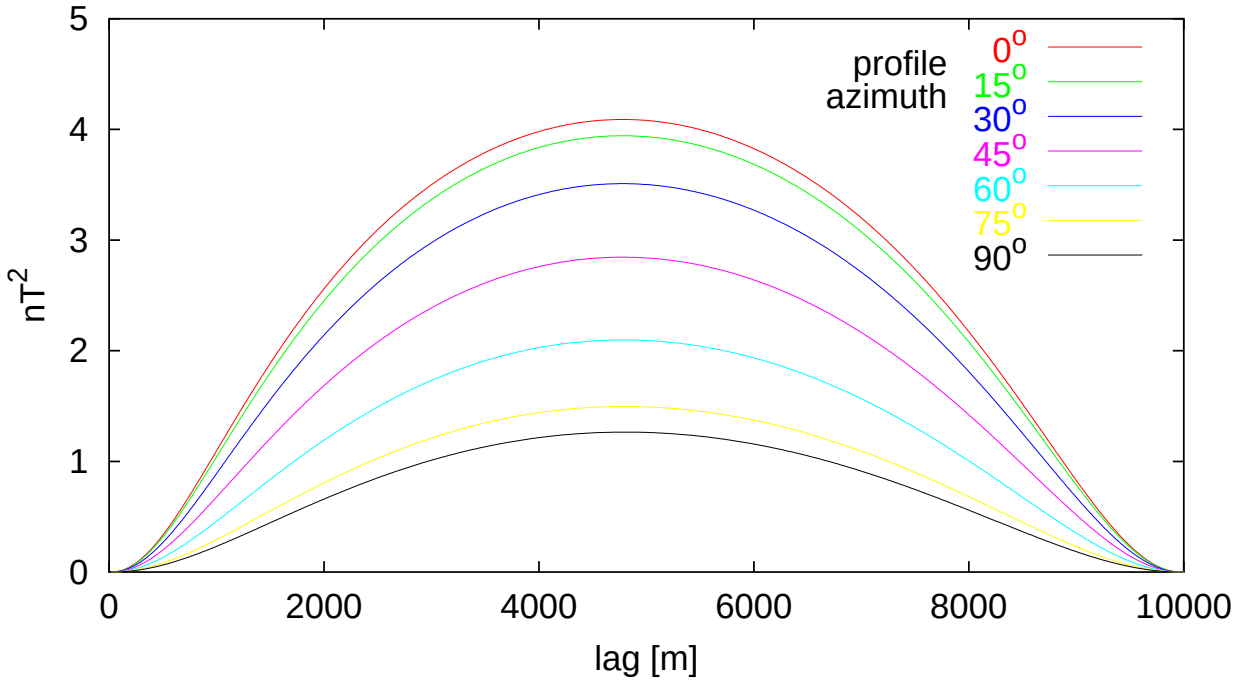

FIG. 4.2: Effect of the profile orientation on the modified model variograms V_y of eq. (4.49) for different profile azimuth angles with $z = 500$ m, $\gamma = 2$ and $n_z = 0$, same case as in Figure 4.1

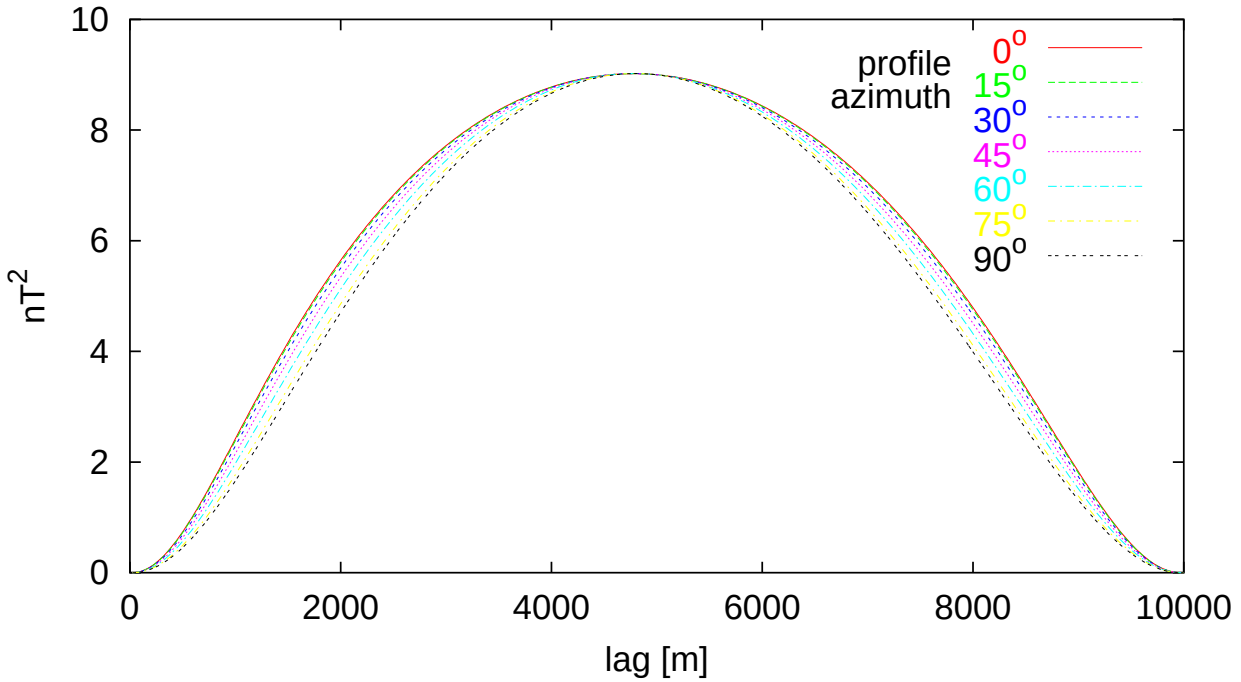

FIG. 4.3: Variograms V_y of Figure 4.2 rescaled to have equal amplitude at lag = 5 km. The variograms for different profile azimuth angles differ not only in amplitude but also in shape.

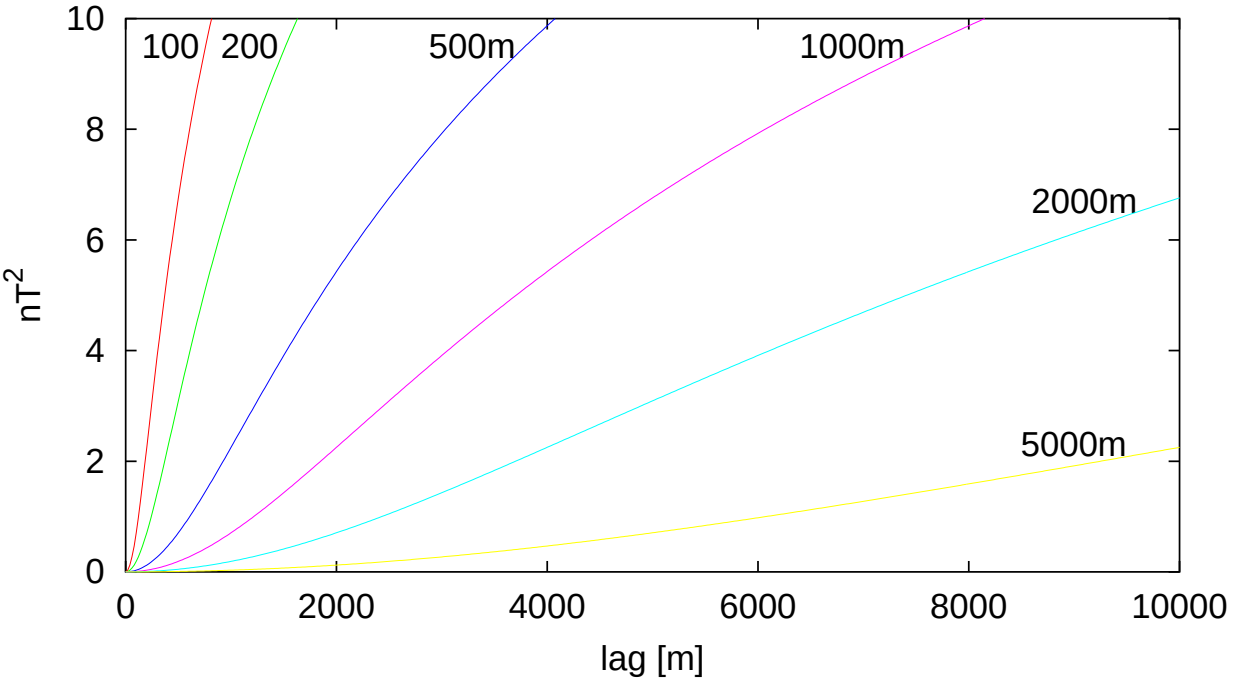

FIG. 4.4: Effect of the depth to source. Displayed are variograms V of eq. (4.29) for $\gamma = 2$.

4.3.3 Depth to source

The effect of depth to source z on the variogram V of eq. (4.29) is displayed in Figure 4.4. With increasing depth to source, the variogram of the potential field experiences a drastic decrease in overall amplitude. However, this overall amplitude is already covered by the intensity parameter c_s. To estimate depth from variogram amplitude, we would have to assume $c_s = \text{constant}$. In general, this assumption is too strong and it is advisable to keep c_s variable. If c_s is kept variable then depth has to be detected solely from differences in variogram shape.

Differences in shape of the modified variogram V_y due to depth are illustrated in Figure 4.5. Since upward continuation suppresses variations of short wavelength stronger than of long wavelength, variogram shape differs primarily at short lags. While there is a significant difference between the variograms for 1000 m and 2000 m depth, the difference at 5000 m depth is negligible. Hence, the maximum resolvable depth is approximately one fifth of the variogram length. From my experience, the window size has to be at least twice the length of the variogram to be estimated. Therefor, a variogram estimated from a given window can resolve depths to not more than one tenth of the window size. The exact ratio depends on further factors, such as the scaling exponent of the source distribution. The smaller β, the better the resolution of depth.

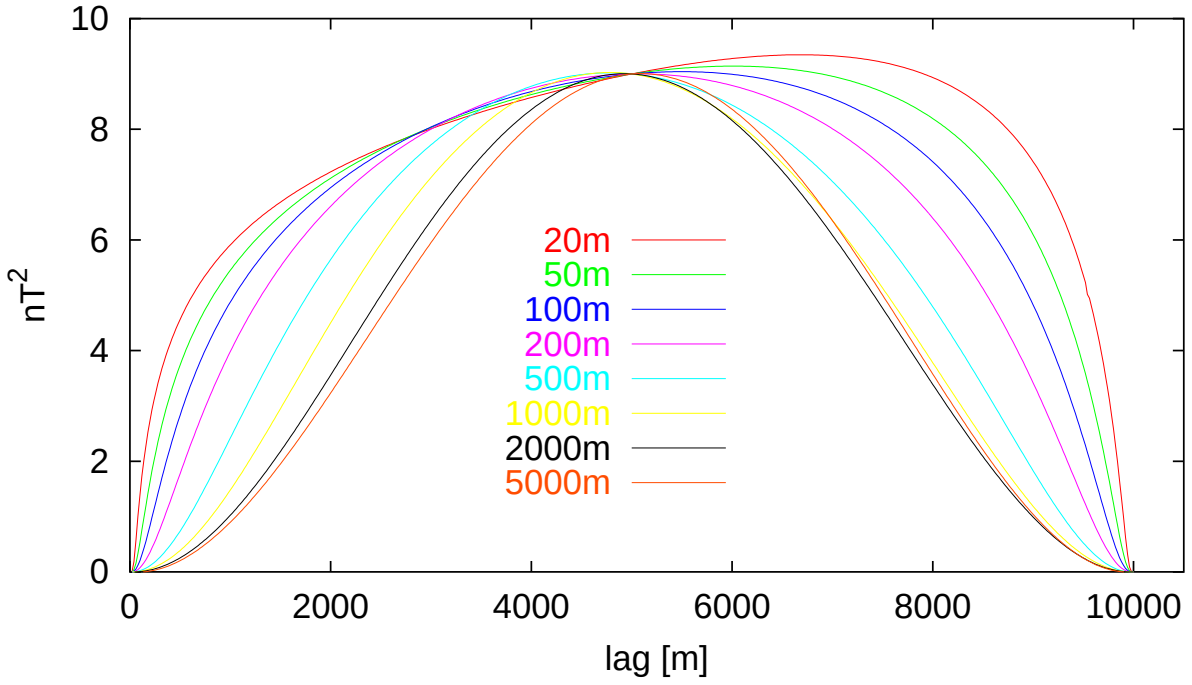

FIG. 4.5: Effect of the depth to source on the variograms V_y of eq. (4.49) for $\gamma = 2$. Variograms are rescaled to intersect at 5 km lag.

4.3.4 Scaling Exponent

The scaling exponent γ determines whether the variogram V (Figure 4.6) is generally convex or concave, i.e., whether it turns upwards ($\gamma > 3$) or towards higher lags ($\gamma < 3$). The scaling exponent influences the shape of the variograms in a similar way as the depth to source. To see this, compare Figure 4.6 with Figure 4.4 for V and Figure 4.7 with Figure 4.5 for V_y. This means that if we observe a smooth magnetic field it can either be caused by a rugged source distribution (small β) at a greater depth, or by a smoother source distribution (larger β) at a shallower depth. A consequence of this ambiguity is that β and z cannot be resolved simultaneously, unless perhaps, by using very large windows.

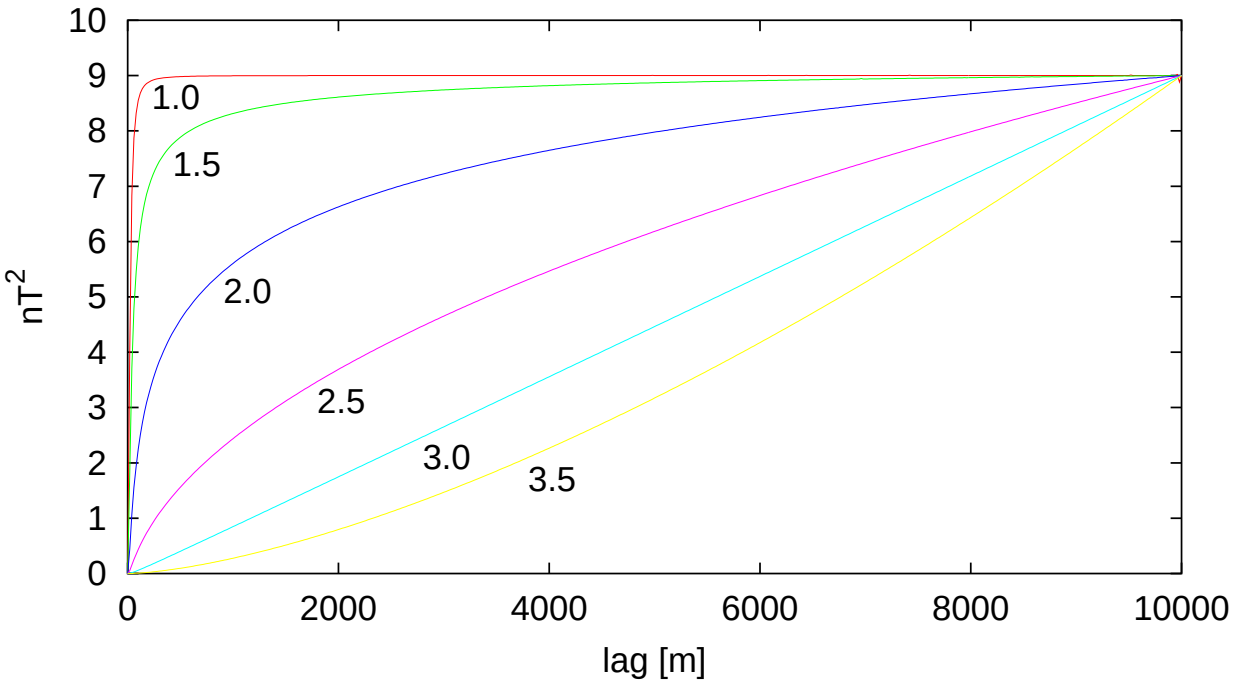

FIG. 4.6: Effect of the scaling exponent γ on the variograms V of eq. (4.29) for $z = 10$ m. The curves are rescaled to intersect at $\tau = 10$ km. The depth z was chosen greater than zero, otherwise the integral in equation (4.29) would not converge for the variograms with $\gamma < 2$.

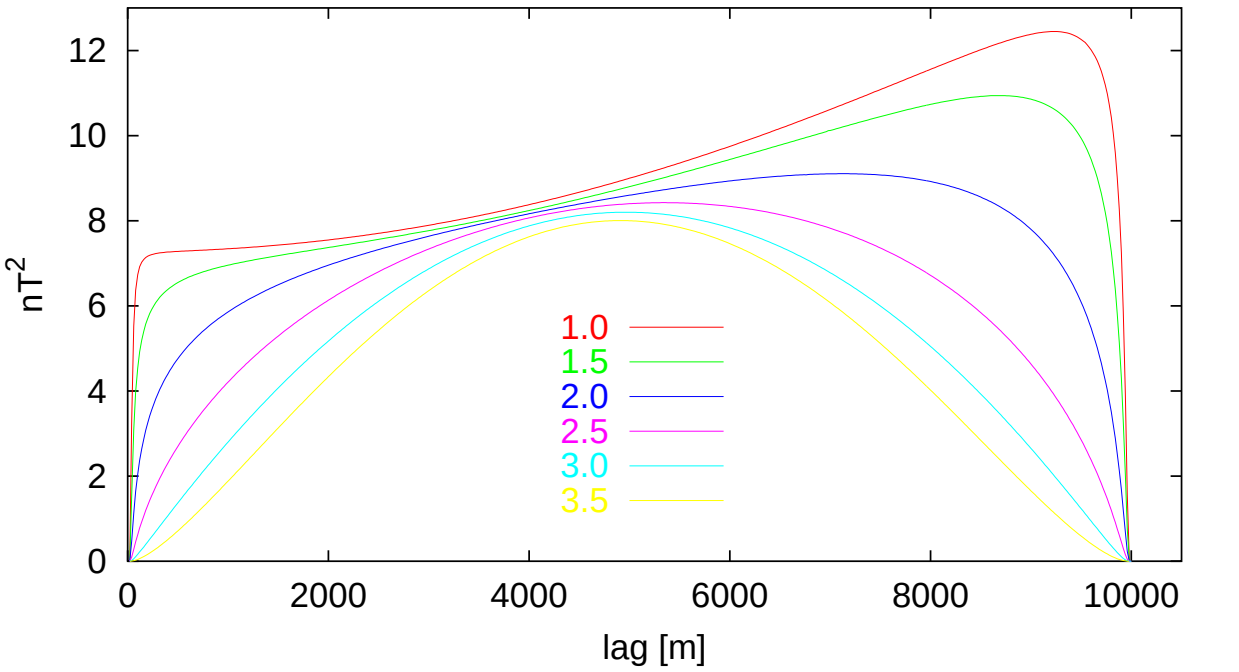

FIG. 4.7: Effect of the scaling exponent γ on the variograms V_y of eq. (4.49) for $z = 10$ m. Variograms are rescaled for better comparison. The scaling exponent influences the shape of the variogram in a similar but not identical way as the depth to source (see Figure 4.5).

4.4 Practical aspects

Following are some additional formulae which are essential in applying the variogram analysis method to real magnetic data sets.

4.4.1 Computing the model variograms

To compute the model variogram defined by equation (4.29) for a given set of model parameters, we have to numerically approximate the integral. At first glance this looks like a technical problem which could be solved by quadrature algorithms available in standard math software packages. However, the term in square brackets tends towards zero for low values of s, whereas $s^{2-\beta}$ tends to infinity. The product of the two terms tends to zero for $\beta < 4$ and to infinity for $\beta > 4$. To integrate numerically over this product can lead to arbitrary results.

A solution to the problem is the following: We use eq. (4.36) with $x = \tau s$ to approximate the Bessel functions in equation (4.29). For small values of τs, say τs smaller than some a, it is sufficient to consider just the first two terms in (4.36). Since this approximation only holds for small τs, we have to split the integral in equation (4.29) into two parts

$$V(\tau) = \int_0^\infty ... = \int_0^{a/\tau} ... + \int_{a/\tau}^\infty =: V_1(\tau, a) + V_2(\tau, a). \tag{4.37}$$

The second integral $V_2(\tau, a)$ is straightforward and can be evaluated with a standard quadrature algorithm. For the first integral, we can use the first two terms in the square brackets of eq. (4.36) and substituting $T = 2T_0 + T_2 + \frac{3}{4}T_4$ in equation (4.29) we arrive at

$$V_1(\tau, a) = \pi c_s (\frac{\mu_0}{2N})^2 B[1/2, (\beta+1)/2][2T_0 + \frac{T_2}{2} + \frac{T_4}{4}]\frac{\tau^2}{4}\int_0^{a/\tau} s^{4-\beta} e^{-2zs} ds. \tag{4.38}$$

The integral can now be solved using the relationship

$$\int_0^u x^{\nu-1} e^{-\mu x} dx = \mu^{-\nu}\Gamma_{inc}(\nu, \mu u), \tag{4.39}$$

where Γ_{inc} is the incomplete Γ-function, leading to

$$V_1(\tau, a) = \pi c_s (\frac{\mu_0}{2N})^2 B[1/2, (\beta+1)/2][2T_0 + \frac{T_2}{2} + \frac{T_4}{4}]2^{\beta-7} z^{\beta-5}\Gamma_{inc}(5-\beta, \frac{2za}{\tau})\tau^2. \tag{4.40}$$

Adding the two parts V_1 and V_2 according to (4.37) then yields the desired model variogram $V(\tau)$.

4.4.2 Estimating the variogram from a segment of a profile

In practice, we want to obtain the best possible estimate from the shortest possible segment of the profile. This can be achieved by utilizing the estimator

$$\widehat{V}(\tau) = \frac{1}{T-\tau}\int_0^{T-\tau} [X(t+\tau) - X(t)]^2 dt, \tag{4.41}$$

where $X(t)$ is the measured field, with $X(0)$ and $X(T)$ at the beginning and end of the segment, respectively. $\widehat{V}$ is a variogram estimated from measured data.

4.4.3 Extended model accounting for linear trends

The model variogram defined by equation (4.29) is the theoretical variogram of the magnetic field due to a horizontally infinite half-space of scaling sources. In practice, however, we are interested only in source parameters within a limited area (window). Furthermore, we want to keep this window as small as possible in order to enhance spatial resolution. Regarding small segments of a measured profile, one often finds a strong linear trend. This trend usually reflects large scale geological features which are unrelated to the local magnetization. Such large scale trends are expected for non-stationary data and are consistent with the variogram models of equations (4.29) and (4.35). However, equations (4.11) and (4.41) show that a linear trend in the data has a dramatic effect on the shape of the estimated variogram. In order to focus the analysis on to the current data analysis window, linear trends in the data have to be dealt with in some way or other. Arguably, this is the key problem in designing a reliable variogram analysis algorithm.

It may appear as the obvious solution to detrend a segment in the usual way, namely, fit a straight line in a least squares sense, subtract it from the data, estimate the variogram from the detrended segment, and compare it with the model variograms of equations (4.29) or (4.35). However, the linear trends are an integral part of these model variograms. Strictly speaking, the model variograms of equations (4.29) and (4.35) do not apply to detrended data. One could ignore this problem and hope that detrending will just lead to lower model scaling exponents. However, this is far from obvious.

A clean solution is to not only detrend the data, but also modify the model variograms to account for the detrending. By the least squares method of detrending the data variograms are altered in a way that I am unable to quantify. In the following, I therefore use the more primitive method of fitting a straight line through the end points of the segment. For this detrending, the modified model variograms can be found as follows:

Let us denote the measured data within the considered segment of the profile by $X(t)$. Let us further denote the beginning of this segment by $t = 0$ and the end by $t = T$ and let us subtract an offset from the data so that $X(0) = 0$. Then we can define a process $Y(t)$, which is derived from $X(t)$ by

$$Y(t) := X(t) - \frac{t}{T}X(T). \tag{4.42}$$

The new process $Y(t)$ has the advantage that the presumed linear trend in $X(t)$ is not reflected in $Y(t)$. The variogram of $Y(t)$ can be estimated from the measured data using equation (4.41). We have a model variogram $V(\tau)$ defined by equation (4.29) for the process $X(t)$ from which we now have to derive the model variogram for $Y(t)$. The idea behind

the following derivation is to answer the question: "If we have a variogram model $V(\tau)$ for the process $X(t)$, what is the expected variogram $\langle V_y(\tau)\rangle$ for the detrended process Y(t)?". Using triangular brackets $\langle\cdot\rangle$ for the expected value, equation (4.41) gives

$$\begin{aligned}
\langle\widehat{V}_y(\tau)\rangle &= \langle\frac{1}{T-\tau}\int_0^{T-\tau}[Y(t+\tau)-Y(t)]^2dt\rangle && (4.43)\\
&= \langle\frac{1}{T-\tau}\int_0^{T-\tau}\{\frac{\tau}{T}X(T)-[X(t+\tau)-X(t)]\}^2dt\rangle && (4.44)\\
&= \langle\frac{\tau^2}{(T-\tau)T^2}\int_0^{T-\tau}X(T)^2dt\rangle+\langle\frac{1}{T-\tau}\int_0^{T-\tau}[X(t+\tau)-X(t)]^2dt\rangle\\
&\quad -\langle\frac{1}{T-\tau}\int_0^{T-\tau}[\frac{2\tau}{T}X(T)X(t+\tau)-\frac{2\tau}{T}X(T)X(t)]dt\rangle && (4.45)\\
&= \frac{\tau^2}{T^2}V(T)+V(\tau)-\frac{1}{T-\tau}\int_0^{T-\tau}[\frac{2\tau}{T}\langle X(T)X(t+\tau)\rangle\\
&\quad +\frac{2\tau}{T}\langle X(T)X(t)\rangle]dt && (4.46)
\end{aligned}$$

Since $X(t)=0$ for $t=0$, the identity (Yaglom, 1986, eqs. 4.222 and 4.224)

$$\langle[X(t+\tau_1)-X(t)][X(t+\tau_2)-X(t)]\rangle=\frac{1}{2}[V(\tau_1)+V(\tau_2)-V(|\tau_1-\tau_2|) \quad (4.47)$$

reduces to

$$\langle X(\tau_1)X(\tau_2)\rangle=\frac{1}{2}[V(\tau_1)+V(\tau_2)-V(|\tau_1-\tau_2|) \quad (4.48)$$

so that

$$\langle V_y(\tau)\rangle=V(\tau)+\frac{\tau^2}{T^2}V(T)-\frac{\tau}{T(T-\tau)}\int_0^{T-\tau}[V(t+\tau)-V(t)+V(T-t)-V(T-t-\tau)]dt. \quad (4.49)$$

Equation (4.49) describes how the model variogram $V(\tau)$ of the original segment $X(t)$ can be transformed into a model variogram $V_y(\tau)$ for the detrended segment $Y(t)$.

Generally speaking, it is essential to detrend a segment prior to estimating its variogram. The least squares method provides a better estimate of trend, but the model variograms for the detrended process may be difficult to compute. For end-point detrending the effect on the model variograms is described by equation (4.49). Unfortunately, the end points are not always a good estimate of trend. Consider, for example, a prominent dike across-line at one side of the data analysis window. Due to the resulting spike at one end of the segment, a straight line through the end points would not reflect the general trend. In practice, the distorting effect of such a dike can be minimized by using segments shorter than the window size and averaging variograms for several segment positions along-line within the same window.

4.5 Conclusion

Assuming self-similar source distributions, I have derived variogram statistical models for ΔT magnetic and g_z gravity data. Variogram models for horizontal and vertical derivatives

of ΔT and g_z (gradiometer data) could be found in a similar way.

Statistical features of ΔT line data are attributed to 4 parameters: (1) orientation of profiles relative to the direction of the main field, (2) intensity c_s, (3) scaling exponent β, and (4) depth z of source. I developed this model to decompose aeromagnetic surveys into maps of c_s, β and z, with the highest possible accuracy and resolution. The intensity c_s can be mapped from single flight lines using a very small window if z is substituted by the survey terrain clearance and β is kept constant (Figure 5.7). Such high resolution maps of c_s are easier to interpret than ΔT maps and can therefore be an attractive way of presenting magnetic data. Basement topography can be estimated keeping β constant and c_s and z variable (Chapter 5.2. Variogram analysis can also be used to map β, as proposed by Maus and Dimri (1995b). However, due to the large window required for estimating β, maps of the scaling exponent are blurred and may be of limited practical use.

Apart from these applications, variograms provide space domain statistical models for magnetic and gravity data. Such statistical models should be useful in filtering, gridding, inversion and other processing techniques.

Chapter 5

Variogram analysis applications I*

Due to the instability of magnetic minerals in oxidizing environments, the magnetization of sediments is usually weak compared with the magnetization of the crystalline basement. In this case, the crystalline basement is equivalent to the magnetic basement, being defined as the uppermost occurrence of rocks carrying a significant magnetization.

ΔT magnetic maps are the smoother the greater the height of the observation plane above the magnetic basement. This effect is quite prominent, as illustrated in Fig. 5.1. The smoothness/ruggedness of the magnetic field is reflected in its power spectrum $P(\mathbf{s})$, where $\mathbf{s}$ is the 2D horizontal wavevector. The higher the relative power for small wavenumbers $|\mathbf{s}|$, the more rugged the appearance of the field. The power $P(\mathbf{s})$ of the magnetic field in the observation plane is related to the power of the field at basement level $P_0(\mathbf{s})$ by

$$P(\mathbf{s}) = P_0(\mathbf{s})\ e^{-2z|\mathbf{s}|}, \tag{5.1}$$

where z is the depth to the basement, hence, the parameter of interest. To obtain z from eq. 5.1, an assumption on the power spectrum $P_0(\mathbf{s})$ of the field at basement level has to be made. Assuming that the $e^{-2z|\mathbf{s}|}$ term dominates the shape of the power spectrum, spectral slope methods (Spector and Grant, 1970) are based on the implicit assumption $P_0 \equiv constant$. Hahn *et al.* (1976) proposed to subtract 10% from these "white depths" for a more reliable depth estimate. Recent years have seen a breakthrough in our understanding of magnetic power spectra with the finding that the magnetic field at source level is self-similar ("fractal") and can be described by a model $P_0(\mathbf{s}) \propto |\mathbf{s}|^{-\gamma}$, with $\gamma \approx 3$ (Gregotski et al., 1991; Pilkington and Todoeschuck, 1993). To correct for self-similar source, Pilkington *et al.* (1994) suggested to divide the power spectrum by $|\mathbf{s}|^{-3}$ before applying a spectral slope method. However, even with this correction depth estimates remain unreliable (Maus and Dimri, 1996), due to several reasons:

For spectral analysis the magnetic flight line data have to be transformed to a regular grid. Since data density is typically 50 times higher along- than across-line, gridding invariably

*Published in *Geophysics* (Maus, Sengpiel, Siemon, Röttger and Tordiffe, 1999)

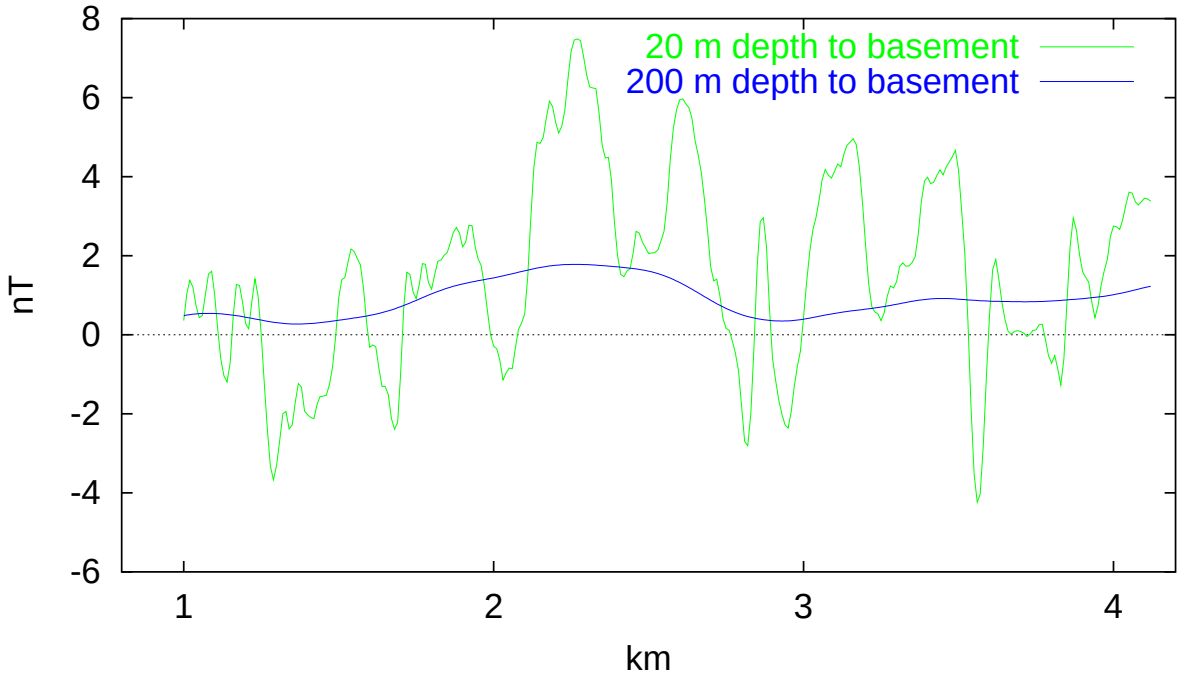

FIG. 5.1: Synthetic ΔT magnetic data on profiles at different heights above a level basement model with self-similar magnetization. To eliminate edge effects the profiles of 3 km length are located over the center of a larger 5 km x 5 km model.

leads to a loss of information. Furthermore, gridded data are likely to be smoother than the actual magnetic field. The subsequent steps of making the grid periodic, FFT and azimuthal averaging again lead to distortions in the power spectrum.

Power spectrum estimation can be avoided altogether by transforming a model power spectrum analytically to the space domain. This approach is intuitively appealing as it means to carry the model without loss of information towards the data, instead of the data towards the model. This difference in approach is illustrated in Fig. 5.2. A spectral analysis in the wavenumber domain (left side) can be substituted by an equivalent auto-correlation analysis (middle) or a variogram analysis (right side in Fig. 5.2) in the space domain. Whether it is better to use the auto-correlation function (ACF) or the variogram depends on the statistical nature of the data. As discussed in Chapter 4.2.1, magnetic and gravity data are better described by variograms than by ACFs.

Here, we demonstrate the utility of the variogram analysis method on helicopter magnetic data of the Omaruru Alluvial Plains in Namibia. First, we describe the spectral model which is based on simplifying assumptions regarding the distribution of magnetization in the crust. Although these assumptions are common to a variety of magnetic methods we find it worthwhile to repeat them here. The use of a spectral model in terms of an equivalent variogram analysis is outlined in the following section. After an introduction to the survey area we illustrate different statistical methods of estimating depth on two sample areas.

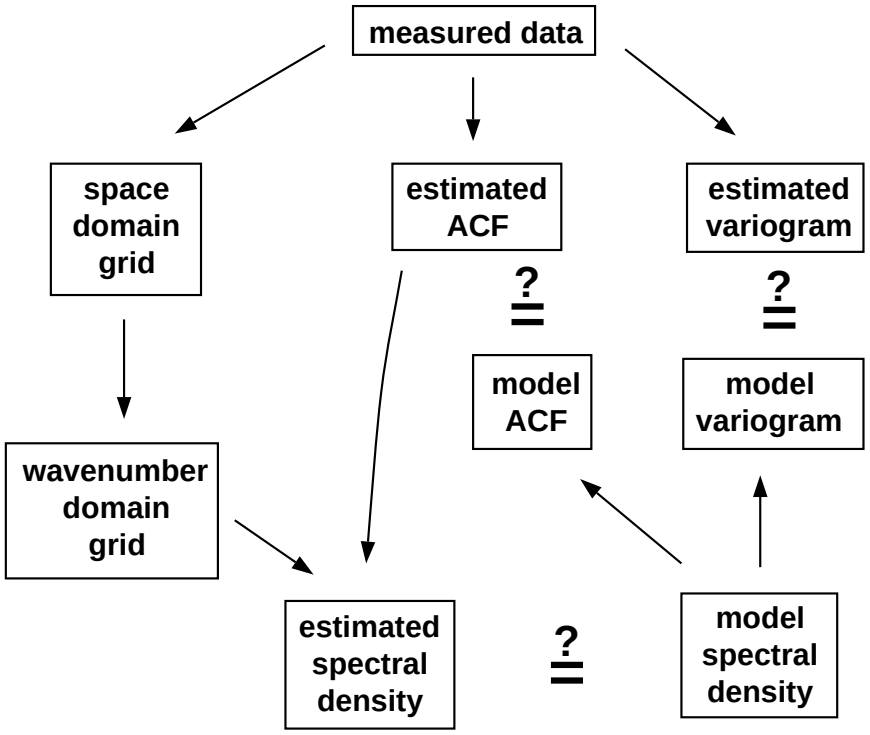

FIG. 5.2: The different possibilities of using a spectral model to invert magnetic data.

We then compare the variogram analysis depths for the whole survey area with the EM resistivities to verify the boundary of the alluvial deposits. A comparison of basement reliefs derived by variogram analysis and an automated spectral slope method (Spector and Grant, 1970) illustrates the improvements that are possible with the new method. Finally, we verify basement depth with drilling results finding a reasonable agreement.

5.1 Spectral model

To derive a realistic model for $P_0(\mathbf{s})$ in eq. 5.1, one has to make assumptions on the statistical distribution of magnetization in the basement rock. The magnetization $\mathbf{M(r)}$ at a location $\mathbf{r}$ is the vector sum of the induced magnetization $\mathbf{M_i(r)}$ and the remanent magnetization $\mathbf{M_r(r)}$. The magnetization $\mathbf{M_i(r)}$, induced by the geomagnetic field $\mathbf{N(r)}$, can be written as

$$\mathbf{M_i(r)} = \overline{\mathbf{X}}\mathbf{(r)N(r)}, \tag{5.2}$$

where $\overline{\mathbf{X}}\mathbf{(r)}$ is a 3D susceptibility tensor. Assuming isotropic susceptibility $\overline{\mathbf{X}}\mathbf{(r)} = \chi\mathbf{(r)}\overline{\mathbf{I}}$, where $\overline{\mathbf{I}}$ is the identity matrix, and a constant inducing geomagnetic field $\mathbf{N(r)} \equiv \mathbf{N_0}$ simplifies eq. 5.2 to

$$\mathbf{M_i(r)} = \chi_i\mathbf{(r)N_0} \tag{5.3}$$

Here, $\chi_i(\mathbf{r})$ is the susceptibility that one would measure from a rock sample in a laboratory.

While induced magnetization can be described by a scalar susceptibility $\chi_i(\mathbf{r})$, remanent magnetization is a true vector field. However, to arrive at a simple statistical model, we have to assume that any non-negligible remanent magnetization is aligned with the normal field. Then, remanent magnetization can be described by

$$\mathbf{M_r}(\mathbf{r}) = \chi_r(\mathbf{r})\mathbf{N_0}, \tag{5.4}$$

similar to the induced magnetization. Possible consequences of this simplifying assumption are discussed in point 2 of section 5.2.3 on limitations of the method. Combining eqs. 5.3 and 5.4, the magnetization $\mathbf{M}(\mathbf{r})$ can be expressed as

$$\mathbf{M}(\mathbf{r}) = [\chi_i(\mathbf{r}) + \chi_r(\mathbf{r})]\mathbf{N_0} = \chi_{i+r}(\mathbf{r})\mathbf{N_0}. \tag{5.5}$$

in terms of an apparent scalar susceptibility distribution $\chi_{i+r}(\mathbf{r})$ in the basement rock. In the next step, a statistical expression for $\chi_{i+r}(\mathbf{r})$ has to be found.

Recent studies suggest that the susceptibility distributions $\chi_i(\mathbf{r})$ and $\chi_{i+r}(\mathbf{r})$ in the Earth's crust are self-similar (Pilkington and Todoeschuck, 1993; Pilkington et al., 1994; Maus and Dimri, 1995b). A characteristic of self-similar random functions is that their power spectrum $P(\mathbf{k})$ is proportional to a power of the wavenumber $\mathbf{k}$, namely $P(\mathbf{k}) \propto |\mathbf{k}|^{-\beta}$, where β is a variable scaling exponent. A self-similar distribution of the susceptibility $\chi_{i+r}(\mathbf{r})$ in the basement rock causes a self-similar magnetic field immediately above the basement (Pilkington and Todoeschuck, 1993; Maus and Dimri, 1995b). In combination with eq. 5.1 this leads to a spectral model

$$P_{\Delta T}(\mathbf{s}) \;=\; c_s(\frac{\mu_0}{2N})^2 B[1/2,(\beta+1)/2] \underbrace{(n_z^2 + H^2\cos^2\theta)^2}_{Dir(\theta)}\; s^{-\beta+1}\exp(-2sz) \tag{5.6}$$

for the ΔT magnetic field in a horizontal observation plane (Chapter 4.1.1). Here, $\mathbf{s}$ is the horizontal wavevector, c_s is the intensity of susceptibility variations, μ_0 is the magnetic permeability of vacuum, $\mathbf{N}$ is the vector of the geomagnetic field, B is the beta function $B(x,y) = \Gamma(x)\Gamma(y)/\Gamma(x+y)$, $Dir(\theta)$ describes the anisotropy of the power spectrum as a function of the angle θ between the horizontal field component $\mathbf{H}$ and the wavevector $\mathbf{s}$, β is the 3D scaling exponent of the susceptibility distribution $\chi_{i+r}(\mathbf{r})$ in the basement rock and z is the height of the observation plane above the magnetic basement.

5.2 Estimating magnetic depth

As illustrated in Fig. 5.2, inversion of a magnetic data set using a spectral model can be carried out in several different ways. Earlier spectral analysis methods pursued the left path in Fig. 5.2. Depth was estimated from linear sections in the power spectrum (Spector and Grant, 1970). There was no analytical expression for the entire power spectrum which

could have been shifted to the space domain. Depth therefore had to be estimated in the wavenumber domain. In contrast, equation (5.6) provides a model for the entire 2D magnetic power spectrum. This spectral model has an exact variogram counterpart in the space domain which is obtained by the integral transform (Yaglom, 1986, p. 435)

$$V(\boldsymbol{\tau}) = \int_{-\infty}^{\infty}\int_{-\infty}^{\infty}[1-\cos(\boldsymbol{\tau}\cdot\mathbf{s})]\,P_{\Delta T}(\mathbf{s})\,du\,dv, \tag{5.7}$$

where $\mathbf{s} = (u, v)$ is the horizontal wavevector and $\boldsymbol{\tau}$ is the corresponding vector separation in the space domain. A variogram $V(\boldsymbol{\tau})$ depicts the expected square of the difference between two data values as a function of their vector separation $\boldsymbol{\tau}$. With equation (5.7) a spectral analysis in the wavenumber domain using eq. 5.6 can be substituted by an equivalent variogram analysis in the space domain. Hence, instead of computing and interpreting power spectra, we analyze variograms. The most important advantage is that variograms can be estimated directly from the flight line data, making use of their higher along-line resolution as compared to grids. Furthermore, computing variograms is simple and straightforward. Variograms are also easier to understand than power spectra, reducing the risk of mis-interpretation.

The model variogram defined by eqs. 5.6 and 5.7 is governed by three unknowns: z, c_s and β. A smooth magnetic field may be caused either by a great depth to source z or a smooth distribution of basement magnetization reflected in a high value of β. Due to this trade-off, only one of the parameters z and β can be resolved at a time. In areas without major changes in the geology of the basement it is reasonable to assume a constant scaling exponent of the susceptibility distribution (Maus and Dimri, 1995b). For the purpose of deriving a relief of the magnetic basement, the optimum values of z and c_s are estimated from the variograms, keeping β constant. Using a lower scaling exponent β leads to greater depth estimates, and vice-versa (Maus and Dimri, 1996). Thus, depth estimation can be calibrated by choosing the constant scaling exponent in such a way that the inversion yields the average sensor altitude for data over outcropping basement.

5.2.1 Inversion

The optimum values for z and c_s are obtained by inversion. An appropriately sized window is moved over the magnetic data set, as illustrated in Fig. 5.3. Plots of model variograms for different values of z indicate that the window size must be at least five times the maximum depth to be resolved (Figure 4.5). The accuracy of depth estimates increases with window size, while the lateral resolution decreases. From our experience, a window size of around twenty times the maximum depth is a good compromise between lateral resolution and accuracy of depth for survey areas with shallow basement. For each position of the window, the variogram of the data within the window is computed and compared with model variograms for a range of z values. The model variograms can be computed beforehand to

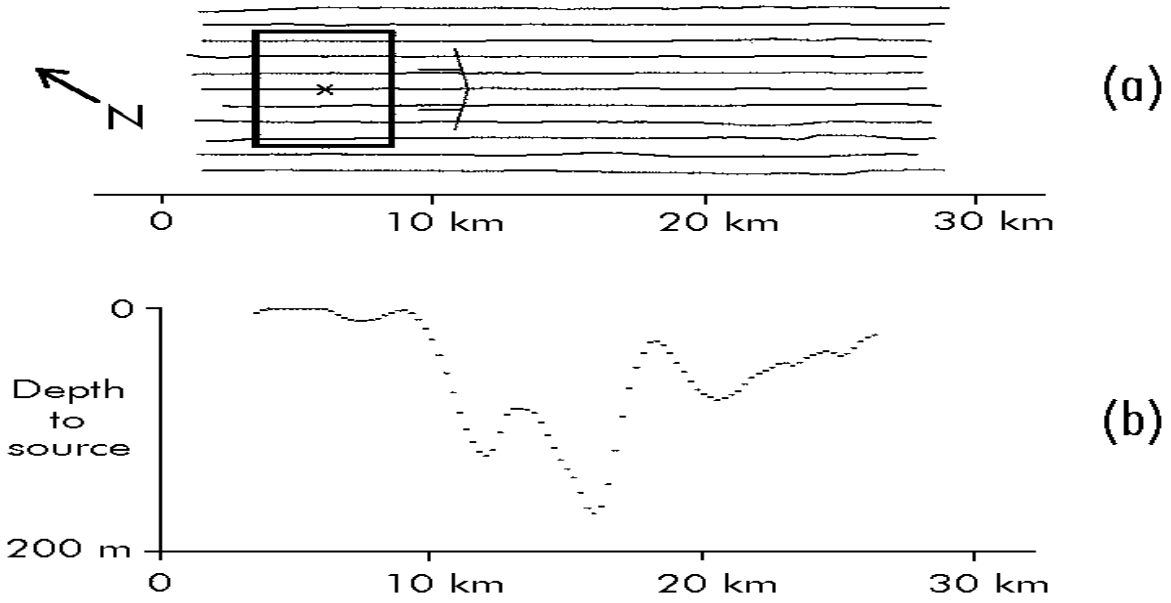

FIG. 5.3: A window is moved over the survey area (a). For each window position the variograms of the intersecting flight lines are computed. The mean variogram is then compared with model variograms to find the optimum depth in a least squares sense. Consecutive depth estimates are plotted here as a profile (b).

save computing time. The best fitting model variogram provides an estimate for the depth to basement. To focus the analysis on to the present window position, a linear trend is removed from the magnetic data of each flight line section before computing its variogram. The model variograms are modified accordingly. Details of this detrending are discussed in Chapter 4.4.3. We utilize only 1D along-line variograms, averaged over adjacent flight lines. In principle, a 2D variogram could be computed from the flight line data within each window. However, the 2D variograms of magnetic data are anisotropic and an analytical solution to the integrals in equation (5.7) does not exist. Apart from the numerical difficulties of a 2D variogram analysis, accuracy may also be affected by line leveling errors. In contrast, the 1D variogram analysis does not require any line leveling at all.

5.2.2 Misfit function

From our experience, variograms of magnetic data have $\lim_{d\to 0} V(d) = 0$ and the main depth information is contained in low lags τ. This motivates using a misfit function

$$\text{Misfit} = \sum_i [\ln V_{est}(\tau_i) - \ln V_{model}(\tau_i)]^2 \tag{5.8}$$

for optimizing depth. Before processing a survey, the assumption $\lim_{d\to 0} V(d) = 0$ should be verified by examining the variograms of sample areas. If the assumption does not hold, eq. (5.8) may have to be modified.

TABLE 5.1: Variogram analysis depth estimates from a real data variogram. Estimated depth strongly depends on the assumed direction of basement magnetization. For example, a magnetic profile over a vertically magnetized basement (incl.= 90^o) at 84 m depth is as smooth as a profile over a basement at 52 m depth with horizontal magnetization perpendicular to the profile direction (incl.=0^o, decl.=90^o).

		declination		
		0^o	16^o	90^o
inclination	0^o	98 m	96 m	52 m
	64^o	86 m	86 m	81 m
	90^o	84 m	84 m	84 m

5.2.3 Limitations

In the following, we list the known sources of error in variogram analysis depth. These limitations are primarily due to the inherent non-uniqueness of the magnetic inverse problem. Similar problems can therefore be expected with all magnetic depth estimation methods.

1. Nonuniqueness between greater source depth and smoother source distribution leads to a trade-off between z and β. The necessary assumption of $\beta = constant$ could be violated by changes in basement lithology.

2. Nonuniqueness of depth versus direction of magnetization is summarized in Table 5.1. A NS profile at the magnetic equator over an induced magnetic source carries stronger texture than a profile in EW direction (hence the well known recommendation to fly NS rather than EW at low magnetic latitudes). The smoothness of an EW profile corresponds to the smoothness of a NS profile at almost twice the altitude above basement. At the magnetic equator, a depth estimate of 98 m from a NS profile could actually be due to a basement at 52 m depth carrying an EW remanent magnetization. Hence, strong horizontal remanent magnetizations are a potential source of error.

3. Magnetic anomalies caused by basement topography cannot be distinguished from anomalies due to intra-basement magnetization contrasts. For example, this can lead to overshooting depth estimates at steep topographic gradients. The ensuing topographic magnetic anomaly constitutes a long wavelength feature, increasing the long to short wavelength power ratio, leading to over-estimated source depth.

4. Care must be taken to eliminate time variations of the magnetic field. Noisy sections of the flight line data have to be excluded from the analysis because they bias depth towards smaller values.

5. Surface or intra-sediment magnetizations obviously reduce depth estimates.

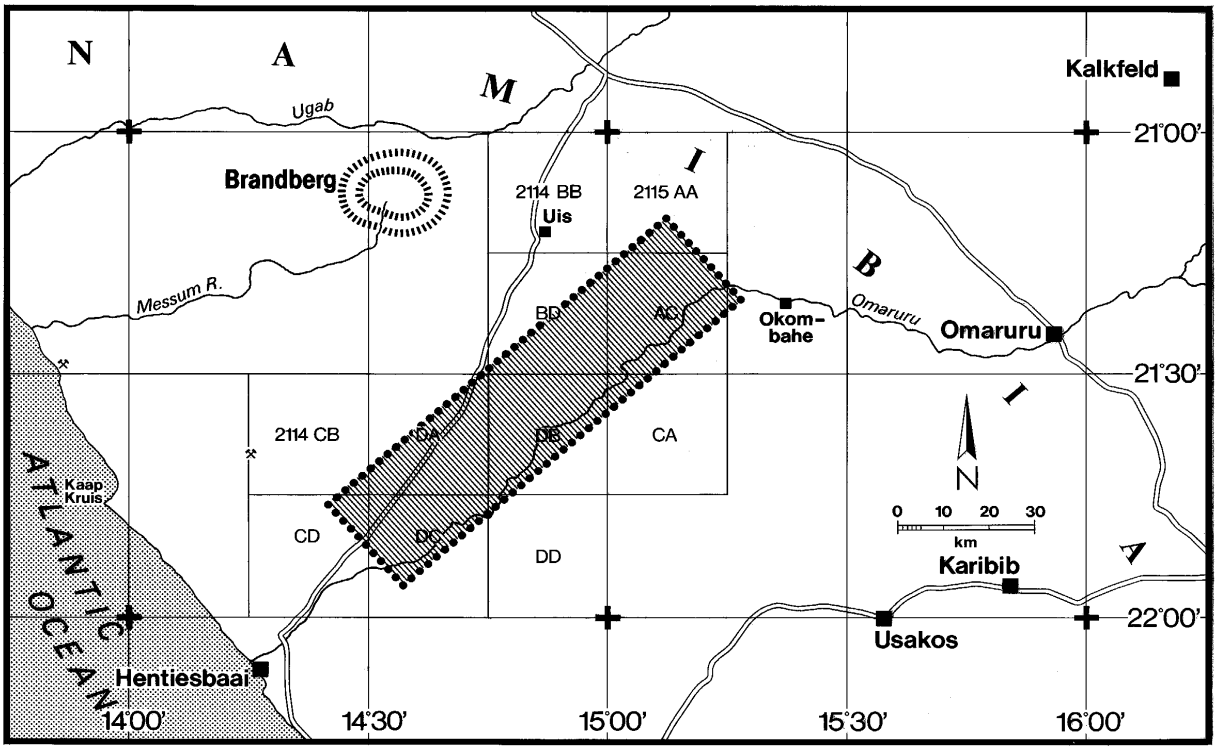

FIG. 5.4: Location and approximate flight lines of the 100 km x 26 km helicopter survey.

5.3 Survey area

In line with the agreement on technical co-operation between Namibia and Germany an area of 100 km x 26 km was surveyed by airborne geophysics (Fig. 5.4) in order to identify proposedly groundwater bearing paleochannels of the Omaruru River. The helicopter survey was flown at constant terrain clearance, the magnetic sensor at approximately 60 m and the EM system at 40 m above terrain.

5.3.1 Geology

The OMAP drainage basin has been involved in tectonic movements since Tertiary times, one faulting event has been dated at Middle to Late Pleistocene or Recent. Seismic activity along two sets of Landsat lineaments, one of which is parallel to the predominant north-easterly direction of Damara faults, suggests that processes of faulting and uplifting are still active (Bittner et al., 1994). The stratigraphy of the test study area in Namibia (Bittner et al., 1994) (Fig. 5.5) can be subdivided into two major components, the older Damara Sequence (Late Proterozoic) comprising granitic, quartzitic and quartz-mica schist lithologies, intruded by mainly northeasterly trending dolerite dikes of Triassic age, and the overlying alluvial deposits which are of Kalahari age (Tertiary to Recent). These so-called Omaruru Alluvial Plains (OMAP) were the target for groundwater exploration (Nawrowski, 1993).

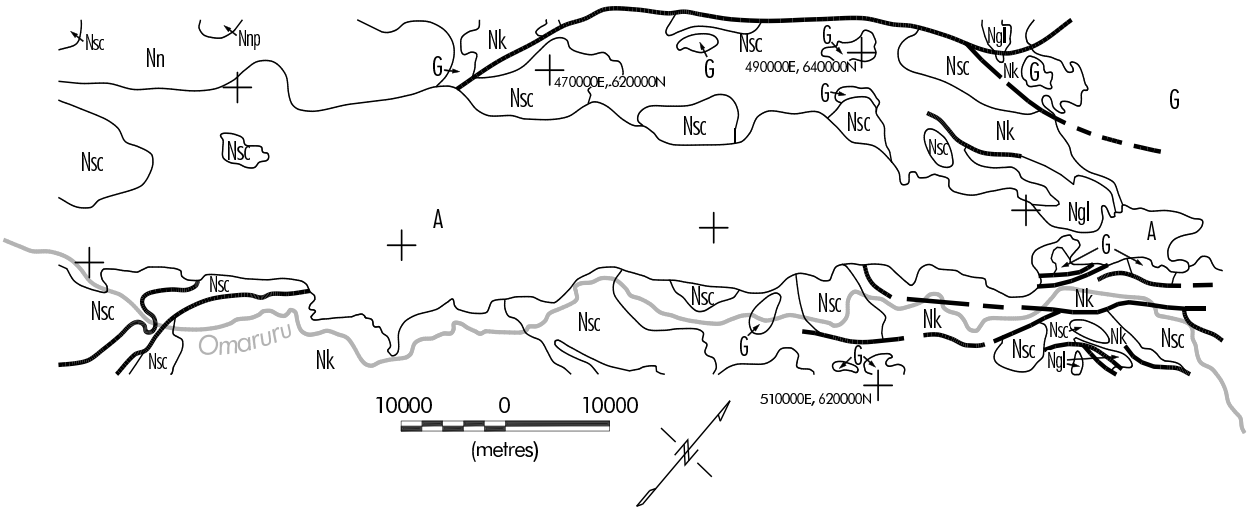

FIG. 5.5: Geological sketch of the survey area, based on the geological map of Namibia 1:1.000.000 (Miller and Schalk, 1980). (A) Alluvium, (G) Granites, (Nsc, Nu, Nk, Nup,Ngl) Damara Orogen Sequence comprising metamorphosed acid volcanics, mica shists and gneissic leucogranites.

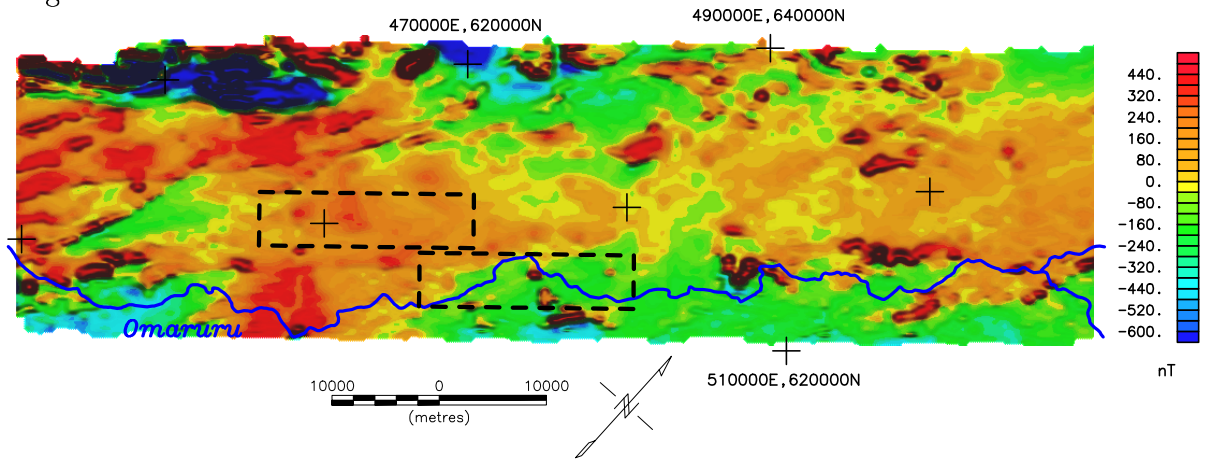

FIG. 5.6: Shaded ΔT total field anomaly map (Paterson and Reeves, 1985) of the survey area with present Omaruru River. Two sample areas are indicated as dashed rectangles.

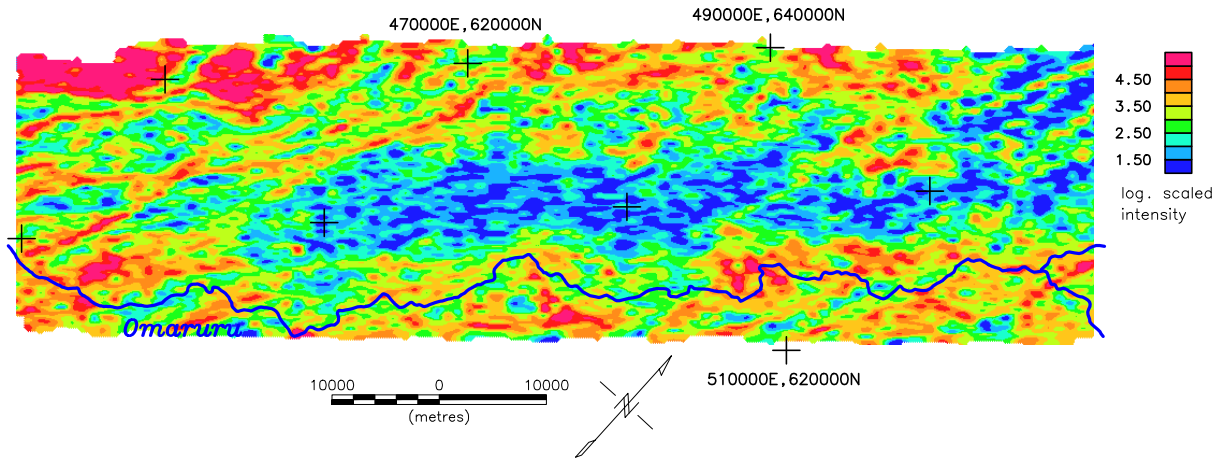

FIG. 5.7: Map of the intensity c_s, estimated by variogram analysis from single 500 m along-line sections of ΔT data, assuming $\beta \equiv 2.6$ and $z =$ terrain clearance. Non-magnetic alluvial deposits along the center of the area are reflected in low c_s values.

The south-easterly displacement of Omaruru drainage paths was probably tectonically induced. Channels have a tendency to migrate down tectonic tilt (Leeder and Alexander, 1987). Variations in channel discharge due to sea-level change, and variations in sedimentary recharge due to climatic change could have been further reasons for channel migration (Alexander et al., 1994).

5.3.2 ΔT and c_s magnetic maps

The total field anomaly map of the survey area is shown in Fig. 5.6. By variogram analysis, the source intensity c_s was estimated from the ΔT flight line data using a 500 m window along single lines and further assuming $\beta \equiv 2.6$ and $z =$ terrain clearance. This high resolution c_s intensity map is shown in Fig. 5.7. The c_s map provides superior near surface resolution of magnetic source, since c_s is estimated from very short along-line ΔT variations, hence, exactly the short wavelength information that is lost in gridding ΔT data. The c_s map is easy to interpret. In contrast to ΔT, c_s is high when magnetization is high and low when magnetization is low.

5.4 Magnetic depth from two sample areas

To illustrate the spectral methods discussed above, we have selected two sample areas of 5 km x 20 km which are indicated in Fig.5.6. The first area has outcropping basement while the second area is situated over the center of one of the main paleochannels. From the drilling results discussed below the depth to basement in the center of the second area is around 200 m, but probably shallower at its sides.

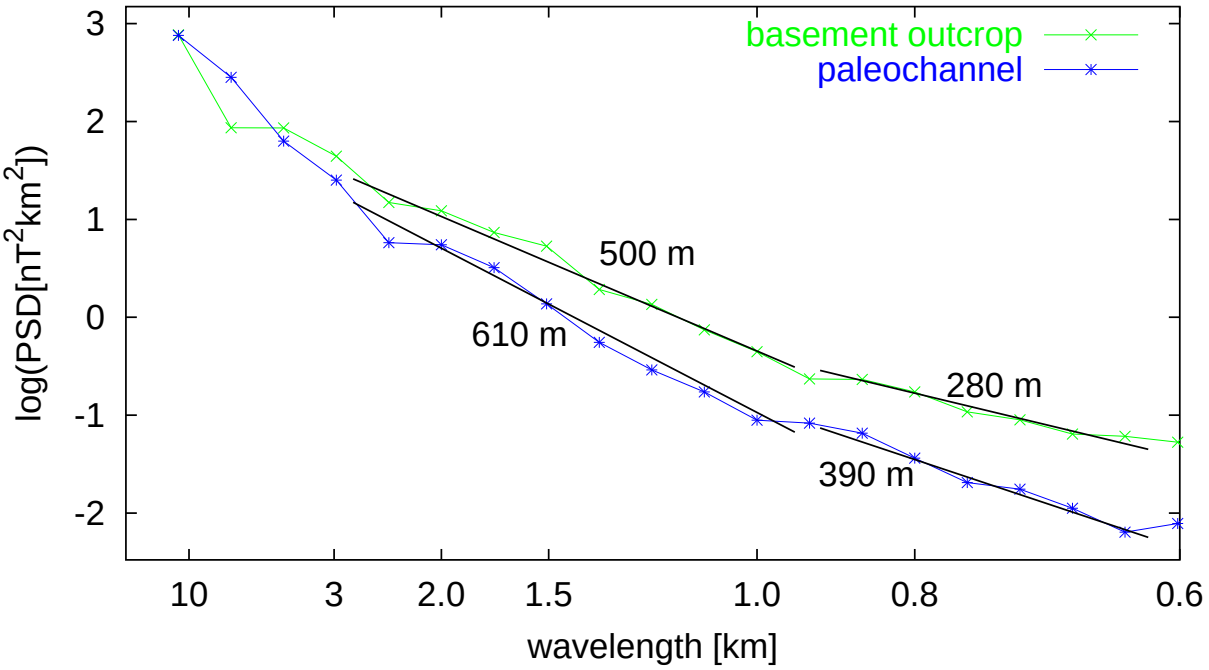

FIG. 5.8: Power spectra of the two areas indicated in Fig. 5.6 with a spectral slope method interpretation. Note the equal difference in depth of 110 m in both wavebands.

5.4.1 Depth from the spectral slope

In previous spectral analysis methods depth is estimated from the slope of the azimuthally averaged power spectrum, as demonstrated in Fig. 5.8. These absolute or *white* depths are at 280 m and 500 m in the first area while they are at 390 m and 610 m in the second area. Pilkington *et al.* (1994) have pointed out that these white depths overestimate true depth. Indeed, it is unlikely that a horizontal source interface would cause a linear section in the power spectrum at all.

Let us now examine relative depth. The difference in slope between areas 1 and 2 is identical in both wavebands and corresponds to a relative difference in depth of 110 m. If we upward continue the spectrum of the paleochannel area by 110 m it matches the spectrum of the area with outcropping basement. This can be interpreted in such a way that the spectrum of the basement magnetic field is identical in both areas, while the vertical distance to the observation plane is greater by 110 m in the paleochannel area. The difference in slope in a fixed waveband therefore provides an estimate for the relative depth to the basement, while the absolute white depths are meaningless.

5.4.2 Depth from the entire spectrum

Instead of comparing slopes in fixed wavebands, the depth factor can be analyzed with greater precision by using a model for the entire power spectrum. This approach is illustrated in

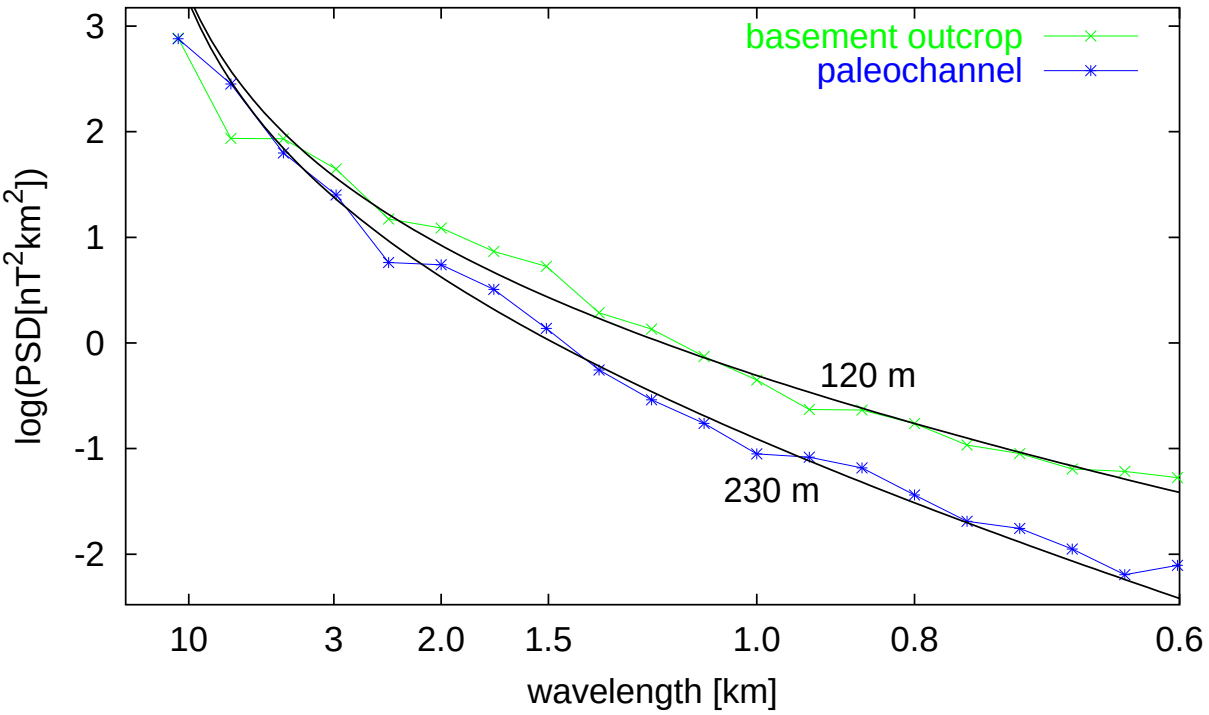

FIG. 5.9: Same power spectra as in Fig. 5.8 interpreted using a self-similar $e^{-2hs}s^{-3}$ model.

Fig. 5.9. Here, a self-similar model $e^{-2hs}s^{-\beta+1}$ is fit to the power spectrum. The best least squares fit for a constant β provides an estimate of relative basement depth. If the correct value of β is known, then even the absolute depth to basement can be obtained by this approach (Maus and Dimri, 1996). Here, we used $\beta = 4$, proposed by Pilkington and Todoeschuck (1995) as the mean scaling exponent of continental crust. Besides explaining the full shapes of the two power spectra, this approach also leads to realistic estimates of absolute depth from the observation plane to the basement. Subtracting the average sensor clearance of 61 m and 56 m gives basement depths below terrain of 59 m and 174 m for the outcrop and the paleochannel area, respectively.

5.4.3 Depth from the variogram

The resolution and accuracy of depth estimation can be improved further by shifting the analysis to the space domain and analyzing variograms, as illustrated in Fig. 5.10. Subtracting the sensor clearance from the model depths gives estimates of 12 m and 184 m for the depth below terrain. In particular for outcropping basement, the variogram analysis depth of 12 m below terrain is much better than the power spectrum depth of 59 m below terrain (Fig. 5.9). The greater power spectrum depth in the latter case is probably caused by the smoothing effect of gridding. The grid does not reflect the full ruggedness of the magnetic field over outcropping basement.

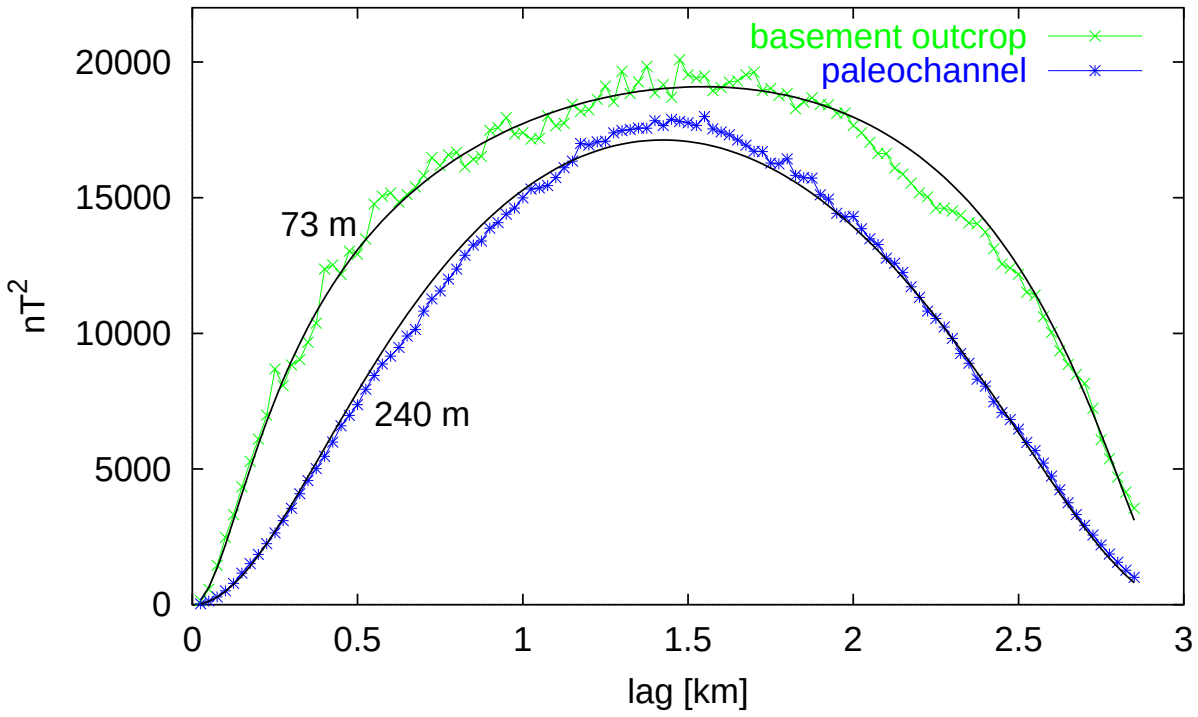

FIG. 5.10: Modified variograms of the two areas in Fig. 5.6 together with the best fitting model variograms indicated as solid lines. For better comparison, the paleochannel variogram is amplified by a factor 4.0.

5.4.4 Calibration of depth

As described above, the scaling exponent β has to be kept at a constant value to be able to resolve depth z. This corresponds to the assumption of a constant shape (but variable amplitude) of the magnetic power spectrum at basement level. Indeed, the spectral slope method is based on the same implicit assumption. A higher scaling exponent leads to shallower depth estimates and vice versa. Looking at variogram analysis depth over outcropping basement we obtain depths close to the sensor terrain clearance for $\beta = 2.6$. It is not clear why this value is so much lower than $\beta = 4$ which gives a realistic interpretation of the power spectra. Both values should in theory be identical. Possible reasons for the deviation are the smoothness of grids, leading to high power spectrum β, and the subtraction of a linear trend before estimating the variograms, leading to low variogram β.

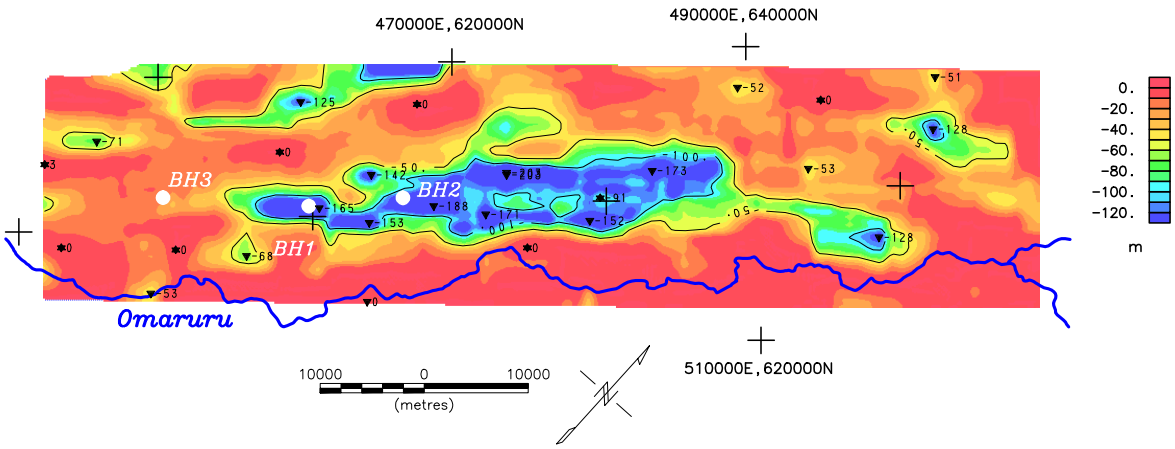

FIG. 5.11: Variogram analysis depths. BH1, BH2 and BH3 indicate the positions of three ground water exploration wells (see table 5.2)

5.5 Results for the entire survey area

We utilized a scaling exponent of $\beta = 2.6$ and a window size of 5 **x** 6 km (along-line **x** across-line) for the variogram analysis (Fig. 5.3). Within this window we calculated the variograms for sections 3 km in length, one every 100 m, and stacked the variograms of the sections along-line as well as across-line. Hence, the resulting variogram is an average of 21 (along-line) x 7 (across-line) = 147 variograms. This gives a better result than using 5 km variograms and stacking only across-line. We moved the window along-line by 100 m increments. Across-line the window position was incremented by one flight line at a time, corresponding to 1 km intervals. The result for the entire survey is shown as depth below terrain in Fig. 5.11.

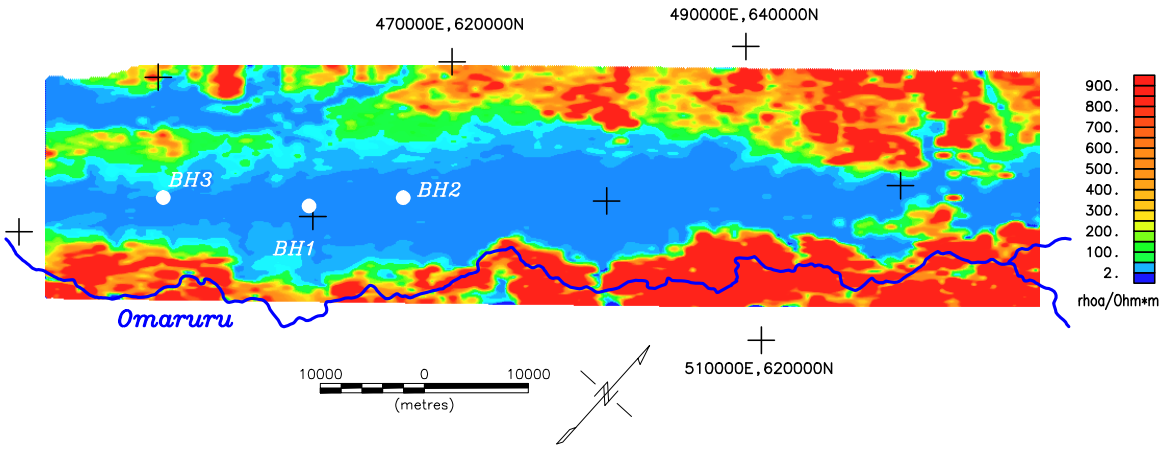

FIG. 5.12: Map of ρ_4 from a 5-layer inversion of measurements from an active 3-channel EM system

5.5.1 Depth versus EM resistivities

To some extent, variogram analysis depths below terrain can be verified by a comparison with measurements from a 3-channel active EM system. The map of ρ_4 from a 5-layer inversion (Sengpiel, 1988), shown in Fig. 5.12, provides a horizontal resistivity cross-section at approximately 30 m depth. High resistivity indicates crystalline basement. Low resistivity is due to sediments. Very low resistivities can be caused by saline water or clay. Areas of low resistivity in Fig. 5.12 should therefore coincide with areas of depth greater than about 20 m in Fig. 5.11. All in all, the agreement between the two maps is good. Some structures which are small relative to the 5 km by 6 km variogram analysis data window are missing in the variogram analysis depth map. This problem is apparent at the high (right) and low (left) margins of the survey area, where narrow paleochannels are poorly resolved. The wider channel in the center of the study area, on the other hand, is mapped quite accurately.

TABLE 5.2: Drilled versus predicted basement depths

	BH1	BH2	BH3
lithology	meta-basalt	granite	amphibolite
drilled depth	141 m	198 m	110 m
variogram analysis depth	163 m	182 m	34 m
error (off sensor)	11 %	6 %	45 %

5.5.2 Basement relief

To display the estimated depth in such a way that paleochannels can be identified, we first subtracted the altitude a.m.s.l. of the Omaruru river at the intersection with each flight line from the topography a.m.s.l. along-line. The Omaruru river then flows always at altitude zero, while it actually descends from around 900 m a.m.s.l. in the North-East to around 300 m in the South-West. This relative ground topography is displayed in Fig. 5.13. We then added the negative basement depth estimates, resulting in a basement relief relative to the present day Omaruru river. The result shown in Fig. 5.14 clearly indicates several paleochannels.

In Fig. 5.15 the corresponding basement relief obtained by an automated spectral slope method is displayed. A window of 6 km x 6 km was moved over the magnetic grid of the survey area. The power spectrum was estimated for each window position using a commercially available software package. This software also provides an estimate of 3-point slope. By trial and error we found the waveband where relative differences in slope give the best estimates of basement depth. As predicted above, absolute depth below terrain ranging from 550 m to 800 m is quite off the mark. Nevertheless, subtracting 550 m leads to a crude but reasonable basement relief.

5.5.3 Drilling results

Of nine proposed groundwater exploration wells, only three were drilled. (BH1, BH2, and BH3 indicated in Figs. 5.11, 5.13 and 5.14). After 129 m of gravel, sand and clay, BH1 encountered weathered doleritic basement sand, weathered meta-basalt at 141 m and fresh meta-basalt at 160 m (variogram analysis prediction 163 m). BH2 found basement sand (magnetite, mica, feldspar) at 192 m and hit a granitic basement at 198 m (variogram analysis prediction 182 m). Further downstream, BH3 found dark basement sand (magnetite, hornblende) at 96 m and an amphibolitic basement at 110 m (variogram analysis prediction 34 m). Unfortunately, no susceptibilities were measured. All wells were dry.

Drilling results versus predicted depths are summerized in Table 5.2. Taking into account the 60 m flight altitude of the magnetic sensor, prediction errors for BH1 and BH2

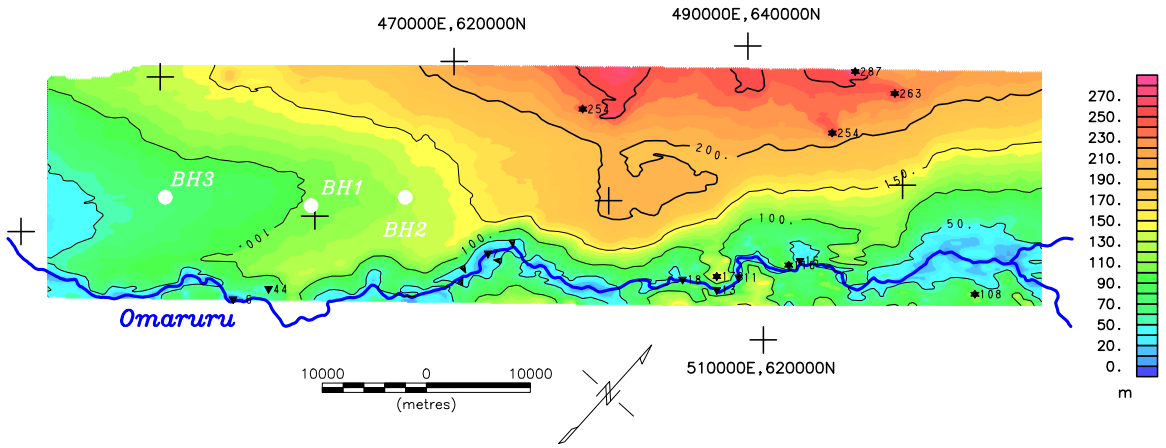

FIG. 5.13: Terrain topography relative to the Omaruru River

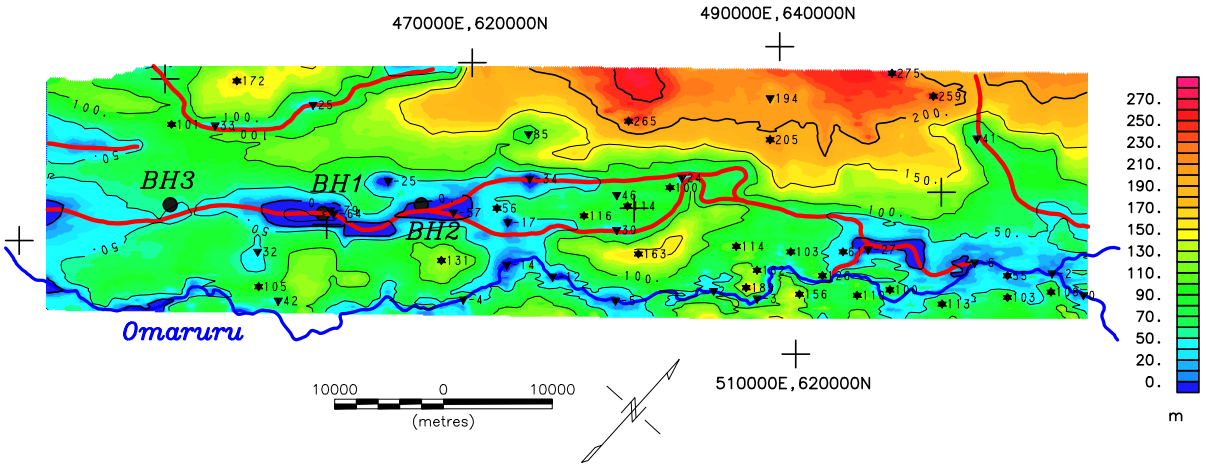

FIG. 5.14: Topography of the magnetic basement obtained by adding the negative variogram analysis depth estimates of Fig. 5.11 to the topography of Fig. 5.13. Our interpretation of possible Omaruru paleochannels is indicated in red. Three groundwater exploration wells BH1, BH2 and BH3 were dry.

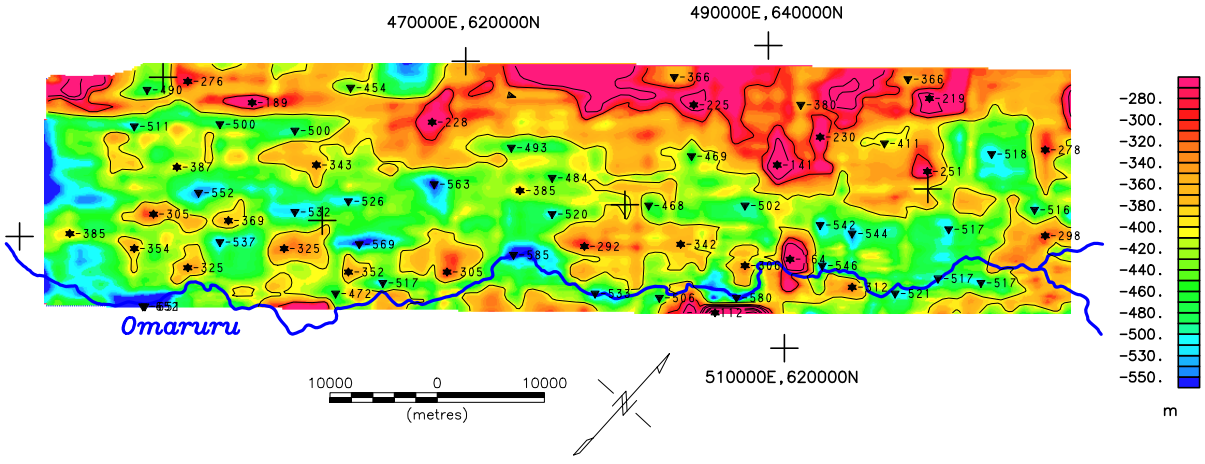

FIG. 5.15: For comparison, magnetic basement topography obtained by an automated spectral slope method. Optimum spectral waveband found by trial and error.

are around 10%. In contrast, the prediction for BH3 is quite off the mark. While variogram analysis depths (Fig. 5.14) correctly indicate the continuation of the central paleochannel, its depth is grossly underestimated. The channel is probably too narrow here to be resolved accurately by a 5 km x 6 km variogram analysis window.

5.6 Discussion and conclusions

The basement topography of the Omaruru Alluvial Plains has been derived by variogram analysis (variogram analysis) of an aeromagnetic survey. The method has been designed to make maximum use of the measured data. We have discussed the non-uniqueness of magnetic depth solutions. Besides depth, properties of magnetic mineral distribution and the direction of magnetization influence the smoothness of the magnetic field. Furthermore, steep gradients in basement topography give rise to long wavelength magnetic anomalies which are not discernible from deep seated intra-basement magnetization contrasts. In view of these inherent difficulties of the magnetic method, our result has remarkable resolution and accuracy. In comparison with the earlier spectral slope methods, variogram analysis has the advantage of

1. making use of the short wavelength along-line information, which is otherwise lost in gridding. This is the key to reliable depth in shallow sedimentary deposits.

2. having no restriction on the shape of the survey area. Variogram analysis can even process single profiles. In contrast, power spectra require rectangular (usually square) subareas.

3. accounting for the fractal distribution of magnetic minerals by using a self-similar spectral model, leading to more accurate depth estimates.

4. avoiding the difficulties (e.g. edge effects) of wavenumber domain power spectrum estimation by using straightforward space domain variograms

Due to 1 and 2, variogram analysis has a strong advantage over power spectrum methods in shallow basins. In deep basins, with basement depths larger than flight line spacing, even grids should contain sufficient high wavenumber information to estimate reliable depth. A power spectrum method could then yield accurate depth, provided the fractal nature of magnetic source is taken into account, e.g., by using eq. (5.6) as a spectral model. The question remains, however, why the data should be arduously transformed to wavenumber domain, when spectral models can be analytically transformed to space domain without loss of information, instead. We argue that a data variogram is easier to estimate and should therefore carry more reliable depth information than a power spectrum, even for surveys of deep basins.

Finally, variogram analysis has an interesting spin-off in terms of a near-surface magnetization intensity map (Fig. 5.7). Variogram analysis intensity is high when magnetization is high, and vice versa, simplifying interpretation. Using very short flight line sections for variogram estimation, maximum use of short wavelength along-line signal can be made. This amplifies small structural features which are usually lost in gridding. Variogram analysis intensity maps could therefore be helpful in detecting weak intra-basinal signatures from high resolution aeromagnetic data in petroleum exploration.

Chapter 6

Variogram analysis applications II*

Depth can be estimated from magnetic data by inverting individual anomalies, e.g. by Euler deconvolution (Reid et al., 1990), or by statistical methods which make use of spectral properties of the field. Spector and Grant's original method (1970) can be improved by taking into account the self-similar (fractal) nature of source (Pilkington et al., 1994; Maus and Dimri, 1996). Directly analyzing line data using variograms (Chapters 4 and 5) leads to further significant improvements in accuracy and resolution. The aim of the study described in this chapter is to verify the quality of variogram depth on synthetic and real data.

We generate a self-similar magnetized basement and synthesize magnetic data in flight lines above this model (Fig. 6.1). Resolution of alternating slopes and channels depends on the relative size of the data analysis window. Features larger than this window size are generally well resolved. Variogram depth is correct on average, hence, it is unbiased. However, depth estimates can over- and undershoot at topographic gradients. Basement ruggedness, unknown scaling exponent of source and non-negligible sediment magnetization may cause further problems, which are studied here. An interesting question is, whether it is preferable to fly along or across the basement topographic trend. The best strategy is to do both, namely, to fly with twice the line spacing in both directions. This regular mesh offers the optimum basement resolution per line km surveyed.

Finally, we process a magnetic survey of the Kuiseb Dune Area. Interpretation is complicated by high instrument noise and variable surface topography. Comparing basement reliefs with drilling results in 15 locations we find an optimum data analysis window size of 5400 m for this survey. This is disappointingly large. Arguably, resolution would have been better if survey lines had followed the dune valleys.

*Published as an expanded abstract, *SEG 70th annual meeting* (Maus, Röttger and Sengpiel, 2000)

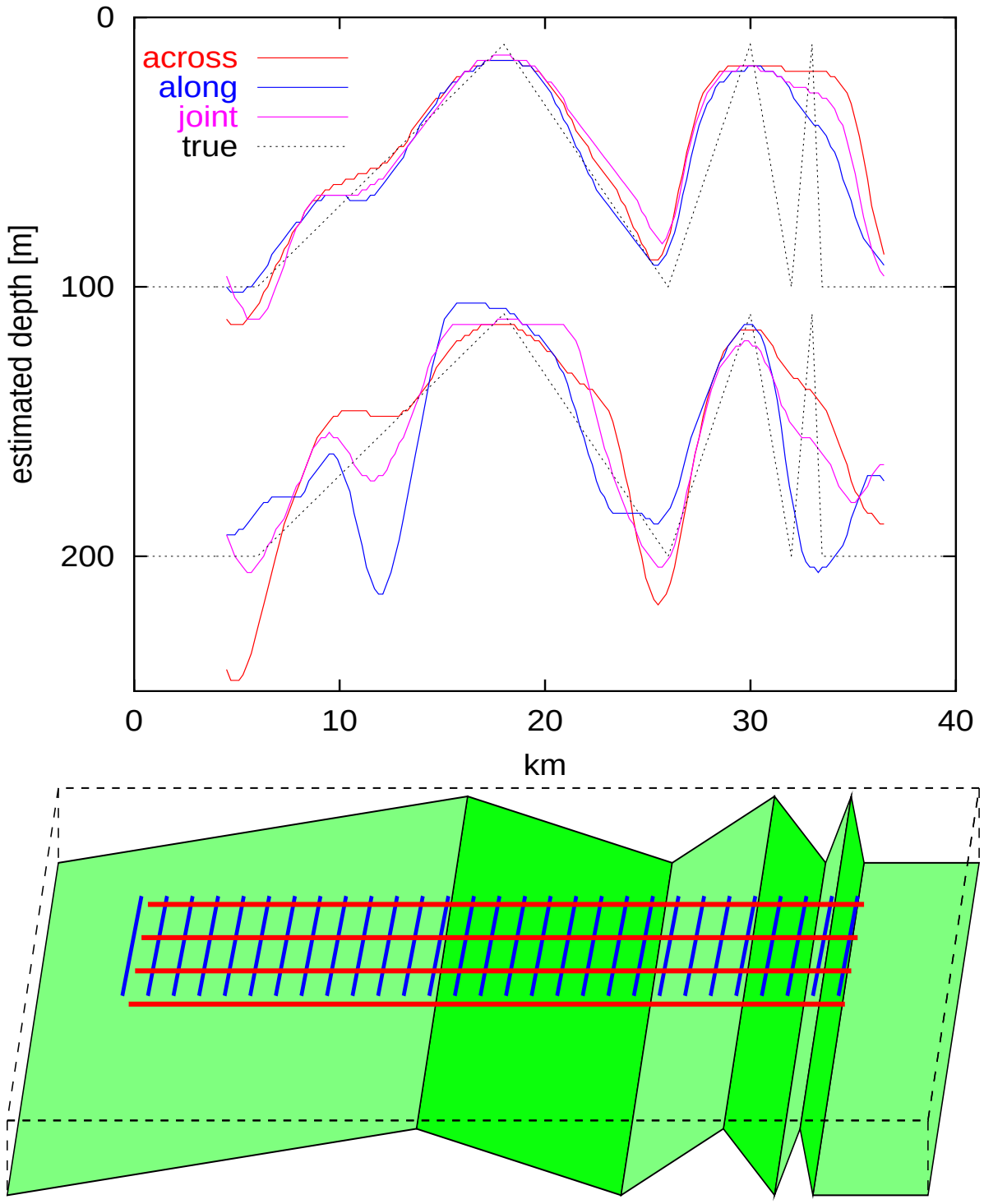

FIG. 6.1: Basement topography is superimposed on a 2D equivalent layer with a self-similar distribution of susceptibility. Depth is estimated from synthetic magnetic data computed for flight lines in horizontal observation planes above the basement model. Note that the vertical scale of the model is strongly exaggerated.

6.1 Synthetic modeling

We generate realistic magnetic flight line data from self-similar source models with imposed topography. Depth estimated from this data is compared with true model depths (e.g. Fig. 6.1) to test the variogram analysis method.

6.1.1 2D equivalent layer models

Any 3D magnetization model can be replaced by an equivalent layer of induced magnetization at the model surface, drastically reducing computation time. A self-similar 3D susceptibility distribution with scaling exponent β causes a magnetic field with scaling exponent $\beta - 1$ in a horizontal observation plane (Maus and Dimri, 1994). The same magnetic field is caused by an equivalent 2D susceptibility layer with scaling exponent $\beta + 1$. Hence, we can substitute a 3D source model with scaling exponent β by a 2D layer with $\beta + 1$.

6.1.2 Self-similar grid synthesis

We fill a grid with random numbers in the wavenumber domain in such a way that the corresponding grid in the space domain has the desired spectrum (Maus and Dimri, 1996). With this method grids can be synthesized which are self-similar up to lags of around 1/4th of its side length. The self-similarity of the grid $G(x, y)$ can be verified on its azimuthally averaged variogram $V(\tau)$

$$V(\tau) = \langle [G(x, y) - G(x + dx, y + dy)]^2 \rangle, \tag{6.1}$$

where $\tau = \sqrt{dx^2 + dy^2}$. The variogram of a self-similar grid with scaling exponent β is proportional to a power of the lag τ, as in $V(\tau) \propto \tau^{\beta-2}$(Yaglom, 1986). Figure 6.2 shows the variogram of a 2048 x 2048 grid with $\beta = 3$ that was produced with this method. While its variogram should increase linearly with the lag, this is only the case for lags up to 1/4th of the grid dimension. However, in the following experiments the data analysis window size is always smaller. Hence, grids synthesized with this method are suitable for the present investigation.

6.1.3 Synthetic magnetic data

Once a self-similar grid is synthesized, the desired models can be produced by superimposing topography. This is valid if vertical variations are small compared with the horizontal scale of the equivalent layer. We use a long strip of basement. Topography is 1D in the sense that it varys along the strip and is constant perpendicular to the strip. Two data sets are synthesized for every model. One with flight lines parallel to the strip (across topography) and one with lines perpendicular to the strip (Fig. 6.1). Magnetic ΔT-data are computed

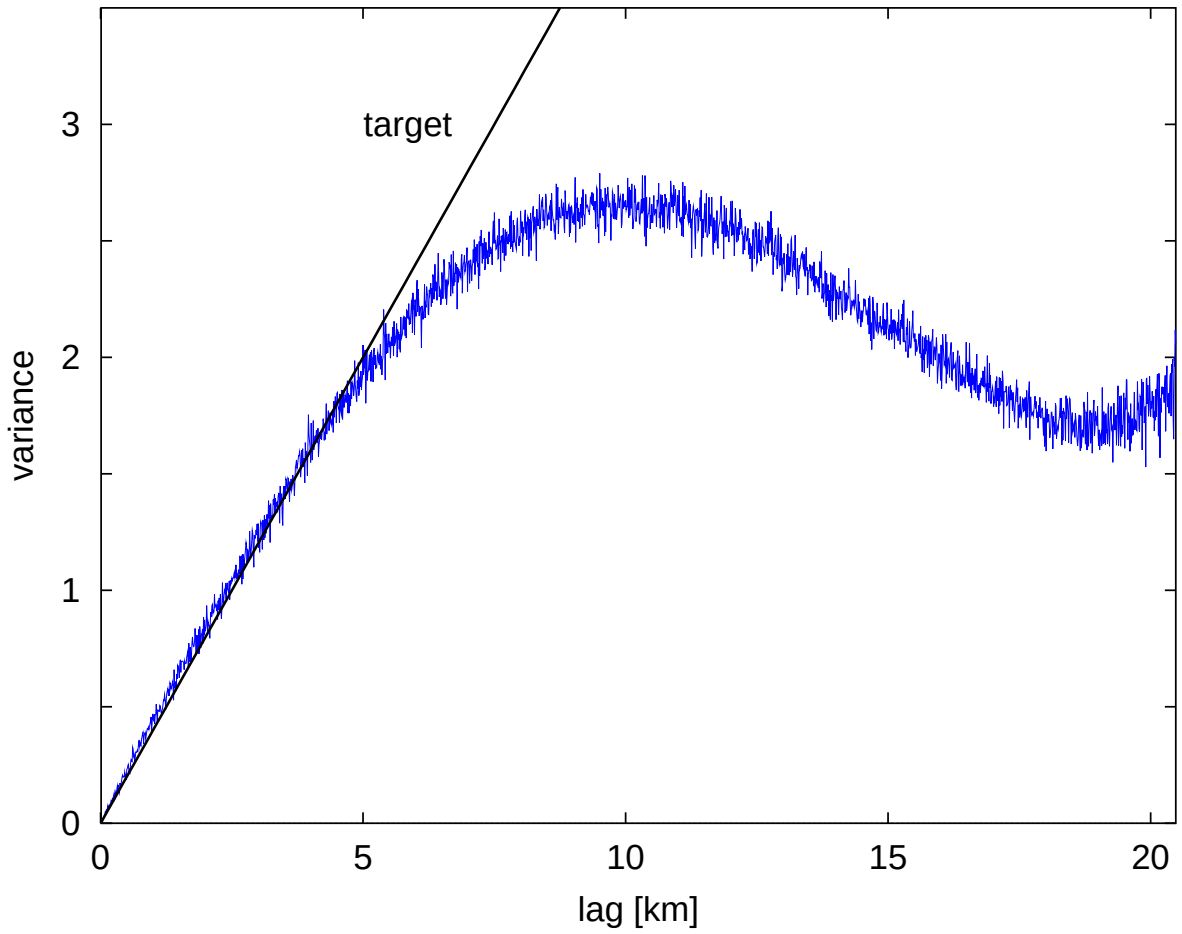

FIG. 6.2: Variogram of a 2048^2 model grid produced by the FFT method. The grid is self-similar up to lags of around 1/4th of its side length.

for a vertical inducing field. In the models, every grid cell represents 10 m x 10 m in nature. However, all model dimensions and depths may be scaled by a constant factor.

6.1.4 Variogram analysis algorithm

We use the same algorithms as in Chapters 4 and 5. The only new feature is that when we estimate depth in a particular location, we average variograms weighted by a Gauss bell shaped function $\exp(-r^2/\sigma^2)$. At $r = \sigma$ the weight function falls off to $e^{-1} \approx 0.37$. We refer to the diameter 2σ as the effective window size. Contributions from further than $r = 3\sigma$, where the weight drops to below 10^{-4}, can be ignored. Using this weight function does not improve the accuracy of depth, but leads to a reasonably smooth basement relief. With uniform weights, instead, the relief shows rectangular or circular artifacts reflecting the cut-off radius. In the synthetic modeling we use an effective window size of 4 km and estimate depth from profiles oriented *across* as well as *along* topography. We also estimate a *joint* depth, where we simultaneously invert half of the profiles in both directions.

6.1.5 Sloping basement

Topography with alternating gradients of increasing slope is superimposed onto the basement strip. Estimated depth is shown in Fig. 6.1. The first three slopes are mapped rather accurately. The length of the third slope is 4 km and thus equal to the effective window size used. Features smaller than this window size are not resolved. Depths from the across topography profiles tend to overshoot. The reason is that when a profile runs from deep basement into shallow basement, a topographic magnetic anomaly ensues. This long wavelength anomaly increases the ratio of long to short wavelength power which is interpreted as greater depth to source. Thus, topographic anomalies can lead to overshooting depth estimates. Along-topography depth does not show this artifact and the most accurate depth is obtained from the bi-directional inversion.

6.1.6 Paleochannels

In locating paleochannels, we would like to know how broad a channel must be in order to be identified by the variogram analysis. We indent channels of decreasing width into the basement strip (Fig. 6.3) and try to locate them using an effective 4 km x 4 km variogram analysis window size. We find that a channel has to be roughly as broad as the size of the analysis window in order to be identified reliably.

6.1.7 Unknown scaling exponent

In practice, the scaling exponent of the basement magnetization can only be guessed. As mentioned above, a susceptibility grid with $\beta = 3$ produces a magnetic field with $\gamma = 1$. For Figure 6.4, depth was therefore estimated using scaling exponents γ of 0.5, 1, and 1.5. It can be seen that a 0.5 uncertainty in the scaling exponent leads to an uncertainty of around 20% in absolute depth. This uncertainty of depth versus smoothness of source follows from the inherent non-uniqueness of the magnetic inverse problem.

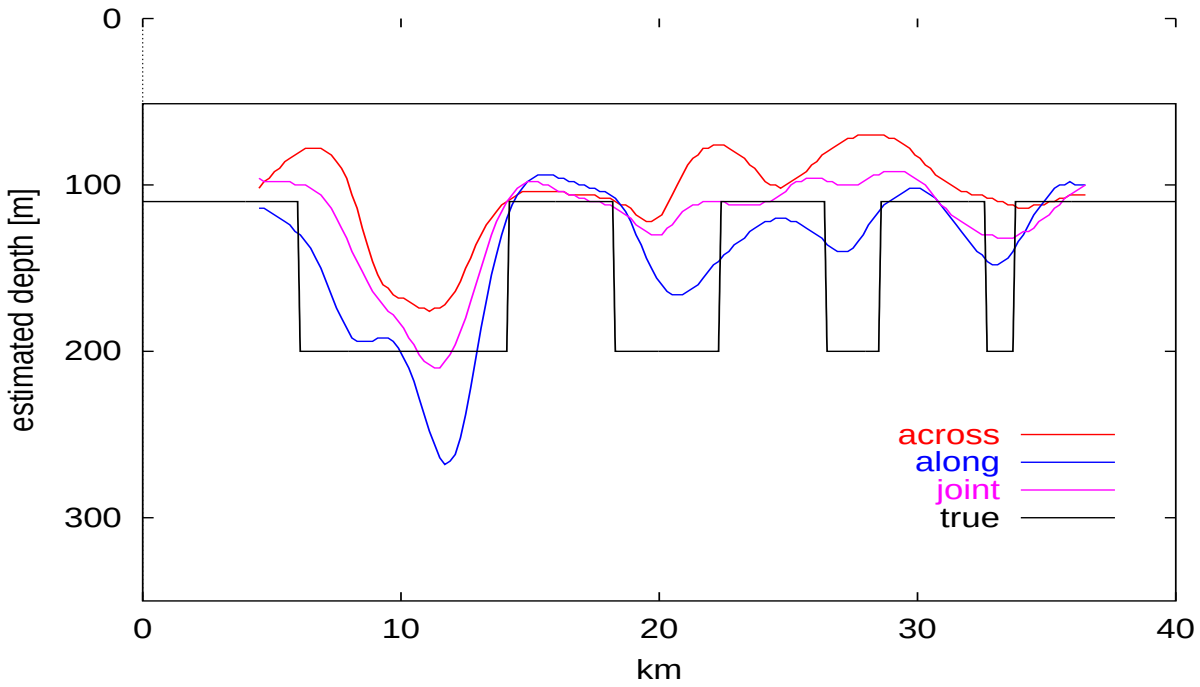

FIG. 6.3: Depth to a basement with channels

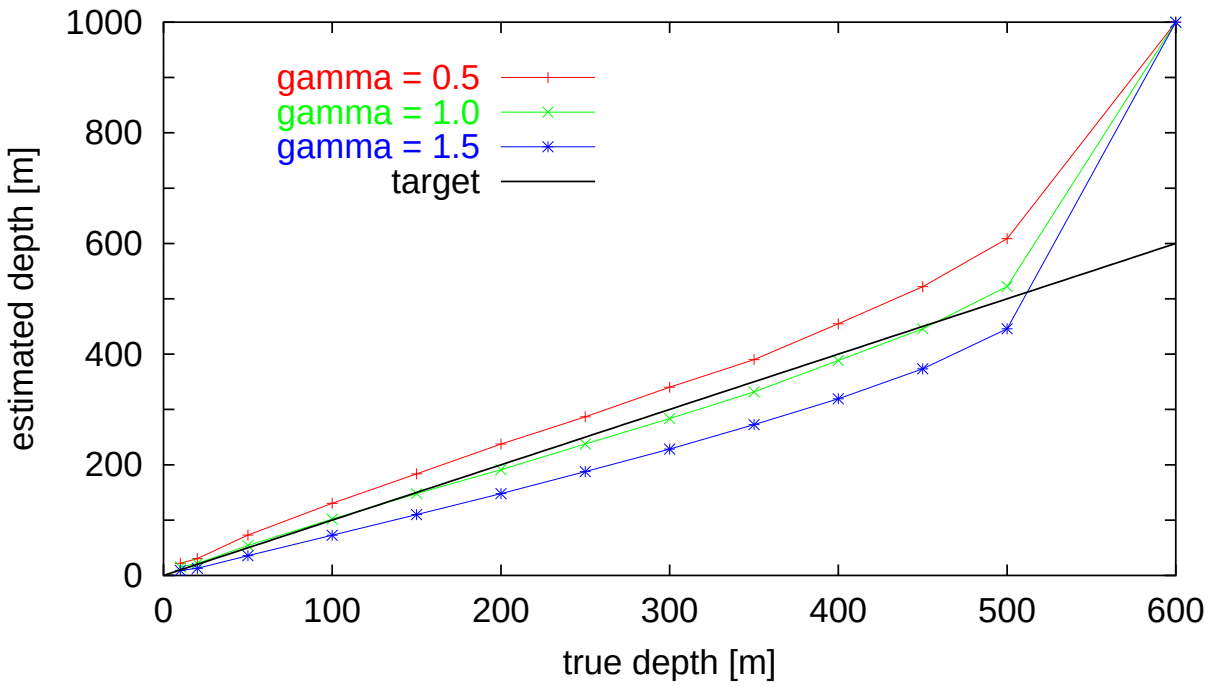

FIG. 6.4: Depth estimated under different assumptions of γ. The correct scaling exponent is $\gamma = 1$

6.1.8 Rugged basement

Small scale variations in basement topography cannot be resolved by variogram analysis. Instead, they lead to a bias in basement depth estimates. A source grid is combined with a self-similar topography grid, representing a basement with self-similar magnetization as well as topography. The superimposed topography grids with $\beta = 2$ are chosen to have zero mean value, 10 m, 20 m, and 50 m standard deviation, and maximum values of 50 m, 100 m, and 250 m, respectively. We find that a rugged basement leads to reduced depth estimates (Fig. 6.5). As a rule of thumb, the estimated depth lies about half-way between the mean and the minimum depth to basement.

6.1.9 Non-negligible sediment magnetization

High resolution magnetic surveys are increasingly employed to map intra-sediment anomalies. Does this contradict the basic assumption of a negligible sediment magnetization in the variogram analysis? We investigate how strong the magnetization of sediments may be without affecting depth estimates. Assuming a survey terrain clearance of 50 m, sediment magnetic fields of decreasing strength are added to the magnetic fields of basements at depths of 100 m, 200 m and 300 m, respectively. Estimated depth is plotted against the ratio of basement to sediment magnetization in Fig. 6.6. The result is reassuring. Even for the greatest depth, corresponding to one tenth of the window size, a susceptibility contrast of around two orders of magnitude is sufficient to allow reliable depth estimation. This is not a very strong contrast for a typical basin.

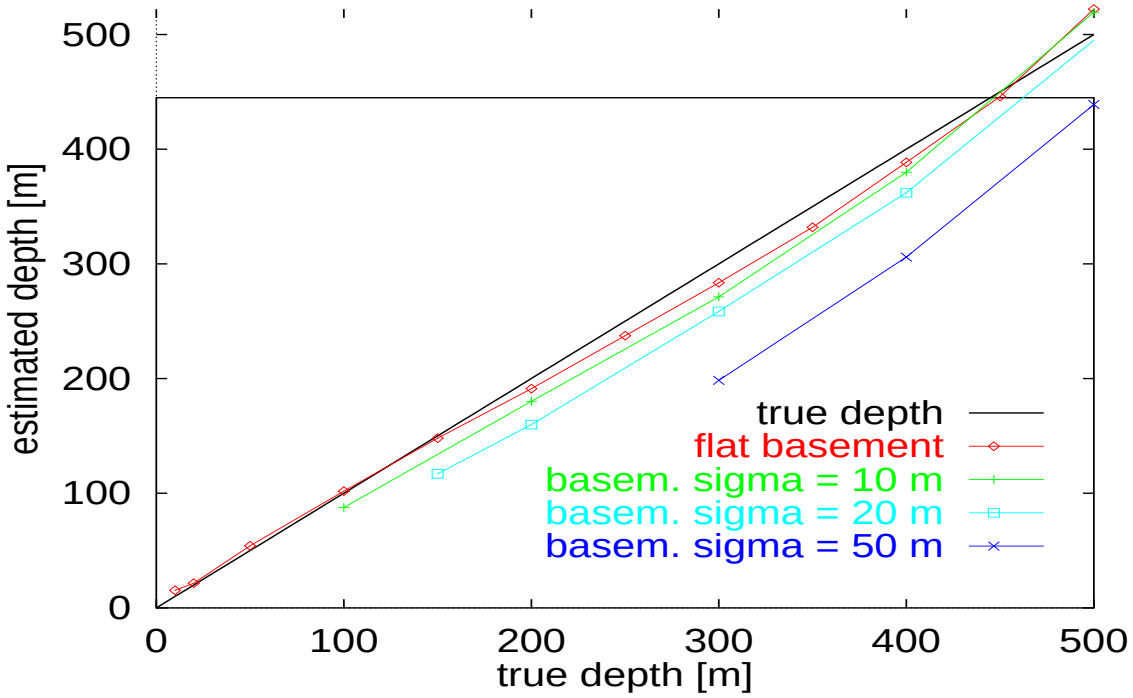

FIG. 6.5: Estimated versus true depth for rugged basement

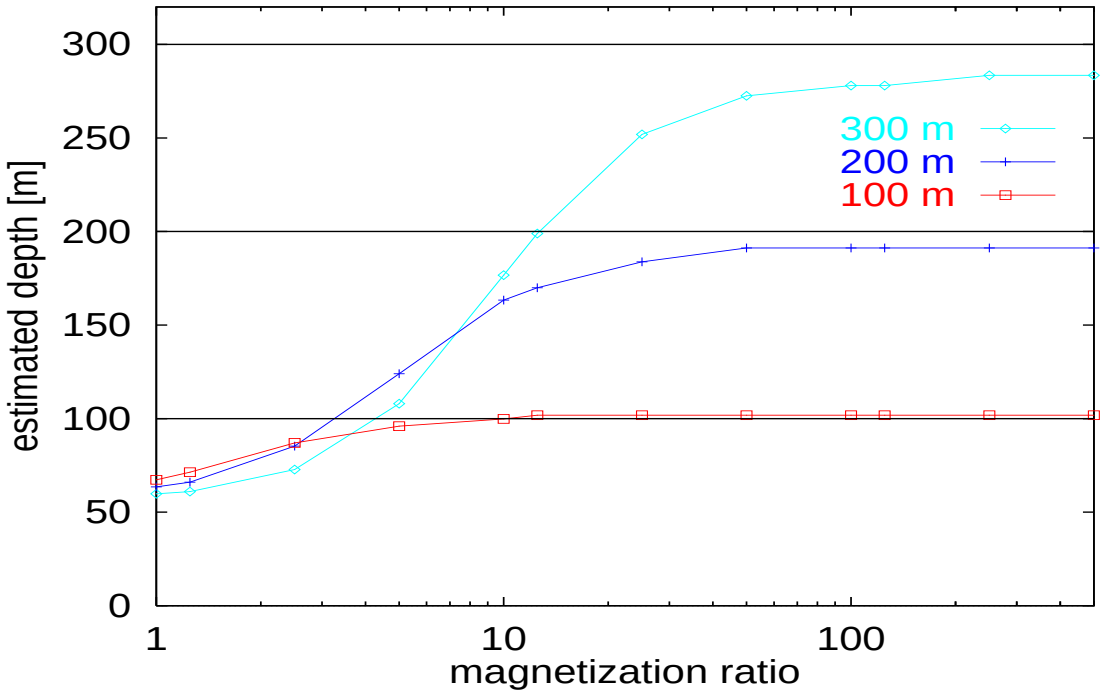

FIG. 6.6: Depth against basement to sediment magnetization

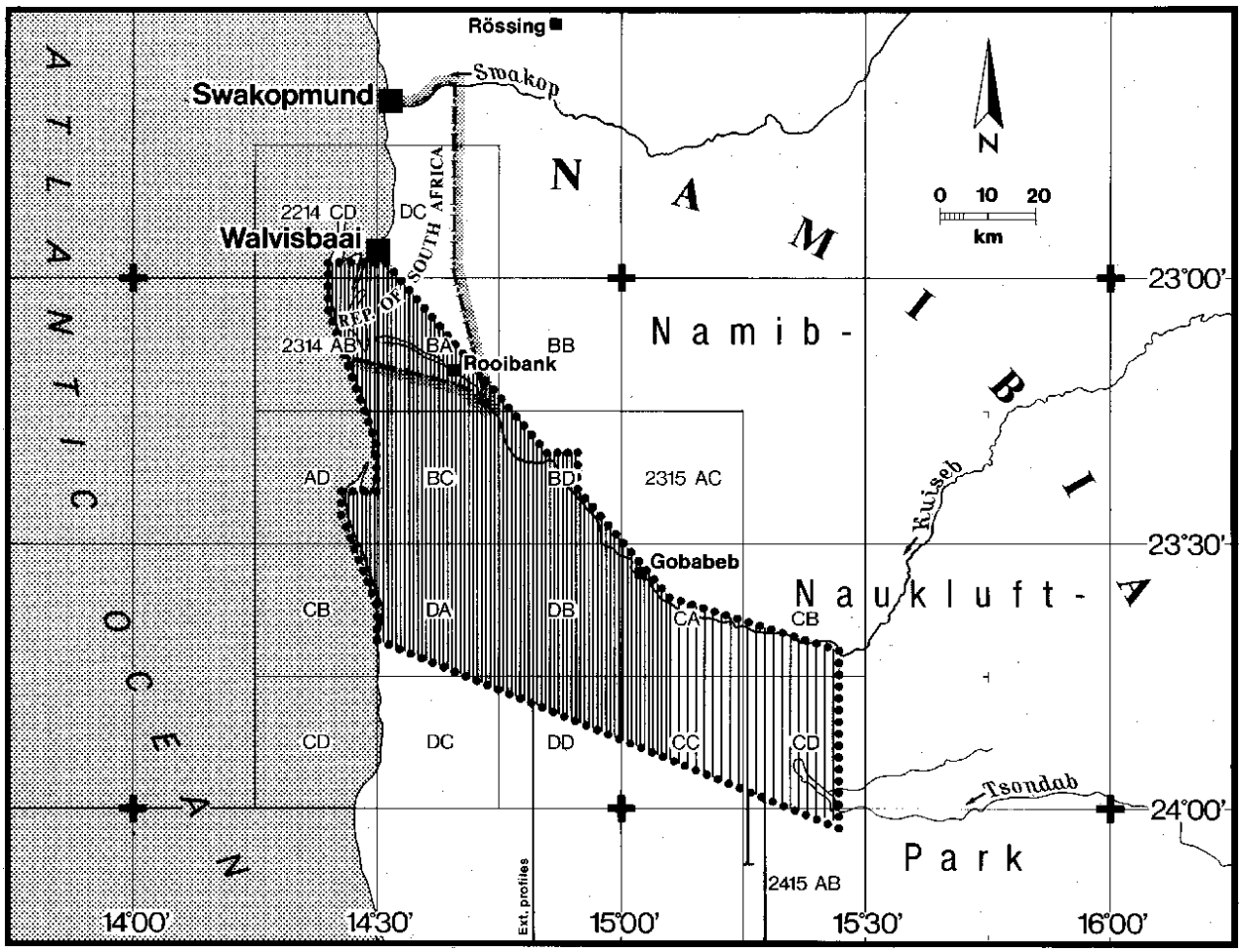

FIG. 6.7: Survey location with a sketch of the flight lines

6.2 Helicopter survey of the Kuiseb Dune Area

The river Kuiseb flows along the northern margin of the Kuiseb Dune Area in Namibia and ends in Walvis Bay (Fig. 6.7). Outcropping basement north of the Kuiseb is covered by up to 200 m of sand and sandstone in the south (Fig. 6.8). On its way, most of the water oozes away and statistically the Kuiseb reaches the sea only once in ten years. Wells along the riverbed make use of the Kuiseb groundwater resource, but part of the groundwater is also known to seep into the dune area and re-emerge on the coast, feeding freshwater lagoons. In 1992, the Kuiseb Dune Area was surveyed by helicopter to identify these seepage paths beneath the sand dunes. The helicopter carried a radiometer, magnetometer and an active 3-channel EM system. 12000 line-km were flown with a line spacing of 0.4 to 1 km and a tie line spacing of 5 to 10 km (Fig. 6.7). EM resistivities indicated some high resistivity fresh water channels. Subsequent drilling confirmed these channels, but fresh water yields were insignificant.

Here, we estimate depth from the magnetic data of the survey by variogram analysis. Two data examples with shallow and deep basement are shown in Figures 6.9 and 6.10,

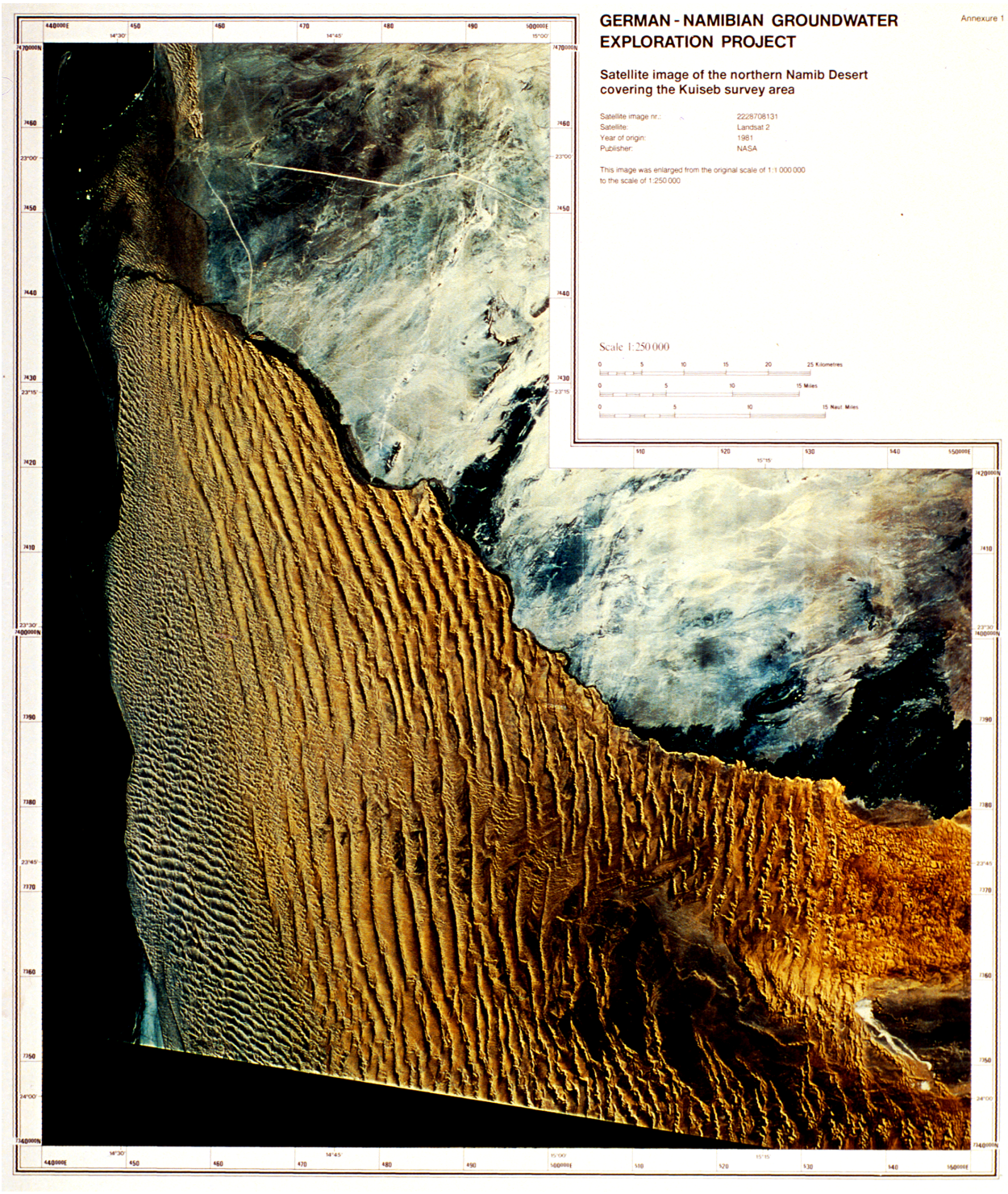

FIG. 6.8: Landsat image of the Kuiseb Dune Area. The dunes encroaching on the river Kuiseb have heights of over 100 meters

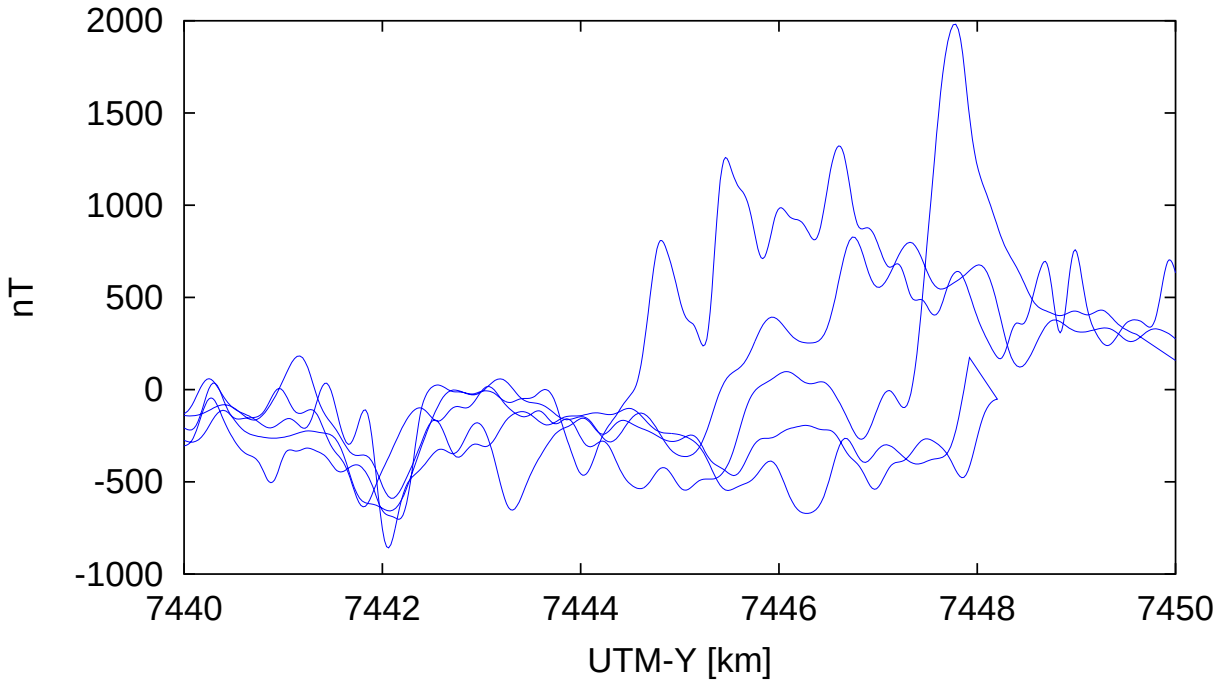

FIG. 6.9: Five adjacent magnetic profiles over an area with outcropping basement. The proximity of the basement is reflected in a rugged appearance of the magnetic field.

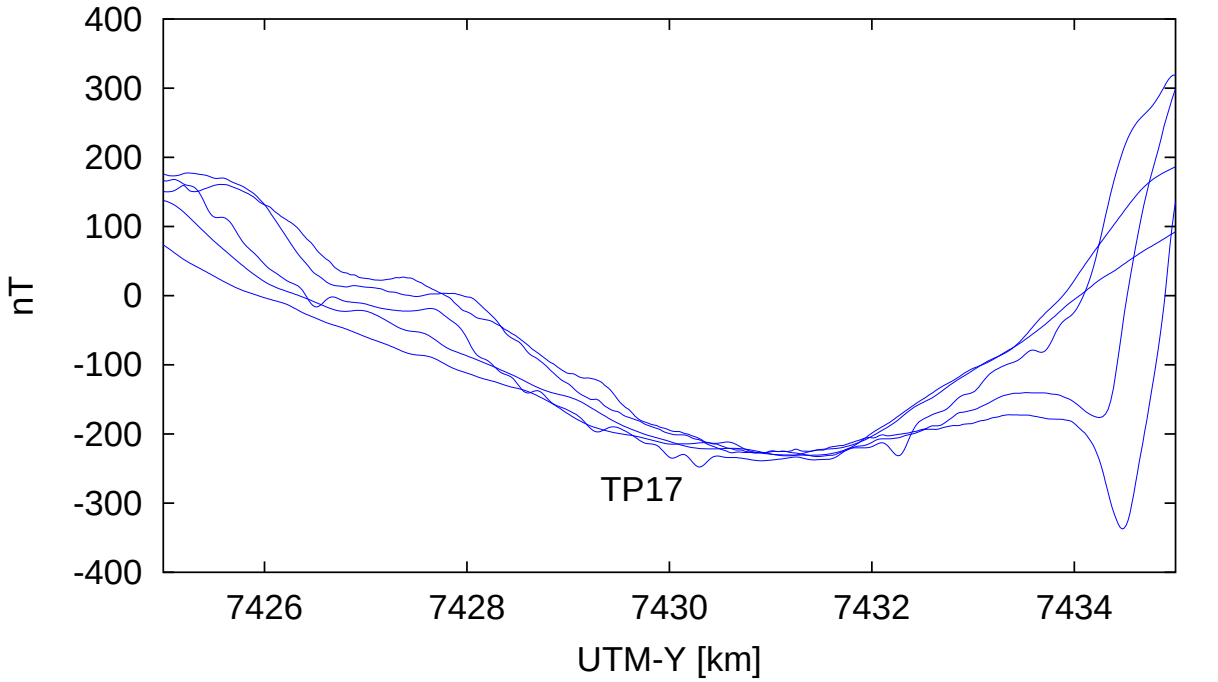

FIG. 6.10: Five adjacent magnetic profiles over an area with deep basement (depth below terrain at test drilling point TP17 around 110 m). The large distance between sources and observation plane leads to a smooth magnetic field.

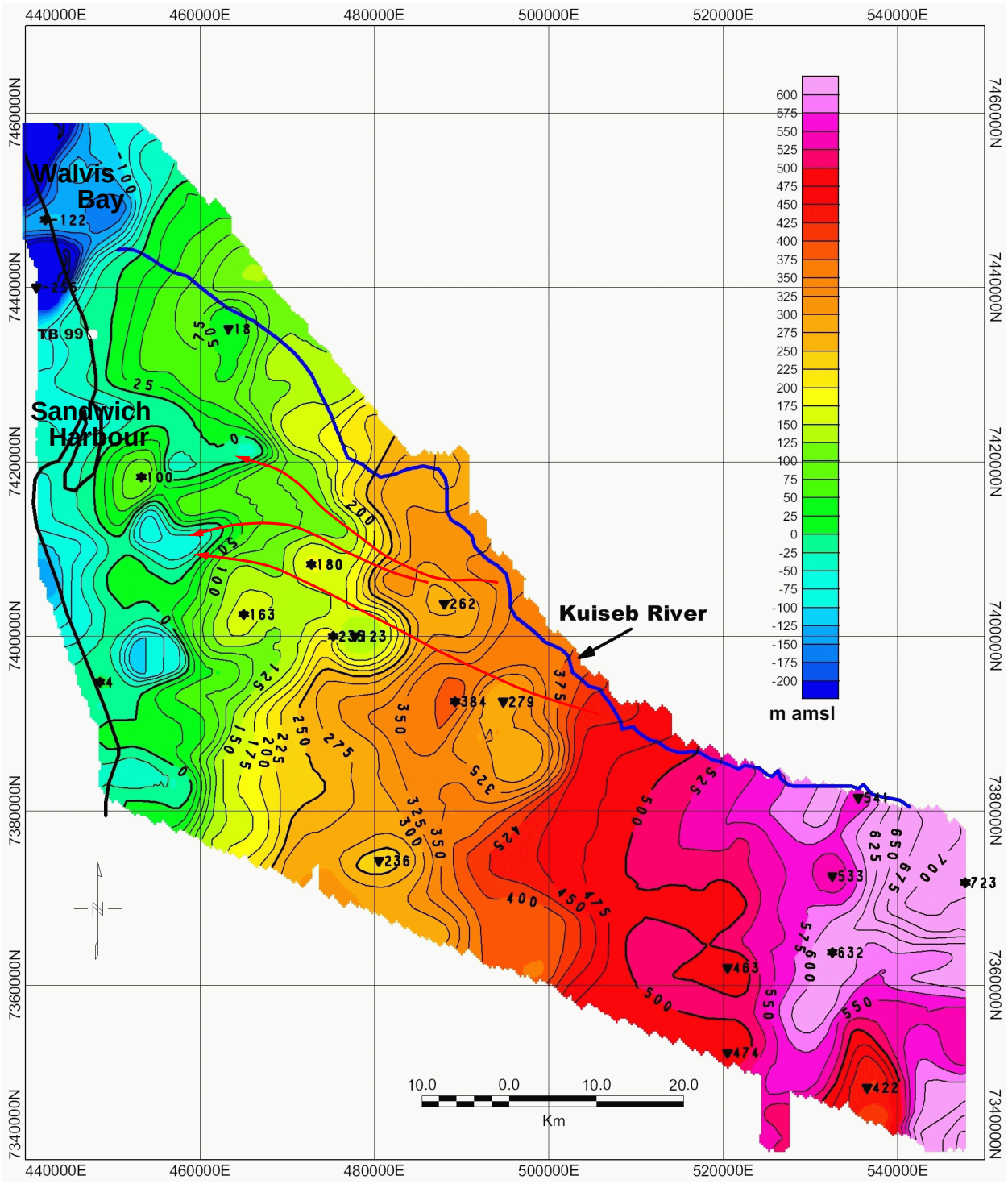

FIG. 6.11: Basement relief estimated using a variogram analysis window size of 4500 m. The relief for the optimum window size of 5400 m has smaller deviations from drilled depth, but shows less detail (see Fig. 6.13). Paleochannels inferred from the map of EM resistivities are shown in red.

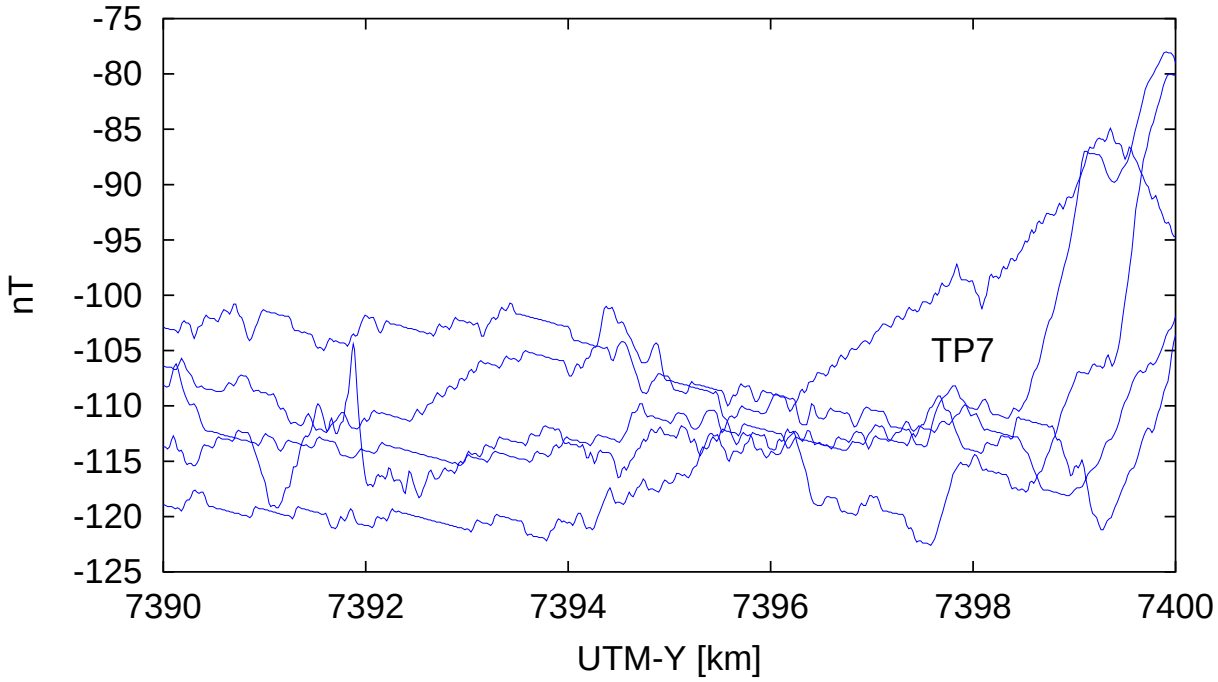

FIG. 6.12: Example of an area with low magnetic signal and high noise (in the order of several nT). At short to intermediate wavelengths the noise is stronger than the signal, which leads to reduced depth estimates (true depth at TP7 is 118 m, estimated to 27 m).

respectively. The estimated basement topography for the entire survey is given in Figure 6.11.

6.2.1 Vertical versus lateral resolution

Variogram analysis of this magnetic data set faces difficulties. The sand dunes of up to 100 m in height are crossed by the survey lines, which were flown at constant terrain clearance (draped survey). Upward continuation to a common reference height is not possible for profile data without making assumptions on the source magnetization. Thus, our observation "plane" actually consists of measurements vertically separated by as much as 100 m, while the depth to be estimated is of the order of 150 m! The presence of instrument noise of up to several nT causes further problems in areas of weak basement magnetization, as illustrated in Figure 6.12

To obtain meaningful depth, large variogram window sizes have to be used. The larger the window, the more accurate the depth estimate. However, this increased accuracy trades off against a decreased lateral resolution of the basement relief. We infer the mean error of the relief from drilled basement depth in 15 locations. Plotting the mean error against the effective window size (Fig. 6.13), we find that accuracy of depth improves up to an optimum window size of 5400 m, i.e. window radius of 2700 m, where the mean relative error is 15% and the absolute error is 25 m. For even larger windows, the increasing accuracy is offset by the decreasing lateral resolution.

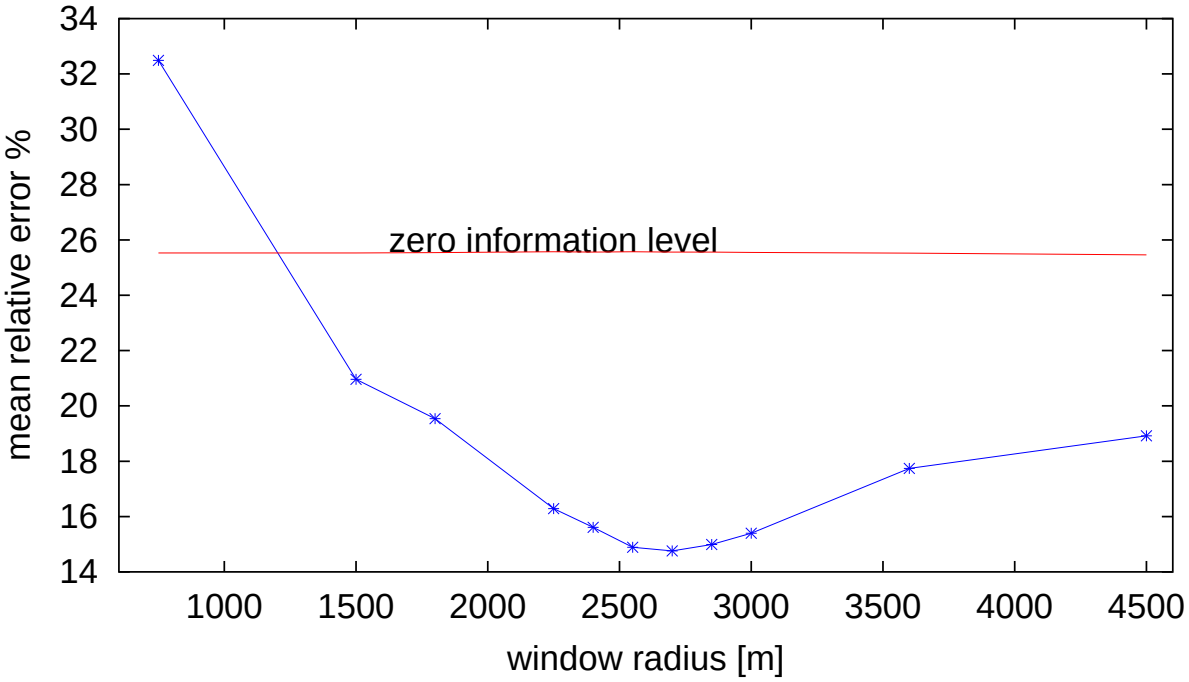

FIG. 6.13: Mean relative error of depth estimates at the drilling locations versus the data window size used in estimating the basement relief. Accuracy of depth increases with the data window radius up to 2700 m. Subsequently, errors increase again due to the decreasing lateral resolution of the relief. Assuming a depth of 150 m below observation level at every drill site gives an unbiased depth estimate with an error of 26%, indicated here as the "zero information level".

Figure 6.11 shows the basement relief for a window size of 4500 m. The large window size required is primarily due to the varying flight altitude above basement. One could try to upward continue the profiles to a reference plane sloping towards the sea. However, this requires assumptions on the source magnetization. In an alternative approach, we discard all data measured above the mean local observation height, shedding 50% of the data. Due to the chopped up profiles, 3/4 of the variograms become incomplete and must be discarded. Consequently, instead of improving, depth estimates deteriorate. Attempts to incorporate the tie lines in a joint inversion also fail to improve the relief. For this purpose the tie line separation would have had to be narrower.

6.3 Discussion and conclusions

Our tests show that variogram analysis depth is unbiased and accurate, subject to certain limitations. Some of these limitations are common to other methods as well.

6.3.1 Conclusions from the synthetic modeling

Comparing variogram depth with true model depth we conclude that

1. the effective data analysis window size must be at least 10-20 times larger than the depth to be resolved

2. topographic features are reliably identified only if they are larger than the window size (Figs. 6.1, 6.3)

3. for rugged basement topography, estimated depth is about half-way between the mean and the minimum depth to basement (Fig. 6.5)

4. due to the inherent non-uniqueness of the magnetic inverse problem, a 0.5 uncertainty in β (which is rather high) leads to a 20% uncertainty in absolute depth

5. a sediment magnetization up to two orders of magnitude less than the basement magnetization does not disturb depth estimates (Fig. 6.6)

6. depth estimated from profiles along constant basement depth is more accurate than from profiles across topography. Hence, flight lines should be aligned with topographic trend to avoid topographic anomalies. Tie lines should be flown dense enough to be useful as an additional source of statistical information. In particular, joint inversion of wide spaced bi-directional profiles gives more accurate depth than a dense equi-directional set of survey lines (Figs. 6.1, 6.3).

6.3.2 Discussion of the Kuiseb Dune Area survey

Variable dune topography and high instrument noise make it difficult to estimate the basement relief from the Kuiseb Dune Area magnetic data. The absolute error of around 25 m against drilled depth is likely to be even larger at the survey boarders, where the analysis window is only half covered with data. While basement depths of 100 m found for Walvis Bay are realistic, the strong gradient to even greater depths in the West is not. The fresh water channel feeding the wetland at Sandwich Harbour has been identified correctly. Presumed troughs along the coast roughly agree with areas of high EM resistivity. It would be interesting to verify the existence of these troughs by drilling.

Most likely, depth estimates would have been more accurate if survey lines had followed the dune valleys and more tie lines had been flown.

6.3.3 A recommendation for aeromagnetic survey design

Our synthetic modeling shows that the information in tie lines could significantly improve depth estimates, provided that the tie lines are not spaced too far apart. In fact, for basement depth estimation, flying a regular mesh would probably give the optimum accuracy at least cost.

Chapter 7

Improved ocean geoid resolution from retracked ERS-1 satellite altimeter waveforms*

Since the publication of the first satellite gravity maps (Haxby et al., 1983; Rapp, 1983), spatial wavelength resolution of satellite gravity has improved considerably, primarily due to the denser track spacing of 6 km and 8 km at the equator during the geodetic missions of Geosat (1985-1990) and ERS-1 (1991-1996), respectively. Satellite gravity is computed by geodetic Fourier methods (Schwarz et al., 1990) from gridded geoid profiles (Haxby et al., 1983) or vertical deflection of geoid (Sandwell and McAdoo, 1990). See Olgiati *et al.* (1995) for a comparison of the two methods. A detailed description of marine gravity mapping from satellite altimetry is given by Sandwell and Smith (1997). Satellite altimeters measure mean sea surface height, which is controlled primarily by the Earth's gravity field, but is also subject to tides, ocean currents and atmospheric effects. In satellite gravity these secondary effects are regarded as noise. After applying various corrections, the sea surface heights serve as estimates of the ocean geoid.

Resolution of along-track geoid profiles can be defined as the wavelength at which the mean square coherence between two exact repeat tracks falls to below 0.5 (Marks and Sailor, 1986). With this definition along-track geoid resolution has improved from 110 km for 1975-1978 Geos-3 data to 50 km for 1978 Seasat data (Marks and Sailor, 1986). In a detailed study of along-track geoid resolution, Yale and Sandwell (1995) find a global average resolution of 38 km and 43 km for pre-edited Geosat and ERS-1 data, respectively. Along-track resolution can be improved to below 30 km by stacking corresponding tracks of the exact repeat missions (ERM), called multi-disciplinary phase for ERS-1. However, the ERM have a track spacing of 164 km (Geosat) and 80 km (ERS-1) which is too wide for high resolution gravity mapping. During the geodetic missions, on the other hand, tracks are not repeated and it is essential to extract as accurate geoid information as possible from every recorded track. This can be

*Published in *Geophysical Journal International* (Maus, Green and Fairhead, 1998)

achieved by reprocessing the raw radar waveform data.

After outlining the basic principles of satellite radar altimetry, we propose a simplified waveform model to improve tracking. Instead of tracking individual travel times, we process a whole sequence of waveforms simultaneously, using a polynomial spline to represent the geoid. To separate geoid signal from noise, one requires a spectral model for the true geoid. Using a relationship between geoid and gravity, we infer the geoid spectrum from large scale land and marine gravity grids. The expected spectrum of the true geoid is then utilized to constrain the smoothness of the spline geoid solutions, thus suppressing noise already at the tracking stage. We tested the algorithm on 3 repeat cycles of the ERS-1 ERM. Coherencies indicate a significant improvement in along-track resolution, in particular for rough sea states.

7.1 Basic principles

After correcting for tides and currents, as far as possible, sea surface height provides an estimate of the ocean geoid N which is related to the gravity potential V by Brun's approximate formula

$$V(x, y, 0) = g_0 N(x, y), \tag{7.1}$$

where g_0 is the normal gravity acceleration. Satellite altimeters are able to measure the sea surface height by sending down radar pulses that are reflected at the sea surface and recorded back on-board the satellite. Since the satellite's smooth orbital path and position is known accurately at any instant, the sea surface topography relative to a reference ellipsoid can be determined. The distance between satellite and sea surface is referred to as range. The range must be measured to an accuracy of centimeters in order to derive geoid anomalies down to wavelengths of 20 km and less.

The energy of the radar pulse reflected from the sea surface does not return to the satellite as a sharp pulse, but is scattered over a considerable period of time. The power of the return signal as a function of time is called a waveform. The waveforms are sampled in 3.03 nanosecond intervals (gates) corresponding to 45 cm in range. Examples of waveforms resulting from calm and rough sea are displayed in Figure 7.1. This figure shows the change in the waveform shape from impulsive to emergent. The ERS-1 satellite transmits 1020 radar pulses per second. 51 consecutive returns are averaged on board the satellite and transmitted to the receiver stations as 20 average waveforms per second, or one every 330 m along-track. On reaching the sea surface, the radar pulse has an effective geodetic footprint between 2 and 7 km, depending on the sea state. Energy reflected at the center of the footprint returns to the satellite earlier than energy reflected at the edges of the footprint. The power of the returning pulse therefore increases from zero to some maximum value over a time interval of about 6 to 60 nanoseconds. This period is referred to as the leading edge. The travel time is

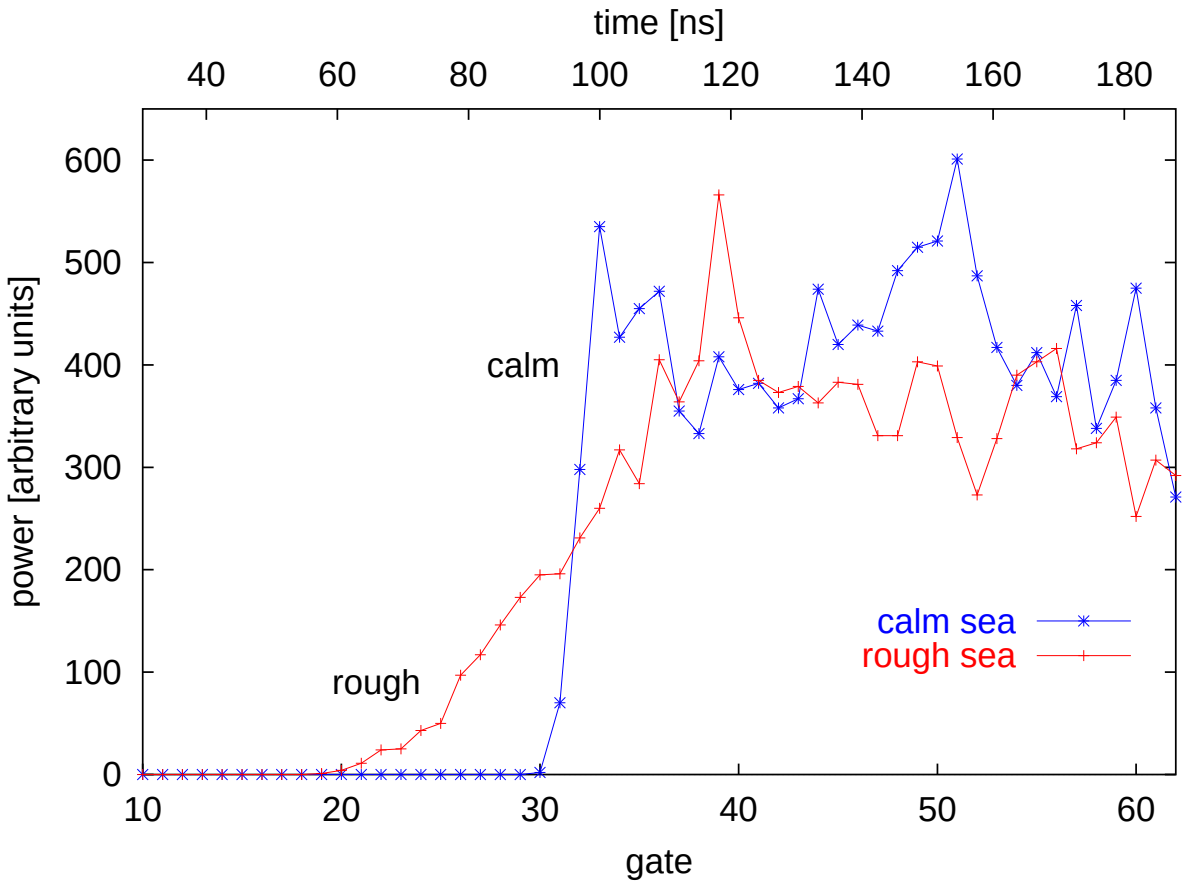

FIG. 7.1: Examples of ERS-1 return radar waveforms for calm (wave height less than 1 m) and rough sea (mean wave height 11 m). The two waveforms differ in the slope of the leading edge as well as in overall amplitude.

the time to the center of the leading edge. The steeper the leading edge, the more accurately the center time of the leading edge can be estimated. The slope of the leading edge depends not only on the diameter of the footprint but also on the roughness of the sea. The calmer the sea, the steeper the leading edge. The subsequent decrease in power is referred to as the trailing edge. The slope of the trailing edge is correlated with the surface wind speed.

7.2 Standard waveform analysis

ERS-1 satellite altimeter products currently used by the Geoscience community are derived from on-board estimates of the return travel time. The ERS-1 on-board tracker uses a model of the return waveform due to Brown (1977). Apparently, it had been planned to reprocess the waveforms later (Tokmakian et al., 1994) using an algorithm of Challenor and Srokosz (1989). The on-board tracking algorithm is based on a waveform model accounting for three waveform parameters: the return travel time, the significant wave height, and the backscattered power (related to the surface wind speed). Each waveform is analyzed separately. The 20 Hz travel time estimates are combined to 10 Hz semi-elementary and

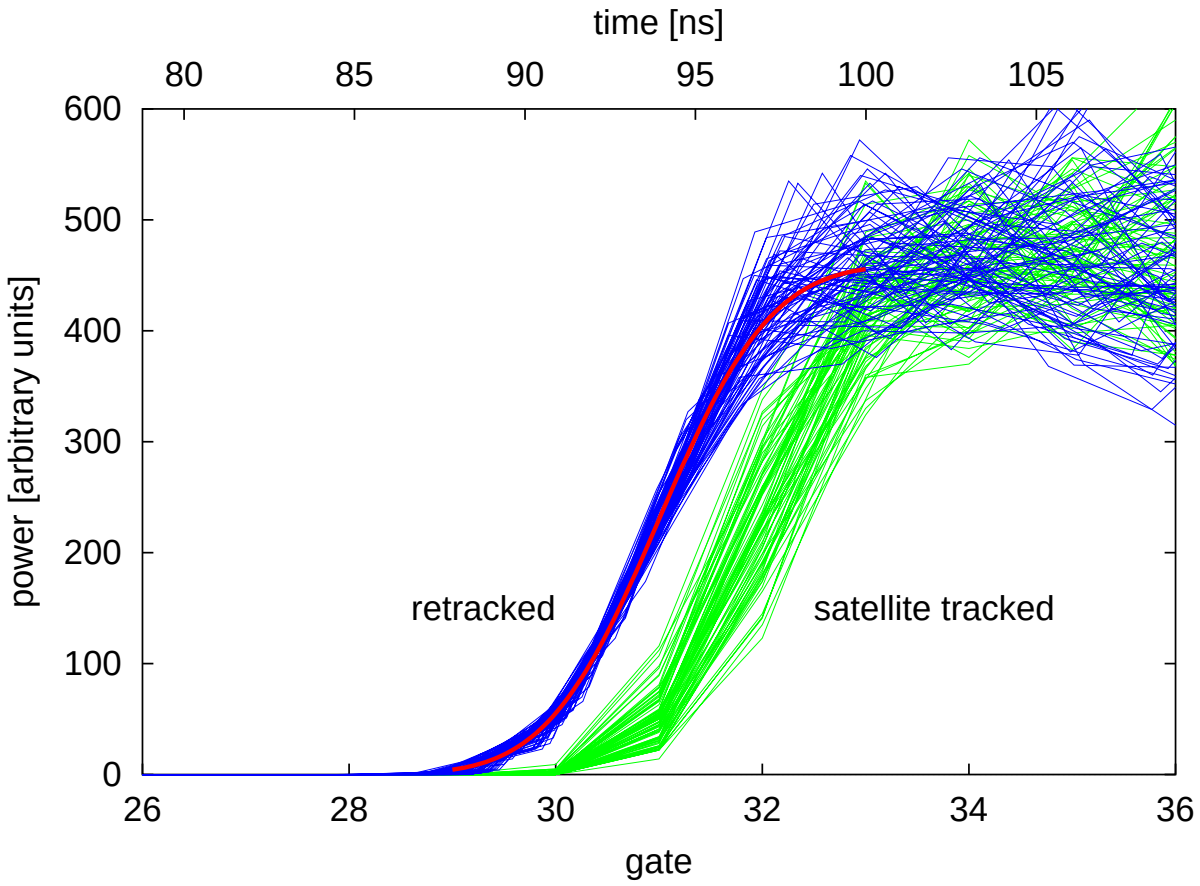

FIG. 7.2: Tracking is equivalent to locating the center position of the leading edge. The performance of a tracking algorithm can be verified by aligning the waveforms in such a way that the estimated center of the leading edge is at a fixed gate (here gate 32 for OPR and gate 31 for this study retracks). The superior quality of the retracked travel times leads to a significantly reduced variance of the waveforms at the leading edge. Here, 80 consecutive waveforms (4 seconds of data) are displayed. The model of equation 7.2 is indicated in red.

1 Hz averages. After applying tidal and atmospheric corrections, these are the European Space agency (ESA) *ERS-1 Ocean Product* (OPR) geoid solutions incorporated in current satellite gravity maps.

7.3 Improved travel time estimates from retracking

For the purpose of estimating geoid height, the only waveform parameter of interest is the return travel time. Travel time estimates can be optimized by concentrating on the exact location of the leading edge. Without attempting to explain the full shape of the waveforms, we re-align the waveforms using a simplified waveform model M with

$$M(amp, \sigma, \tau; t) = \frac{amp}{2}[1 + \mathrm{erf}(\sigma(t - 31 + \tau))], \tag{7.2}$$

where amp is the amplitude of the waveform, σ controls the slope of the leading edge, τ is the center time (lag) of the leading edge, t is the time along the waveform and erf is the error

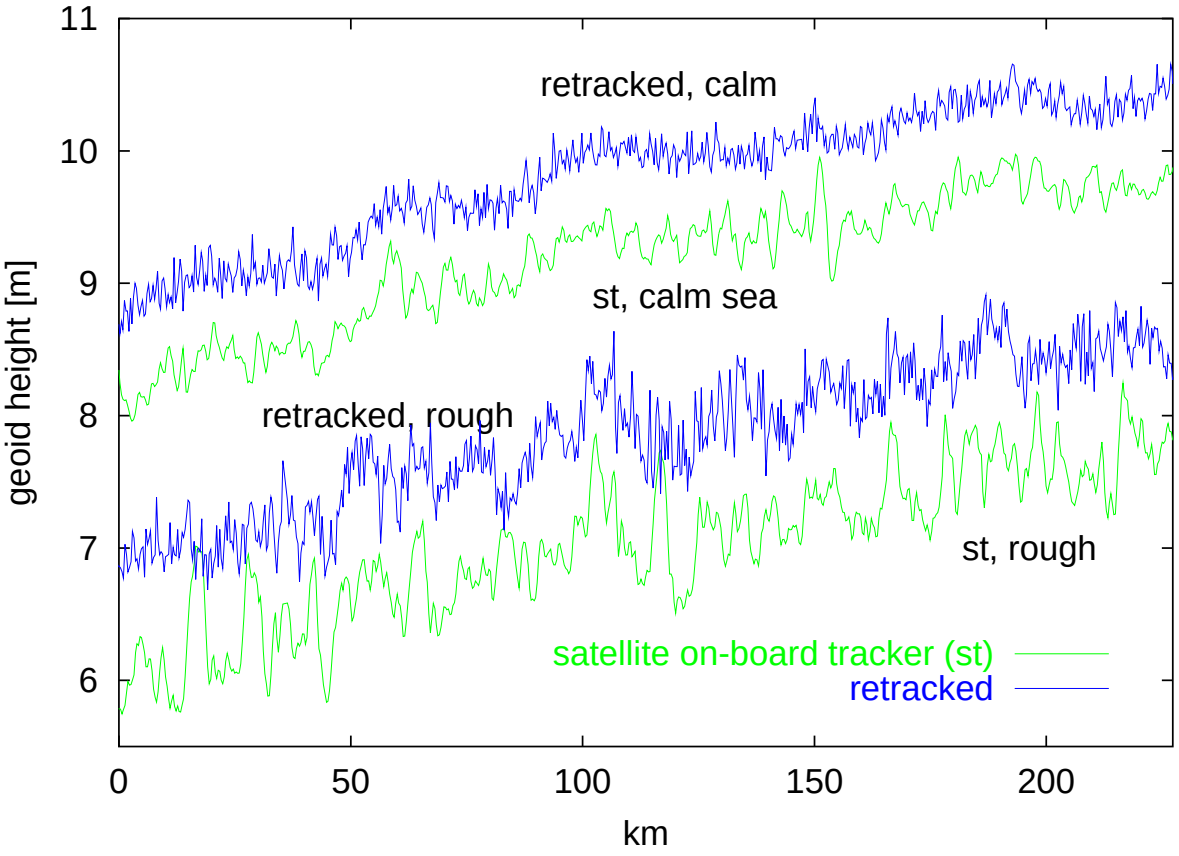

FIG. 7.3: Satellite on-board tracker (st) versus retracked geoid heights for two repeat tracks with calm and very rough sea conditions from a low-signal-high-noise area (45^o S, 130^o E) in the southern Pacific Ocean. Retracking significantly reduces the noise at intermediate wavelengths. This is particularly obvious for the calm sea track. Offsets have been added to separate the signals for clarity.

function. Both τ and t are measured in gates, and can be non-integer valued. An example of this model curve is shown as a dashed line in Figure 7.2.

7.3.1 Misfit function

To find the optimum center positions τ_k of a sequence of nw waveforms $W_k(t)$, with $k = 1..nw$, we use an L_2-Norm misfit function E with

$$E(amp, \sigma, \tau_1, ..., \tau_{nw}) = \sum_{k=1}^{nw} \sum_{i=mingate}^{maxgate} \left[\frac{W_k(i) - M(amp, \sigma, \tau_k, i)}{W_k(i) + offset} \right]^2 . \quad (7.3)$$

The smaller the chosen value of $offset$, the more significance is placed on the lower front of the leading edge. With amplitudes around 400, a value of $offset = 50$ produces good results. $Mingate$ and $maxgate$ have to be chosen in such a way as to include precisely the full leading edge, taking into account its varying center position and slope.

7.3.2 Inversion

We find the minimum of the misfit function in equation (7.3) by a modified Gauss-Newton algorithm, using the analytical first and second derivatives of $E(amp, \sigma, \tau_1, ..., \tau_{nw})$. We rescale the parameters amp and σ by $\sigma' = \ln \sigma$ and $amp' = (amp + amp_{offset})/amp_{factor}$ so that amp' and σ' have an expected value of zero at the solution and a unit perturbation leads to an equal change in the misfit function for all parameters. The optimization for a sequence of nw waveforms yields return travel time corrections $\tau_1..\tau_{nw}$ which are added onto the OPR return travel times. The improvement in the corresponding ranges is demonstrated in Figure 7.2, which shows a sequence of consecutive waveforms, normalized on the OPR estimate of the waveform onset. The retracked waveforms show a significant decrease in scatter.

Figure 7.3 shows the improved quality of retracked geoid height estimates. Nevertheless, retracking alone does not completely remove the high frequency noise. This noise is due to the uncertainty of tracking waveforms which are sampled at a bin width of 3.03 ns, corresponding to 45.45 cm in range. To reduce this high frequency noise, the practice until now has been to compute 1 second averages of the 1/20 second range estimates. However, the resulting 1 Hz ranges (e.g. Figure 7.9) are still noisy and have to undergo further low pass filtering before they can be used in subsequent processing stages. The Ocean Product (OPR) also provides 10 Hz semi-elementary averages, which are sometimes used instead of the 1 Hz averages.

Instead of filtering the 20 Hz range estimates, we suppress noise already at the tracking stage. This is achieved by using splines to model the geoid and by imposing smoothness constraints on the polynomial coefficients of the spline.

7.4 Spline geoid solution

Instead of estimating travel times from individual waveforms, we invert a 20 second sequence (132 km window) of 408 waveforms simultaneously. The k'th radar pulse (actually 51 pulses) was reflected from the sea surface at utc_k universal time. The time stamp utc_k can be translated to the exact location of the satellite. Let y_k be the corresponding (unknown) true geoid height. Then y_k can be expressed as a geoid polynomial with respect to universal time utc_k as

$$y_k = \sum_{j=0}^{n} a_j T_j(utc_k), \tag{7.4}$$

where T_j are the base polynomials of order j, n is the maximum order and a_j are the coefficients of the polynomial. We utilize $T_j(x) = \cos jx,\ x \in [0, \pi]$ as base polynomials, up to an order of $n = 40$. With a window size of 132 km we are thus able to represent wavelengths down to 6 km, corresponding to the approximate across-track resolution of

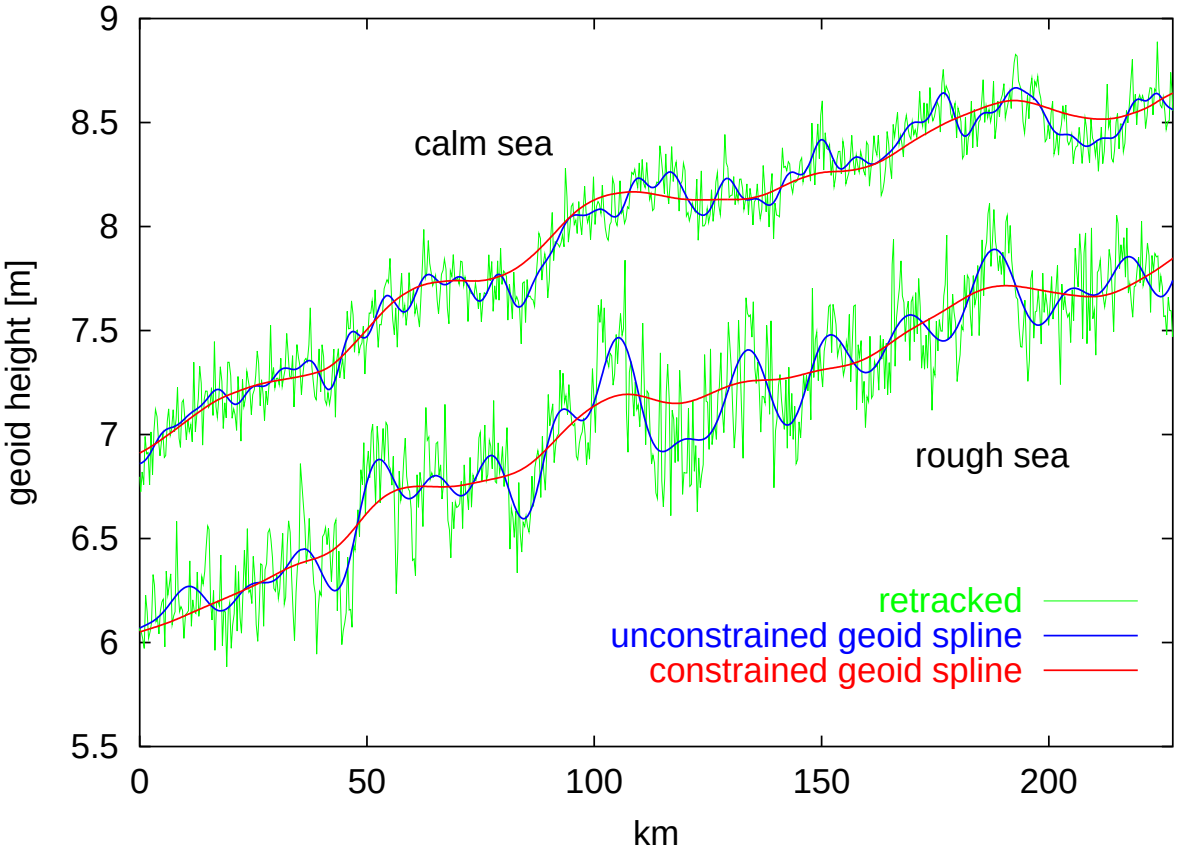

FIG. 7.4: Spline geoid solutions superimposed on the retracked geoid height estimates for two repeat tracks. Offsets have been added to separate the two tracks for clarity. Fitting an unconstrained polynomial directly to the retracked heights leads to unwanted oscillations in the geoid solution. These oscillations can be removed by imposing a penalty for high power in high order polynomial coefficients and fitting the thus constrained polynomial directly to the waveform data. It is important to understand that the polynomial is not fitted to the retracked travel times. Instead, the original waveforms are processed using a polynomial as a continuous geoid model. Thus, we estimate 41 geoid polynomial coefficients instead of 408 individual travel times in each window. Polynomials in overlapping windows are combined to a spline geoid solution.

combined Geosat and ERS-1 data. The 6 km cutoff is clearly visible in the spline spectrum of Figure 7.5.

The geoid height y_k to be estimated is related to the OPR range z_k by

$$y_k = alt_k - z_k + (3.03ns \cdot c \cdot \tau_k)/2 \tag{7.5}$$

where alt_k is the altitude of the satellite above the reference ellipsoid, c is the speed of light and τ_k is the lag correction of the k'th waveform, measured in gates of 3.03 nanoseconds. This gives an expression

$$\tau_k(a_0, ..., a_n) = \frac{2}{3.03ns \cdot c}\left[z_k - alt_k + \sum_{j=0}^{n} a_j T_j(utc_k)\right] \tag{7.6}$$

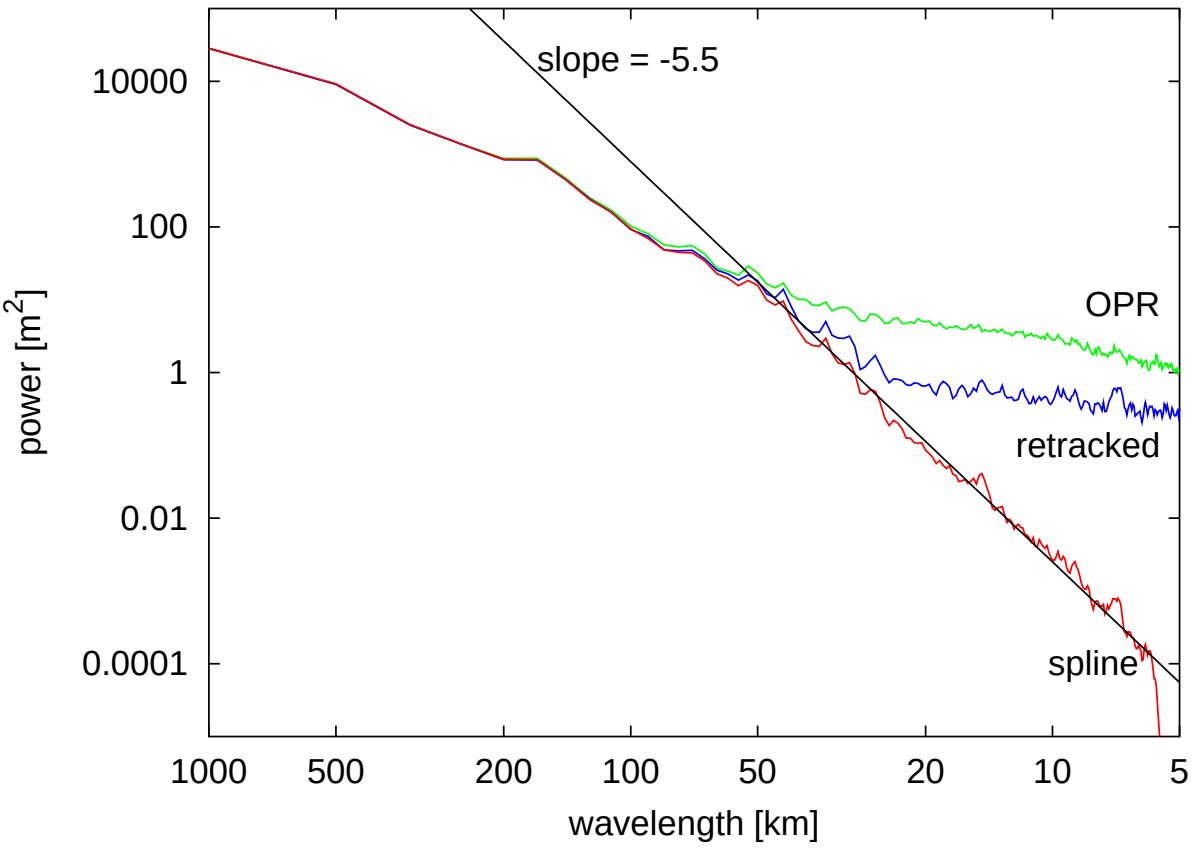

FIG. 7.5: Power spectra of along-track geoid solutions estimated using a 1140 km window. The line with a slope of -5.5 depicts the expected power spectrum of the true geoid at short wavelengths. Noise begins to dominate the *Ocean Product* geoid already at wavelengths around 50 km. As reflected in these power spectra, this noise can be reduced significantly by retracking the waveforms. A truly realistic geoid solution can be obtained by using a polynomial spline and imposing spectral constraints on the polynomial coefficients in the inversion.

relating the lag corrections of the waveforms to the coefficients of the geoid polynomial of equation (7.4). In the previous section, equations (7.2) and (7.3) were utilized to compute lag corrections for the OPR return travel times. Substituting $\tau_k(a_0, ..., a_n)$ of equation (7.6) for τ in equation (7.2) and using the same misfit function of equation (7.3), we can now optimize 41 geoid polynomial coefficients a_j instead of 408 individual waveform lags τ_k. The optimum lags τ_k can then be computed from the optimum coefficients $a_0, ..., a_n$ using equation (7.6). For the optimization, the coefficients again have to be rescaled in order to have an expected value of zero near the solution, which is achieved by a simple linear transform. For 408 waveforms and a polynomial of degree 40, the modified Gauss-Newton algorithm converges within 5 to 8 iterations. Solutions in adjacent windows are combined to a spline geoid solution.

One of the advantages of this approach is that spectral constraints can be imposed in

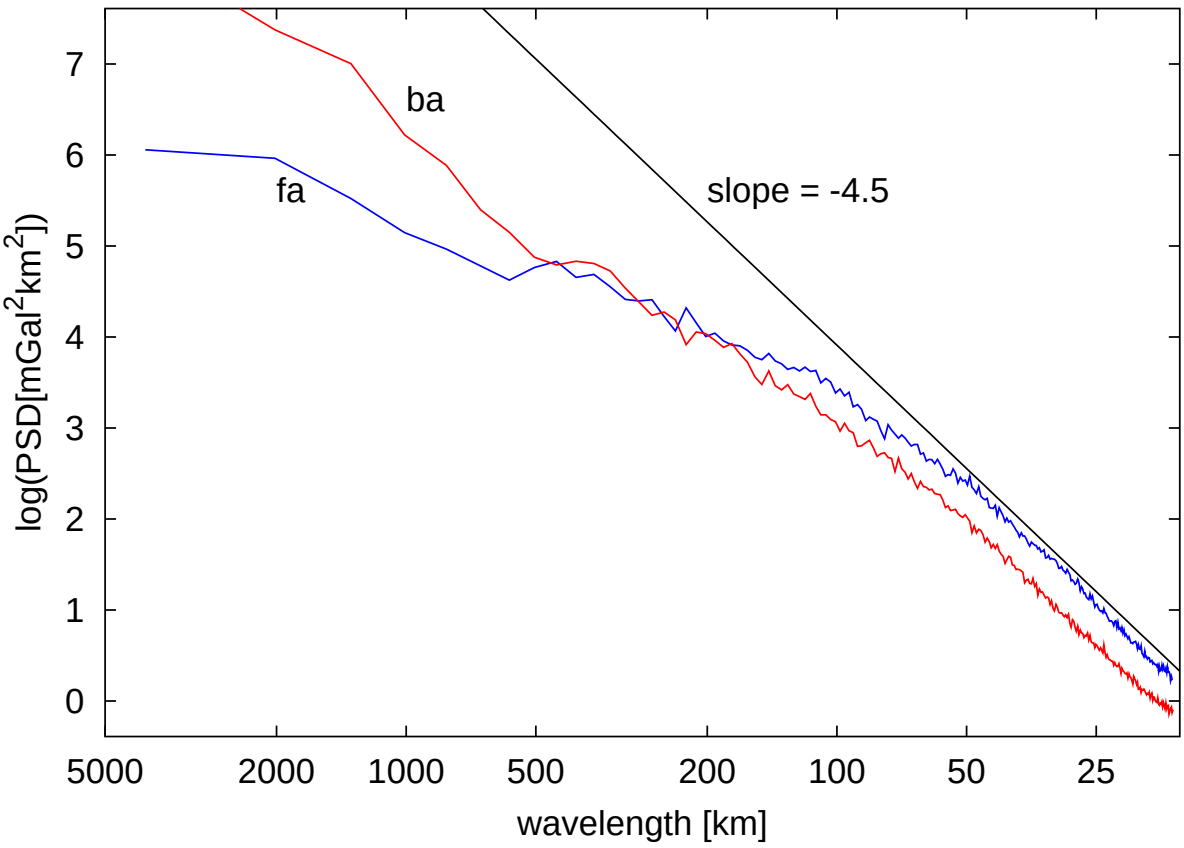

FIG. 7.6: Sample power spectra for 8 km free air (fa) and Bouguer anomaly (ba) grids of a 4000 x 4000 km^2 area covering the Siberian Craton. Grids in Lambert Conformal projection. Due to the absence of topographic anomalies, Bouguer has less power at short wavelengths than free air gravity. However, starting at about 50 km wavelength, isostatic compensation reduces the power in long wavelength free air gravity anomalies. It is interesting to note that both power spectra run parallel at short wavelengths and, hence, have the same scaling exponent of ~ 4.5.

the optimization on the coefficients of the spline. If no constraints are imposed, the geoid solution is smooth but tends to oscillate (Fig. 7.4). The corresponding power spectrum of the along-track geoid (Fig. 7.5) has the typical curved shape of gravity power spectra at long wavelengths (see Figure 7.6 and discussion in the following section), but turns white (=noisy) towards short wavelengths. For a realistic geoid the spectrum should continue decreasing with a slope that can be determined from non-satellite gravity grids as follows:

7.5 Expected power spectrum of the true geoid

A spectral model for the geoid can be inferred from the power spectra of free air gravity data. Let us assume that the statistical properties of free air gravity over land (for which large, accurate grids are readily available) are comparable to those of ocean gravity. Figure 7.6

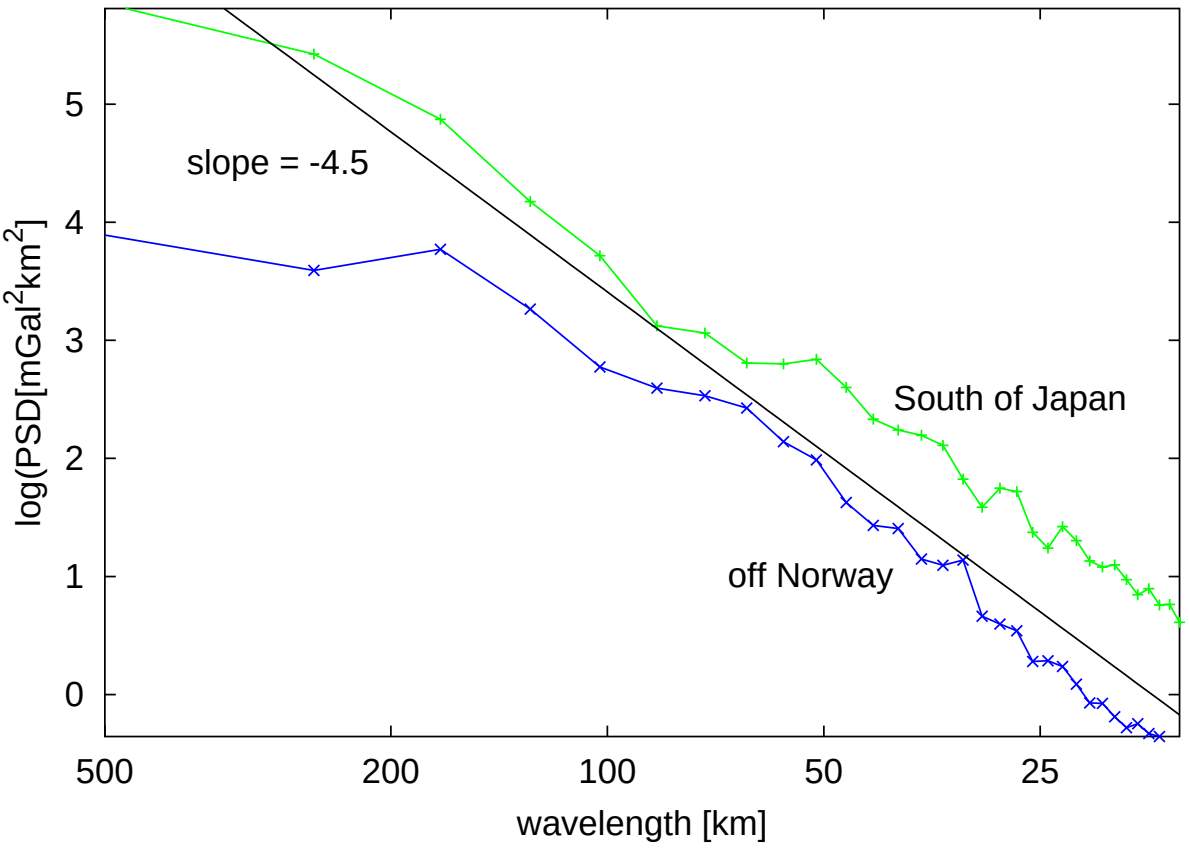

FIG. 7.7: Marine gravity power spectra for 8 km grids in Lambert Conformal projection covering two areas of approximately 320 x 320 km^2 south of Japan and off the coast of Norway.

shows the free air and Bouguer gravity power spectra of a 4000 x 4000 km^2 area of the Siberian Craton in log-log scale. Starting at short wavelengths (right), both power spectra increase towards long wavelengths (left) with a steady slope of 4.5, indicating self-similarity of the gravity field with a scaling exponent of $\gamma_g^{2D} = 4.5$. Here, the index "2D" indicates that this is the scaling exponent of the 2D power spectrum, which is different from the 1D power spectrum of profiles of the same data-set (Maus and Dimri, 1994). The scaling exponent governs the overall smoothness of a random function. High values indicate a smooth function, whereas low values indicate roughness. *White noise* has a scaling exponent of zero.

It is interesting to note that at short wavelengths free air and Bouguer gravity follow the same scaling law, reflected in equal scaling exponents. The self-similarity of the gravity field is probably due to a self-similar density distribution in the Crust (Pilkington and Todoeschuck, 1990; Maus and Dimri, 1996) combined with self-similar topographic anomalies (Chapin, 1996). Above wavelengths of around 50 km the slope of the power spectrum decreases, indicating a reduced power for long wavelength gravity anomalies. This is probably due to isostatic compensation of topography (Chapin, 1996), but could also indicate a limited depth

extent of source, as has been shown for magnetic power spectra (Chapter 3).

A power spectrum similar to Figure 7.6 can be found in Chapin (1996, Figure 3) for the free air gravity grid of South America produced at the University of Leeds. It has a slope of around 4.7 at wavelengths below 100 km. Maus and Dimri (1996) find a scaling exponent of 4.6 for the Bouguer gravity of the Paradox Basin Salt Anticline Region in Utah. These values of 4.5, 4.7 and 4.6 are fairly consistent, leading us to the conclusion that the gravity field over land has a scaling exponent of $\gamma_g^{2D} \approx 4.5$, be it free air or Bouguer.

7.5.1 Scaling exponent of ocean gravity

To investigate, whether the same scaling law applies to ocean gravity, we have analyzed two 8 km marine gravity grids, one off the Norwegian Coast and one south of Japan. With side lengths of around 320 km the grids are much smaller than the ones for land gravity. Consequently, their power spectra are less accurate. Nevertheless, they confirm a scaling exponent of around 4.5 for ocean gravity (Fig. 7.7). Hence, it seems that there is no fundamental difference in the smoothness of land and marine gravity fields.

From the scaling exponent of gravity one can derive the scaling exponent of the along-track geoid as follows: With a scaling exponent of gravity γ_g^{2D}, the scaling exponent of the gravity potential is $\gamma_V^{2D} = \gamma_g^{2D} + 2$ (Maus and Dimri, 1994). With Brun's formula (7.1) the scaling exponent of the geoid is approximately equal to the 2D scaling exponent of the gravity potential. Furthermore, using the general relationship $\gamma^{1D} = \gamma^{2D} - 1$ we get $\gamma_{geoid}^{1D} \approx \gamma_g^{2D} + 1$. Hence, in a first approximation, the spectrum of the along-track geoid in log-log scale is expected to decrease with a slope of around 5.5 towards short wavelengths. This can be utilized as additional information in the waveform retracking.

7.6 Enforcing a realistic geoid solution

The aim of this study is to improve the accuracy of geoid solutions derived from sea surface height measurements. These geoid solutions are contaminated by two sources of noise. Beside the error in sea surface height due to instrument error and atmospheric effects, the deviation between sea surface height and geoid due to ocean dynamics is also noise in the context of this study. Here, any deviation of a geoid solution from the true geoid is referred to as *noise*, be it due to instrument error, ocean currents or imperfect tidal models.

Figure 7.5 shows the power spectrum of along-track geoid solutions for the Atlantic Ocean. At wavelengths smaller than 50 km the *Ocean Product* turns *white* due to high frequency noise. In contrast, the retracked geoid solution turns white only at wavelengths shorter than 30 km. The conventional way to deal with this noise is to average and filter the along-track geoid heights until they have the desired power spectrum. Hence, an optimum travel time is picked from each waveform, the travel times are converted to geoid heights and finally the

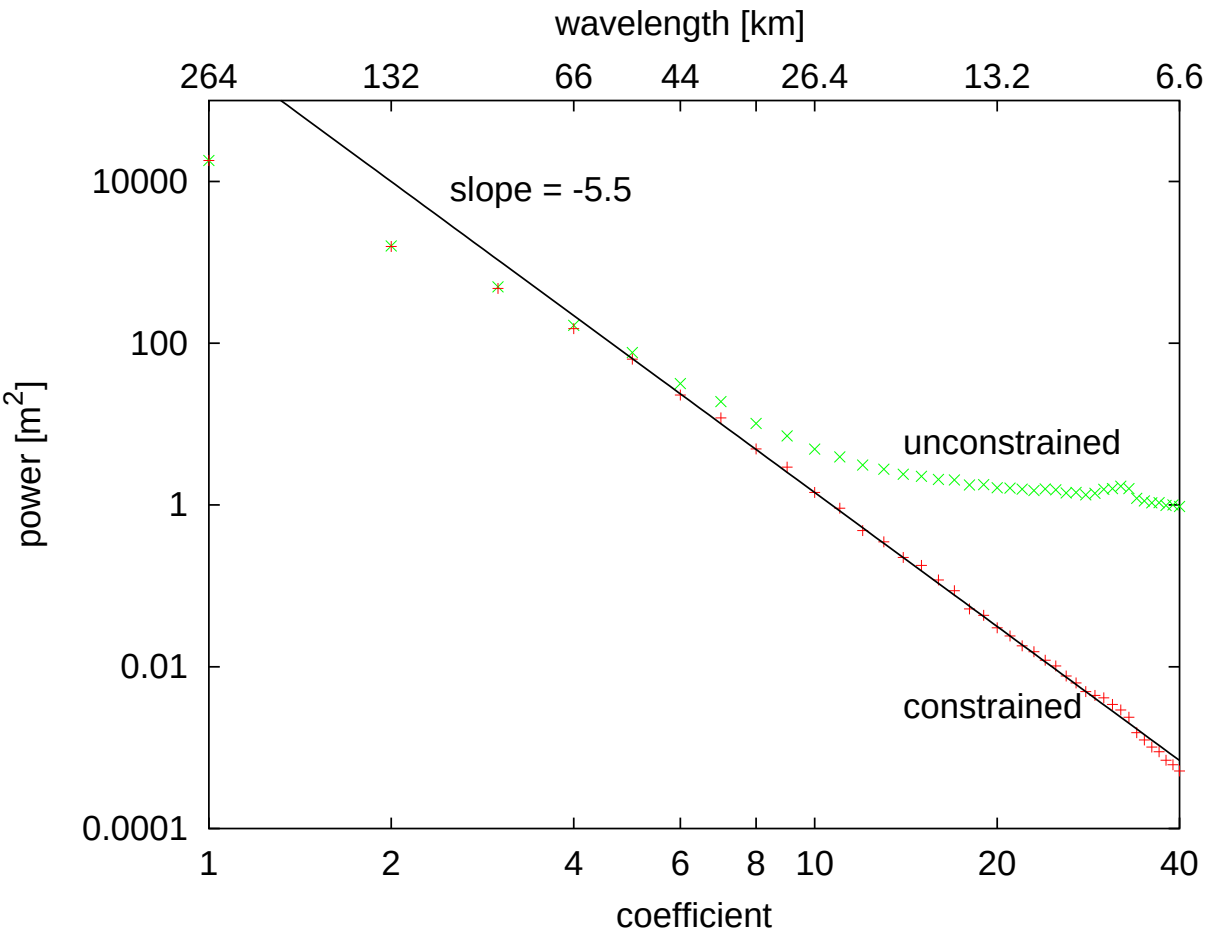

FIG. 7.8: Power spectra of polynomial coefficients. The smoothness of spline geoid solutions can be controlled via the power spectrum of its polynomial coefficients. A realistic geoid power spectrum decreases with a slope of approximately -5.5 towards high coefficients.

heights are filtered. The disadvantage of this approach is that the uncertainty of each pick, which also constitutes an important source of information, is lost prior to the filtering stage. To extract maximum information from the measurements, a realistic geoid model has to be fitted directly to the waveform data. As argued above, the power spectrum of a realistic geoid decays with a slope of approximately 5.5 towards high wavenumbers in log-log scale.

7.6.1 Penalty for oscillating solutions

To enforce a steady slope of 5.5 at short wavelength powers, we introduce a penalty for spline solutions with high power in high order polynomial coefficients (= short wavelengths). This penalty is added to the misfit function in order to increase the misfit for oscillating solutions. It can vary depending on sea condition to prevent over-damping of calm sea data. We add a simple penalty to the misfit function of equation (7.3), given by

$$E' = E + damp \cdot \sum_{j=0}^{n} a_j^2 \; j^{\alpha}, \tag{7.7}$$

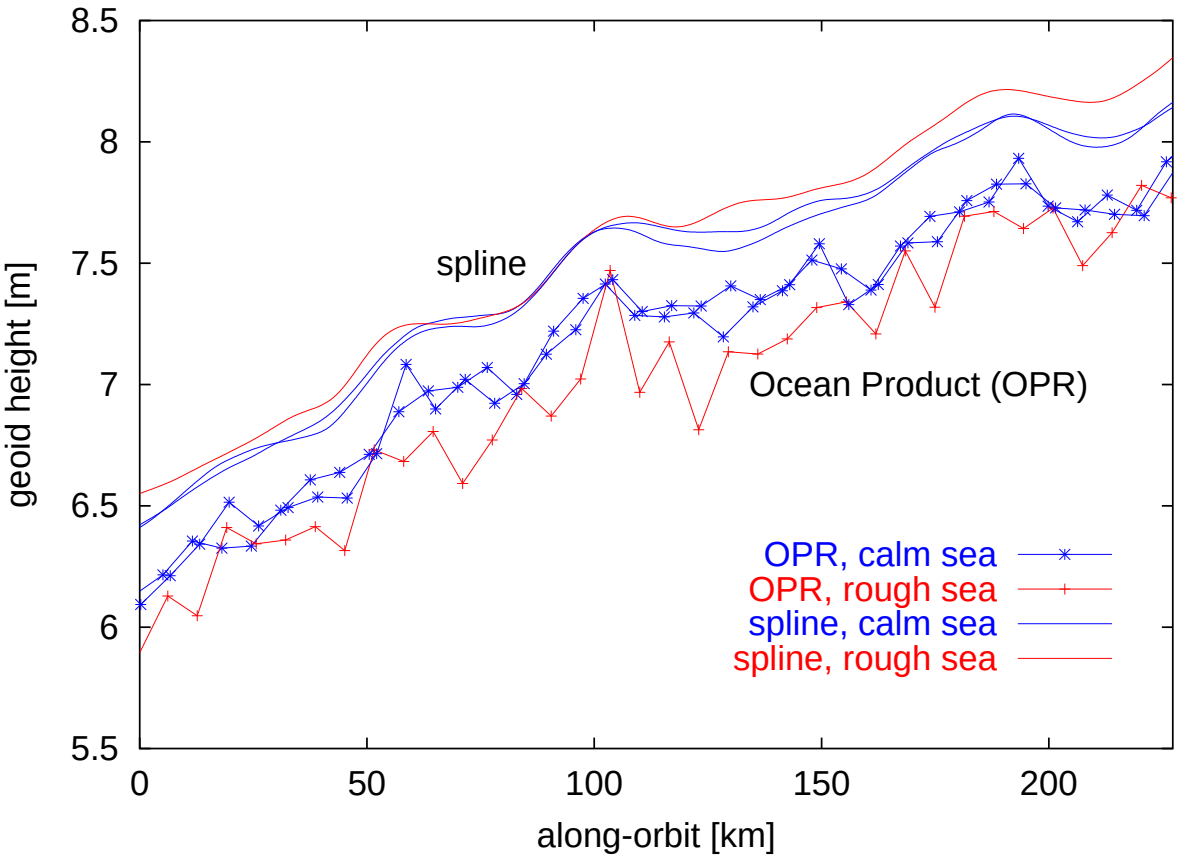

FIG. 7.9: *Ocean Product* 1 Hz geoid heights versus this study's spline geoid solutions for three repeat tracks. Offsets have been added to separate the two kinds of solutions for clarity. Our constrained spline geoid solution shows a remarkable degree of consistency in the repeat profiles, even for the track with very rough sea (mean wave height > 10 m).

where *damp* and α are two parameters which are chosen by trial and error to enforce the desired spectral density of the geoid. We utilized constant values of $damp = 10^{-6}$ and $\alpha = 3$. With this penalty included in the misfit function, the coefficients of the spline polynomials are optimized in two respects, simultaneously. The corresponding travel times have to match the observed waveforms and the spectrum of the coefficients has to decrease with a slope of 5.5 towards short wavelengths. The result of such an inversion is shown in Figures 7.4 and 7.9. The corresponding spectrum of coefficients is shown together with the spectrum of the unconstrained inversion in Figure 7.8.

Our approach is designed to obtain the best possible geoid solution. In a similar way one could estimate sea surface height variations due to ocean currents. One would require a spectral model of these variations, subtract a geoid model from the sea surface heights and invert the waveforms as described above. In this case, deviations of the geoid model from the true geoid would be considered as noise.

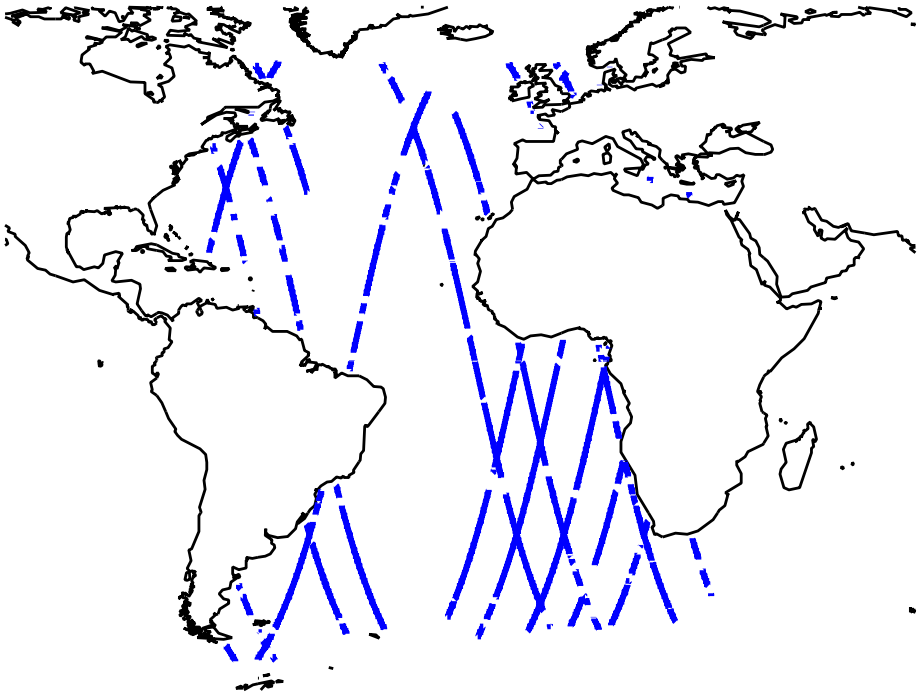

FIG. 7.10: Location of sections used for estimating along-track coherence. Only tracks for which all 3 repeat tracks were present and free of instrument error were chosen. No data was excluded for other reasons.

7.7 Coherence of repeat tracks

The spatial resolution of along-track geoid solutions can be evaluated by regarding the mean squared coherence between repeat tracks (Marks and Sailor, 1986; Sandwell and McAdoo, 1990), defined by

$$coh^2(k) = \frac{f_{TU}(k)^2}{f_T(k) f_U(k)}, \tag{7.8}$$

where k is the wavenumber, f_{TU} is the cross-spectral density and f_T and f_U are the individual spectral densities (power spectra) of tracks T and U. The coherence can be interpreted as the correlation between two signals as a function of the wavelength. If, for a given wavelength, the coherence is close to 1, the information in both signals coincides and features of this wavelength are resolved. A coherence close to zero, on the other hand, indicates that the information at this wavelength is inconsistent. Coherencies of repeat track geoid solutions are close to 1 at long wavelengths and taper off to zero for short wavelengths. The wavelength at which the mean squared coherence falls to below 0.5 can be considered as the spatial resolution. It should be kept in mind, however, that resolution defined in this manner depends on the relative strength of signal and noise, which varies from area to area. Yale, Sandwell and Smith (1995) find a ERS-1 resolution of 50 km for a low-signal-high-noise

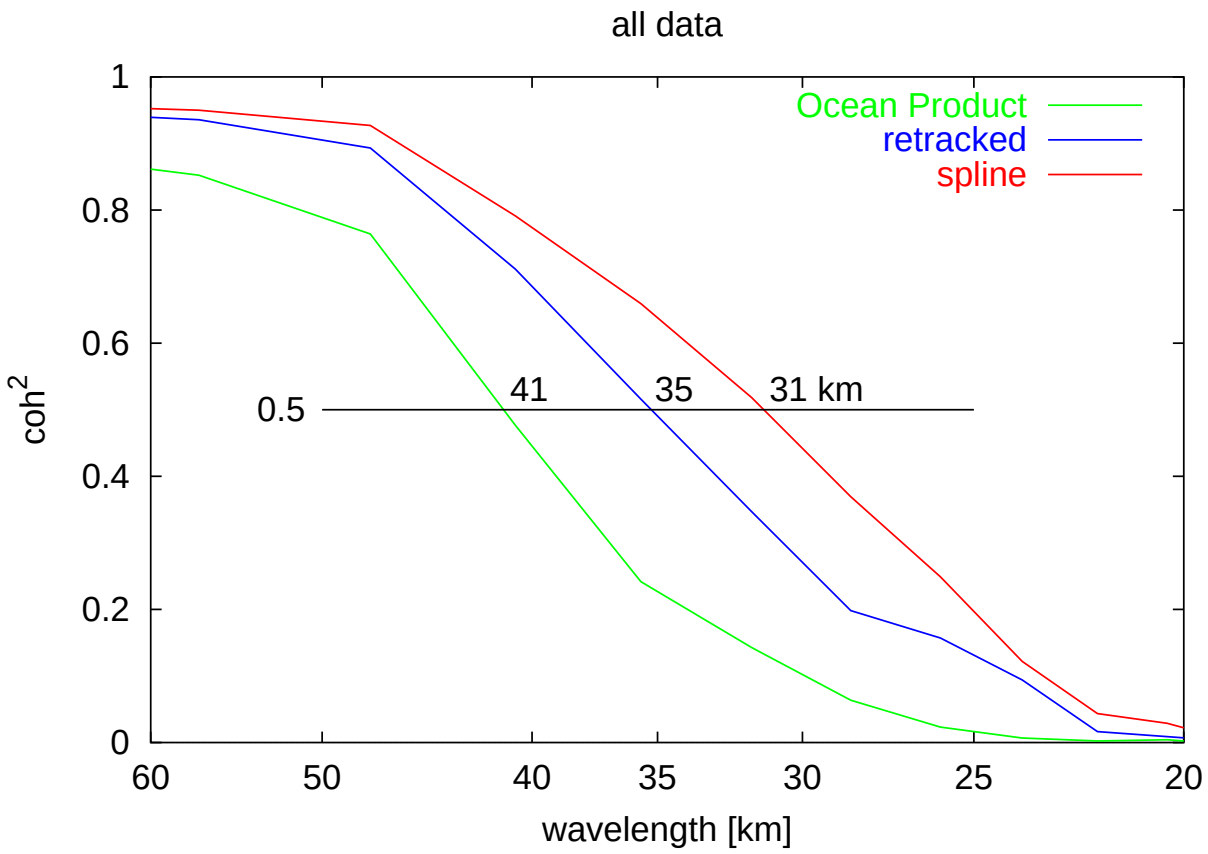

FIG. 7.11: Coherence, estimated from pairs of repeat tracks over the Atlantic Ocean using a 285 km window. The data is taken from three corresponding 42-orbit sequences of the 35-day multi-disciplinary phase.

area in the southern Pacific and 38 km for a high-signal-low-noise area at the Mid-Atlantic Ridge. For shallow areas with strong short-wavelength gravity signal, such as the continental margins, resolution may be even better.

7.7.1 Study area

To compare our geoid-solution against the Ocean-Product we used 42-orbit sequences of 3 corresponding repeat tracks from the 35-day exact repeat mission (multi-disciplinary phase). We selected the Atlantic Ocean as a study area and dismissed data of latitudes greater than 60^o to avoid errors due to sea ice. Waveforms over land, in ice tracking mode, or with range, waveform, tracking or location error were excluded from the analysis. Finally, we cut the along-track geoid solutions into corresponding sections in which all three repeat tracks were present, *Ocean Product* as well as waveform data. From these sections (Fig. 7.10) the coherence between tracks was estimated using a 285 km window. The result is shown in Figures 7.11-7.13.

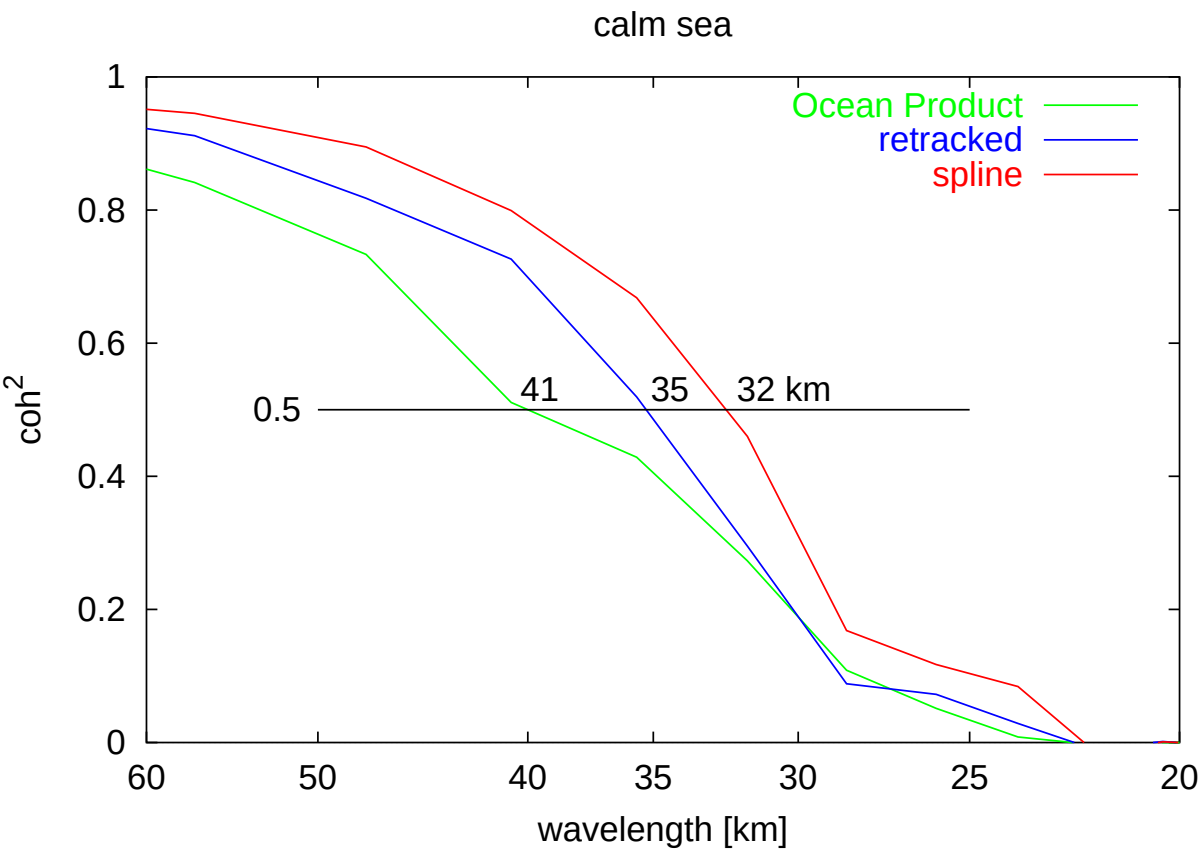

FIG. 7.12: Coherence for all pairs with a mean wave height less than 2 m in both tracks.

7.7.2 Results

The overall coherence (Figures 7.11) shows that the geoid solution obtained by retracking travel times of individual waveforms has a significantly improved resolution of 35 km over the 41 km resolution of the *Ocean Product*. This resolution can be improved further to 31 km by including a geoid spectral model at the tracking stage.

To investigate the influence of the sea state on geoid resolution, we have classified all pairs of tracks into a calm group (Fig. 7.12) for which the mean wave height of both tracks is less than 2 m, and the the complementary rough group (Fig. 7.13), for which at least one of the tracks has a mean wave height above 2 m. The comparison shows that while our retracked and spline geoid solutions are robust with regard to the sea state the quality of the *Ocean Product* deteriorates to 47 km already at very moderate wave heights.

7.8 Conclusions

We have described a new approach towards ocean geoid estimation from satellite altimeter waveform data. Earlier tracking schemes utilized complicated models attempting to explain the entire waveform. Furthermore, each waveform was inverted separately, as if it were a

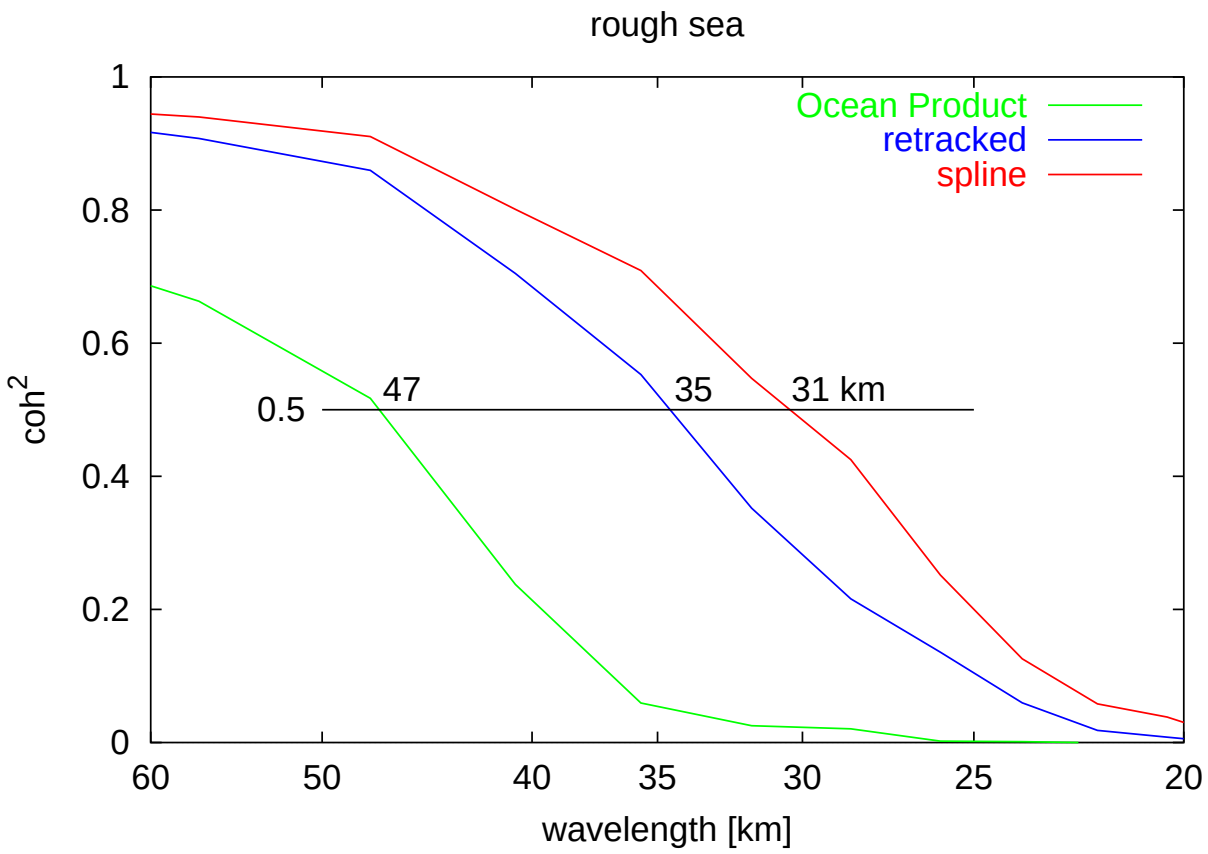

FIG. 7.13: Coherence for the complementary group to Figure 7.12, namely all pairs with a mean wave height of more than 2 m in at least one of the tracks. The absolute coherencies should not be compared with the absolute coherencies in Figure 7.12 because they do not cover the same area. The relative difference in coherence between curves in one plot, however, demonstrates that the quality of the *Ocean Product* deteriorates significantly with increasing wave height, in contrast to this study's geoid solutions.

statistical event unrelated to the adjacent waveforms. Instead, we align a whole sequence of waveforms simultaneously. A spline geoid model is fit to the sequence of waveforms in such a way that the variance at the leading edge is minimized. By introducing a penalty for high power in high order spline polynomial coefficients, the power spectrum of the spline solution is forced to take on the shape of the true geoid power spectrum. The coherence of repeat tracks shows a significant improvement in along-track geoid resolution from 41 km to 31 km. The quality of our geoid solution is maintained at rough sea states, where an improvement from 47 km to 31 km was achieved. This is particularly important for processing Geodetic Mission data where, due to the absence of repeat tracks, a noisy track cannot be substituted.

Chapter 8

On the parametrization of field models for satellite magnetic data

Backus (1986) shows that the magnetic field on a sphere $S(b)$ of radius b is uniquely parametrized by three scalars $g(\theta, \phi)$, $k(\theta, \phi)$ and $q(\theta, \phi)$, corresponding to internal toroidal, external toroidal and poloidal electric currents through the surface of the sphere. A dipole field is an example of a poloidal field and a circular current is an example of a toroidal field. In applying this simple parametrization to satellite magnetic data, one has to take into account that satellite orbits are elliptical, rather than circular, and decrease in radius with the lifetime of the satellite. For example, altitudes range from 350 km to 550 km for Magsat and from 650 km to 850 km for Ørsted. As pointed out by Olsen (1997), the above parametrization is applicable to a spherical shell $S(a, c)$ with $a \leq r \leq c$ if all currents passing through the shell are purely radial. Representing g, k and q as sums of spherical harmonics then leads to a discretization which may be referred to as being of order zero in r. Using such a discretization, Olsen (1997) inverted Magsat data estimating the radial components of ionospheric current systems.

Since currents are primarily field-aligned at satellite altitude, Backus (1986) suggests to substitute the toroidal field scalar q by the relative density α of field-aligned currents through $S(a, c)$ as a third parameter. Due to practical difficulties in implementing this scheme, Olsen (1997) proposes a radial Taylor series expansion of the toroidal field scalar q, instead. This requires an efficient definition of first, second and higher order radial contributions to q. Arguably, Olsen's initial scheme is not optimal in this sense. In the following we therefore propose an improved radial expansion scheme based on the presumed radial divergence of ionospheric currents.

8.1 First order radial expansion of the magnetic field scalars

Making use of $\boldsymbol{\nabla} \cdot \mathbf{B} = 0$, the magnetic field is conveniently represented in spherical coordinates (r, θ, ϕ) as

$$\mathbf{B}(r, \theta, \phi) = \boldsymbol{\nabla} \times \boldsymbol{\Lambda} p(r, \theta, \phi) + \boldsymbol{\Lambda} q(r, \theta, \phi), \tag{8.1}$$

where $\boldsymbol{\Lambda} = \hat{\boldsymbol{\phi}}\partial_\theta - (\hat{\boldsymbol{\theta}}/\sin\theta)\partial_\phi$ is the surface curl, $\hat{\boldsymbol{\theta}}$ and $\hat{\boldsymbol{\phi}}$ are local unit vectors of the co-latitude and longitude, and p and q are the Mie scalars of the poloidal and toroidal magnetic field, respectively (Backus, 1986; Backus et al., 1996). The sources of the magnetic field are electric currents $\mathbf{J}$ with

$$\begin{aligned} \mu_0 \mathbf{J}(r, \theta, \phi) &= \boldsymbol{\nabla} \times \mathbf{B}(r, \theta, \phi) && (8.2) \\ &= \boldsymbol{\nabla} \times \boldsymbol{\Lambda} q(r, \theta, \phi) + \boldsymbol{\Lambda}[-\nabla^2 p(r, \theta, \phi)] && (8.3) \\ \mathbf{J}(r, \theta, \phi) &= \boldsymbol{\nabla} \times \boldsymbol{\Lambda} \tilde{p}(r, \theta, \phi) + \boldsymbol{\Lambda} \tilde{q}(r, \theta, \phi), && (8.4) \end{aligned}$$

where $\tilde{p} = q/\mu_0$ and $\tilde{q} = -\nabla^2 p/\mu_0$ are the poloidal and toroidal current scalars. Making assumptions on the radial divergence of ionospheric electric currents, we propose first, second and higher order radial parametrizations of the poloidal and toroidal magnetic field scalars p and q.

A satellite measures the three vector components of the magnetic field on an elliptical orbit with rotating orbital axis, with the additional complication that the magnetic field is not constant in time. Any inversion attempting to estimate more than three sets of scalar parameters from these measurements is likely to face stability problems. The obvious choice for a 3 parameter model is to quantify the internal poloidal, external poloidal and the toroidal magnetic field by one parameter each.

8.1.1 First order poloidal scalar p

A consistent separation of the poloidal field into internal and external parts in the shell $S(a, c)$ is only possible with the assumption that there are no toroidal currents in $S(a, c)$. Then we can write the poloidal scalar p in terms of the traditional Gauss coefficients g_ℓ^m and k_ℓ^m as

$$p(r, \theta, \phi) = a \sum_{\ell=1}^{\infty} \sum_{m=-\ell}^{\ell} [-\frac{1}{\ell} g_\ell^m \left(\frac{a}{r}\right)^{\ell+1} + \frac{1}{\ell+1} k_\ell^m \left(\frac{r}{a}\right)^{\ell}] \; \beta_\ell^m(\theta, \phi) \tag{8.5}$$

where β_ℓ^m are surface spherical harmonics in arbitrary normalization. Note that there is an incorrect sign in the corresponding formula of Backus (1986, eq. 58d), reproduced in Backus *et al.* (1996, eq. 5.3.15).

8.1.2 First order toroidal scalar q

The toroidal field scalar q on $S(r)$ is fully determined by the radial component J_r of the current density $\mathbf{J}$ at $S(r)$, as can be seen from eq. (8.29) below. Thus, the radial decay of the toroidal field scalar q can be inferred from the presumed radial decay of the radial current density J_r. Electrical currents at satellite altitude are primarily field-aligned. Hence,

$$\mathbf{J}(r,\theta,\phi) = J(r,\theta,\phi)\,\frac{\mathbf{B}(r,\theta,\phi)}{|\mathbf{B}(r,\theta,\phi)|} \tag{8.6}$$

$$\boldsymbol{\nabla}\cdot\mathbf{J} = \mathbf{B}\cdot\boldsymbol{\nabla}\frac{J}{|\mathbf{B}|} + \frac{J}{|\mathbf{B}|}\boldsymbol{\nabla}\cdot\mathbf{B}. \tag{8.7}$$

Since $\boldsymbol{\nabla}\cdot\mathbf{J} = 0$ and $\boldsymbol{\nabla}\cdot\mathbf{B} = 0$

$$0 = \mathbf{B}\cdot\boldsymbol{\nabla}\frac{J}{|\mathbf{B}|}. \tag{8.8}$$

Thus, the ratio $J/|\mathbf{B}|$ can change only in directions perpendicular to the field lines. In other words, the strength $J = |\mathbf{J}|$ of the current along a field line behaves in the same way as the strength of the magnetic field. To first order, the magnetic field at satellite altitude is dipolar. For a dipole field $|\mathbf{B}| \propto r^{-3}\sqrt{1+3\cos^2\theta}$. Consequently, for two locations $\mathbf{r}_0$ and $\mathbf{r}_1$ on the same field line we have

$$J(\mathbf{r}_1) = \left(\frac{r_0}{r_1}\right)^3 \underbrace{\sqrt{\frac{1+3\cos^2\theta_1}{1+3\cos^2\theta_0}}}_{Q}\, J(\mathbf{r}_0). \tag{8.9}$$

To obtain the behavior of J_r along a field line, we need to first derive the corresponding relation for the tangential current density J_θ. With

$$J_\theta(\mathbf{r}) = \frac{\sin\theta}{\sqrt{1+3\cos^2\theta}} J(\mathbf{r}), \tag{8.10}$$

we obtain the behavior along a field line as

$$J_\theta(\mathbf{r}_1) = \frac{\sin\theta_1}{\sin\theta_0}\left(\frac{r_0}{r_1}\right)^3 J_\theta(\mathbf{r}_0). \tag{8.11}$$

Along a field line the latitudes satisfy the relation (Siebert, 1965, eq. A 5.24)

$$\frac{\sin^2\theta_1}{\sin^2\theta_0} = \frac{r_1}{r_0}, \tag{8.12}$$

which simplifies eq. (8.11) to

$$J_\theta(\mathbf{r}_1)^2 = \left(\frac{r_0}{r_1}\right)^5 J_\theta(\mathbf{r}_0)^2. \tag{8.13}$$

Taking J^2 from eq. (8.9) and J_θ^2 from eq. (8.13) we can now infer the behavior of the radial component J_r as

$$\begin{aligned} J_r(\mathbf{r}_1)^2 &= J(\mathbf{r}_1)^2 - J_\theta(\mathbf{r}_1)^2 \\ &= \left(\frac{r_0}{r_1}\right)^6 Q^2 J(\mathbf{r}_0)^2 - \left(\frac{r_0}{r_1}\right)^5 J_\theta(\mathbf{r}_0)^2. \end{aligned} \tag{8.14}$$

For small $r_1 - r_0$ we can neglect the shift in latitude along a field line, giving $\theta_1 \approx \theta_0$ and $Q \approx 1$. Using this approximation in eq. (8.14) gives

$$J_r(r_1,\theta,\phi)^2 \approx \left(\frac{r_0}{r_1}\right)^6 J(r_0,\theta,\phi)^2 - \left(\frac{r_0}{r_1}\right)^5 J_\theta(r_0,\theta,\phi)^2. \tag{8.15}$$

On average, the power of a dipolar vector field is split 2:1 between the radial and tangential directions (Holme and Jackson, 1997, eqs. 11-13). Denoting the average over the surface of a sphere by $\langle\cdot\rangle$, we then have

$$\langle J_r^2\rangle = 2\langle J_\theta^2\rangle = \frac{2}{3}\langle J^2\rangle. \tag{8.16}$$

Using (8.16) in (8.15) yields on average

$$\langle J_r(r_1,\theta,\phi)^2\rangle \approx \left(\frac{r_0}{r_1}\right)^6 \left(\frac{3}{2} - \frac{r_1}{2r_0}\right) \langle J_r(r_0,\theta,\phi)^2\rangle \tag{8.17}$$

$$J_r(r_1,\theta,\phi) \approx \underbrace{\left(\frac{r_0}{r_1}\right)^3 \sqrt{\frac{3}{2} - \frac{r_1}{2r_0}}}_{\rho_J(r_0,r_1)} J_r(r_0,\theta,\phi) \tag{8.18}$$

motivating the assumption

$$q(r,\theta,\phi) = \underbrace{\left(\frac{a}{r}\right)^2 \sqrt{\frac{3}{2} - \frac{r}{2a}}}_{\rho(a,r)} q(a,\theta,\phi) \tag{8.19}$$

which leads to the ansatz

$$q(r,\theta,\phi) = \rho(a,r) \sum_{\ell=1}^{\infty} \sum_{m=-\ell}^{\ell} q_\ell^m \beta_\ell^m(\theta,\phi), \tag{8.20}$$

suitable for $r/a \ll 3$. One may object that (8.18) is not a good approximation near the equator. Consider, for example, a hypothetical situation in which the current density is zero everywhere except on a field line crossing the magnetic equator at r_{max} with $r_0 < r_{max} < r_1$. Then, (8.18) gives $J_r(r_1,\theta,\phi)$ as some fraction of $J_r(r_0,\theta,\phi)$, while the true current density is everywhere equal to zero on $S(r_1)$ with $r_1 > r_{max}$. However, real field-aligned current systems are strong at high latitudes, and since $J_r = 0$ at the magnetic equator, the equatorial regions should anyway contribute little to the toroidal magnetic field. A test of (8.18) for a white field-aligned current density distribution is given in section 8.3, below.

8.1.3 First order magnetic field model

Using Backus' notation and omitting the arguments (r,θ,ϕ) and (θ,ϕ) for clarity, equation (8.1) can be rewritten as

$$\mathbf{B} = \hat{\mathbf{r}}\frac{\nabla_1^2 p}{r} - \boldsymbol{\nabla}_1 \frac{\partial_r r p}{r} + \boldsymbol{\Lambda} q \tag{8.21}$$

$$= \hat{\mathbf{r}}\frac{\nabla_1^2 p}{r} - \hat{\boldsymbol{\theta}}\left(\frac{1}{r}\partial_r r \partial_\theta p + \frac{1}{\sin\theta}\partial_\phi q\right) - \hat{\boldsymbol{\phi}}\left(\frac{1}{r\sin\theta}\partial_r r \partial_\phi p - \partial_\theta q\right) \tag{8.22}$$

with $\hat{\mathbf{r}}$, $\hat{\boldsymbol{\theta}}$ and $\hat{\boldsymbol{\phi}}$ as the local unit vectors and surface gradient $\boldsymbol{\nabla}_1 = r\boldsymbol{\nabla} - \mathbf{r}\partial_r = \hat{\boldsymbol{\theta}}\partial_\theta + (\hat{\boldsymbol{\phi}}/\sin\theta)\partial_\phi$ and surface curl $\boldsymbol{\Lambda} = \hat{\mathbf{r}} \times \boldsymbol{\nabla}_1 = \hat{\boldsymbol{\phi}}\partial_\theta - (\hat{\boldsymbol{\theta}}/\sin\theta)\partial_\phi$. With ansatz (8.5) and using $\nabla_1^2 \beta_\ell^m = -\ell(\ell+1)\beta_\ell^m$

$$\nabla_1^2 p = a \sum_{\ell=1}^{\infty} \sum_{m=-\ell}^{\ell} [(\ell+1) g_\ell^m \left(\frac{a}{r}\right)^{\ell+1} - \ell k_\ell^m \left(\frac{r}{a}\right)^{\ell}] \beta_\ell^m \tag{8.23}$$

and

$$\partial_r r \partial_\theta p = a \sum_{\ell=1}^{\infty} \sum_{m=-\ell}^{\ell} [g_\ell^m \left(\frac{a}{r}\right)^{\ell+1} + k_\ell^m \left(\frac{r}{a}\right)^{\ell}] \partial_\theta \beta_\ell^m \tag{8.24}$$

Using (8.23), (8.24) and ansatz (8.20) for q in (8.22) finally gives

$$\begin{aligned} \mathbf{B} &= \sum_{\ell=1}^{\infty} \sum_{m=-\ell}^{\ell} \hat{\mathbf{r}} [(\ell+1) g_\ell^m \left(\frac{a}{r}\right)^{\ell+2} - \ell k_\ell^m \left(\frac{r}{a}\right)^{\ell-1}] \ \beta_\ell^m \\ &- \hat{\boldsymbol{\theta}} \{ [g_\ell^m \left(\frac{a}{r}\right)^{\ell+2} + k_\ell^m \left(\frac{r}{a}\right)^{\ell-1}] \partial_\theta \ \beta_\ell^m + \frac{\rho(a,r)}{\sin\theta} q_\ell^m \partial_\phi \beta_\ell^m \} \\ &- \hat{\boldsymbol{\phi}} \{ [g_\ell^m \left(\frac{a}{r}\right)^{\ell+2} + k_\ell^m \left(\frac{r}{a}\right)^{\ell-1}] \frac{\partial_\phi \beta_\ell^m}{\sin\theta} - \rho(a,r) q_\ell^m \partial_\theta \beta_\ell^m \}, \end{aligned} \tag{8.25}$$

where arguments (r, θ, ϕ) and (θ, ϕ) have been omitted for $\mathbf{B}$ and β_ℓ^m, respectively. For the special case of $r \equiv a$ this equation reduces to the equations discussed in Backus *et al.* (1996, p. 189-192).

8.1.4 First order electric currents

Having assumed that there are no toroidal currents in $S(a,c)$, the remaining poloidal currents in $S(a,c)$ are

$$\begin{aligned} \mu_0 \mathbf{J} &= \boldsymbol{\nabla} \times \boldsymbol{\Lambda} q \\ &= \hat{\mathbf{r}} \frac{\nabla_1^2 q}{r} - \boldsymbol{\nabla}_1 \frac{\partial_r r q}{r} \\ &= \hat{\mathbf{r}} \frac{\nabla_1^2 q}{r} - \hat{\boldsymbol{\theta}} \partial_\theta \frac{\partial_r r q}{r} - \hat{\boldsymbol{\phi}} \frac{1}{\sin\theta} \partial_\phi \frac{\partial_r r q}{r} \end{aligned} \tag{8.26}$$

and using ansatz (8.20) for q we have

$$\frac{\partial_r r q}{r} = -\frac{6a - r}{6ar - 2r^2} q \tag{8.27}$$

$$\nabla_1^2 q = -\ell(\ell+1) q \tag{8.28}$$

With (8.27) and (8.28) the currents (8.26) are

$$\mu_0 \mathbf{J} = \frac{\rho(a,r)}{r} \sum_{\ell=1}^{\infty} \sum_{m=-\ell}^{\ell} q_\ell^m \left[-\hat{\mathbf{r}} \ell(\ell+1) \beta_\ell^m + \hat{\boldsymbol{\theta}} \frac{6a - r}{6a - 2r} \partial_\theta \beta_\ell^m + \hat{\boldsymbol{\phi}} \frac{6a - r}{(6a - 2r)\sin\theta} \partial_\phi \beta_\ell^m \right]. \tag{8.29}$$

where again arguments (r, θ, ϕ) and (θ, ϕ) for $\mathbf{J}$ and β_ℓ^m have been dropped.

8.2 Higher order radial expansion

Due to the rotation of the principal axis of the elliptical orbit, a satellite samples the magnetic field not only in the azimuthal but also in the radial direction. However, time variations of the entire field render it difficult to actually extract the radial behavior of the field. The situation will improve with the advent of additional satellites. A simultaneous inversion of multiple data sets will provide additional field information in the radial direction and, thus, may allow for the estimation of higher order model coefficients.

8.2.1 Higher order scalars for p

Including further scalars for p means to drop the previous assumption that there are no toroidal currents in $S(a,c)$. The radial behavior of a toroidal current component would have to be inferred from the underlying physical cause. For an unknown cause, we can argue that the surface of $S(r)$ increases with r^2, hence, the currents on this surface are likely to decrease with r^{-2} due to spherical divergence. From eqs. (8.4) and (8.33) it can be seen that this corresponds to adding a scalar to p which is constant in r:

$$p^{(2)}(r,\theta,\phi) = a\sum_{\ell=1}^{\infty}\sum_{m=-\ell}^{\ell} p_{\ell,m}^{(2)}\beta_\ell^m(\theta,\phi) \tag{8.30}$$

We then obtain an additional contribution to the magnetic field

$$\begin{aligned}
\mathbf{B} &= \hat{\mathbf{r}}\frac{\nabla_1^2 p^{(2)}}{r} - \hat{\boldsymbol{\theta}}\frac{1}{r}\partial_r r\partial_\theta p^{(2)} - \hat{\boldsymbol{\phi}}\frac{1}{r\sin\theta}\partial_r r\partial_\phi p^{(2)} && (8.31)\\
&= \frac{a}{r}\sum_{\ell=1}^{\infty}\sum_{m=-\ell}^{\ell} p_{\ell,m}^{(2)}\left[-\hat{\mathbf{r}}\ell(\ell+1) - \hat{\boldsymbol{\theta}}\partial_\theta\ \beta_\ell^m - \hat{\boldsymbol{\phi}}\frac{1}{\sin\theta}\partial_\phi\ \beta_\ell^m\right], && (8.32)
\end{aligned}$$

due to the additional electric currents

$$\begin{aligned}
\mu_0\mathbf{J} &= -\boldsymbol{\Lambda}(\nabla^2 p^{(2)})\\
&= -\boldsymbol{\Lambda}\frac{1}{r^2}(\underbrace{r\partial_r^2 r p^{(2)}}_{=0} + \nabla_1^2 p^{(2)})\\
&= -(\hat{\boldsymbol{\phi}}\partial_\theta - \frac{1}{\sin\theta}\hat{\boldsymbol{\theta}}\partial_\phi)\frac{\nabla_1^2 p^{(2)}}{r^2}\\
&= \frac{a}{r^2}\sum_{\ell=1}^{\infty}\sum_{m=-\ell}^{\ell} p_{\ell,m}^{(2)}\left[\hat{\boldsymbol{\theta}}\ell(\ell+1)\partial_\theta\ \beta_\ell^m - \hat{\boldsymbol{\phi}}\frac{\ell(\ell+1)}{\sin\theta}\partial_\phi\beta_\ell^m\right] && (8.33)
\end{aligned}$$

For as yet unknown physical reasons it could turn out to be sensible to include further scalars for p decaying more or less rapidly in r.

8.2.2 Higher order scalars for q

The factor $\rho(a,r)$ in approximation (8.19) has a decay rate between r^{-2} and r^{-3}. In the hypothetical situation where data availability allowed for the estimation of higher order

scalars for q, one could substitute the single scalar $q \propto \rho(a,r)$ in (8.19) by several scalars with decay rates centered around $\rho(a,r)$. The first two scalars would then be $q^{(1)} \propto r^{-2}$ and $q^{(2)} \propto r^{-3}$ with

$$q^{(1)}(r,\theta,\phi) = \frac{a^2}{r^2}\sum_{\ell=1}^{\infty}\sum_{m=-\ell}^{\ell} q_{\ell,m}^{(1)}\beta_\ell^m(\theta,\phi) \tag{8.34}$$

$$q^{(2)}(r,\theta,\phi) = \frac{a^3}{r^3}\sum_{\ell=1}^{\infty}\sum_{m=-\ell}^{\ell} q_{\ell,m}^{(2)}\beta_\ell^m(\theta,\phi), \tag{8.35}$$

contributing to the magnetic field by

$$\mathbf{B}^{(1)} = \frac{a^2}{r^2}\sum_{\ell=1}^{\infty}\sum_{m=-\ell}^{\ell} q_{\ell,m}^{(1)}\left[\frac{-\hat{\boldsymbol{\theta}}}{\sin\theta}\partial_\phi\beta_\ell^m + \hat{\boldsymbol{\phi}}\partial_\theta\beta_\ell^m\right] \tag{8.36}$$

$$\mathbf{B}^{(2)} = \frac{a^3}{r^3}\sum_{\ell=1}^{\infty}\sum_{m=-\ell}^{\ell} q_{\ell,m}^{(2)}\left[\frac{-\hat{\boldsymbol{\theta}}}{\sin\theta}\partial_\phi\beta_\ell^m + \hat{\boldsymbol{\phi}}\partial_\theta\beta_\ell^m\right]. \tag{8.37}$$

The corresponding source currents can be derived using

$$\nabla_1^2 q = -\ell(\ell+1)q \tag{8.38}$$

$$\frac{\partial_r r q^{(1)}}{r} = \frac{q^{(1)}}{r} - 2\frac{q^{(1)}}{r} = -\frac{q^{(1)}}{r} \tag{8.39}$$

$$\frac{\partial_r r q^{(2)}}{r} = \frac{q^{(2)}}{r} - 3\frac{q^{(2)}}{r} = -2\frac{q^{(2)}}{r}. \tag{8.40}$$

in eq. (8.26), giving

$$\mu_0\mathbf{J}^{(1)} = \frac{a^2}{r^3}\sum_{\ell=1}^{\infty}\sum_{m=-\ell}^{\ell} q_{\ell,m}^{(1)}\left[-\hat{\mathbf{r}}\ell(\ell+1)\beta_\ell^m + \hat{\boldsymbol{\theta}}\partial_\theta\beta_\ell^m + \frac{\hat{\boldsymbol{\phi}}}{\sin\theta}\partial_\phi\beta_\ell^m\right] \tag{8.41}$$

$$\mu_0\mathbf{J}^{(2)} = \frac{a^3}{r^4}\sum_{\ell=1}^{\infty}\sum_{m=-\ell}^{\ell} q_{\ell,m}^{(2)}\left[-\hat{\mathbf{r}}\ell(\ell+1)\beta_\ell^m + 2\hat{\boldsymbol{\theta}}\partial_\theta\beta_\ell^m + \frac{2\hat{\boldsymbol{\phi}}}{\sin\theta}\partial_\phi\beta_\ell^m\right], \tag{8.42}$$

where again the arguments (r,θ,ϕ) and (θ,ϕ) for $\mathbf{J}$ and β_ℓ^m have been dropped.

8.3 Radial decay of a dipolar field-aligned electric current system

In this section, we compare the true radial decay of a white dipolar field-aligned current system with the decay predicted by approximation (8.18) for the coefficients of its spherical harmonic expansion. We first synthesize a current density J on the sphere $S(r_0)$ with a white spectrum in the band of spherical harmonic degrees 1-16. Here, we understand a white spectrum in the sense of the definitions in Chapter 1.1. The white spectrum is gained by generating random values for the spherical harmonic coefficients and normalizing these in such a way that the total power spectral density is equal for each degree ℓ. Then the current

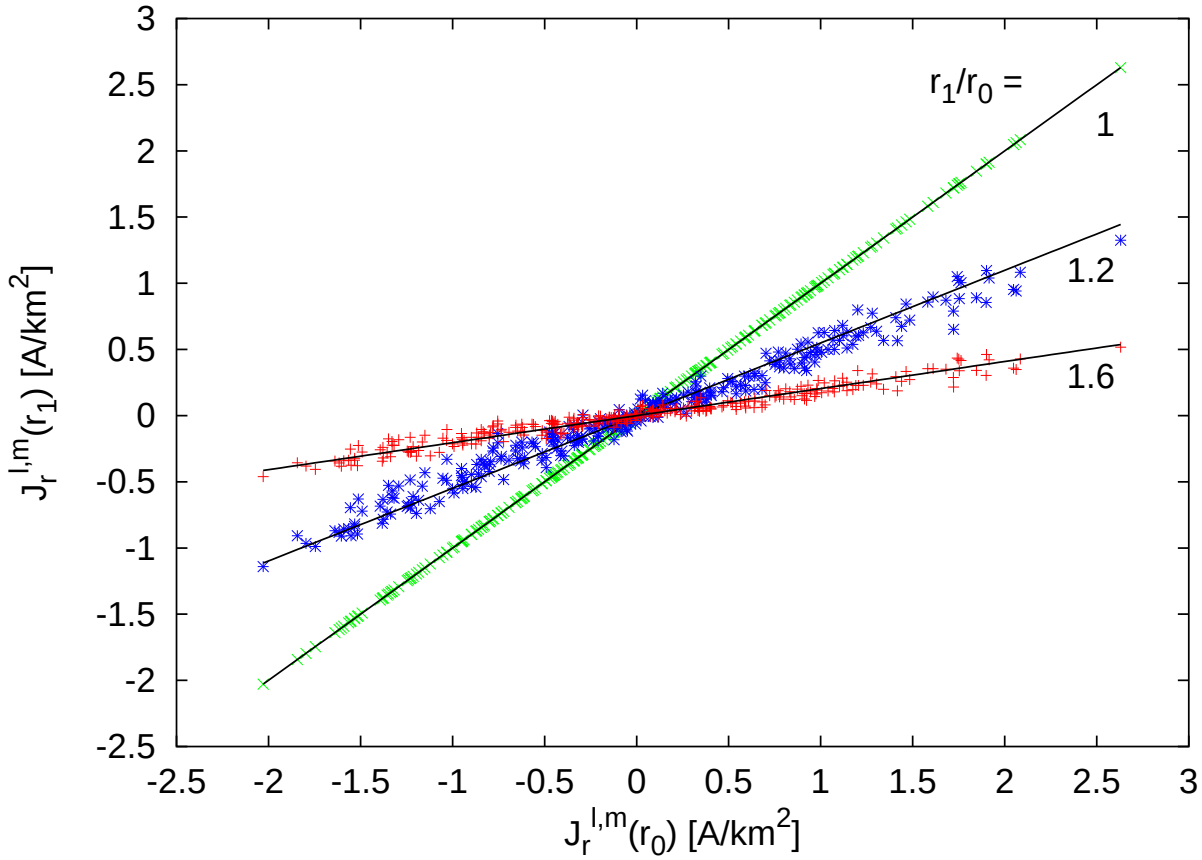

FIG. 8.1: Synthetic white noise current system, aligned to a dipole field. The exact spherical harmonic coefficients of the radial current density at radius r_1 are plotted against the corresponding coefficients at radius r_0. The solid lines give the prediction according to approximation (8.18).

densities $J(r_0, \theta_g, \phi_g)$ are computed for the Gauss-Legendre quadrature points (θ_g, ϕ_g) by a reverse spherical harmonic transform. The values at the angular locations (θ_g, ϕ_g) completely define the coefficients of a spherical harmonic expansion up to a given degree. Taking the radial current component $J_r(r_0, \theta_g, \phi_g)$ and transforming forward gives the spherical harmonic coefficients of the radial current density at $S(r_0)$. These coefficients are directly related to the spherical harmonic expansion of the toroidal field scalar q on $S(r_0)$, as can be seen from eq. (8.29). To find the exact radial current component $J_r(r_1, \theta_g, \phi_g)$ and thus the exact field scalar $q(r_1, \theta_g, \phi_g)$ on $S(r_1)$ at a radius $r_1 > r_0$, we follow the Gauss-Legendre quadrature points (θ_g, ϕ_g) from $S(r_1)$ down along the field lines into the points (θ'_g, ϕ'_g) on the lower sphere $S(r_0)$, using the relation

$$\theta(r_0) = \begin{cases} \arcsin[\sqrt{\frac{r_0}{r_1}}\,\sin\theta(r_1)] & \text{for } \theta \le \pi/2 \\ \pi - \arcsin[\sqrt{\frac{r_0}{r_1}}\,\sin\theta(r_1)] & \text{for } \theta > \pi/2, \end{cases} \tag{8.43}$$

which follows from eq. (8.12). Then we compute the radial current component $J_r(r_0, \theta'_g, \phi'_g)$ for these locations from the spherical harmonic expansion of J_r on $S(r_0)$ and upward continue

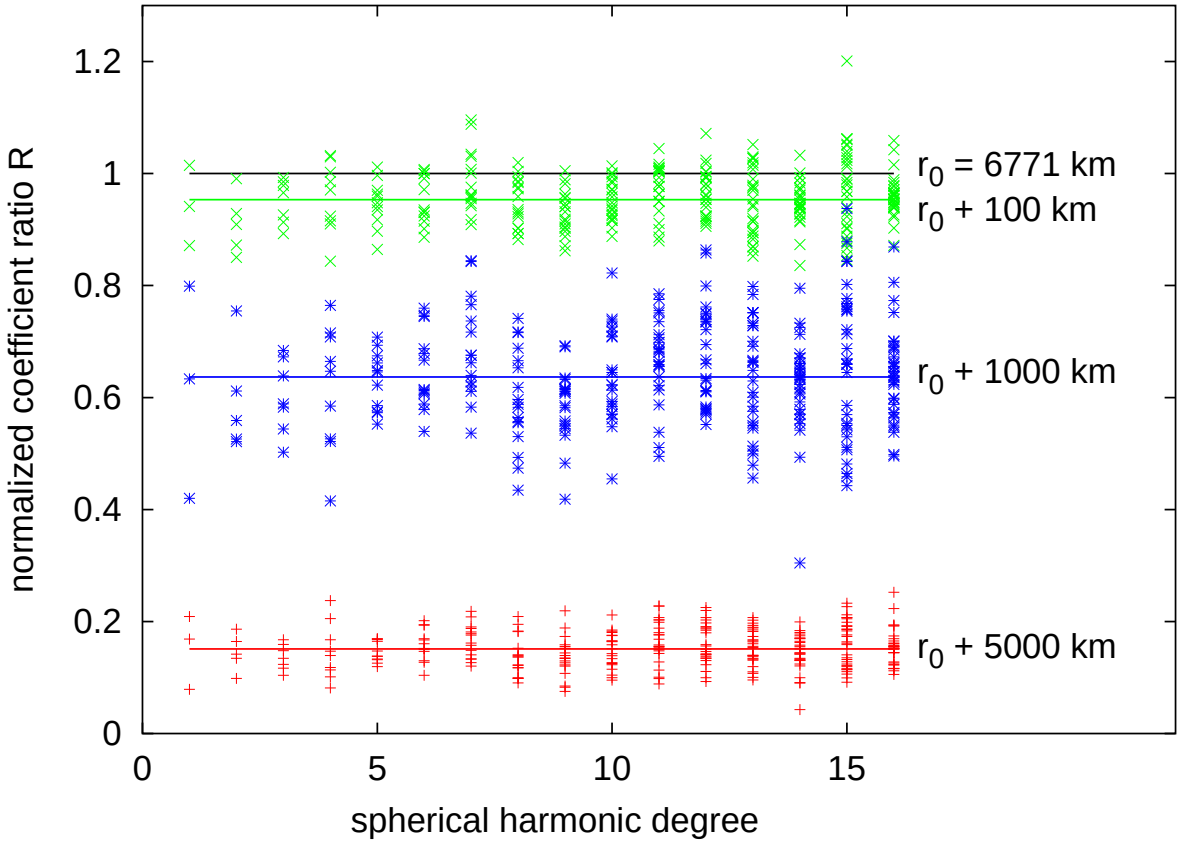

FIG. 8.2: Here, the coefficient ratio is normalized to the mean amplitude in each spherical harmonic degree, according to eq. (8.45), and is then plotted against the degree. The solid lines give the predicted ratio $\rho_J(r_0, r_1)$, as defined in relation (8.18).

it along each field line into the Gauss-Legendre quadrature points (θ_g, ϕ_g) on $S(r_1)$, using

$$J_r(r_1, \theta_g, \phi_g) = \left(\frac{r_0}{r_1}\right)^3 \frac{\cos\theta_g}{\cos\theta'_g}\, J_r(r_0, \theta'_g, \phi'_g). \tag{8.44}$$

The forward spherical harmonic expansion then gives the exact coefficients of the radial current density on $S(r_1)$, which can be compared with the ones predicted from the coefficients at $S(r_0)$ using approximation (8.18) for each individual spherical harmonic expansion coefficient. The exact expansion coefficients for J_r on $S(r_1)$ are plotted against the coefficients on $S(r_0)$ in Figure 8.1. The solid lines give the prediction according to approximation (8.18). For a satellite at 400 km altitude the radial ratios of 1.2 and 1.6 correspond to radial separations of 1350 km and 4000 km, respectively. For these large distances the approximation is surprisingly good. To analyze the quality of the approximation for smaller radial separations, let us define the coefficient ratio, normalized to the mean amplitude in the spherical harmonic degree, as

$$R = \frac{J_r^{\ell,m}(r_1) - \rho_J(r_0, r_1) J_r^{\ell,m}(r_0)}{\sqrt{\frac{1}{2\ell+1}\sum_{m=-\ell}^{\ell}[J_r^{\ell,m}(r_0)]^2}} + \rho_J(r_0, r_1) \tag{8.45}$$

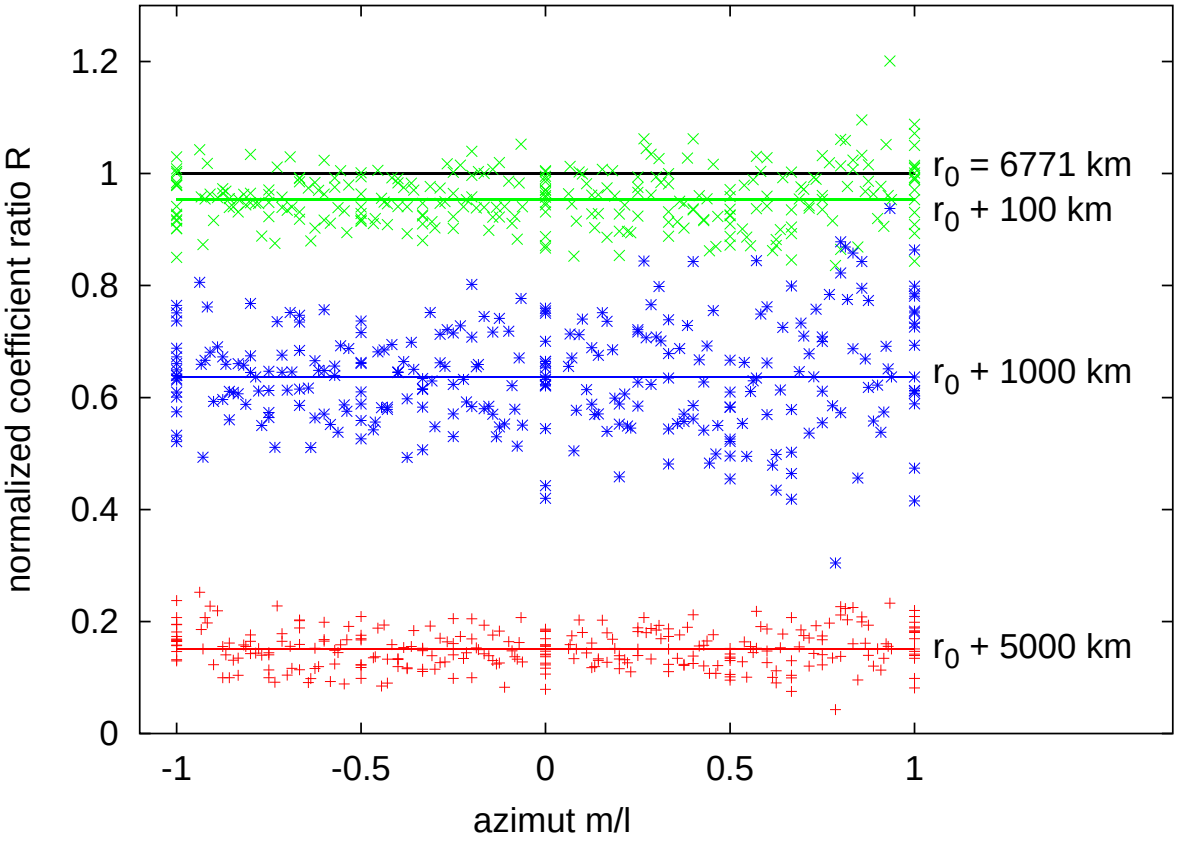

FIG. 8.3: The coefficient ratio R of eq. (8.45) is displayed against the azimuth m/ℓ. Surprisingly, the quality of the approximation (8.18) depends neither on the degree ℓ (see Fig. 8.2) nor on the order m.

where $\rho_J(r_0, r_1)$ is the ratio of $J_r(r_1)/J_r(r_0)$ predicted by approximation (8.18). In Figures 8.2 and 8.3 the ratio R of definition (8.45) is plotted against the spherical harmonic degree and against the azimuth m/ℓ. It is interesting to see that the prediction error depends neither on the degree nor on the azimuth.

The utility of approximation (8.18) is further scrutinized by plotting the deviation of the predicted radial current density $\rho_J(r_0, r_1)J_r(r_0, \theta, \phi)$ from its true value $J_r(r_1, \theta, \phi)$ against the height difference $r_1 - r_0$. The relative root of the mean square (RMS) error

$$\mathrm{E_{rel}} = \sqrt{\frac{\langle [J_r(r_1, \theta, \phi) - \rho_J(r_0, r_1) J_r(r_0, \theta, \phi)]^2 \rangle}{\langle [J_r(r_1, \theta, \phi)]^2 \rangle}} \tag{8.46}$$

can be computed directly from the spherical harmonic coefficients of the true and the predicted radial current densities. In Figure 8.4, the lower curve gives the error for $\rho_J(r_0, r_1)$ as defined in relation (8.18) and the upper curve for the crude approximation $\rho_J(r_0, r_1) \equiv 1$. The prediction error of approximation (8.18) increases strongly to around 5% for a height difference of 100 km, but then exhibits only a moderate further increase to 12% for 500 km difference in height. In these examples, r_0 is taken as the mean Earth radius plus 400 km.

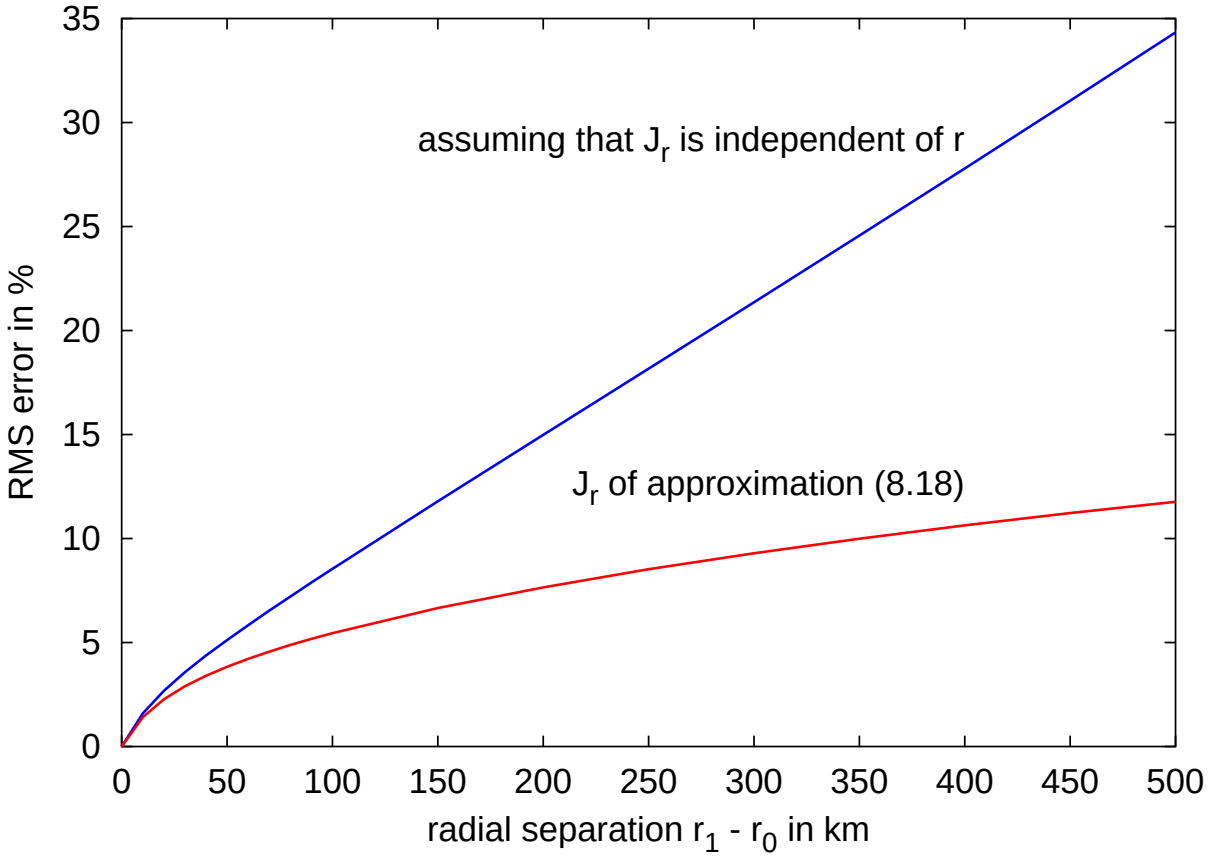

FIG. 8.4: Root of the mean square (RMS) error of the radial current prediction $\rho_J(r_0, r_1)J_r(r_0)$ for $S(r_1)$, relative to the true RMS strength of $J_r(r_1)$, computed using eq. (8.46). For the upper curve the radial dependence of J_r has been neglected, which corresponds to setting $\rho_J(r_0, r_1) \equiv 1$ in eq. (8.46)

In summary, Figures 8.1 to 8.4 show that the prediction according to approximation (8.18) is correct on average. Errors are rather large for small radial separations but increase only slowly with increasing $r_1 - r_0$. In particular, none of the spherical harmonic coefficients experiences a change in sign. Hence, approximation (8.18) is likely to provide a simple and fairly accurate way of dealing with field-aligned currents. It may be particularly useful for the joint inversion of synchronous data from multiple satellites at different heights.

8.4 Discussion and conclusions

The interpretation of satellite magnetic data requires an efficient discretization of the magnetic field in the shell of measurements $S(a, c)$. We need one set of parameters each for the poloidal fields due to currents internal to $S(a)$ and external to $S(c)$. Backus (1986) suggests to use a third parameter α for field-aligned currents through $S(a, c)$. As a simple alternative, we propose to expand the toroidal magnetic field scalar q according to the mean radial behavior inferred from a dipolar system of field-aligned currents. Comparing the exact

radial behavior of the current density in a synthetic field-aligned current system with our approximation, we find that the approximation is correct on average and surprisingly stable for large radial separations. However, whether the ansatz is indeed useful in practice will have to be verified on real satellite data.

Future synchronous measurements by multiple satellites will improve the spatial and temporal resolution of the magnetic field. For such data one may consider extending the model space to include poloidal fields due to toroidal currents in $S(a, c)$, and higher order toroidal field scalars. The spherical harmonic degree up to which to expand each of these parameters depends on the scope of the investigation and the quality of the data. Two important issues have not been addressed here. One is how to deal with the temporal variation of the ionospheric current systems. The other is the problem of continuing the Gauss coefficients g_ℓ^m and k_ℓ^m in eq. (8.5) from satellite altitude down to the Earth's surface, which requires further models for the electric current systems in between.

References

Alexander, J., Bridge, J. S., Leeder, M. R., Collier, R. E. L., and Gawthorpe, R. L., 1994, Holocene meander-belt evolution in an active extensional basin, Southwest Montana: J. Sed. Res., **B64, 4**, 542–559.

Arkani-Hamed, J., and Dyment, J., 1996, Magnetic potential and magnetization contrasts of the earth's lithosphere: J. Geophys. Res., **101**, 11,401–11425.

Arkani-Hamed, J., Langel, R. A., and Purucker, M., 1994, Scalar magnetic anomaly maps of Earth derived from POGO and Magsat data: J. Geophys. Res., **99**, 24,075–24,090.

Backus, G., Parker, R., and Constable, C., 1996, Foundations of geomagnetism: Cambridge Univ. Press.

Backus, G., 1986, Poloidal and toroidal fields in geomagnetic field modeling: Rev. Geophys., **24**, 75–109.

Bhattacharyya, B. K., and Leu, L. K., 1975, Analysis of magnetic anomalies over Yellowstone National Park: mapping Curie point isothermal surface for geothermal reconnaissance: J. Geophys. Res., **80**, 4461–4465.

Bittner, A., Sengpiel, K. P., Siemon, B., Röttger, B., Voß, W., and Pielawa, J., 1994, Exploration drilling proposal:, volume B-II BGR-Archives No. 112 775, Hannover.

Blakely, R. J., 1988, Curie temperature isotherm analysis and tectonic implications of aeromagnetic data from Nevada: J. Geophys. Res., **93**, 11817–11832.

Blakely, R. J., 1995, Potential theory in gravity and magnetic applications: Cambridge Univ. Press.

Bloxham, J., and Jackson, A., 1992, Time-dependent mapping of the magnetic field at the core-mantle boundary: J. Geophys. Res., **97**, 19537–19563.

Brown, G. S., 1977, The average impulse response of a rough surface and its applications: IEEE Trans. Antennas Propagat., **25**, 67–74.

Cain, J. C., Wang, Z., Kluth, C., and Schmitz, D. R., 1989, Derivation of a geomagnetic model to n = 63: Geophys. J. Int., **97**, 431–441.

Challenor, P. G., and Srokosz, M. A., 1989, The extraction of geophysical parameters from radar altimeter return from a non-linear sea surface, *in* Brooks, S. R., Ed., Mathematics in Remote Sensing: Oxford: Clarendon Press, 257–268.

Chapin, D. A., 1996, A deterministic approach towards isostatic gravity residuals-A case study from South America: Geophysics, **61**, 1022–1033.

Connard, G., Couch, R., and Gemperle, M., 1983, Analysis of aeromagnetic measurements from the Cascade Range in central Oregon: Geophysics, **48**, 376–390.

Cressie, N. A. C., 1993, Statistics for spatial data: John Wiley.

Forsberg, R., Local covariance functions and density distributions:, Technical Report 356, Dept. of Geod. Sci. and Surv., Ohio State Univ., Columbus, 1984.

Frost, B. R., and Shive, P. N., 1986, Magnetic mineralogy of the lower continental crust: J. Geophys. Res., **91**, 6513–6521.

Goff, J. A., and Jordan, T. H., 1988, Stochastic modeling of seafloor morphology: Inversion of sea beam data for second-order statistics: J. Geophys. Res., **93**, 13589–13608.

Gradsteyn, I. S., and Ryzhik, I. M., 1994, Table of integrals, series, and products: Academic Press Ltd, London.

Green, C. M., Fairhead, J. D., and Maus, S., 1998, Satellite derived gravity: Where we are and what's next: Leading Edge, **17**, 77–79.

Gregotski, M. E., Jensen, O. G., and Arkani-Hamed, J., 1991, Fractal stochastic modeling of aeromagnetic data: Geophysics, **56**, 1706–1715.

Hahn, A., Kind, E. G., and Mishra, D. C., 1976, Depth estimation of magnetic sources by means of Fourier amplitude spectra: Geophys. Prosp., **24**, 287–308.

Hanssen, A., 1997, Multidimensional multitaper spectral estimation: Signal Processing, **58**, 327–332.

Haxby, W. F., Karner, G. D., LaBreque, J. L., and Weissel, J. K., 1983, Digital images of combined oceanic and continental data sets and their use in tectonic studies: EOS, **64**, 995–1004.

Herzfeld, U. C., and Brodscholl, A. L., 1994, On the geologic structure of the Explora Escarpment (Weddell Sea, Antarctica) revealed by satellite and shipboard data evaluation: Marine Geophys. Res., **16**, 325–345.

Holme, R., and Jackson, A., 1997, The cause and treatment of attitude errors in near-earth geomagnetic data: Phys Earth Planet. Inter., **103**, 375–388.

Jackson, A., 1990, Statistical treatment of crustal magnetization: Geophys. J. Int., **119**, 991–998.

Jackson, A., 1994, Accounting for crustal magnetization in models of the core magnetic field: Geophys. J. Int., **103**, 657–673.

Jackson, A., 1996, Bounding the long-wavelength crustal magnetic field: Phys. Earth Planet. Int., **98**, 283–302.

Kaula, W. M., 1967, Theory of statistical analysis of data distributed over a sphere: Rev. Geophys., **5**, no. 1, 83–107.

Kolmogorov, A. N., 1941, Local structure of turbulence in an incompressible fluid at very high Reynolds numbers: Dokl. Akad. Nauk SSSR, **30**, no. 4, 299–303.

Kolmogorov, A. N., 1961, Local structure of turbulence in an incompressible fluid at very high Reynolds numbers (english translation), *in* Friedlander, S. K., and Topper, L., Eds., Turbulence. Classical papers on statistical theory: Interscience, Ney York, 151–155.

Langel, R. A., and Estes, R. H., 1982, A geomagnetic field spectrum: Geophys. Res. Lett., **9**, 250–253.

Leeder, M. R., and Alexander, J., 1987, The origin and tectonic significance of asymmetrical meander belts: Sedimentology, **34**, 217–226.

Lemoine, F. G., Pavlis, N. K., Kenyon, S. C., Rapp, R. H., Pavlis, E. C., and Chao, B. F., 1998, New high-resolution model developed for Earth's gravitational field: EOS, **79,9**, 113, 117–118.

Lowes, F. J., 1966, Mean-square values on sphere of spherical harmonic vector fields: J. Geophys. Res., **71**, 2179.

Lowes, F. J., 1974, Spatial power spectrum of the main geomagnetic field, and extrapolation to the core: Geophys. J. R. astr. Soc., **36**, 717–730.

Mandelbrot, B. B., 1983, The fractal geometry of nature: W. H. Freeman.

Marks, K. M., and Sailor, R. V., 1986, Comparison of GEOS-3 and SEASAT altimeter resolution capabilities: Geophys. Res. Lett., **13**, 697–700.

Mauersberger, P., 1956, Das Mittel der Energiedichte des geomagnetischen Hauptfeldes an der Erdoberfläche und seine säkulare Änderung: Gerlands Beitr. Geophys., **65**, 207–2015.

Maus, S., and Dimri, V. P., 1994, Scaling properties of potential fields due to scaling sources: Geophys. Res. Lett., **21**, 891–894.

Maus, S., and Dimri, V. P., 1995a, Basin depth estimation using scaling properties of potential fields: J. Ass. Expl. Geophys., **16**, 131–139.

Maus, S., and Dimri, V. P. 1995b, Potential field power spectrum inversion for scaling geology: J. Geophys. Res., **100**, 12605–12616.

Maus, S., and Dimri, V. P., 1996, Depth estimation from the scaling power spectrum of potential fields?: Geophys. J. Int., **124**, 113–120.

Maus, S., Pohl, J., Soffel, H., and Saradeth, S., 1993, Interpretation of an aerogeophysical survey (gamma ray spectrometry, electromagnetics and magnetics) in the KTB area: KTB-Report, **93-2**, 317–318.

Maus, S., Sengpiel, K. P., and Tordiffe, E. A. W., 1996, Variogram analysis of magnetic data to identify paleochannels of the Omaruru River in Namibia: 66th Ann. Internat. Mtg., Soc. Expl. Geophys., Expanded Abstracts, 1381–1383.

Maus, S., Gordon, D., and Fairhead, J. D., 1997, Curie-temperature depth estimation using a self-similar magnetization model: Geophys. J. Int., **129**, 163–168.

Maus, S., Green, C. M., and Fairhead, J. D., 1998, Improved ocean geoid resolution from retracked ERS-1 satellite altimeter waveforms: Geophys. J. Int., **134**, 243–253.

Maus, S., Sengpiel, K. P., Siemon, B., Röttger, B., and Tordiffe, E. A. W., 1999, Variogram analysis of helicopter magnetic data to identify paleochannels of the Omaruru River, Namibia: Geophysics, **64**, no. 3, 785–794.

Maus, S., Röttger, B., and Sengpiel, K. P., 2000, Magnetic variogram depth: tests on synthetic and real data: 70th Ann. Internat. Mtg., Soc. Expl. Geophys., Expanded Abstracts.

Maus, S., 1995, Potential field power spectrum inversion for scaling geology: Ph.D. thesis, Osmania University, Hyderabad, India.

Maus, S., 1996, Scaling statistical analysis of magnetic and gravity data: 66th Ann. Internat. Mtg., Soc. Expl. Geophys., Expanded Abstracts, 1419–1421.

Maus, S., 1999, Variogram analysis of magnetic and gravity data: Geophysics, **64**, no. 3, 776–784.

Maus, S., 2000, Is there an observable lack of reciprocity in PKP(DF) travel times?: Geophys. J. Int., in print.

Mayhew, M. A., Johnson, B. D., and Wasilewski, P. J., 1985, A review of problems and progress in studies of satellite magnetic anomalies: J. Geophys. Res., **90**, 2511–2522.

McKenzie, D., 1994, The relationship between topography and gravity on Earth and Venus: Icarus, **112**, 55–88.

McLeod, M. G., and Coleman, P. J., 1980, Spatial power spectra of the crustal geomagnetic field and core magnetic field: Phys. Earth Planet. Inter., **23**, 5–19.

McLeod, M. G., 1996, Spatial and temporal power spectra of the geomagnetic field: J. Geophys. Res., **101**, 2745–2763.

Miller, R. M., and Schalk, K. E. L., 1980, Geological Map of Namibia scale 1:1.000.000: Geological Survey, Windhoek, Namibia.

Naidu, P. S., 1968, Spectrum of the potential field due to randomly distributed sources: Geophysics, **33**, 337–345.

Nawrowski, J., 1993, An overview of the hydrogeology in the Omaruru Alluvial Plains (OMAP): Geohydrology Division Memorandum, DWA, Windhoek.

Negi, J. G., Agrawal, P. K., and Rao, K. N. N., 1983, Three-dimensional model of the Koyna area of Maharashtra State (India) based on the spectral analysis of aeromagnetic data: Geophysics, **48**, 964–974.

O'Brien, M. S., Parker, R. L., and Constable, C. G., 1999, Magnetic power spectrum of the ocean crust on large scales: J. Geophys. Res., **104**, 29,189–29,202.

Okubo, Y., and Matsunaga, T., 1994, Curie point depth in northeast Japan and its correlation with regional thermal structure and seismicity: J. Geophys. Res., **99**, 22363–22371.

Okubo, Y., Graf, R. J., Hansen, R. O., Ogawa, K., and Tsu, H., 1985, Curie point depths of the island of Kyushu and surrounding areas, Japan: Geophysics, **50**, 481–494.

Olgiati, A., Balmino, G., Sarrailh, M., and Green, C. M., 1995, Gravity anomalies from satellite altimetry; comparison between computation via geoid heights and via deflections of the vertical: Bulletin Geodesique, **69**, 252–260.

Olsen, N., 1997, Ionospheric F region currents at middle and low latitudes estimated from Magsat data: J. Geophys. Res., **102**, no. A3, 4563–4576.

Parker, R. L., and O'Brien, M. S., 1997, Spectral analysis of vector magnetic field profiles: J. Geophys. Res., **102**, 24,815–24,824.

Paterson, N. R., and Reeves, C. R., 1985, Applications of gravity and magnetic surveys: The state-of-the-art in 1985: Geophysics, **50**, 2558–2594.

Pilkington, M., and Todoeschuck, J. P., 1990, Stochastic inversion for scaling geology: Geophys. J. Int., **102**, 205–217.

Pilkington, M., and Todoeschuck, J. P., 1993, Fractal magnetization of continental crust: Geophys. Res. Lett., **20**, 627–630.

Pilkington, M., and Todoeschuck, J. P., 1995, Scaling nature of crustal susceptibilities: Geophys. Res. Lett., **22**, 779–782.

Pilkington, M., Todoeschuck, J. P., and Gregotski, M. E., 1994, Using fractal crustal magnetization models in magnetic interpretation: Geophys. Prosp., **42**, 677–692.

Priestley, M. B., 1981, Spectral analysis and time series:, volume 2: Multivariate series, prediction and control Academic Press.

Rapp, R. H., 1983, The determination of geoid undulations and gravity anomalies from Seasat altimeter data: J. Geophys. Res., **88**, 1552–1562.

Rapp, R. H., 1986, Gravity anomalies and sea surface heights derived from a combined GEOS 3/Seasat altimeter data set: J. Geophys. Res., **91**, 4867–4876.

Rapp, R. H., 1989, The decay of the spectrum of the gravitational potential and the topography for the Earth: Geophys. J. Int., **99**, 449–455.

Reid, A. B., Allsop, J. M., Granser, H., Millett, A. J., and Somerton, I. W., 1990, Magnetic interpretation in three dimensions using euler deconvolution: Geophysics, **55**, 80–91.

Riedel, K. S., and Sidorenko, A., 1995, Minimum bias multiple taper spectral estimation: IEEE Trans. Sig. Proc., **43**, no. 1, 188–195.

Sandwell, D. T., and McAdoo, D. C., 1990, High-accuracy, high-resolution gravity profiles from 2 years of Geosat exact repeat mission: J. Geophys. Res., **95**, 3049–3060.

Sandwell, D. T., and Smith, W. H. F., 1997, Marine gravity anomaly from Geosat and ERS-1 satellite altimetry: J. Geophys. Res., **102**, 10039–10054.

Schlinger, C. M., 1985, Magnetization of lower crust and interpretation of regional crustal anomalies: Example from Lofoten and Vesterøalen, Norway: J. Geophys. Res., **90**, 11484–11504.

Schwarz, K. P., Sideris, M. G., and Forsberg, R., 1990, The use of FFT techniques in physical geodesy: Geophys. J. Int., **100**, 485–514.

Sengpiel, K. P., Maus, S., and Röttger, B., 2000, Calculated configuration and relative magnetisation of the basement rocks in the Kuiseb Dune helicopter survey area:, *in* Follow-up report Vol. 3 BGR-Archives No. 117 600, Hannover.

Sengpiel, K.-P., 1988, Approximate inversion of airborne EM data from a multi-layered ground: Geophys. Prosp., **36**, 446–459.

Serson, P. H., and Hannaford, W. L. W., 1957, A statistical analysis of magnetic profiles: J. Geophys. Res., **62**, 1–18.

Shuey, R. T., Schellinger, D. K., Tripp, A. C., and Alley, L. B., 1977, Curie depth determination from aeromagnetic spectra: Geophys. J. R. astr. Soc., **50**, 75–101.

Siebert, M., 1965, Zur theorie erdmagnetischer pulsationen mit breitenabhängigen perioden:, Mitteilungen aus dem Max-Planck-Institut für Aeronomie Springer Verlag.

Spector, A., and Grant, F. S., 1970, Statistical models for interpreting aeromagnetic data: Geophysics, **35**, 293–302.

Tokmakian, R. T., Challenor, P. G., Guymer, T. H., and Srokosz, M. A., 1994, The U.K. EODC ERS-1 altimeter oceans processing scheme: Int. J. Remote Sensing, **15**, 939–962.

Turcotte, D. L., 1987, A fractal interpretation of topography and geoid spectra on the Earth, Moon, Venus, and Mars: J. Geophys. Res., **92**, E597–E601.

Vacquier, V., and Affleck, J., 1941, A computation of the average depth to the bottom of the Earth's magnetic crust, based on a statistical study of local magnetic anomalies: Trans. Am. Geophys. Union, **22**, 446–450.

Wasilewski, P. J., and Mayhew, M. A., 1992, The Moho as a magnetic boundary revisited: Geophys. Res. Lett., **19**, 2259–2262.

Wasilewski, P. J., Thomas, H. H., and Mayhew, M. A., 1979, The Moho as a magnetic boundary: Geophys. Res. Lett., **6**, 541–544.

Whaler, K. A., 1994, Downward continuation of Magsat lithospheric anomalies to the Earth's surface: Geophys. J. Int., **116**, 267–278.

Yaglom, A. M., 1986, Correlation theory of stationary and related random functions:, volume 1 Springer-Verlag New York.

Yale, M. M., Sandwell, D. T., and Smith, W. H. F., 1995, Comparison of along-track resolution of stacked Geosat, ERS-1, and Topex satellite altimeters: J. Geophys. Res., **100**, 16117–15127.

Index